# A Survey of Beam Asymmetries in Semi-Exclusive Electron Scattering on $^4$He and $^{12}$C

BY

Dan Protopopescu

B.S., Bucharest University, 1996
M.S., Bucharest University, 1997

DISSERTATION

Submitted to the University of New Hampshire
in partial fulfillment of
the requirements for the degree of

Doctor of Philosophy

in

Physics

December 2002

This dissertation has been examined and approved.

Director, F. William Hersman
Professor of Physics

John R. Calarco
Professor of Physics

John F. Dawson
Professor of Physics

Maurik Holtrop
Professor of Physics

James Ryan
Professor of Physics

Lawrence Weinstein
Professor of Physics (ODU)

Date

# Dedication

*Profesorului N. Ghiordănescu, care a crezut în mine*

*pe vremea când chiuleam ca un derbedeu.*

# Acknowledgments

Lots of thanks to Prof. S. Stepanyan who patiently supervised my on-site activity at Jlab and had to deal with hundreds of questions that I found necessary to ask along these three years. Without him, my Jlab experience would have been different.

From the University of New Haphshire Physics department I would like to thank my advisor Bill Hersman for his continuous support and patience during my graduate years and to John Calarco, John Dawson and Maurik Holtrop for fruitful discussions.

A very important contribution during the work on this thesis came from Prof. Larry Weinstein of Old Dominion University, VA, to whom I would like to thank for guidance and active involvement. The most detailed comments and suggestions during the finalization of this material came from Larry. Without his feedback, this material would have been less rigourous.

I would like to thank to Jan Ryckebusch and Dimitri Debruyne of Gent University, Belgium, and to James Kelly of U. Maryland for providing us with theoretical calculations and useful comments.

Not of less importance, I would also like to acknowledge the crucial contribution of the staff of the Accelerator and Physics Divisions of the TJNAF as well as the outstanding support of the Hall B technical staff.

This work has been supported by research grants from the U.S. Department of Energy.

# Table of Contents

# List of Tables

# List of Figures

# ABSTRACT

A Survey of Beam Asymmetries in Semi-Exclusive Electron Scattering on $^4$He and $^{12}$C

by

Dan Protopopescu
University of New Hampshire, December, 2002

A study of the polarized electron beam asymmetry in semi-exclusive $(e, e'p)$ reactions on $^4$He and $^{12}$C over a large kinematic range has been performed. The beam asymmetry $A'_{LT}$ is related to the imaginary part of the longitudinal-transverse interference and therefore it vanishes in reactions proceeding through a channel with a single dominant mechanism. In quasifree nucleon knockout, the helicity asymmetry provides an unambiguous signature for the interference between direct knockout and rescattering amplitudes. The data were taken in April-May 1999 using polarized beams of energies between 2.2 and 4.4 GeV, with the CEBAF Large Acceptance Spectrometer (CLAS) detector located in Hall B at the Jefferson Laboratory, VA. The measured asymmetries compare well with the theoretical predictions.

# CHAPTER 1

# INTRODUCTION

Over the last several decades, electron scattering has proved to be a powerful tool for the study of the structure and dynamics of atomic nuclei. This is because the leptonic part of the interaction, described by the quantum electrodynamics (QED), is well understood and the only uncertainties in modeling the reaction are restricted to the nuclear part, i.e. to the physics governing the structure and the dynamics of the nucleus.

Electron scattering can be used to investigate a variety of nuclear and nucleonic properties. Since electrons interact very weakly, their mean free path within nuclear matter is large enough to probe the entire nuclear volume. Therefore, deeply bound nucleons can be studied. This is an important advantage over studies employing hadronic probes, which have larger cross-sections and therefore higher event rates, but whose sensitivity is restricted mainly to the nuclear surface. From a theoretical point of view, the weak character of the electromagnetic interaction allows the use of the Born approximation, which greatly simplifies the form of the scattering cross-section.

In electron scattering, the incident electron transfers energy ($\omega$) and momentum ($\boldsymbol{q}$) to the target via exchange of a virtual photon. Here one finds the advantage of electron scattering over real photon experiments in that that one can vary the transferred momentum $\boldsymbol{q}$ and energy $\omega$ of the virtual photon independently from each other, allowing a wider range

of flexibility in the choice of kinematics.

At momentum transfers $|\boldsymbol{q}|$ above several hundreds of MeV/c, the virtual photon's wavelength is of the the order of $10^{-15}$ m so that it can resolve objects of the size of the nucleon. At this scale, the nucleus behaves as a collection of strongly interacting individual nucleons, with the effects of nucleon structure modeled by electromagnetic form-factors that describe the charge and magnetization distributions of the nucleons. The modeling of a typical many-body nucleus ($A > 3$) at this scale is based on the independent single-particle (s.p.) model, where nucleons move independently within a mean-field potential. The single-particle potential can be obtained using a Hartree-Fock technique, with three-body forces and density dependencies added later.

Since the electron scattering can transfer a rather low energy combined with a large momentum, it favors the direct interaction with a single nucleon. Among those kinematics, the quasielastic regime is the most suitable for the study of the single particle structure of the nucleus. The quasielastic regime is centered around an energy transfer $\omega = Q^2/2M$ ($x_B = 1$), where M is the mass of the nucleon and $Q$ is the four-momentum transfer. This is the same relation as for the free electron-nucleon scattering process. In a quasielastic $(e, e'N)$ reaction, all the energy and momentum of the virtual photon can be transferred to the outgoing nucleon, so that energy and momentum conservation allows the initial nucleon's energy and momentum to be specified. Coincident $(e, e'p)$ measurements can be used in conjunction with the plane wave impulse approximation (PWIA)[1] to determine the combined nucleon-hole energy and momentum distribution, the so-called spectral function of the target nucleus.

During the last forty years, coincident $(e, e'p)$ scattering has been extensively used to probe the single particle properties of nuclei, starting with the pioneering experiments of

Amaldi *et al.* in 1964 [1] and Campos Venuti *et al.* in 1973 [2], which demonstrated the existence of shell-model orbitals. Experimental work in this field was later pursued in Tokyo (Nakamura *et al.* 1976 [3]) and Saclay (Mougey *et al.* 1976 [4], Frullani and Mougey 1984 [5]), where the properties of the bound and outgoing nucleon wave functions were investigated in detail. More recent measurements were performed at NIKHEF (de Witt Huberts 1990 [6], Leuschner *et al.* 1994 [7]), MIT-BATES (Finn *et al.* 1984 [8], Lourie *et al.* 1986 [9], Ulmer *et al.* 1987 [10], Weinstein *et al.* 1990 [11], Holtrop *et al.* 1998 [12] , Dolfini *et al.* 1999 [13]), Mainz (Blomqvist *et al.* 1995 [14]) and in the last several years at TJNAF (Gao *et al.* 2000 [15], Ulmer *et al.* 2001 [16]).

While $(e, e'p)$ can conclusively establish single particle knockout as the dominant reaction channel, this reaction has sufficient sensitivity and selectivity to idetify and characterize secondary processes. There is evidence to suggest that other reaction channels contribute to the strength in this region, like meson exchange currents[1] (MEC), $\Delta$-isobar[1] configurations, multi-nucleon knockout or final-state rescattering. Gaining an understanding of these secondary processes has become the subject of intense experimental and theoretical investigations.

The first findings came from measurements involving the Rosenbluth separation of the longitudinal and transverse components of the cross-section. If the process taking place at quasielastic kinematics would be truly quasifree, then the longitudinal and transverse components of the spectral function, $S_L$ and $S_T$, should be equal. This is because $S_L$ and $S_T$ correspond to the probability of finding a nucleon by coupling to its charge or by coupling to its magnetism, respectively. Indeed, in measurements of the coincidence $(e, e'p)$ reaction in quasielastic kinematics on $^3$He, the longitudinal and transverse components of

[1] explained in chapter 2

the spectral function $S_L$ and $S_T$ were found equal, as expected [17, 18]. However, for heavier nuclei like $^4$He or $^{12}$C the picture gets more complicated. Ducret *et al.* found out that the longitudinal strength in $^4$He is suppressed with respect to the transverse one by 20-40% [19]. For $^{12}$C at quasielastic kinematics, Ulmer *et al.* (1987) found $S_L$ and $S_T$ to be equal for two-body breakup but observed an enhancement of $S_T$ over $S_L$ at higher missing energies. It was speculated that the enhancement may come from some new transverse process involving two or more nucleons.

One of the main requirements towards a quantitative interpretation of the data is a better understanding of the final-state interaction (FSI) supported by a relativistic theory that includes single-nucleon, multi-nucleon and non-nucleonic degrees of freedom [20]. Our theoretical colleagues can provide us now with advanced models that include these ingredients. To gain a clear understanding of FSI effects, these models need to be tested on experimental observables that are especially sensitive to final state interactions.

The effects of FSI can not be separated directly in a cross-section measurement. They can be identified, however, through their interference with the dominant process. Thus the ideal observable is the beam helicity asymmetry, $A'_{LT}$, because it arises from the interference between the amplitudes corresponding to direct knockout and to rescattering through FSI [21, 22].

In general, $A'_{LT}$ corresponds to the longitudinal-transverse interference component of the hadron tensor. It vanishes whenever the reaction proceeds through a channel with a single dominant phase because in this case the hadron tensor is real. Therefore, at least two interfering complex reaction amplitudes with different phases are necessary to produce a non-zero $A'_{LT}$. $A'_{LT}$ is expected to be highly sensitive to FSI and much less to other effects like, for example, MEC. $A'_{LT}$ provides the best observable for monitoring rescattering effects

in knockout reactions [23]. This observable lets us test our models in the intermediate $Q^2$ region which is not yet well understood. The DWIA[2] is the usual approach at low four-momentum transfer ($Q^2 < 1\,\mathrm{GeV}^2/\mathrm{c}^2$). At high $Q^2$, where the scattering becomes highly diffractive, the potential description becomes impractical and Glauber multiple-scattering theory becomes the natural framework for the qualitative description of FSI. For the intermediate region we have the optical model in eikonal approximation (OMEA)[1] developed by the Gent group [24] with the purpose of bridging the two regimes.

Measurements of $A'_{LT}$ require polarized electron beams. In this case the differential cross-section contains two terms: a helicity-independent term $\Sigma$ and a helicity-dependent term $h\Delta$, with $h$ standing for the electron helicity $h = \pm 1$. They can be separated in the helicity asymmetry $A'_{LT}$ defined as[1]

$$A'_{LT} = \frac{d\sigma^+ - d\sigma^-}{d\sigma^+ + d\sigma^-} = \frac{\Delta}{\Sigma} \tag{1.1}$$

and measured by simply flipping the beam helicity. In this formula, the $d\sigma^+$ and $d\sigma^-$ denote differential cross-sections corresponding to the "+1" and "–1" helicities, respectively. Uncertainties induced by acceptance are in this case eliminated and microscopic factors are not required for comparison with the theory.

In the past, spin degrees of freedom were seldom considered, mainly due to the technical difficulties raised by the task of preparing polarized beams and targets. Since reliable high-current polarized electron sources are available, at Mainz, MIT-Bates and NIKHEF, for intermediate-energy physics, and at TJNAF for higher energies, measurements of $A'_{LT}$ have became possible. Two previous measurements of $A'_{LT}$ were carried out at MIT-Bates by

[2] explained in chapter 2

Mandeville *etal.*, 1994 [25] and Jiang *etal.*, 1998 [26][3]. The measurements of Mandeville *et al.* revealed that the $A'_{LT}$ shows a great sensitivity to the choice of the optical model and that only small corrections are necessary to compensate for the effects due to $\Delta$-isobar configurations. Jiang *et al.* found reasonable agreement between the measurements of $A'_{LT}$ and DWIA predictions. One issue that both Mandeville *et al.* and Jiang *et al.* agreed upon is that more data, with higher statistical accuracy, would be necessary in order to further test the existing models.

To date, no measurements of $A'_{LT}$ in $^4$He were done. But $^4$He is interesting in that that it is a simple enough nucleus to be modeled theoretically and, despite being a four-body system, $^4$He is a high density nucleus. The latter is a good reason to believe that an exhaustive analysis of FSI effects in $^4$He would give a good insight to the significance of these effects in heavier nuclei.

The object of this thesis is a survey of $A'_{LT}$ asymmetries in $(\vec{e}, e'p)$ reactions on $^{12}$C and $^4$He in the quasielastic regime, exploring kinematics not previously accessible. The focus is on the following issues:

1. How much of the strength in the quasielastic peak is due to something other than direct knockout ?

2. Can a low luminosity, large acceptance device achieve sufficient statistics on these asymmetries in fine enough kinematic bins to make relevant comparisons ?

3. What is the nature of the non-quasielastic strength in the quasielastic peak and can present models account for it ?

4. We have models which successfully reproduce the $L$, $T$, $LT$ components of the cross-

[3]see footnote for Jiang *et al.* in Chapter 2

section. Are they comparably accurate in describing the $LT'$ term ?

The outline of this thesis is as follows. In Chapter 2 the formalism for the relevant A$(\vec{e}, e'p)$ observables and kinematics is reviewed and a brief description of the theoretical models is given. A brief discussion of the previous measurements of $A'_{LT}$ is also included. The experimental setup at TJNAF (JLab), where the measurements were taken, is presented in Chapter 3. The analysis techniques, including detector calibrations, data corrections and cuts, are discussed in Chapter 4. The physics extraction and the comparison with theory are done in Chapter 5, which ends with a summary and an outlook.

# CHAPTER 2

# The $(\vec{e}, e'p)$ Reaction

The extraction of physical information from measured A$(\vec{e}, e'p)$ asymmetries involves some theoretical modeling of which the major ingredients are: (1) the initial bound state, (2) the final scattering proton wave-functions and (3) electromagnetic electron-nucleus coupling.

At lower values of $Q^2$ ($Q^2 < 1\,\mathrm{GeV}^2/\mathrm{c}^2$), the usual approach is the use of DWIA (distorted wave impulse approximation), well tested by more than two decades of high-quality electron scattering data. DWIA is based on the assumption that the initial (bound) and final (scattering) states of the struck nucleon can be computed in a potential model while the off-shell electron-nucleus coupling can be put in a corrected electron-proton form. At high momentum-energy transfer ($Q^2 > 1\ \mathrm{GeV}^2/\mathrm{c}^2$), most theoretical work is based on a Glauber model [41]. The Glauber theory is very successful in describing small-angle proton-nucleus scattering at higher energies [42] and is considered as a baseline for calculating the effect of final state interactions in high-energy (e,e'p) reactions. The Glauber theory is a multiple-scattering extension of the standard eikonal approximation that relates the ejected particle's distorted wave function to the elastic proton scattering amplitude by means of a profile function [43].

A fully relativistic model for the description of A$(e, e'p)$ reactions that bridges the gap between the low and intermediate energy regimes, described in [24, 44], was used for the

calculations that accompany our data. Structure functions and polarization observables calculated with these models were previously successfully tested against $^4$he, $^{12}$C and $^{16}$O data [45]. The longitudinal-transverse response function was found to be sensitive to relativistic effects.

In the first sections of this chapter we will define the kinematic variables and review some cross-section basics. Then a brief account of the ingredients of the three theoretical models mentioned above will be given. The chapter will close with a detailed discussion of the previous measurements of $A'_{LT}$.

## 2.1 Kinematics

In one-proton knockout experiments, an electron and a proton are detected in coincidence and therefore their energy and momentum are measured. If only one reaction channel is open, i.e. if the state of the residual nucleus is fixed through the kinematics, then we have an exclusive reaction. On the other hand, if the residual nucleus is left in a continuum state and can fragment, one is dealing with an inclusive reaction where more complicated processes take place.

The one-photon-exchange approximation (OPEA) will be used here. This approximation assumes that the incoming electron and the nucleus (nucleon) interact through the exchange of one single virtual photon. The OPEA approximation is easily justified in QED by the fact that the probability for each additional photon exchange is diminished by a factor of $Z\alpha \approx Z/137 \ll 1$.

Electron scattering in the one-photon-exchange approximation is schematically shown in figure 2-1. The target nucleus has $A$ nucleons. Except for $q$, where we use the convention $Q^2 = -q_\nu q^\nu \geq 0$, we denote the four-vectors by capital letters $K, P, P'$ etc. and the three-

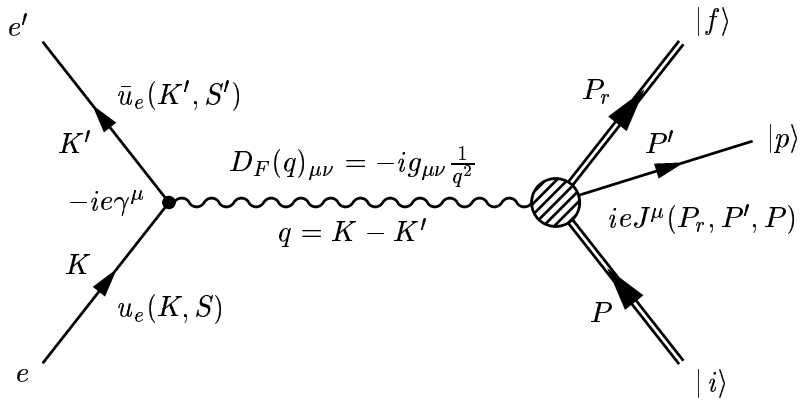


Figure 2-1: Lowest order graph for the exclusive $(\vec{e}, e'p)$ electron scattering process.

vectors by bold lower case letters $\boldsymbol{q}, \boldsymbol{k}, \boldsymbol{p}, \boldsymbol{p'}$ etc.

The missing energy $E_m$ and momentum $p_m$ can be reconstructed as:

$$E_m = \omega - T_p - T_r \qquad \boldsymbol{p}_m = \boldsymbol{q} - \boldsymbol{p'} \tag{2.1}$$

where $\boldsymbol{q} = \boldsymbol{k} - \boldsymbol{k'}$ and, $\omega = E_e - E'_e$ are the momentum and energy transferred by the electron, respectively, $T_p$ is the outgoing proton's kinetic energy and $T_r$ is the kinetic energy of the recoiling system.

If final-state interactions (FSI) can be neglected, then $\boldsymbol{p}_m$ would be equal and opposite to the initial momentum $\boldsymbol{p}$ of the emitted proton, thus giving information about the energy and momentum distribution of the protons in the nucleus.

Referring to the threshold separation energy of the proton,

$$\Delta E = m_p + M_{A-1} - M_A$$

one obtains from (2.1)

$$E_m = \Delta E + E^* \tag{2.2}$$

where $E^*$ is the excitation energy of the residual nucleus A-1.

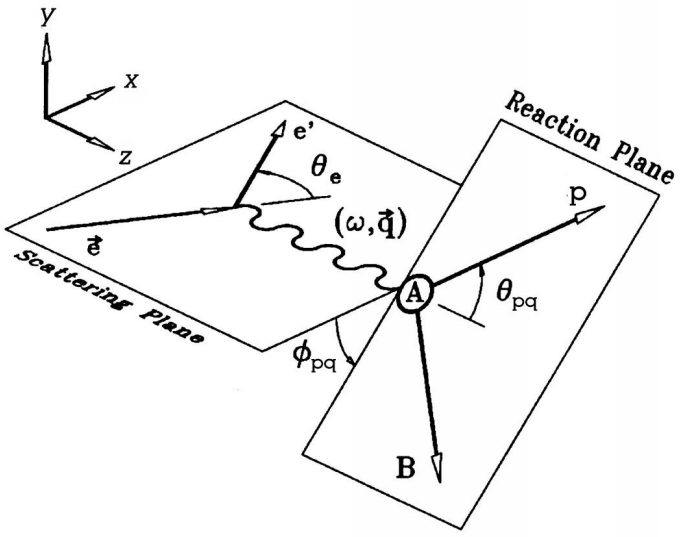


Figure 2-2: Kinematics for the semi-exclusive $(\vec{e}, e'p)$ process. (figure from [13]).

## 2.2 The $(\vec{e}, e'p)$ Differential Cross-Section

Electron scattering in the one-photon-exchange approximation (OPEA) described by the diagram in Fig. 2-1 is schematically illustrated in figure 2-2. An electron of initial energy $E_e$ scatters through an angle $\theta_e$ to a final energy $E'_e$. The scattering and reaction planes are explicitly shown. The target nucleus is denoted A and the recoiling system is denoted B. The ejected proton is detected in coincidence with the scattered electron $e'$. The coordinate system is chosen so that the $z$-axis lies along the momentum transfer $\boldsymbol{q}$ and the $y$-axis is perpendicular to the scattering plane, parallel to $\boldsymbol{k} \times \boldsymbol{k'}$. In the ultra-relativistic limit the electron helicity states $h = +1$ and $h = -1$ correspond to spin parallel and antiparallel to $\boldsymbol{k}$, respectively. In diagram (2-1) the virtual photon is represented by the propagator $D_F(Q)_{\mu\nu} = ig_{\mu\nu}/Q^2$.

The differential scattering cross-section in the laboratory frame can be written as [40]:

$$d\sigma = \frac{1}{\beta}\frac{m_e^2}{E_e E_e'}\overline{\sum_{if}}|\mathcal{M}_{fi}|^2\,\frac{d^3\boldsymbol{k'}}{(2\pi)^3}\frac{M_r}{E_r}\frac{d^3\boldsymbol{p_r}}{(2\pi)^3}\frac{m_p}{E_p}\frac{d^3\boldsymbol{p'}}{(2\pi)^3}(2\pi)^4\delta^{(4)}(q+P-P'-P_r) \tag{2.3}$$

where $\beta = |\boldsymbol{k}|/E_e = |\boldsymbol{v}_e| \approx 1$ and the sum corresponds to the appropriate average over the initial states and sum over the final states. The invariant matrix element $\mathcal{M}_{fi}$ corresponding to the given process depends on the electromagnetic electron current $j_\mu(K', S'; K, S)$ and nuclear electromagnetic transition current $J^\mu(P_r, P'; P)_{fi}$ as

$$\mathcal{M}_{fi} = e\sqrt{\frac{E_e E_e'}{m_e^2}}\,j_\mu(K', S'; K, S)\frac{i}{Q^2}J^\mu(P_r, P'; P)_{fi} \tag{2.4}$$

where $(-e)$ is the electron charge.

In semi-exclusive measurements, the momentum of the residual nucleus is not determined and then one can integrate (2.3) over $\boldsymbol{p_r}$ to obtain

$$\frac{d^5\sigma}{dE_e' d\Omega_e d\Omega_p} = \frac{m_e^2 m_p}{(2\pi)^5}\frac{M_r}{M_A}\frac{k'}{k}p' f_{rec}^{-1}\overline{\sum_{if}}|\mathcal{M}_{fi}|^2 \tag{2.5}$$

where $M_r$ is the mass of the recoiling $A-1$ system and $f_{rec}$ is the hadronic recoil factor

$$f_{rec} = \left|\,1 + \frac{\omega p' - qE_p\cos\theta_{pq}}{p' M_A}\,\right| \tag{2.6}$$

and $\theta_{pq}$ is the angle between $\boldsymbol{q}$ and $\boldsymbol{p}_p$ (see Fig. 2-2). It is customary to write

$$\overline{\sum_{if}}|\mathcal{M}_{fi}|^2 = \left(\frac{4\pi\alpha}{Q^2}\right)^2 l_{\mu\nu}(K', S'; K, S)W^{\mu\nu}(Q)_{fi} \tag{2.7}$$

where $\alpha = e^2/4\pi \simeq 1/137$ is the fine structure constant and $l_{\mu\nu}(K', S'; K, S)$ and $W^{\mu\nu}(Q)_{fi}$

are the leptonic and the nuclear tensors, respectively, defined as

$$l_{\mu\nu}(K',S';K,S) \equiv \overline{\sum_{if}} (\bar{u_e}(K',S')\gamma_\mu u_e(K,S))^* \, (\bar{u_e}(K',S')\gamma_\nu u_e(K,S)) \tag{2.8}$$

$$W^{\mu\nu}(Q) \equiv \overline{\sum_{if}} J^{*\mu}(Q)_{fi} J^\nu(Q)_{fi} \tag{2.9}$$

The tensor $W^{\mu\nu}(Q)$ incorporates all the structure and dynamics information about the nucleus, but as we said, the leptonic tensor $l_{\mu\nu}$ contains no secrets.

In general, the cross section (2.5) for the scattering of arbitrarily polarized electrons from nuclei contains up to four types of terms, depending on whether the incident and/or scattered electrons are polarized [39]. In our experiment, a longitudinally polarized beam is employed but the spin of the scattered electrons is not measured. In these conditions, $l_{\mu\nu}(K',S';K,S) \equiv l_{\mu\nu}(K';K,S)$ and we retain two terms only

$$\left(\frac{d^5\sigma}{dE'_e d\Omega_e d\Omega_p}\right)^h_{fi} = \Sigma_{fi} + h\Delta_{fi} \tag{2.10}$$

where $fi$ refers to the transition from an initial state labeled $i$ to a final hadronic state labeled $f$ which involves the final nuclear state $E_r$ accompanied by the emission of a proton $p'$, and $h$ is the helicity state. The term $\Sigma_{fi}$ is independent of the electron polarization.

If one does the algebra, one finds out that the contraction of the electron and nuclear tensors from (2.8,2.9) can be put in the form [40]:

$$4m_e^2 \, l_{\mu\nu}(K';K,S) W^{\mu\nu}(Q)_{fi} = v_o \sum_i v_i R_i \tag{2.11}$$

where the label $i$ takes the values $L, T, LT, TT, T', LT'$, $\underline{TT}$, $\underline{LT}$, $\underline{LT'}$. These labels refer to the longitudinal and transverse components of the virtual photon polarization and therefore,

they correspond to the electromagnetic current components with respect to the direction of $\boldsymbol{q} = \boldsymbol{k} - \boldsymbol{k'}$. Double subscripts indicate interference terms. For longitudinally polarized beams, the underlined factors are suppressed by a factor of $m_e/E_e$. In the energy range in which our experiment was done, $m_e/E_e \ll 1$ and we neglect these terms. More, if the target is unpolarized, the $T'$ term vanishes as well. Now the nuclear structure and dynamics information is contained in the response functions $R_i$ and the electron kinematics in the factors[1] $v_i$:

$$\begin{aligned} v_L &= \left(\frac{Q^2}{|\boldsymbol{q}|^2}\right)^2 \\ v_T &= \frac{Q^2}{2|\boldsymbol{q}|^2} + \tan^2\frac{\theta_e}{2} \\ v_{TT} &= -\frac{Q^2}{2|\boldsymbol{q}|^2} \\ v_{LT} &= -\frac{Q^2}{|\boldsymbol{q}|^2\sqrt{2}}\left(\frac{Q^2}{2|\boldsymbol{q}|^2} + \tan^2\frac{\theta_e}{2}\right)^{1/2} \\ v'_{LT} &= -\frac{Q^2}{|\boldsymbol{q}|^2\sqrt{2}}\tan\frac{\theta_e}{2} \end{aligned} \tag{2.12}$$

and $v_o$ is defined as $v_o = (E_e + E'_e)^2 - |\boldsymbol{q}|^2$. If we want the azimuthal dependence on $\phi_{pq}$ to be shown explicitly, the differential cross section in the laboratory frame (2.10) looks like

$$\begin{aligned} \left(\frac{d^5\sigma}{dE'_e d\Omega_e d\Omega_p}\right)^h_{fi} &= K\sigma_M(v_T f_T + v_L f_L + v_{TT} f_{TT}\cos 2\phi_{pq} + v_{LT} f_{LT}\cos\phi_{pq} \\ &\quad + h v'_{LT} f'_{LT}\sin\phi_{pq}) = \Sigma_{fi} + h\Delta_{fi} \end{aligned} \tag{2.13}$$

$\sigma_M$ is the Mott cross section, corresponding to elastic Coulomb scattering from an infinitely

[1] in our notation, the prime from the label is moved to the function name, e.g. $v_{LT'} \to v'_{LT}$

massive point target, and $K$ includes the phase-space and recoil factors:

$$\sigma_M = \frac{\alpha^2 \cos^2(\theta_e/2)}{4E_e^2 \sin^4(\theta_e/2)} \qquad K = \frac{m_p M_r}{8\pi^3 M_A} p' f_{rec}^{-1} \tag{2.14}$$

The response functions which make up the cross section (2.13) provide independent observables which are sensitive selectively to various aspects of the nuclear current. Hence, in addition to measuring cross sections, the extraction of these additional observables can considerably help us achieve a complete picture of the structure and dynamics of the nucleus.

## 2.3 Beam Helicity Asymmetry

The contribution of the $LT'$ term from (2.10) to the total cross-section (2.13) can be experimentally measured with minimal systematic errors in the form of the beam helicity asymmetry:

$$A'_{LT} = \frac{d^5\sigma^+ - d^5\sigma^-}{d^5\sigma^+ + d^5\sigma^-} \tag{2.15}$$

where $\sigma^+$ and $\sigma^-$ are the cross sections corresponding to positive and negative incident electron helicity, respectively. Due to its complex dependence on $\phi_{pq}$, the $A'_{LT}$ asymmetry gives a precise account of the relative strengths of the relevant amplitudes:

$$A'_{LT} = \frac{v'_{LT} f'_{LT} \sin\phi_{pq}}{v_L f_L + v_T f_T + v_{LT} f_{LT} \cos\phi_{pq} + v_{TT} f_{TT} \cos 2\phi_{pq}} \tag{2.16}$$

In what follows we will investigate what type of theoretical models could be used to predict the behavior of $A'_{LT}$ from (2.16).

## 2.4 Initial Bound State

The traditional approach to the study of nuclear structure and the nucleon-nucleon interaction used to be a non-relativistic Scrödinger framework, where nuclei are regarded as bound states of nucleons interacting via two- and three-body potentials. More sophisticated nucleon-nucleon potentials accommodate meson exchange currents as well as relativistic effects (section 2.7.2).

Following the discussion from [24], relativistic models have several advantages compared to the non-relativistic ones: in a field-theoretic approach the mesonic degrees of freedom can be implemented right from the start and the relativistic kinematics and spin-orbit interaction (which is inserted by hand in non-relativistic approaches) emerge naturally.

The modern approach is based on a relativistic quantum field theory where nucleons interact with each other by exchanging mesons, as originally introduced by Walecka in [50]. In the "$\sigma - \omega$" model, which is an extension of the Walecka approach, nucleons ($\psi$) interact with scalar mesons ($\phi$) through a Yukawa coupling ($\bar{\psi}\psi\phi$) and with neutral vector mesons ($V_\mu$) that couple to the conserved baryon current $\bar{\psi}\gamma_\mu\psi$. The model was extended to include $\pi$ and $\rho$ mesons, as well as coupling to the photon field. The Lagrangian density used in [24] is:

$$\begin{aligned}
\mathcal{L} &= \bar{\psi}(i\not{\partial} - M)\psi + \frac{1}{2}(\partial_\mu\phi\partial^\mu\phi - m_s^2\phi^2) - \frac{1}{4}G_{\mu\nu}G^{\mu\nu} + \frac{1}{2}m_\nu^2 V_\mu V^\mu \\
&- g_\nu\bar{\psi}\gamma_\mu\psi V^\mu + g_s\bar{\psi}\psi\phi + \frac{1}{2}(\partial_\mu\boldsymbol{\pi}\cdot\partial^\mu\boldsymbol{\pi} - m_\pi^2\boldsymbol{\pi}\cdot\boldsymbol{\pi}) - ig_\pi\bar{\psi}\gamma_5\boldsymbol{\tau}\cdot\boldsymbol{\pi}\psi \\
&- \frac{1}{4}\boldsymbol{B}_{\mu\nu}\boldsymbol{B}^{\mu\nu} + \frac{1}{2}m_\rho^2\boldsymbol{b}_\mu\cdot\boldsymbol{b}^\mu - \frac{1}{2}g_\rho\bar{\psi}\gamma_\mu\boldsymbol{\tau}\cdot\boldsymbol{b}^\mu\psi - \frac{1}{4}F_{\mu\nu}F^{\mu\nu} \\
&- eA_\mu[\bar{\psi}\gamma^\mu\frac{1}{2}(1+\tau_3)\psi + (\boldsymbol{b}_\nu\times\boldsymbol{B}^{\mu\nu})_3 + (\boldsymbol{\pi}\times(\partial^\mu\boldsymbol{\pi} + g_\rho(\boldsymbol{\pi}\times\boldsymbol{b}^\mu)))_3]
\end{aligned} \tag{2.17}$$

with $M$ the nucleon mass, $m_s$ and $m_\nu$ the scalar and vector meson masses, $\boldsymbol{\pi}$, $\boldsymbol{b}_\mu$ and $A_\mu$ the pion, rho and Maxwell fields, respectively, while $\boldsymbol{B}^{\mu\nu}$ and $F^{\mu\nu}$ are the rho meson and electromagnetic field strengths.

The complete problem is approximated by replacing the meson fields with their expectation values:

$$\langle \phi(r) \rangle = \phi_0(r) \qquad \langle V^\mu(r) \rangle = \delta^{\mu 0} V_0(r) \tag{2.18}$$

The infinite-matter approximation from [50] was replaced by a relativistic Hartree approximation which leads to a theory similar in content except that one has to deal with a finite system.

The Hartree approximation leads to a set of coupled equations for the fields. The entering nucleon masses and coupling constants are taken from experiment or calculated from limit conditions.

Starting from an initial guess of the scalar and vector potential in a Woods-Saxon form, the Dirac equations are solved iteratively. Once the nucleon wave functions are obtained, the densities of the meson fields are reevaluated.

The initial bound-state wavefunction used with DWIA is calculated within the NLSH model of Sharma, Nagarajan and Ring [92].

## 2.5 Electron-nucleon Coupling

The matrix elements of the nucleon current are written as

$$\langle P_f, S_f | \hat{J}^\mu | P_i S_i \rangle = \bar{u}_f(P_f, S_f) \Gamma^\mu(q^\mu, P_f, P_i) u_i(P_i, S_i) \tag{2.19}$$

where $\Gamma^\mu$ is the electromagnetic vertex function for the nucleon and $u_i$, $u_f$ are the nucleon spinors. For a *free* nucleon, $\Gamma^\mu$ can be expressed in several fully equivalent forms, of which the most widely used are

$$\Gamma^\mu_{cc1} = G_M(Q^2)\gamma_\mu - \frac{\kappa}{2m_p}F_2(Q^2)(P_i^\mu + P_f^\mu) \tag{2.20}$$

$$\Gamma^\mu_{cc2} = F_1(Q^2)\gamma_\mu + i\frac{\kappa}{2m_p}F_2(Q^2)\sigma^{\mu\nu}q_\nu \tag{2.21}$$

Here $F_1$ and $F_2$ are the Dirac and Pauli form factors, respectively, $\sigma^{\mu\nu} = \frac{1}{2}i(\gamma^\mu\gamma^\nu - \gamma^\nu\gamma^\mu)$, and $G_M = F_1 + \kappa F_2$ is the Sachs magnetic form-factor where $\kappa$ is the anomalous magnetic moment of the proton. When considering bound (off-shell) protons, however, the above functions are no longer equivalent.

In calculations of $(e, e'p)$ reactions on finite nuclei, current conservation is restored by hand, using one of the substitutions

$$J_3 \to \frac{\omega}{q}J_0 \qquad \Longrightarrow \qquad J_\mu = (J_0, J_1, J_2, \frac{\omega}{q}J_0), \tag{2.22}$$

$$J_0 \to \frac{q}{\omega}J_3 \qquad \Longrightarrow \qquad J_\mu = (\frac{q}{\omega}J_3, J_1, J_2, J_3) \tag{2.23}$$

or, for example

$$J_\mu \to J_\mu + \frac{J_\nu q^\nu}{Q^2}q_\mu$$

The expression (2.22) is in general preferred because the charge distribution $J_0$ of the target is usually better known from experiment. However, the ambiguities introduced by the choice of one or the other current conservation restoration scheme decrease with increasing $Q^2$ [24].

The transition matrix element (2.4) corresponding to the electron scattering process in

its most general form is

$$\mathcal{M}_{fi} = j_\mu \Pi_{\mu\nu} J^\nu \tag{2.24}$$

where $j_\mu$ is the leptonic (electron) current and $\Pi_{\mu\nu}$ is the photon propagator which reduces in the Feynman gauge to $D_{\mu\nu} = ig_{\mu\nu}/Q^2$. The explicit form of $\Pi_{\mu\nu}$ is gauge dependent and, in consequence, so is the matrix element. The most frequently adopted is the Coulomb gauge where $\mathcal{M}_{fi}$ is written as

$$\mathcal{M}_{Coulomb} = \frac{i}{\boldsymbol{q}^2} j_0 J_0 - \frac{i}{Q^2}\left(\boldsymbol{j}\cdot\boldsymbol{J} - \frac{(\boldsymbol{q}\cdot\boldsymbol{j})(\boldsymbol{q}\cdot\boldsymbol{J})}{\boldsymbol{q}^2}\right) \tag{2.25}$$

which is the result of using the Feynman propagator in (2.24) with the substitution (2.22) for the nucleon current. Another choice would be

$$\mathcal{M}_{Weyl} = -\frac{i}{Q^2}\left(\boldsymbol{j}\cdot\boldsymbol{J} - \frac{(\boldsymbol{q}\cdot\boldsymbol{j})(\boldsymbol{q}\cdot\boldsymbol{J})}{\boldsymbol{q}^2}\right) \tag{2.26}$$

obtained in the same manner but using (2.23) this time.

## 2.6 Final State Interactions

The most straightforward approach to $(e, e'p)$ scattering is the plane wave impulse approximation (PWIA), where the wave function of the outgoing proton is approximated with a plane wave as if the outgoing proton does not interact with the residual nucleus anymore.

When this residual interaction is to be considered, though, some corrections to this simplistic model are needed. When the final state interaction is taken into account as a distortion of the wave function of the outgoing proton, one gets the next approximation, the DWIA, where the 'D' stands for 'distorted'. In this model, the interaction between the

outgoing proton and the residual nucleus is modeled by an optical potential.

At high four-momentum transfers, the optical potential approach becomes inaccurate since the scattering is increasingly diffractive. The final state interaction is then modeled as multiple rescattering of the outgoing proton on the individual nucleons.

### 2.6.1 Impulse Approximation

The impulse approximation (IA) is based on the assumptions that the nucleus can be treated as a collection of noninteracting nucleons and that the dynamical behavior of the individual nucleons is not modified by the nuclear medium. In these conditions, the nuclear current is given by the sum of the currents of the individual nucleons treated as free particles, *i.e.* $J^\mu$ is written as

$$J^\mu(P_r, P'; P)_{fi} = J^\mu(Q)_{fi} = \bar{u}_f \Gamma^\mu(P', P_i) u_i \tag{2.27}$$

with $P_i$ the initial proton momentum within the nucleus, $u_i$ and $u_f$ the proton (distorted) spinors and $\Gamma^\mu$ the electromagnetic vertex function for the nucleon.

### 2.6.2 Plane Wave Impulse Approximation

When the impulse approximation (2.27) is used in conjunction with the assumption that the outgoing proton wave function can be approximated with a plane wave (no FSI), one obtains the Plane Wave Impulse Approximation (PWIA).

In general, the scattering state $\chi^{(-)}_{Ea}$ and the bound state $\psi_{Ea}$ are solutions of the eigen-

value equations:

$$\sum_l \mathcal{H}_{ml}(E)\psi_{l,Ea} = E\psi_{m,Ea} \tag{2.28}$$

$$\sum_l \mathcal{H}^{\dagger}_{ml}(E+\omega)\chi^{(-)}_{l,Ea} = (E+\omega)\chi^{(-)}_{m,Ea} \tag{2.29}$$

where $\mathcal{H}_{ml}(E)$ is a one-body Hamiltonian of the Feshbach form but referred to the residual nucleus. The $|Ea\rangle$ are the eigenstates of the residual nucleus with A-1 nucleons characterized by the energy E and an additional set of quantum numbers $a$ [23].

In the PWIA the scattering wave function in momentum space $\chi^{(-)}_{Ea}$ from (2.29) becomes a delta-function centered on the observed momentum of the outgoing nucleon. In this approximation, the integral

$$J^{\mu}(Q)_{fi} = \int d\boldsymbol{p}\, e^{i\boldsymbol{q}\cdot\boldsymbol{r}}\, \chi^{(-)}_{Ea}(\boldsymbol{p}+\boldsymbol{q})(\hat{J}^{\mu}_{eff})_{Ea}(\boldsymbol{p},\boldsymbol{q})\psi_{Ea}(\boldsymbol{p})\sqrt{S_{\alpha}(E)} \tag{2.30}$$

can be performed immediately with the result that in the coincidence $(e,e'p)$ cross-section a factorization is possible between the electron-nucleon interaction and the nuclear structure part given by the diagonal spectral density $S(E,\boldsymbol{p})$. The PWIA cross-section has the form:

$$\frac{d^5\sigma}{dE'_e d\Omega_e d\Omega_p} = K\sigma_{ep}S(E,\boldsymbol{p}) \tag{2.31}$$

with $K$ given by (2.14) and $\sigma_{ep}$ is the off-shell electron-proton cross section [49]. The spectral function $S(E,\boldsymbol{p})$ contains all the information on the single particle properties of the nucleus. Equation (2.31) tells that this type of reaction is able to give detailed information on the single-particle structure of the nuclei.

The explicit expressions for the structure functions $f_i$ (eq. 2.13) are easily obtained in

PWIA. The nuclear structure part of the electron-nucleon interaction can be factorized out such that:

$$f_i = S(E, \boldsymbol{p})\, g_i \tag{2.32}$$

where the index $i$ is the one from (2.11) and the functions $g_i$ contain the separated contributions to the elementary electron-nucleon scattering cross-section.

The PWIA is able to reproduce the qualitative features of the nuclear response and in particular it explains the peaks in the cross-section that reflect the shell structure of the nucleus. However, it can not give a quantitative description of the experimental data. The most important correction needed is for the effects of FSI, as will be discussed in the following subsection.

### 2.6.3 Distorted Wave Impulse Approximation

In general, the nucleon scattering state $\chi^{(-)}_{Ea}$ is an eigenfunction of the Feshbach Hamiltonian $\mathcal{H}^{\dagger}(E_i+\omega)$ from eq. (2.29). The solution to this problem is simplified in DWIA by replacing $\mathcal{H}$ with an optical potential, which simulates the medium-field interaction between the residual nucleus and the ejected nucleon. The optical potential is complex with a real part describing the average potential energy of the nucleon crossing the nuclear medium and an imaginary part which takes into account the loss of flux due to inelastic processes.

### 2.6.4 Eikonal Approximation

This approximation covers a situation in which the potential $V(\boldsymbol{r})$ varies very little over a distance of the order of a wavelength $\lambda$ (which can be regarded as small). The potential itself need not be weak as long as $E \gg |V|$. The exact wave function $u^{(+)}_{\boldsymbol{p},s}$ is replaced by

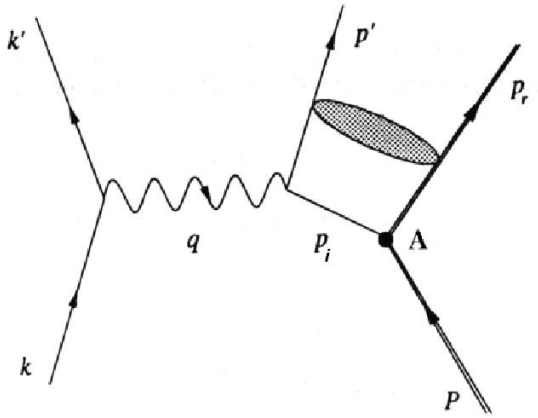


Figure 2-3: Diagram for the semi-exclusive (e,e'p) reaction. The DWIA adds to the PWIA diagram the FSI, symbolized here by the shaded area.

the semi-classical:

$$u^{(+)}_{\boldsymbol{p},s} = e^{i\boldsymbol{p}\cdot\boldsymbol{r}} e^{iS(\boldsymbol{r})} \chi_{\frac{1}{2}m_s} \tag{2.33}$$

with the eikonal phase

$$S(\boldsymbol{b}, z) = -\frac{m_p}{\kappa} \int_{-\infty}^{z} dz' \{V_c(\boldsymbol{b}, z') + V_{so}(\boldsymbol{b}, z') \times [\boldsymbol{\sigma} \cdot (\boldsymbol{b} \times \boldsymbol{\kappa}) - i\kappa z']\} \tag{2.34}$$

where we introduced the notation $\boldsymbol{r} \equiv (\boldsymbol{b}, z)$, $V_c$ and $V_{so}$ are the central and spin-orbit components of the potential $V$, respectively, and $\kappa$ is the average momentum defined as

$$\kappa = \frac{1}{2}(\boldsymbol{p'} + \boldsymbol{q})$$

where $\boldsymbol{q} = \boldsymbol{p'} - \boldsymbol{p}_i$ and $q \gg p_i$. In quasielastic regime that we calculate, will set $\boldsymbol{q} = \boldsymbol{p'}$.

### 2.6.5 Optical Model Eikonal Approximation

The OMEA is an optical model based on a fully relativistic framework, using a relativistic optical potential in conjunction with the eikonal approximation. Its validity ranges from intermediate to high $Q^2$.

The inelastic contributions to the exit channel are taken into account by the complex optical potential constructed from fits to *nucleon-nucleus* data. The scattering wave function is proportional to

$$\Psi^{(+)}_{\boldsymbol{p},S} = \sqrt{\frac{E+m_p}{2m_p}}\, e^{iS(\boldsymbol{r})} \begin{bmatrix} 1 \\ \frac{1}{E+m_p+V_s-V_v}(\boldsymbol{\sigma}\cdot\boldsymbol{p}) \end{bmatrix} \exp(i\boldsymbol{p}\cdot\boldsymbol{r})\, \chi_{\frac{1}{2}m_s} \tag{2.35}$$

with the eikonal phase given by (2.34) and $V_c$ and $V_{so}$ obtained from global optical potential fits. It is normalized so that:

$$\lim_{r\to\infty} \Psi^{(+)}_{\boldsymbol{p},S}(\boldsymbol{r}) = \Psi^{PWIA}_{\boldsymbol{p},S}(\boldsymbol{r}) \tag{2.36}$$

The optical potential used with the OMEA calculations contained in this thesis is that of Cooper *et al.* [48]. By fitting proton elastic scattering data in the energy range of 20–1040 MeV, they succeeded in obtaining a set of energy-dependent potentials for $^{12}$C , $^{40}$Ca, $^{90}$Zr and $^{208}$Pb [2]. The general form of their potential is:

$$\begin{aligned} \mathcal{U}(r,E,A) &= V^v(E,A)f^v(r,E,A) + V^s(E,A)f^s(r,E,A) \\ &\quad - iW^v(E,A)g^v(r,E,A) \\ &\quad + iW^s(E,A)g^s(r,E,A), \end{aligned} \tag{2.37}$$

[2] but not for $^4$He

where the superscripts $v$ and $s$ refer to volume and surface peaked terms and the geometries are parametrized through the functions $f^v(E,A) = f^v(R(E,A), a(E,A))$. Same for $f^s, g^v, g^s$. The energy and mass dependence of the potential are parametrized in a set of polynomials in the expressions of $V^v(E,A), R(E,A)$ and $a(E,A)$. The model provides a set of 264 parameters, which are determined by comparison with the data.

One must note, however, that in OMEA the optical potential is used in a completely different manner compared to DWIA. While the OMEA uses (2.34) to integrate along the path of the outgoing nucleon, the DWIA solves (2.29) with the Hamiltonian replaced by the optical potential.

### 2.6.6 Relativistic Multiple-Scattering Glauber Approximation

For proton kinetic energies $T_p \geq 1\,\mathrm{GeV}$, the use of optical potentials appears no longer justifiable in view of the highly inelastic character of the elementary proton-nucleon scattering process. An alternative is offered by an extension of the eikonal method, namely the Glauber multiple-scattering method.

The RMSGA is a relativistic generalization of the Glauber approach, in which the wavefunction of the escaping proton is written as:

$$\Psi^{(+)}_{\boldsymbol{p},S} = \sqrt{\frac{E+m_p}{2m_p}}\,\hat{S}\begin{bmatrix} 1 \\ \frac{1}{E+m_p}(\boldsymbol{\sigma}\cdot\boldsymbol{p}) \end{bmatrix} \exp(i\boldsymbol{p}\cdot\boldsymbol{r})\,\chi_{\frac{1}{2}m_s} \tag{2.38}$$

The operator $\hat{S}$ defines the action of subsequent collisions that the outgoing proton undergoes with the spectator nucleons

$$\hat{S}(\boldsymbol{r},\boldsymbol{r}_2,\boldsymbol{r}_3,\ldots,\boldsymbol{r}_A) = \prod_{j=2}^{A}\left[1-\Gamma(\boldsymbol{b}-\boldsymbol{b}_j)\theta(z-z_j)\right] \tag{2.39}$$

where $\theta(z - z_j)$ ensures that the ejectile only interacts with other nucleons if they are localized in its forward propagation path. The spectator nucleons are considered as frozen and the collisions are considered elastic or mildly elastic. $\Gamma(\boldsymbol{b} - \boldsymbol{b}_j)$ is the profile function for elastic $pN$ scattering

$$\Gamma(p_f, b) = \frac{\sigma_{pN}^{tot}(1 - i\epsilon_{pN})}{4\pi(\beta_{pN})^2} \exp\left(-\frac{b^2}{2\beta_{pN}^2}\right) \tag{2.40}$$

with the *proton-nucleon* scattering parameters taken directly from nucleon-nucleon scattering measurements (appendix D.1). These parameters are the total $pN$ cross-section $\sigma_{pN}^{tot}$, the slope parameters $\beta_{pN}$ and the ratios of the real to imaginary part of the scattering amplitude $\epsilon_{pN}$.

## 2.7 Review of Previous Experiments

### 2.7.1 Cross-section measurements

The analysis of the $^{12}$C$(e, e'p)$ reaction gives a nice example of what can be learned from quasifree electron knockout on light nuclei. This reaction has been studied in great detail and with high-resolution experiments [3, 4, 9, 10, 11, 12].

Figure 2-4 shows missing energy spectra of the $^{12}$C$(e, e'p)$ reaction from experiments done in 1976 at Saclay [4] (a) and Tokyo [3] (b). Three regions, present on the missing energy spectrum of all nuclei, can be seen on (Fig.2-4.a): at low $E_m$ they are peaks corresponding to the valence states, then weakly excited states and at higher energy a large bump appears containing the continuum states, corresponding in $^{12}$C to proton knockout from the $(1s_{1/2})$ level or to more complicated mechanisms.

High energy resolution ($\sim 1\,$MeV) of the Mougey *et al.* experiment allows to isolate

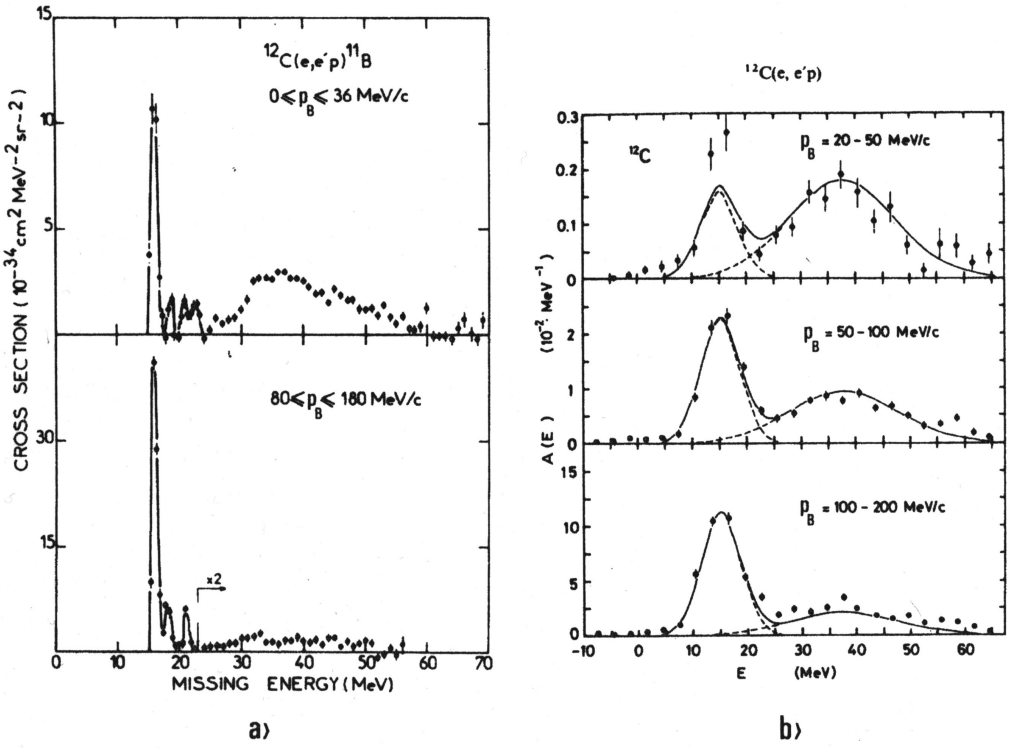


Figure 2-4: Missing energy spectra for the $^{12}$C$(e, e'p)$ reaction, within different missing momentum ($p_B$) bins: (a) from J. Mougey *et al.* [4] (1976). (b) from K. Nakamura *et al.* [3] (1976). The data is well reproduced by DWIA.

the first few levels of the residual $^{11}$B nucleus (Fig. 2-4.a): the ground state ($\frac{3}{2}^-$) at approximately 16 MeV in $E_m$, the $E_x = 2.12$ MeV excited state ($\frac{1}{2}^-$, $E_m \approx 18$ MeV) and the $E_x = 5.02$ MeV state ($\frac{3}{2}^-$, $E_m \approx 21$ MeV). The relative strengths of the three $p$-states were measured to be 74, 13 and 9%, respectively, with a residual 4% attributed to higher excitations. A short-lived, low-energy component of the $1s$-hole strength for the $\frac{1}{2}^+$ level ($E_x = 6.79$ MeV) can be seen as a wide peak centered around 40 MeV on Fig. 2-4.b. The spreading of the $1s$-hole strength indicates the breakdown of the simplest single-particle (IPSM) picture.

Figure 2.7.1 shows the missing energy spectrum measured by R. Lourie *et al.* [9]. The two $p$-shell excitations mentioned above ($\frac{1}{2}^-$ and $\frac{3}{2}^-$) are not resolved here. A uniform

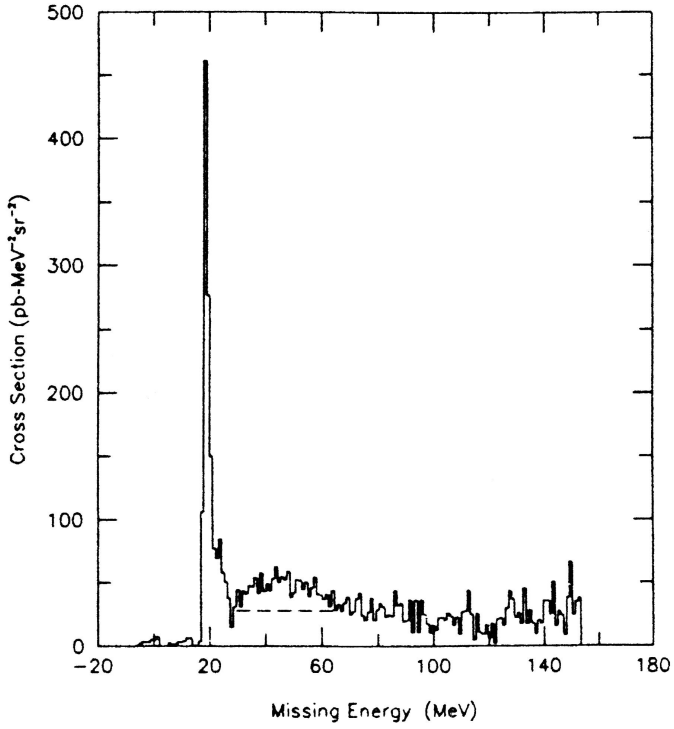


Figure 2-5: Missing energy spectra for $^{12}C(e,e'p)$ at quasielastic kinematics from R. Lourie *et al.* [9]. The area above the dashed line is attributed to the $s$-shell.

continuum strength is found in the missing energy region extending from the $s$-shell up to the highest measured value. This strength can be partly attributed to two-body and multinucleon emission.

A more recent experiment on $^{16}O$ could be cited in order to illustrate the presence of multi-particle contributions at high $E_m$. $^{16}O$ has been a favorite nucleus for theorists, being a doubly closed-shell nucleus whose structure is easier to model than other nuclei. Experimentally, oxygen has been studied extensively. However, it is not as convenient a target as carbon for example, hence less experimental data are available from $^{16}O(e,e'p)$ reactions [7, 14].

Figure 2-6 shows cross-sections measured by N. Liyanage *et al.* for $^{16}O(e,e'p)$, as a

function of missing energy at $E_{beam} = 2.4\,\mathrm{GeV}$, for various proton angles $2.5^o < \theta_{pq} < 20^O$. The average missing momentum increases with $\theta_{pq}$ from 50 MeV/c to 340 MeV/c. The data are accompanied by several sets of calculations. The prominent peaks at 12 MeV and 18 MeV in $E_m$ are due to $p$-shell proton knockout. At the lowest missing momentum, $p_{miss} = 50\,\mathrm{MeV/c}$, the broad peak centered at $E_m = 40\,\mathrm{MeV}$ is due predominantly to knockout of protons from the $1s_{1/2}$ state. With increasing $p_{miss}$, this peak is less prominent until it vanishes completely beneath a flat background for $p_{miss} > 200\,\mathrm{MeV/c}$. At these values of missing momentum or for $E_m > 60\,\mathrm{MeV}$ the cross-section does not depend on $E_m$ and only very weakly of $p_{miss}$.

DWIA calculations by Kelly [53] accurately describe the $1p$-shell cross-section up to missing momenta of 340 MeV/c (see also. J. Gao *et al.* [15]). At larger $p_{miss}$, the DWIA cross-section is much smaller than the measured one. Relativistic DWIA calculations by other authors [55] show similar results, confirming the attribution of the large missing momentum cross-section to non-single-nucleon knockout. The importance of these mechanisms increases with $p_{miss}$ such that at missing momenta above 300 MeV/c they become dominant.

The $(e, e'pn)$ and $(e, e'pp)$ contributions to $(e, e'p)$ are taken into account by the Ryckebusch calculation [54] including pion-exchange currents, IC as well as central and tensor SRC (dashed line on Figure 2-6). The flat cross-section predicted by this calculation is consistent with the data but it can account for only half of the measured cross-section. This hints toward additional contributions from MEC and two-nucleon knockout [52]. Measurements of additional observables are needed to verify these contributions.

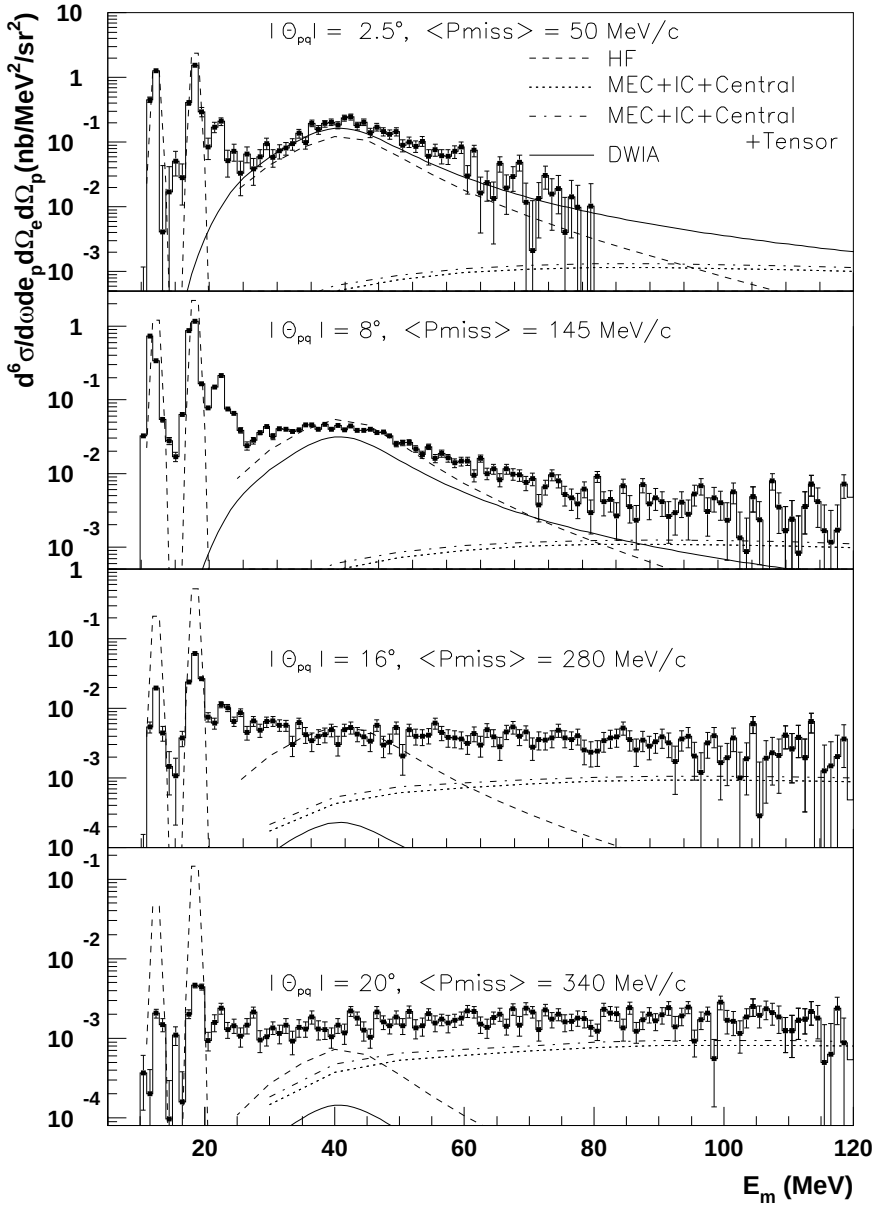


Figure 2-6: $^{16}$O$(e,e'p)$ cross-section measured at different outgoing proton angles as a function of missing energy from N. Liyanage *et al.* [52]. The curves show the single-particle strength calculated by J. Kelly ($s$-shell only, solid curve) and by J. Ryckebusch (dashed curve), folded with the Lorentzian parameterization of Mahaux. The dotted line shows the Ryckebusch *et al.* calculations of the $(e,e'pn)$ and $(e,e'pp)$ contributions to $(e,e'p)$ including MEC, IC and central correlations, while the dot-dashed line also includes tensor correlations. (from N. Liyanage *et al.* [52]).

### 2.7.2 $A'_{LT}$ measurements

Two experiments measured of $A'_{LT}$ in $^{12}$C$(e, e'p)$ reactions, both at the MIT-Bates laboratory. To date, we are not aware of any measurements of $A'_{LT}$ with $^4$He targets.

The first measurement of the helicity asymmetry on $^{12}$C was carried out in 1994 and is reported by Mandeville *et al.* [25] and Dolfini *et al.* [13]. They used a 560 MeV beam with a duty factor of 0.6% and a polarization $P_B = (34 \pm 4)\%$. P-shell proton knockout data were taken for the $^{12}$C (e,e'p)$^{11}$B reaction in the quasielastic kinematics at a momentum transfer $q$ = 370 MeV/c. Measurements were made for two different angles ($21^o$ and $29^o$) of the outgoing proton momentum with respect to the momentum transfer $\boldsymbol{q}$, with an out-of-plane spectrometer (OOPS) located at $\phi_{pq} = 90^o$ (above the scattering plane). By performing an absolute measurement of the helicity-independent part of the cross-section, they also extracted the fifth response function:

$$f'_{LT} = \frac{A'_{LT}\Sigma}{K\sigma_M v'_{LT}}$$

Their results are shown in figure 2-7, along with DWIA calculations. The point at $\theta_{pq} = 0^o$ in Fig.2.7(a), taken as a systematic error check, is measured with deuterium in parallel kinematics, where $f'_{LT}$ should be null. The theoretical calculations that accompany the three data points were performed in the DWIA framework employing different mean-field optical models to describe FSI.

Figure 2.7(a) is taken from reference [25]. The optical potentials used with DWIA are the ones of Schwandt *et al.* [57] and Comfort & Karp (CK) [58]. Figure 2.7(b) is taken from reference [13]. The optical potentials used are the ones of Schwandt *et al.* (S), Comfort & Karp (CK), Giannini & Ricco (GR) [60] and Jackson & Abdul-Jalil (JA) [59].

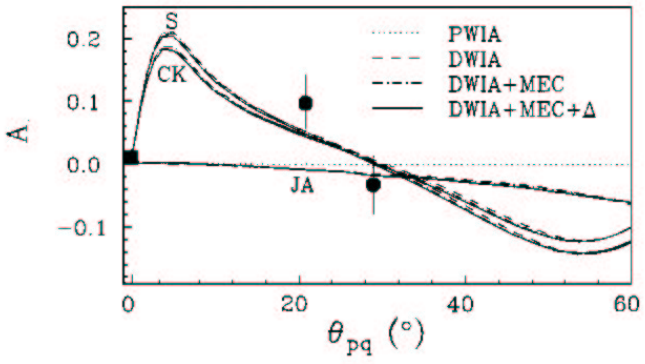


(a) The $A'_{LT}$ asymmetry measurement reported in [25].

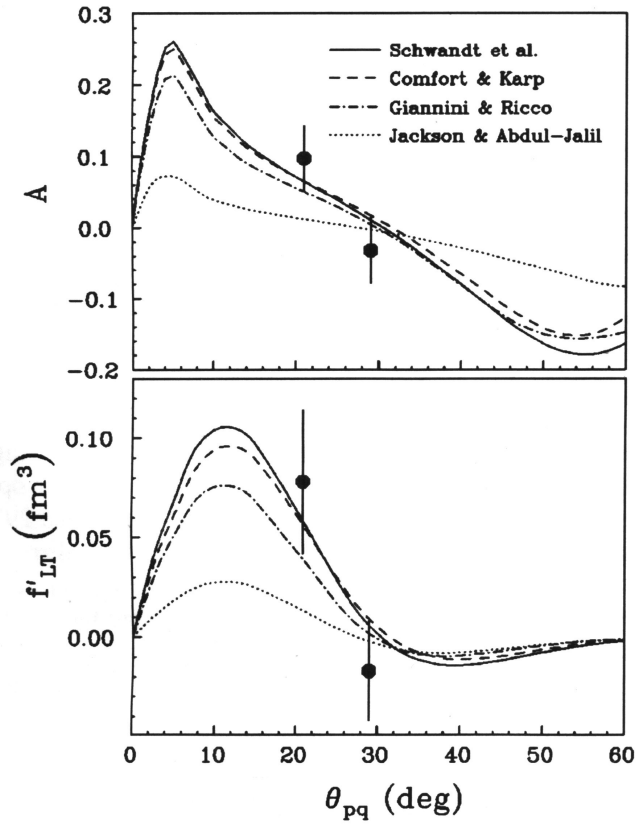


(b) The $A'_{LT}$ and fifth response function $f'_{LT}$ reported in [13].

Figure 2-7: The $A'_{LT}$ asymmetry and the fifth response function $f'_{LT}$ measured in $^{12}\mathrm{C}(e,e'p)^{11}\mathrm{B}$ reaction at $q = 370$ MeV/c, $Q^2 = 0.13$ GeV$^2$/c$^2$, for p-shell knockout, measured at BATES [25, 13]. The theoretical curves are explained in the text.

Each potential includes real and imaginary central terms and a real spin-orbit component. The S and JA potentials additionally include very small imaginary spin-orbit contributions. The CK and S potentials use volume wells for the imaginary central term, while GR and JA use surface absorption. The S and CK potentials are quite similar in strength and shape but they differ mostly at small radii. The JA potential has a much smaller depth of the real and imaginary central wells. The real spin-orbit part of JA is sharply peaked at a radius that is small compared to those of the other potentials. The GR potential produces an asymmetry that is not very different from S and CK, yet the shape of its imaginary central well is much different from the one featured in those potentials and GR has a smaller depth of the real spin-orbit well. Comparatively with the cross-section, where only the absorbing imaginary central term of these potentials produces a visible effect, in the asymmetry all terms were found to contribute significantly [13]. However, we must note that more recent discussions [56] revealed that the optical potentials of Schwandt *et al.* (S) [57] and Jackson & Abdul-Jalil (JA) [59] are inappropriate for the comparison with the Bates results. The Schwandt potential is optimized for $A \geq 40$ and $80 \leq T_p \leq 180$ MeV and does not extrapolate well in either mass or energy, while the Abdul-Jalil potential creates particles for $T_p \sim 50$ MeV (the imaginary central potential has the wrong sign). Therefore, any correspondence between data and the calculations using these two potentials is now considered irrelevant. We will tacitly exclude the respective curves from the following discussion.

The curves in Fig. 2.7(a) are corrected for meson exchange currents (MEC) and $\Delta$-isobar configurations. These contributions were found to produce only small variations. All calculations were corrected for Coulomb distortion of the incident electron. The results for $f'_{LT}$ were scaled to fit the data.

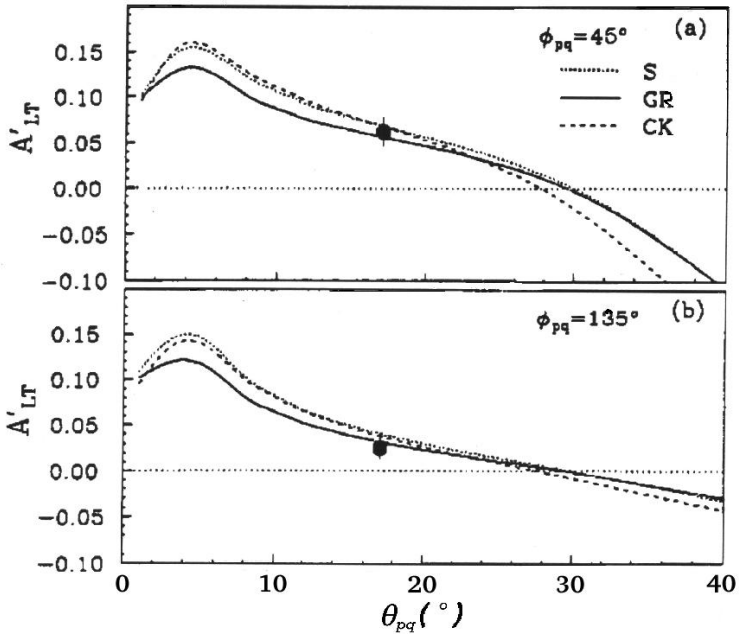


Figure 2-8: The $A'_{LT}$ asymmetry for $q = 0.35$ GeV/c, $\omega = 0.072$ GeV ($Q^2 = 0.128$ GeV$^2$/c$^2$), for p-shell knockout on $^{12}$C , measured at BATES by X.Jiang *et al.* [26]. The three curves correspond to different choices of optical potential (explained in the text).

The $^{12}$C $s$-shell asymmetries measured by Mandeville *et al.* were complicated by the large $p$-shell radiative tail. Approximating the valence shell contribution in the 32 MeV and 45 MeV region with the peak value, they reported asymmetries of $(-0.47 \pm 0.48)$ at $\theta_{pq} = 21^o$ and $(-0.15 \pm 0.56)$ at $\theta_{pq} = 29^o$.

Jiang *et al.* [26] measured $A'_{LT}$ for slightly different kinematics (Fig.2-8). At the same beam energy, they measured the $A'_{LT}$ asymmetry for $q = 0.35$ GeV/c, $\omega = 0.072$ GeV, for p-shell knockout on $^{12}$C. They also measured the $A_{LT}$ and the response functions $f'_{LT}$ and $f_{LT}$. While the $A'_{LT}$ is mostly sensitive to FSI, the $A_{LT}$ is sensitive to the details of nuclear structure.

For comparison with the theory, Jiang *et al.* used DWIA calculations with the optical potentials of Schwandt *et al.* (S), Giannini & Ricco (GR) [60] and Comfort & Karp (CK)

[58]. The three choices of potential were found to give similar predictions for $A'_{LT}$ (see figure 2-8), in acceptable agreement with the measured points, but they found significant disagreements for $f_{LT}$.

Within the range of the data, all theory curves seem to be compatible. However, no trend could be deduced without additional $\theta_{pq}$ points. The data was too limited to draw a conclusion more interesting that "consistent with DWIA". From this point of view, both experiments were considered sub-optimal.

More data with higher statistical precision were deemed necessary to gauge the accuracy of the mean-field treatment of FSI. But the inherent accuracy of helicity asymmetry measurements and their insensitivity to mechanisms other than FSI qualifies them as an excellent tool not only for this task but also for evaluating effects consistently beyond the mean-field approach. This work follows exactly in this direction.

# Notes to chapter 2

## MEC - Meson exchange currents

The nuclear environment significantly modifies the impulse approximation (IA) nuclear current. Besides nucleons, other degrees of freedom are effective at low and intermediate energies (section 2.4). They are associated with low-lying mesons such as $\pi$ ($J^\pi = 0^-, I = 1, m_\pi = 139.6$ MeV/c), $\rho$ ($1^-, 1,770$ MeV/c) and $\omega$ ($1^-, 0,783$ MeV/c), together with nucleon excitations, basically the $\Delta(1232)$ resonance ($3/2^+, 3/2, 1232$ MeV/c). When considering two interacting nucleons, such degrees of freedom play a role by adding a two-body contribution too the IA current. An important part of such a contribution is due to the exchange nature of the nucleon-nucleon interaction that arises from the charge-carrying particles exchanged by the nucleons with the applied electromagnetic field. As the exchanged particle is a meson, they are known as *meson exchange currents (MEC)*. They are isovector contributions to the longitudinal (L) component of the current and they are model-independent in the sense that they contain no parameters not already present in the nucleon-nucleon interaction.

## $\Delta$-isobar configurations

The $\Delta$-resonance is an intermediate configuration that gives rise to a transverse (T) current. This belongs to the category of model-dependent currents in the sense that they can not be deduced from the nucleon-nucleon potential or from the continuity equation for the nuclear current.

# CHAPTER 3

# Experimental Setup

The experiment has been performed at the Thomas Jefferson National Accelerator Facility, in Newport News, Virginia, in April–May, 1999. The data was taken in the Hall B of the facility and made use of the $4\pi$ CLAS detector. CLAS is the acronym for **C**EBAF[1] **L**arge **A**cceptance **S**pectrometer. The following sections give a general description of the accelerator and of the subsystems of the detector.

## 3.1 Accelerator

The CEBAF accelerator is a superconducting radio frequency (RF) electron accelerator. It was commissioned during the early 1990s and produced its first experimental beam in October of 1994. The accelerator delivers beam to three experimental halls, denoted as A, B and C in figure 3-1. The construction of a fourth hall, D, is underway.

The accelerator uses a state-of-the-art photocathode gun system that is capable of delivering beams of high polarization and high current to Hall A and Hall C while maintaining high polarization low current beam delivery to Hall B. An RF chopping system operating at 499 MHz is used to develop a 3-beam 1.4971 GHz bunch train at 100 keV. The beam is then longitudinally compressed in the bunching section to provide 2 ps bunches, which are then

[1] CEBAF is also an acronym, standing for Continuous Electron Beam Accelerator Facility

accelerated to just over 1% of the total machine energy in the remaining injector section. The beam polarization, optics and energy are verified in the injector matching region prior to injection into the main machine.

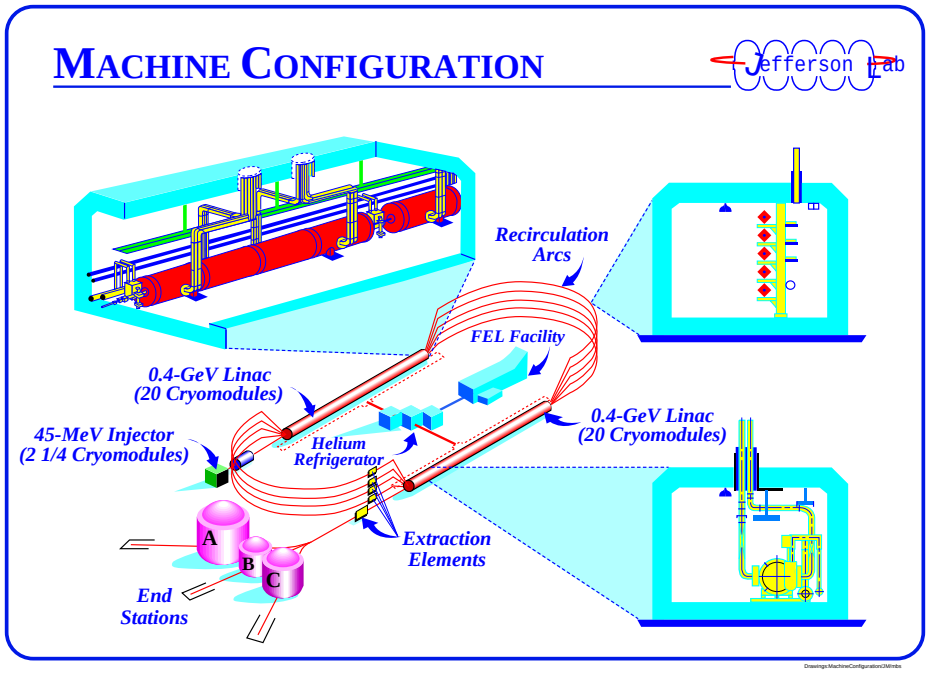


Figure 3-1: The CEBAF Accelerator. The three blowup boxes show (clockwise from upper l.h.s.): one of the linac cryomodules, a cross section of the tunnel with the five recirculating arcs, and a cross section of a cryomodule.

The beam from the injector is accelerated through a unique recirculating beamline that looks something like a racetrack (see Fig. 3-1), with two linear accelerators joined by two $180^o$ arcs with a radius of 80 meters. Twenty cryomodules, each containing eight superconducting niobium cavities, line the two linear accelerators. Liquid helium, produced at the Lab's Central Helium Liquefier (CHL), keeps the accelerating cavities superconducting at a temperature of 2 K. The linac energies are set identical and the RF cavities are phased to provide maximum acceleration. Subsequent passes through the accelerator are phased

to maximum energy gain by adjusting the length of travel in the dogleg section of the preceding arc. Quadrupole and dipole magnets in the tunnel steer and focus the beam as it passes through each arc. More than 2,200 magnets keep the beam on a precise path and tightly focused.

Beam is directed into an experimental hall's transport channel using magnetic or RF extraction. The RF scheme uses 499 MHz cavities, which kick every third bunch out of the machine. The beam is recirculated up to five times into the linacs and then delivered to the experimental halls simultaneously.

The maximum beam energy available is approximately 5.5 GeV with an energy spread of 0.01% or better. The maximum current is about 200$\mu$A with a beam spot size at the target of 0.5 mm. Typical beam currents in Hall B are 2–20 nA.

## 3.2 The CLAS Detector

A large acceptance spectrometer is needed in experiments that require the detection of several uncorrelated particles in the hadronic final state or in measurements where the luminosity is limited by the beam, target or accidental background.

The CLAS is such a detector [61], having a nearly $4\pi$ sr coverage, consisting of drift chambers to determine the paths of charged particles, gas Čerenkov counters for electron identification, scintillation counters for measurement of time-of-flight (TOF), and electromagnetic calorimeters to identify showering particles such as electrons and photons. The trigger is formed using fast coincidences between the Čerenkov counters, TOF counters or electromagnetic calorimeters. The integrated charge passing through the target is measured by a Faraday cup located at the end of the beam line.

The six sectors between the coils are individually instrumented to form six independent

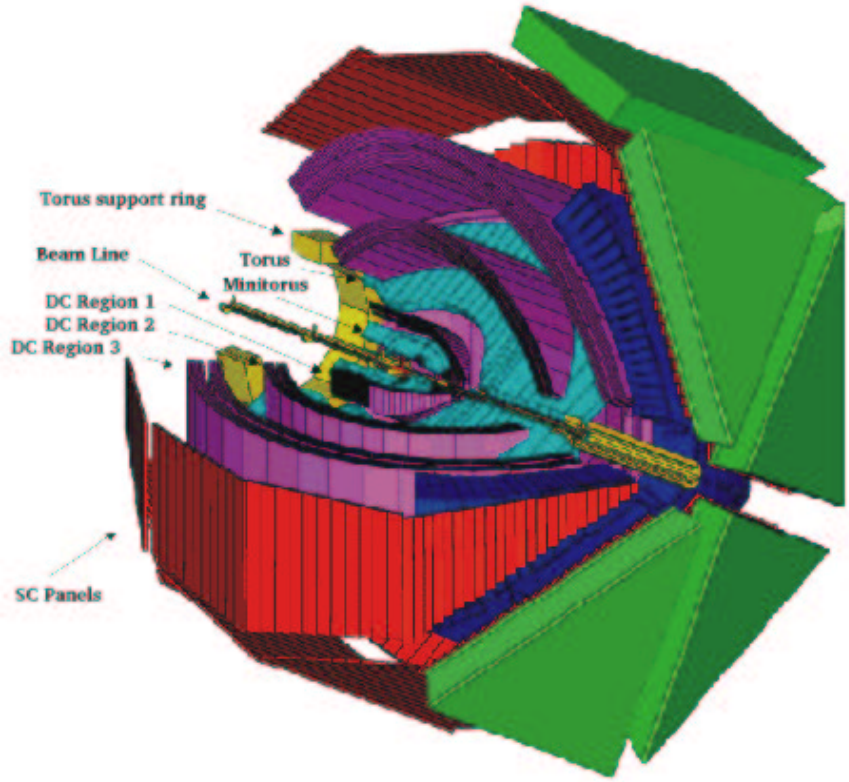


Figure 3-2: Three dimensional view of CLAS (produced with GSIM). The electron calorimeter is shown in green, the red boxes represent the TOF counters (SC) and the dark blue boxes are the Čerenkov counters. The three layers of drift chambers (DC) are shaded in purple. The target is located in the center of the detector, on the beam axis.

magnetic spectrometers. This makes a good basis for the desired high-luminosity operation and high count-rate capability.

The coverage range of CLAS in the laboratory frame is from $8^o$ to $140^o$ for charged particles and from $8^o$ to $60^o$ for neutral particles. CLAS can detect two or more coincidence particles in the final state with a signal to background ratio of 1/1000 or better at luminosities of up to $10^{34}$ $\mathrm{cm}^{-2}\mathrm{sec}^{-1}$.

### 3.2.1 Toroidal Magnet

The magnetic field of CLAS is generated by six toroidal iron-free superconducting coils [62] arranged around the beam axis to produce a circular field with a maximum intensity of about 2 T. The geometry of the coils (see Fig. 3-3), about 5 m long and 2.5 m wide, is optimized for experiments using fixed targets and electron beams with energy in the range of a few GeV. Each superconducting coil has 80 turns of cable in conduit conductor, cooled with liquid helium in a forced flow scheme, ensuring the most effective heat removal. They operate at a current of 10 kA. The magnetic field created has the maximum value in the forward direction (2 T) and drops by a factor of five at large angles. The center region of the spectrometer is field-free, to allow polarized target operation.

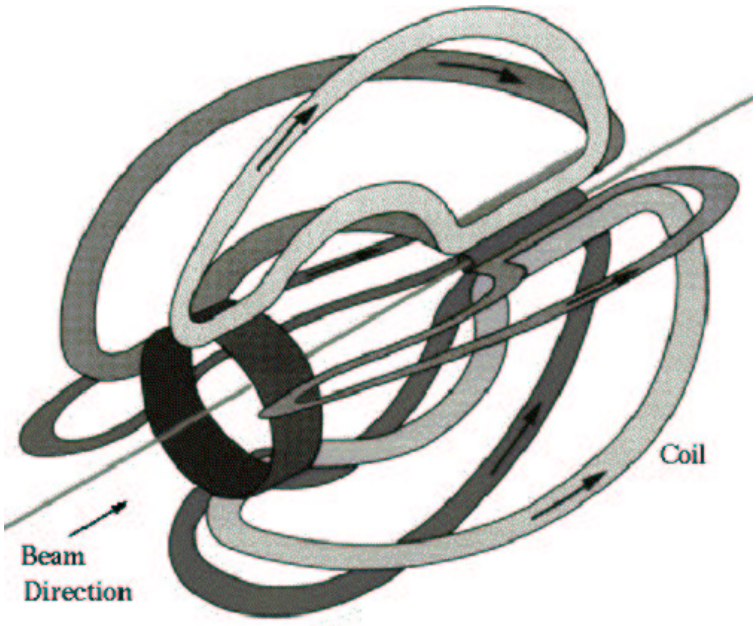


Figure 3-3: The CLAS superconducting toroidal magnet.

A magnetic field to sweep away low energy (background) electrons is generated by a

small toroidal coil inserted into the cavity of the large superconducting magnet (Minitorus in Fig. 3-2). The field created by this shield is small compared to the field of the main coils, but the Møller electron background elimination is excellent: nearly a factor of 100 in background rejection in the region enclosed by the first drift chambers layer (DC Region 1 in Fig. 3-2).

### 3.2.2 Drift Chambers

Charged particles in CLAS are tracked using multi-wire drift chambers (DC) [63]. The drift chambers cover a geometrical range of $8^o$ to $140^o$ in polar angle and 80% of the azimuthal range, and track particles with momenta above 0.2 GeV/c. The drift chambers are arranged in three regions (Fig. 3-2): DC Region 1 is located closest to the target, within the (nearly) field free region inside the Torus bore, and is used to determine the initial direction of charged particle tracks. DC Region 2 [98] is located between the Torus coils, in the region of strong toroidal magnetic field, and is used to obtain a second measurement of the particle track at a point where the curvature is maximal, in order to achieve good energy resolution. DC Region 3 is located outside the coils, again in a region with low magnetic field, and measures the final direction of charged particles headed towards the outer Time-of-Flight counters, Čerenkov counters and electromagnetic calorimeters.

Each region consists of six separate sectors, one for each of the six sectors of the CLAS. Each region within a given sector contains one axial superlayer with up to 1200 sense wires in six layers (4 layers in the case of DC Region 1) and one stereo superlayer with sense wires in six layers at an angle of $6^o$ with respect to the axial wires. This setup allows the measurement of both polar angle $\theta$ and azimuthal angle $\phi$ of the track. The wires are arranged into a hexagonal pattern, with each sense wire surrounded by six shared field

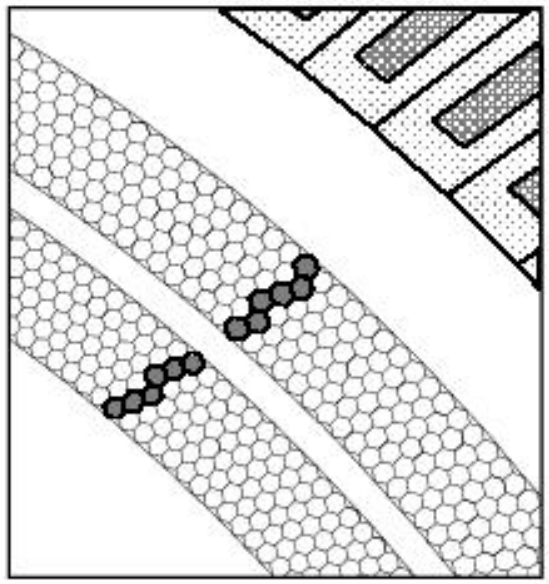

Figure 3-4: Superlayers in Region 3 of the drift chambers. Each hexagon represents a drift cell, with sense wires at the center of the hexagon and field wires at the vertices. A track is produced here by signals from the shaded cells.

wires (Fig. 3-4). The hexagonal configuration has been chosen as a good approximation of the ideal circular cell in which the drift/time relation is independent of the entrance angle. Each superlayer is surrounded with a row of guard wires to minimize edge effects.

The gas filling the drift chambers is a mixture of 9/10 Ar and 1/10 $CO_2$, which gives a drift velocity of up to 0.04 m/$\mu$s and an operating voltage plateau of several hundred volts. The average layer efficiency is greater than 98%.

The hits within each superlayer are combined to form a track segment. Then the obtained segments from different superlayers are linked together to form a track. This gives a momentum within 5% error of the true value. In a second stage, the start time signal from the scintillator counters is used to obtain the drift time which is converted into distance from the center of the cell. The resolution obtained using time information is better than

0.4%.

The DC drift time resolution is only 1 ns while proton/pion discrimination for momenta up to 2.5 GeV/c requires a 300 ps resolution. This is obtained by combining the drift chamber and time-of-flight information, will be described in the next subsection.

### 3.2.3 Scintillation Counters

Particle identification and triggering[2] are done by a Time-Of-Flight (TOF) system [64], consisting of a layer of scintillator counters just outside the tracking system. The scintillators are positioned outside the DC Region 3 and Čerenkovs to reduce multiple scattering and production of knockout electrons (see Fig. 3-2). Each scintillator paddle is placed perpendicular to the beam direction, so that each counter subtends approximately $2^o$ of the scattering angle. The scintillators are parallel to the axial drift chamber wires and span the azimuthal angular range of each sector.

There are a total of 57 scintillators per sector, each with PMTs at both ends. The last 18, covering the backward angles, are paired into 9 logical counters, so that the resulting system has 48 logical counters (often referred to as 'paddles') per sector. The lengths of the counters vary from 445 cm in the center region, to 32 cm at the forward and backward edges. The first 23 paddles (r.h.s. in Fig. 3-5) and the last four paddles are 15 cm wide while the rest of them are 22 cm wide. The scintillation detector subsystem sums a total area of about 206 $m^2$.

The maximum counting rate in the scintillators occurs in the forward direction. At a luminosity of $10^{34}$ $cm^{-2}s^{-1}$, the hadronic rate per scintillator at $\theta = 10^o$ is 5 kHz. This rate is only 0.5 kHz at $\theta = 90^o$. At small angles, better timing resolution is naturally achieved

[2] except for electrons

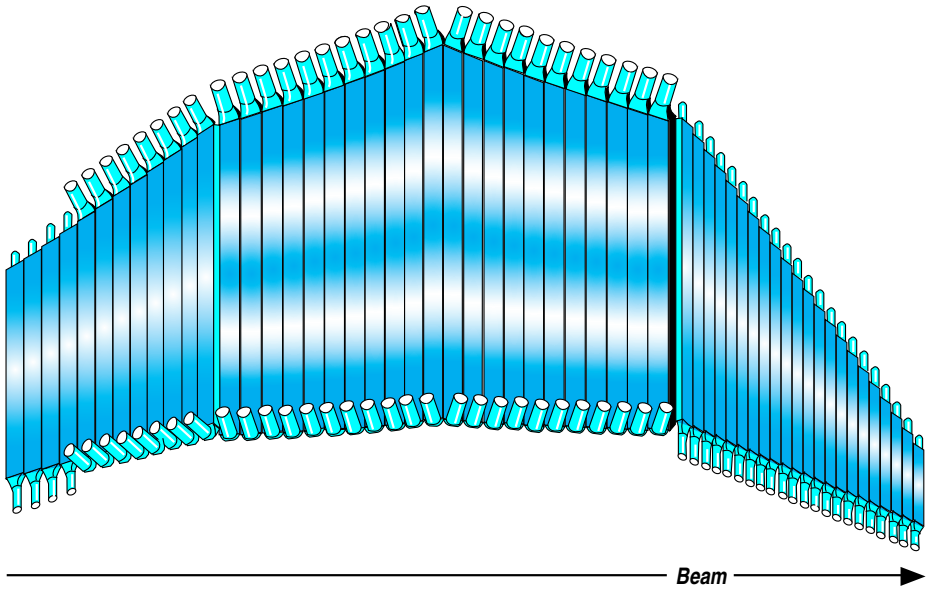


Figure 3-5: The four panels of scintillators that equip one sector. The dimensions and the readout configuration differ from one scintillator to another.

due to the smaller paddle length and better velocity resolution is obtained due to the longer distance from the target to the scintillator array. The average time resolution for electrons is 163 ps [64]. When combined with magnetic analysis, this allows good separation of the particles in the final state, though this is somewhat limited by the track and momentum reconstruction and the paddle-to-paddle calibration[3].

The Time-Of-Flight system of CLAS was designed, built and tested at the University of New Hampshire. It was constructed over five years and delivered to the hall in June 1996.

### 3.2.4 Čerenkov Counters

The Čerenkov counters [65] are used to identify electrons and separate them from pions and other charged particles. In electron scattering experiments, the primary charged particle background is due to negative pions. For measurements of inclusive cross sections, the

[3]see section 4.1.7

ratio of the pions misidentified as electrons to the true electrons must be below 0.01. The gas Čerenkov counters ensure a typical rejection power of 100:1, which is sufficient when $N_{\pi^-}/N_{e^-} < 1$.

Pions may be misidentified when they produce knockon electrons with velocity greater than the Čerenkov threshold. These are produced in the $C_4F_{10}$ radiator gas, in the entrance window or in the material of the last layer of the DC. Fortunately, the efficiency of detecting these electrons is lower than that for the primary particles because a large fraction of them is produced at unfavorable angles.

Due to the symmetry of the toroidal magnet, the azimuthal angle of the scattered particles remains almost unchanged after they pass through the magnetic field. Then there is a high correlation between the angle of the particles and their position in the detector. The detectors consist of a three-mirror system that focuses the light from particles with different azimuthal angles to a point near the coil, where a photomultiplier with sensitivity to single photoelectrons is situated. The detectors of each sector (see Fig. 3-6-a) are divided into two halves, each half containing 18 optical modules and subtending a $\Delta\phi \approx 25^o$ azimuthal angle and approximately $15^o$ in $\theta$. Thus, there are 12 units around the beam axis for each $\theta$ interval, up to $45^o$. The components of the Čerenkov counters are mounted on a triangular-shaped aluminum frame and protected with a 0.08 mm Tedlar PVF film sandwiched around a sheet of mylar.

The efficiency of the Čerenkov counters is better than 98% in the fiducial region [65, 82].

### 3.2.5 Electromagnetic Shower Calorimeters

In order to achieve acceptable e/$\pi$ discrimination and to detect photons and other neutral particles, CLAS is equipped with an electromagnetic shower calorimeter (EC) that covers

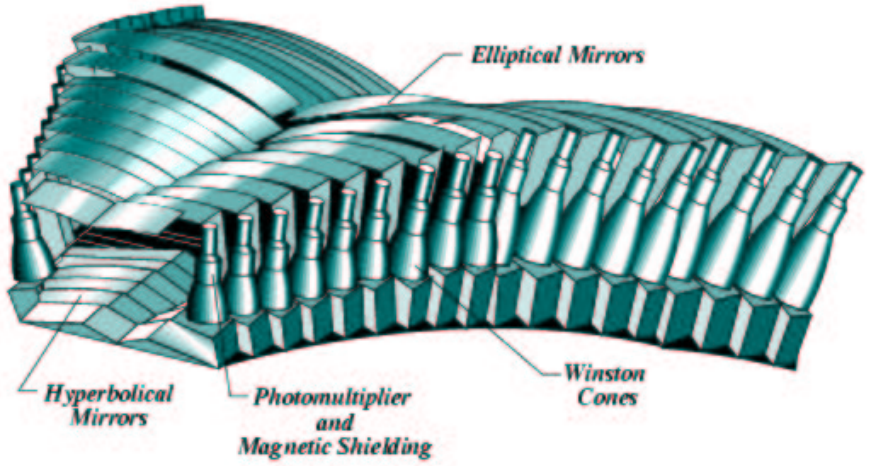


(a)

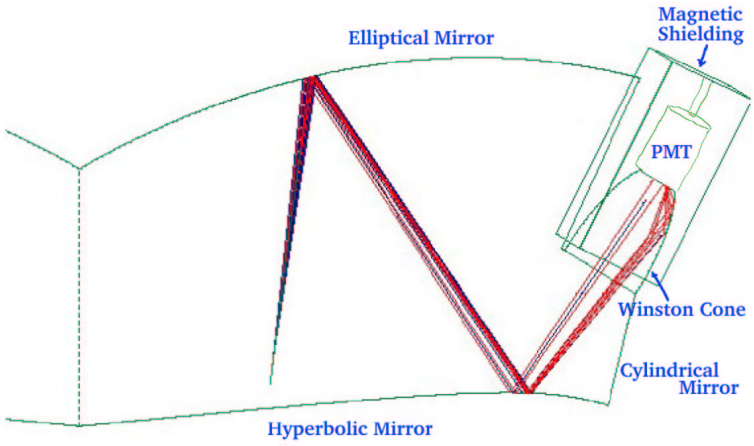


(b)

Figure 3-6: Čerenkov counters system: (a) Each sector is equipped with 36 optical modules (b) Simplified ray tracing scheme in a CC module: Čerenkov light from electrons is reflected twice from the mirrors into the Winston cone, which focuses the light into the photomultiplier (PMT).

polar angles from $8^o$ to $45^o$ in all sectors. For two of the sectors, the coverage is extended up to $60^o$ with the large angle calorimeters (LAC).

The importance of calorimeters [66] in the detection system, as said before, is in particle identification. In electron scattering, the information provided by the calorimeters, in conjunction with the information from the CC, is used for pion and electron identification (at $E_e > 0.5$ GeV). The electromagnetic calorimeters are also used to reconstruct $\pi^0$ and $\eta$ by identifying their $2\gamma$ decay products (for $E_\gamma > 0.2$ GeV) and for neutron identification and discrimination between photons and neutrons.

The calorimeters feature a lead-scintillator sandwich design consisting of alternating layers of scintillator strips and lead sheets, with a total thickness of 16 radiation lengths. A lead/scintillator ratio of 0.21 is used, requiring 39 cm of scintillator and 8.4 cm of lead per module. With this ratio, approximately 1/3 of the energy in an electromagnetic shower is deposited in the scintillator.

The lead-scintillator sandwich for the forward calorimeters has a triangular shape and is composed of 39 layers of BC412 scintillator 10 mm thick with 2.2 mm Pb sheets in between. Each layer is composed of 36 scintillator strips parallel with one side of the triangle (see Fig. 3-7-a), the orientation of the strips changing by $120^o$ between two adjacent layers. The three orientations, labeled U, V, W, provide stereo information on the hit position. Each of the U, V, W orientations, containing 13 layers, is subdivided into an inner and an outer stack, containing 5 and 8 layers respectively. This allows an improved hadron identification by longitudinal sampling of the shower. There are 1296 photomultipliers (PMT) and 8424 scintillator strips in the forward electromagnetic calorimeters subsystem.

The two large angle calorimeters (LAC) that equip sectors 1 and 2 (see Fig.3-2) have a different design. Each pyramidal trunk shape LAC module consists of 33 layers, each com-

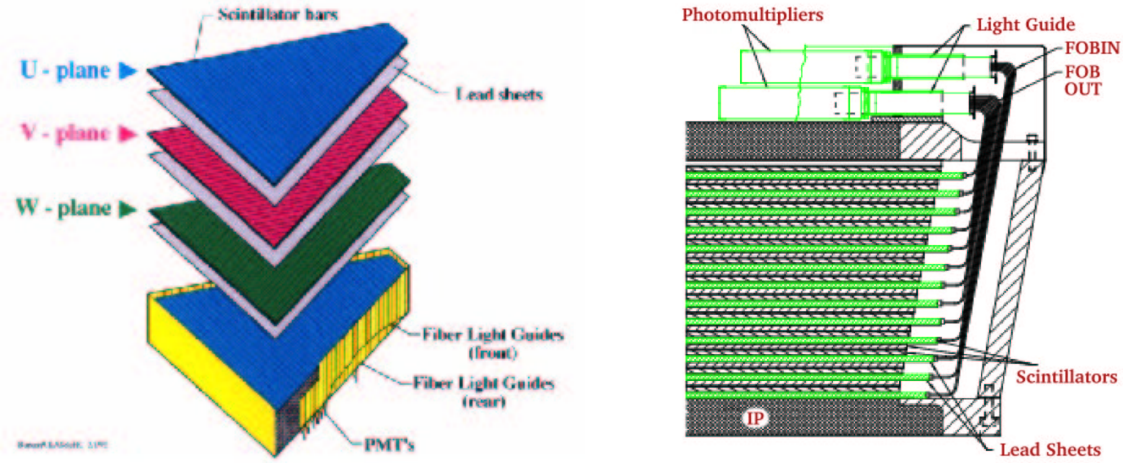


(a) (b)

Figure 3-7: Forward electromagnetic calorimeters : (a) exploded view of one of the modules and (b) scheme of the EC light readout system where we denoted FOBIN-fiber optic bundle inner, FOBOUT-fiber optic bundle outer, IP-composite inner plate.

posed of a 0.20 cm thick lead foil and NE110A plastic scintillator bars with an average width of 10 cm and 1.5 cm thick. The module thickness corresponds to 12.9 radiation lengths. Teflon sheets of 0.2 mm thickness are inserted between the lead foils and scintillators while 0.2 mm thick Teflon strips separate each pair of contiguous scintillators bars in order to avoid optical crossover. Each layer is rotated by $90^o$ to form a 40×24 matrix of 10×10 $cm^2$ cells. Each LAC module is vertically divided in an inner and an outer part to improve electron/pion discrimination.

The technical parameters of the CLAS Čerenkov counters detector subsystem are summarized below:

1. Fast (less than 100 ns) total energy sum for trigger
2. $e/\gamma$ energy resolution $\sigma_E/E \leq 0.1/\sqrt{E(\mathrm{GeV})}$
3. Position resolution $\delta r \approx 2$ cm at 1 GeV

4. $\pi/e$ rejection greater than 99% at energies greater than 1 GeV
5. Mass resolution for two-photon decays $\delta m/m \leq 0.5$ GeV
6. Neutron detection efficiency greater than 50% for $E_n > 0.5$ GeV
7. Time-of-flight resolution around 0.4 ns

## 3.3 Polarized Electron Source

The polarized electron source at CEBAF is an optically pumped strained GaAs crystal. In this device, a 780nm laser is used to project circularly polarized light onto the crystal. The laser is pulsed to the accelerator frequency of 0.5 GHz and the bunch-length is 50 ps. Left and right circular polarization of the laser beam are obtained with a Pockels Cell (PC) by applying the voltage corresponding to the quarter wave retardation.

To eliminate possible bias, the helicity was flipped at a 30 Hz frequency and was phase locked to the 60 Hz AC cycle. Helicity pulses are associated in pairs of opposite helicity. The leading pulse helicity is chosen by a 24-bit pseudo-random number generator which also sends a signal to the DAQ to be recorded in the data file. Due to special demands imposed by the HAPPEX [106] experiment that was running in parallel in Hall A, this helicity signal was delayed by 8 pairs and therefore the true helicity had to be determined afterwards in the data analysis (appendix C).

Another precaution that was taken was to insert periodically in the laser beam a half-wave plate, which reverses helicities and thus provides a useful systematic check. The half wave plate position was saved in the EPICS database and is listed in appendix C.

Beam polarization in Hall B is measured with a Møller polarimeter. In this device, the polarization is determined from the asymmetry of the counting rates when the helicity of the beam is reversed. About 20 minutes of measurement time or 3 M events are needed to

take data with a statistical error below 1%.

The online analysis results of the polarization measurements were saved in the runtime logbook [107, 108], and are presented in figure 3-8. A detailed analysis of this data is presented in appendix C. For the purpose of this analysis, the beam polarization value used is $P_B = (63 \pm 2 \pm 3)\%$ as will be detailed in the next chapter.

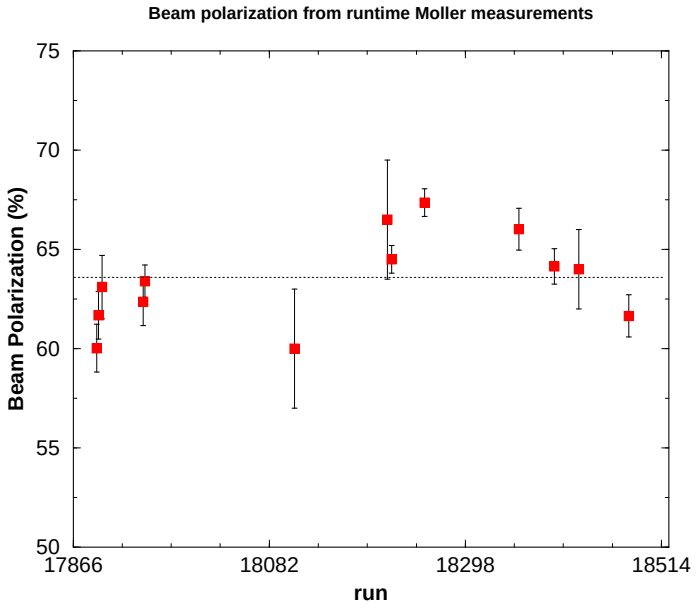


Figure 3-8: The electron beam polarization during the E2A run period as obtained from online analysis of the Møller measurements. The dotted line corresponds to the mean value.

## 3.4 Targets

Of the four targets employed by the E2A run, this thesis presents results obtained with $^4$He and $^{12}$C. These two targets differ from each other by state of aggregation, geometry and by their position along the beamline. A blueprint of the CLAS target system is presented in figure D.2 in the appendices.

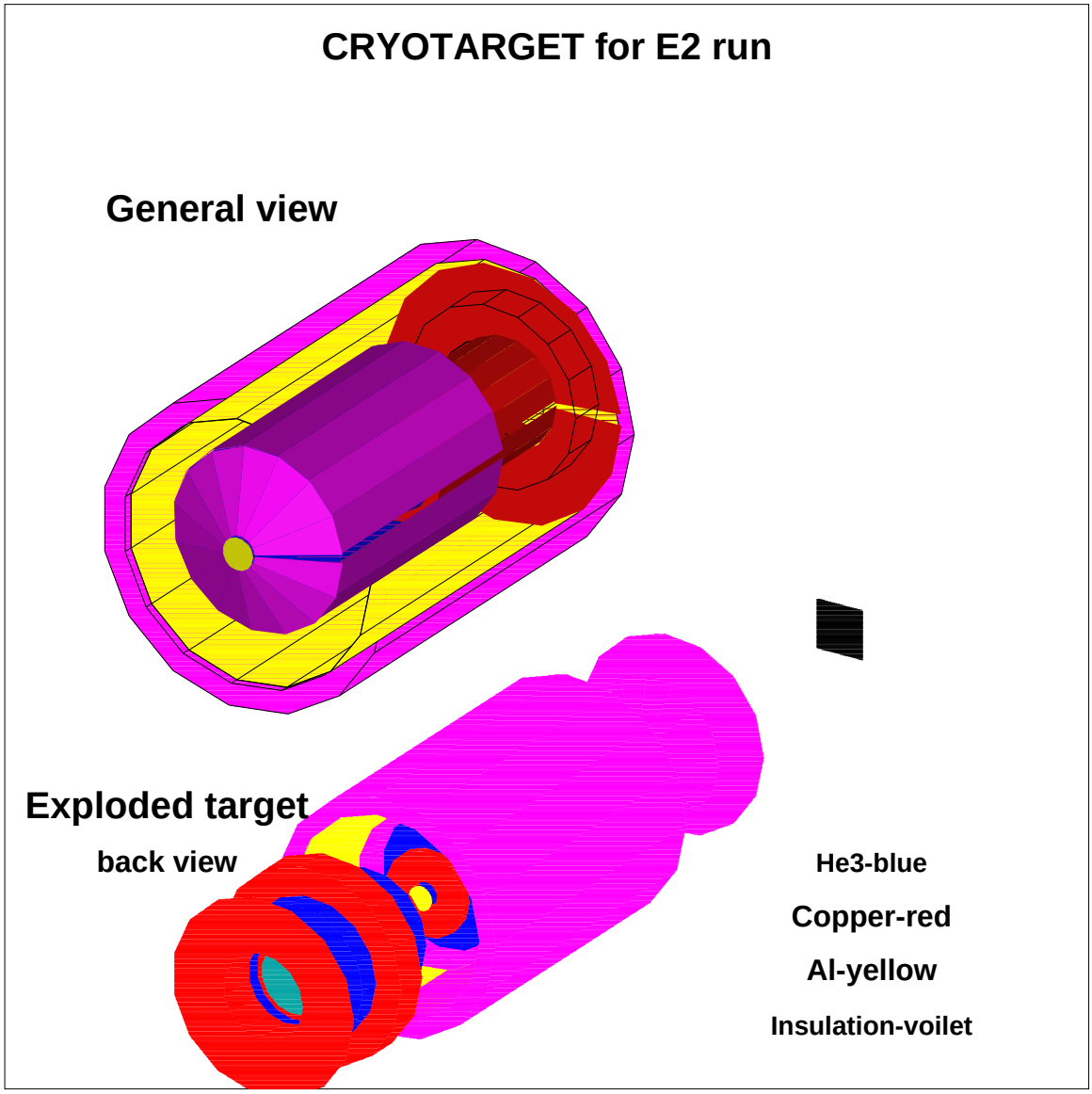


Figure 3-9: Targets for the E2A run: liquid $^4$He filled areas are drawn in blue. The small black square on the right is the solid $^{12}$C target. The beam line coincides with the symmetry axis of the cylinder and the beam comes from the right. The $^4$He circulation system is not shown.

| Target cell | # 1 | # 2 | # 3 |
|---|---|---|---|
| Time period | Apr 15 - May 7 | May 8 - May 12 | May 12 - May 15 |
| Contents | $^4$He | $^4$He | $^3$He |
| Cell length (cm) | 4.99 | 3.72 | 4.13 |
| Cell diameter (cm) | 0.97 | 2.77 | 2.77 |
| Position relative to the center of CLAS | -0.1 cm | -0.625 cm | -0.635 cm |
| Materials used | Polystyrene ($\rho = 0.03$ g/cm$^3$) Mylar ($\rho = 1.39$ g/cm$^3$) Aluminum Al ($\rho = 2.7$ g/cm$^3$) | Mylar Al | Mylar Al |

Table 3.1: Liquid target cell parameters (courtesy of N. Dashyan [67] and R. Niyazov [70]).

The liquid helium is contained in a target cell maintained at a low temperature by a cryogenic system. The target cell, shown in figure 3-9, is a cylinder flat at one end and slightly rounded at the other, mounted on a trunk-conical base and covered with insulation. The liquid helium is circulated through a system of pipes, as can be seen in figure D.2. Three different cells used during the E2A run period are listed in table 3.1. The cells differ from each other by the dimensions of some components, by the thickness of the insulation as well as by position along the beamline.

The solid $^{12}$C target is a thin square plate of 9×9 mm and about 1 mm thick. The solid target is inserted into the beamline by the action of a lever (see Fig. D.2).

## 3.5 Trigger and Data Acquisition

The triggering system is designed to select events of interest and reject background processes, and must be effective at the run parameters of CLAS, that is at a luminosity of $10^{34}$

$cm^{-2}s^{-1}$, corresponding to a hadronic interaction rate of approximately $10^6$ $s^{-1}$.

The LEVEL 1 trigger establishes the time bases for digitization. It uses the hit pattern in scintillator (SC) and Čerenkov (CC) layers and the energy deposited in the electromagnetic calorimeters. The analog signals from the EC are summed together within subregions and each of these sums is then compared against a threshold value set within the hardware. The LEVEL 1 trigger is programmed by specifying which hits and sums over the threshold from each sector must be in coincidence.

During our data taking the trigger scheme was as follows:

- For 1.1 and 2.2 GeV runs: EC and CC hits in the same sector and EC $>$ 300 MeV electron equivalent
- For 4.4 GeV beam energy: EC hit but EC $>$ 1 GeV electron equivalent. The higher threshold was set to avoid solid angle losses by the CC at this beam energy.

The average event size for the CLAS is 5 kbytes, and the event rate was up to 2.2 kHz. The events are written to tape at about the same rate (in the worst case at 80% of this rate).

Figure 3-10 shows the CLAS trigger scheme for the E2A run. Since the physics covered by E2A was rather varied, the only constraint on the recorded events was that they contain an electron, which means that only Level 1 trigger was used. In this case, the data flow is as follows: The signals from the detector go to the front end controllers (ROC) and the pretriggers. The pretriggers initiate the readout from the particular detector subsystem and are also inputed into the Level 1 trigger. If there is a trigger, then the data signals are read out and transferred to the Event Builder (EB) process running on clon10 and temporarily stored on the Data Distribution (DD) ring in a shared memory area. From here, an event recorder (ER) process writes the data to the RAID (Redundant Array of

Inexpensive Disks). Later on, the data is transferred to the tape silo for permanent storage.

In the analysis chapter, we will discuss the connection between this trigger scheme and electron identification.

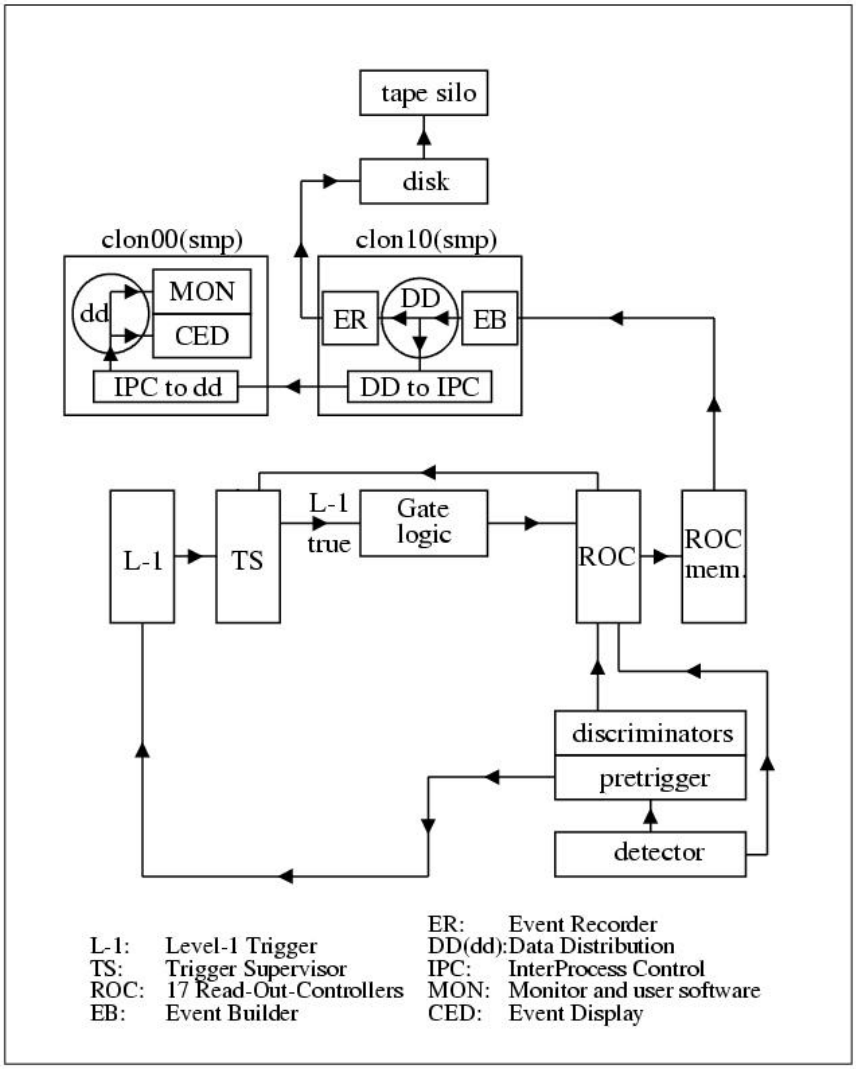


Figure 3-10: CLAS Data Acquisition Scheme for E2A: The signals from the detector go to the front end controllers (ROC) and the pretriggers. The pretriggers initiate the readout from the particular detector subsystem and are also inputed into the Level 1 trigger. If there is a trigger, then the data signals are read out and transferred to the Event Builder (EB) process and temporarily stored on the Data Distribution (DD) ring. From here, an event recorder (ER) process writes the data to the RAID. The data is later transferred to the tape SILO for permanent storage. (diagram courtesy of K. Loukachine).

# CHAPTER 4

# Calibrations and Analysis

The scope of experiment E98-104 is the measurement of the helicity asymmetry of the semi-exclusive electron scattering cross section on several target nuclei. E98-104 is one of the seven experiments comprising the CLAS E2 group.

The E2A data were taken between April $15^{th}$ and May $27^{th}$, 1999. This run period used about half of the total E2 approved runtime, summing 34 days, for a total of 456 hours of active data accumulation. A second run period took place in May-June 2002.

During E2A, data on $^{3}$He, $^{4}$He, $^{12}$C and $^{56}$Fe targets at three beam energies: 1.162, 2.262 and 4.462 GeV (referred to as 1.1, 2.2 and 4.4 GeV) was taken. Data were acquired with the CLAS "single electron trigger". A total of 2300 M physics triggers from $\vec{e}A$ interactions were recorded on tape. The average (nucleon) luminosity during the run was $\mathcal{L} = 7 \times 10^{33}\, sec^{-1} cm^{-2}$. At low energies, the luminosity was limited by the CLAS DAQ, at high energies the limitation come from the high occupancy of the CLAS Region 1 DC.

This thesis covers the $^{4}$He and $^{12}$C measurements at 2.2 and 4.4 GeV beam energies. The data accumulated with the $^{12}$C target amount to 756M triggers (3.0 Tb of data), divided in 323M triggers (1.6 Tb) at 2.2 GeV and 346M triggers (1.2 Tb) at 4.4 GeV (also four days of 1.1 GeV yielding 87M triggers (230 Gb) were taken). Liquid target $^{4}$He data amount to 752M triggers (2.8 Tb of data), divided as follows: 310M triggers (1.2 Tb) at 2.2 GeV and

442M triggers (1.6 Tb) at 4.4 GeV. Additional empty target calibration data were taken for each beam energy.

We have described the flow of the data at the end of section 3.5. There we saw that the raw data from the detector is saved in BOS [68] format on the tape silo (see figure 3-10) for permanent storage. From this point, the off-line processing starts.

Processing the data, or COOKING, involves taking a file of BOS banks produced by the on-line data acquisition system (RAW file) and producing a file containing higher level information, such as four-vectors [69]. This job is performed by a program called RECSIS (REConstruction and analySIS package), which is the engine for the reconstruction scheme. RECSIS reads an input file of raw BOS banks, obtains the necessary calibration constants to properly analyze these banks and produces a BOS file containing various reconstruction banks, referred to as a COOKED file. The output from RECSIS is then used as input for various monitoring and calibrations programs.

Calibration programs generally read a RAW or COOKED data file of BOS banks and produce some calibration constants typically in ASCII text format. The user must then place these calibration constants into the proper map. Monitoring programs produce ASCII reports and histograms which can be archived in the off-line databases.

There are two important databases for off-line processing, the Map-manager database and the off-line database. The Map-manager database (often referred to as the calibration database) stores calibration constants used by the reconstruction and analysis codes while the off-line database stores monitoring information in a convenient form for assessing the quality of the cooked data.

These COOKING/CALIBRATION sequences were repeated several times (referred to as passes), since the calibration of some detector subsystems requires previous calibration

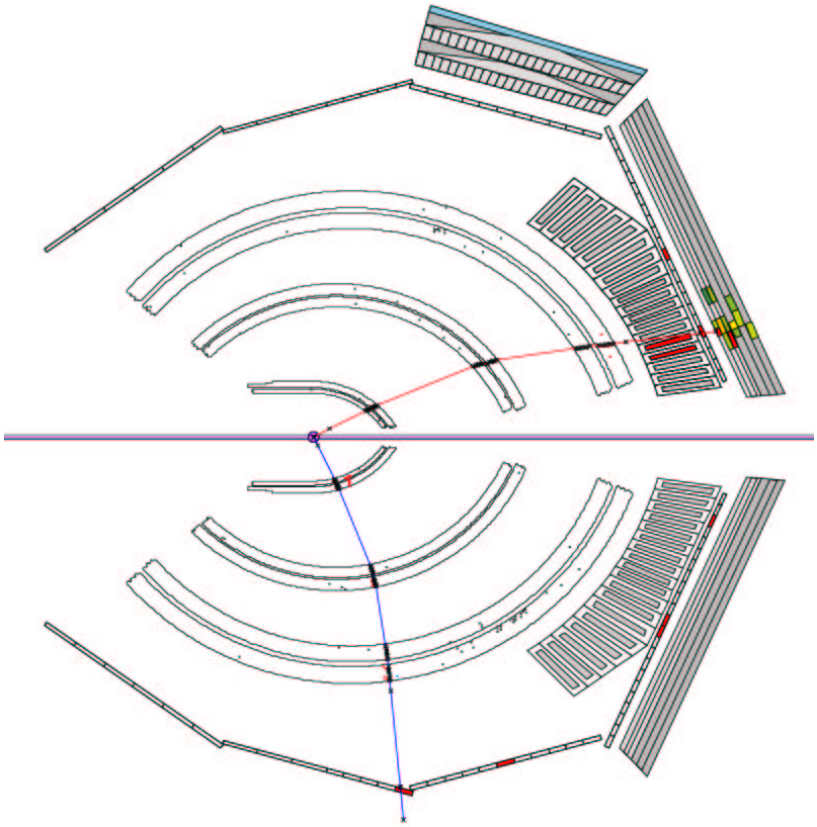

Figure 4-1: Snapshot of a CLAS Event Display (CED) screen to illustrate RECSIS track reconstruction. The display shows a cross-section through two diametrally opposite sectors of CLAS. The inbending track is the electron that gives the trigger. The outbending track corresponds to a positive particle.

of others.

After the calibration of all subsystems was done, the BOS files were cooked for the last time, in what we call the production `pass1`. In this process, only the specific BOS-banks that are relevant for the physics analyses of the Multihadron Group were selected.

Then each individual analysis group did an additional filtering of the data, which was put in either `ntuple10` or `rootDST` format. These two formats are compact and contain only the essential physics information. The cooked data was stored back on the SILO. In our case, we also had the possibility to download *all* the rootDST data onto the local raid-disk

at UNH-NPG.

To measure beam helicity asymmetries, we developed our own software based on the E2AnaTool [99, 100] package. One code scans through the events in the Root event tree, selects the $(e, e'p)$ events based on certain criteria, and saves them in a skim file. This takes several hours. Then in only a few minutes, a second code parses this skimmed data file, selects the desired kinematics and outputs the results in various formats: graphic, text file etc.

The calibration, data reduction and some analysis software writing were shared by the entire Multihadron Group, while the specific physics analyses were done separately within the individual groups associated with the experiment.

Since in the Time-of-Flight calibration we were directly involved, the following section provides a relatively detailed description of this procedure. Shorter procedure description are provided for the DC [70] and EC [71] calibrations while for the calibration of the Čerenkov counters, the reader is directly pointed towards references [72, 101].

# DETECTOR CALIBRATION

## 4.1 TOF Calibration

The scintillator counters are essential for charged hadron identification without which the study of complex final states composed of protons, pions, etc., would not be possible. The quality of particle identification in CLAS therefore depends primarily on the precise tuning of the Time-of-Flight components. As builders of the TOF, the UNH-NPG group had the task of calibrating the Time-of-Flight system.

| CALIBRATION STEP | | REQUIRES |
|---|---|---|
| 1 | Pedestals | dedicated data |
| 2 | TDC calibration | dedicated data |
| 3 | Time-walk correction | laser data |
| 4 | Left-right alignment | raw data |
| 5 | Energy loss | L-R time alignment at SC BOS-bank level |
| 6 | Attenuation length | L-R time alignment at SC BOS-bank level |
| 7 | Effective velocity | all of the above and good Time-Based Tracking |
| 8 | RF parameters | all of the above |
| 9 | Paddle-to-paddle delays | all of the above |
| 10 | RF offsets | all of the above |

Table 4.1: The TOF calibration sequence [73]. Good Time-Based Tracking (TBT) for the steps 7 and up necessitates previous DC calibration [70].

The calibration procedure [64] consists of: calibration of individual TDC channels, left-right PMT alignment and/or energy loss, attenuation length calibrations, effective velocity calibration, then counter-to-counter delay adjustment and, when this is done, an overall RF (accelerator Radio Frequency) offset calibration.

### 4.1.1 Pedestals and TDC Calibration

The ADC thresholds are called pedestals and are measured by taking data with a dedicated DAQ configuration. The data are analyzed online and the resulting constants are saved into the calibration database.

The channel-to-time calibrations of all the CLAS TDCs, except the drift chamber TDCs is performed using a special pulser run and the responses of each TDC for various delays between START and STOP are analyzed. A quadratic equation is used to convert the TDC channel number $T$ to actual time $t$(ns):

$$t = c_0 + c_1 T + c_2 T^2 \tag{4.1}$$

The parameters $c_1$ and $c_2$ are saved in the calibration database. The $c_0$ parameter is not relevant since a left-right calibration will be done later on.

### 4.1.2 Time-walk Corrections

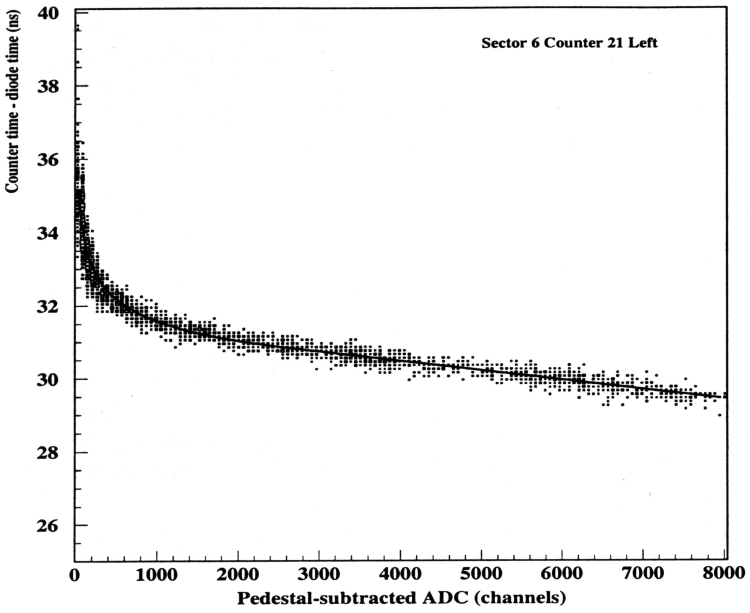


Figure 4-2: Typical dependence of the TDC times (ns) versus pulse height (ADC counts). The fit is done with with the function in eq.4.2. (from [64])

Time-walk is an instrumental shift in the time measured using a leading-edge discriminator that is due to different time-rise in the analog pulse for different pulse heights. The time-walk correction is implemented in the software using the function

$$t_w = t - f_w\left(\frac{A_P}{\tau}\right) + f_w\left(\frac{600}{\tau}\right) \tag{4.2}$$

where $A_P$ is the pedestal-corrected ADC channel number, $\tau$ is the channel corresponding

to the leading-edge discriminator threshold of 20mV ($\approx$ 35 channels) and $f_w(x)$ is the time-walk correction function. The figure 600 corresponds to the minimum ionizing particle (MIP) channel setting, where $t_w \to t$. The correction function $f_w(x)$ is obtained for each PMT separately using laser calibration data. In general, a function of three parameters is used:

$$f_w(x) = \begin{cases} ax^{-b} & \text{if } x \leq c \\ ac^{-b}(b+1) - xabc^{-(b+1)} & \text{if } x > c \end{cases}$$

This function first drops abruptly and then changes to a slow linear decrease, which corresponds to saturation of the PMT-s (see figure 4-2). The fit parameters $a, b, c$ are saved in the calibration database.

### 4.1.3 Left-Right PMT Alignment

Establishing the left-right signals time offsets is crucial for hit position identification in the scintillator paddle. The left-right alignment is a crude adjustment of these offsets, the fine tuning being done when the effective velocity of light in the scintillator is calibrated (subsection 4.1.5).

Raw data is used to obtain histograms of the quantity

$$\ell = TDC(left) - TDC(right)$$

using the existing database offset values. If the offsets are not correct, the distribution is not centered (see Fig.4-3.a) The edges of the $x$-projection for each counter should be symmetric with respect to zero. The value of the left-right offset is determined as

$$\Delta t = \ell / v_{eff}$$

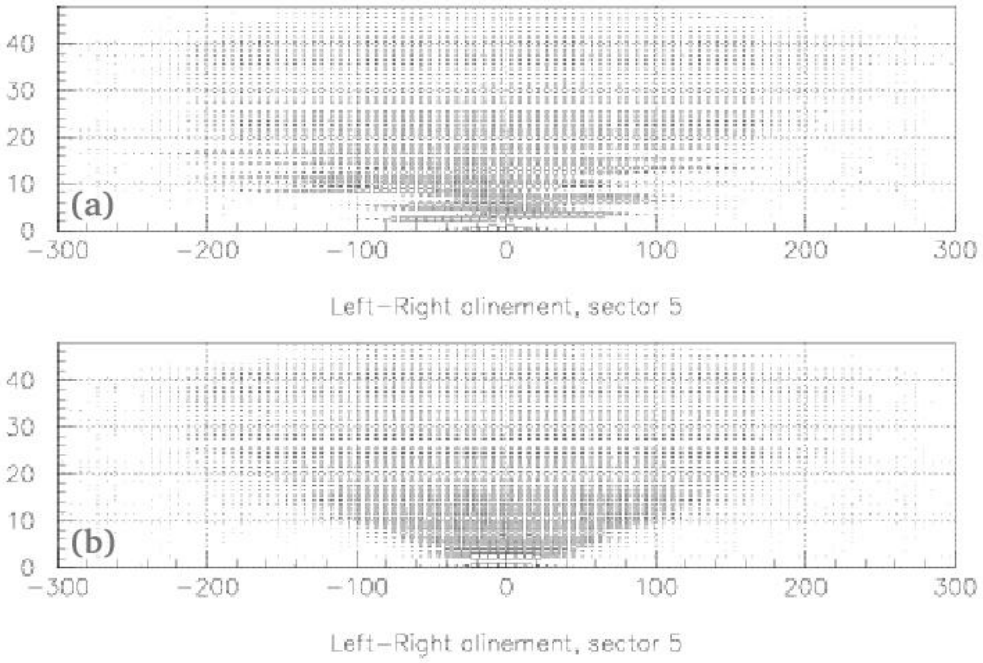


Figure 4-3: Example of left-right alignment of TOF counters. The vertical axis is the TOF counter number.(from [64])

where $v_{eff}$ is the effective velocity of light in the scintillator material, taken to be 16 cm/ns at this stage. Once the calibration database offset is incremented by the obtained $\Delta t$, the distribution must look like Fig.4-3(b).

The codes used to perform this calibration are `tof_calib` and `tdc_lr.kumac` from the `sc_calib` software package.

### 4.1.4 Energy Loss and Attenuation Length Calibration

For high quality calibration of CLAS we want the scintillator counters to be able to separate pions from protons without relying on timing information. The dependence of the deposited energy on momentum is different for proton and pions, and thus pions and protons can be separated once the energy loss $\delta E/\delta x$ in the scintillator material and the attenuation length

($\lambda$) for each counter are precisely calibrated.

The measured pulse heights normalized to the calibrated MIP peak value are used to reconstruct the energy deposited in the scintillators:

$$\begin{aligned} A_L &= \frac{N_L}{k} E_L \exp(-(L/2 - y)/\lambda) \\ A_R &= \frac{N_R}{k} E_R \exp(-(L/2 + y)/\lambda) \end{aligned} \tag{4.3}$$

where $A_i$ is the pedestal-corrected ADC channel, $E_i$ $(i = L, R)$ is the deposited energy, $k = 10$ MeV, $L$ is the length of the scintillator and $y$ is the hit position measured from the center of the detector. The normalization constants $N_i$ correspond to the peak heights of minimum ionizing particles (MIP) normally incident at the center of the scintillator.

The geometrical mean of the left and right signals is:

$$\bar{A} = \sqrt{A_L A_R} = \alpha E_d \exp(-L/2\lambda) \tag{4.4}$$

where $\alpha = \sqrt{N_L N_R}/k$. The quantity $E_d = \sqrt{E_L E_R}$ is a position-invariant measure of the deposited energy.

To measure the geometric mean of the MIP peak position in each counter, loose timing cuts are employed to select the pions used in the calibration. This method requires that a reasonable timing calibration has been previously done. The geometric mean position is obtained by a fit of the dependence in figure 4.4(a). The desired value of $\bar{A}$ is 600.

To calculate $E_d$ from eq.(4.4), normally incident minimum ionizing particles are used to measure the quantity $\alpha \exp(-L/2\lambda)$. A plot of $\ln(A_L/A_R)$ versus $y$ is shown in figure 4.4(b). The slope of the linear fit is equal to $\lambda/2$ and the offset is equal to $\ln(N_L E_L/N_R E_R)$.

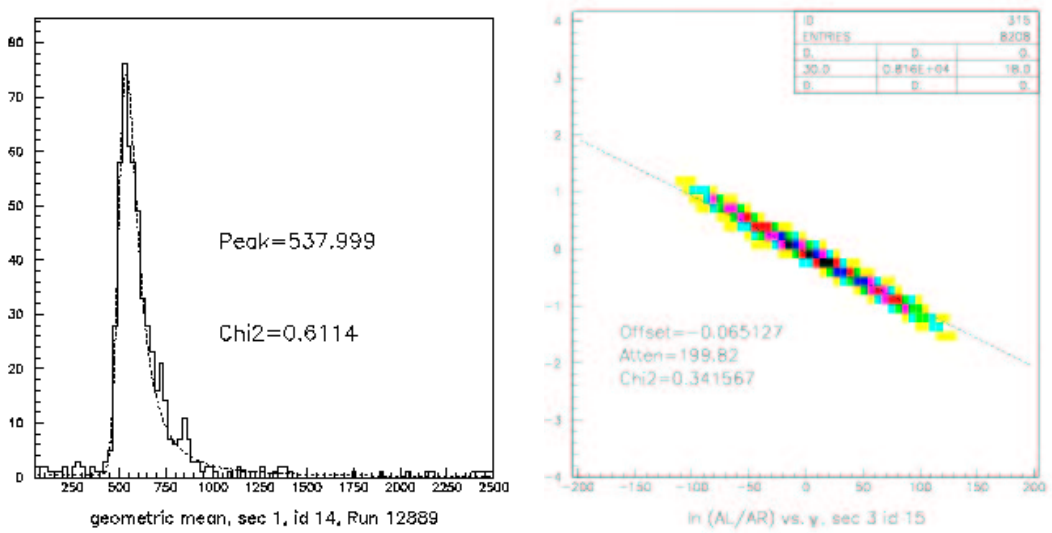


(a) (b)

Figure 4-4: Monitoring histogram showing (a) the fit to the geometric mean of the energy loss for MIP-s in the counter and (b) correctly calibrated attenuation length and energy loss. (from [64]).

Figure 4-5 shows the measured dependence $E_d = E_d(p)$ after the calibration. The energy loss of the protons increases quadratically with momentum until they begin to penetrate the scintillator, at which point their energy loss follows the Bethe-Bloch formula.

At low momenta, the pion and proton bands are well separated, whereas above momenta of 0.8 GeV/c they start to merge, since protons become MIP-s. Therefore, this criteria of pion-proton separation is not suitable for analysis and is used only to provide a reasonably clean pion sample for the next calibration steps.

The procedure outlined in this section is based on standard CLAS calibration software and was semi-automatized using the `tofs` shell script attached in appendix D.3.

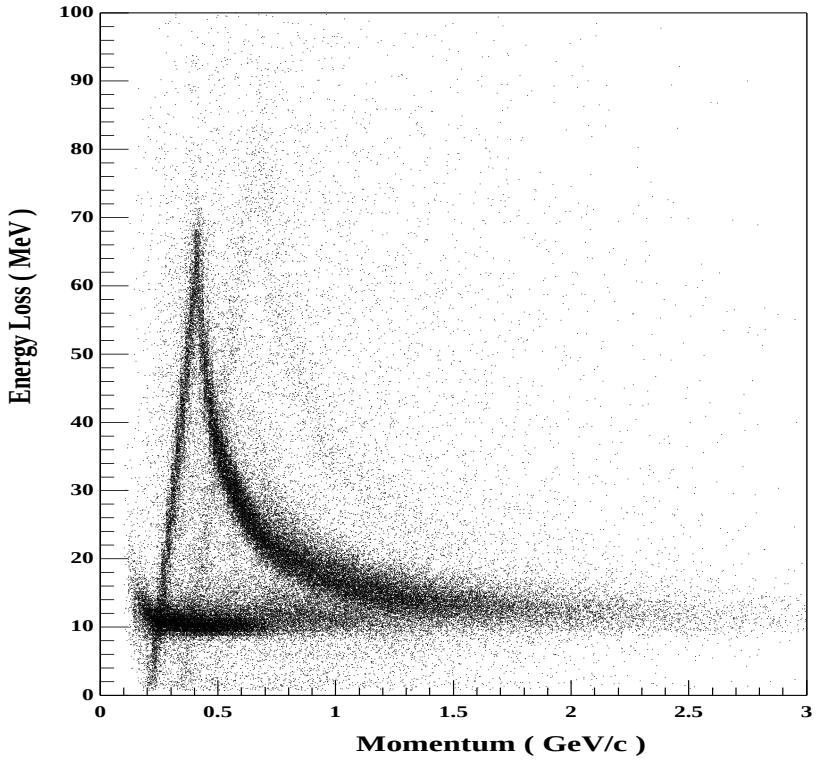


Figure 4-5: Energy loss in the scintillator material versus particle momenta. One can clearly distinguish the protons and pions and also a weak deuteron band.

### 4.1.5 Effective Velocity Correction

The position $y$ of a hit along the length of the scintillator can be determined from the timing information from the left and right tubes

$$y = v_{eff}(t_L - t_R - t_{offset})/2$$

The constants can be calibrated using the position $y$ from DC tracking. The dependence of the quantity $t_L - t_R$ versus $y$ can be fitted with a linear curve to determine the constants $v_{eff}$ and $t_{offset}$ for each scintillator paddle. This procedure is accomplished using the program `veff`.

### 4.1.6 RF Parameters

The RF-signal from the accelerator was used as the reference timing signal for the CLAS particle identification. This signal is generated for every electron bunch, therefore with a frequency of $\nu_{acc} = 1.4971$ GHz (section 3.1). The beam arriving to Hall B consists of 2 ps bunches separated by 2 ns intervals. The RF signal is sent to the three experimental halls with a prescale factor of 40.

Each CLAS trigger is caused by an electron from one of these bunches. Ideally, one would like to be able to identify the bunch containing the electron which caused a particular event, but this is impossible to do, because of the prescale factor, which means that only one out of 40 RF-signals is sent to the experimental halls.

However, for the TOF calibration purposes, it is adequate enough to be able to align the timing of all scintillator counters to the same RF bunch, because all electron bunches delivered into Hall B are separated by a constant time interval:

$$\Delta T = \frac{3}{\nu_{acc}} = \frac{3}{1.4971 \text{ GHz}} \approx 2.0039 \text{ ns} \tag{4.5}$$

where the factor 3 comes from the fact that the beam is shared among the three experimental halls. The RF signal is sent to the halls every $40 \times \Delta T$ ns. We define the *RF offset* as the delay time between the RF signal and the averaged event time.

To have an acceptable TOF calibration for a large data sample the RF offset must be adjusted throughout the run period. For each beginning of a run period, as well as for each beam energy change, the RF phase changes and new offsets must be determined [73]. The RF calibration is done using the program `rf.mon`. One must note that this step needs to be repeated after the paddle-to-paddle calibration.

### 4.1.7 Paddle-to-paddle Calibration

Once all individual scintillator counters have been calibrated, one has to ensure that their signals are aligned with respect to the accelerator RF signal, which is used as a reference signal for particle identification. This is done by introducing a time delay in the software for each counter.

The TOF timing of a hit at position $y$ is calculated as the average of the times from the two ends of the fired scintillator:

$$T_{SC} = \frac{T_L + T_R}{2} \tag{4.6}$$

where $T_L$ and $T_T$ are the times measured by the two TDCs.

In the first stage of the paddle-to-paddle calibration all scintillator strips are aligned to one of the RF-signals coming to the experimental hall. One can calculate the difference between the event start time, using the signal from the hit scintillator counter, and the RF time as:

$$\Delta\tau = (T_{SC} - T_{flight}) - T_{RF} \tag{4.7}$$

where $T_{SC}$ is the time in nanoseconds measured by the scintillator, $T_{flight}$ is the flight time of the particle from the target vertex to the scintillator and $T_{RF}$ is the time when RF-signal arrives to the TDC-s in Hall B. All these times are measured with respect to the CLAS trigger signal.

The distribution of the number of events versus $\Delta\tau$ for a single channel is shown in Fig. 4-6-a. The multiple peaks on this plot arise because only one out of forty RF-signals is sent to Hall-B, while the observed event can be caused by an electron from any of the forty electron bunches. The peaks must be separated by exactly 2.0039 ns if the TOF TDC-s and the TDC of the RF-signal are calibrated correctly. As a matter of fact, this plot is

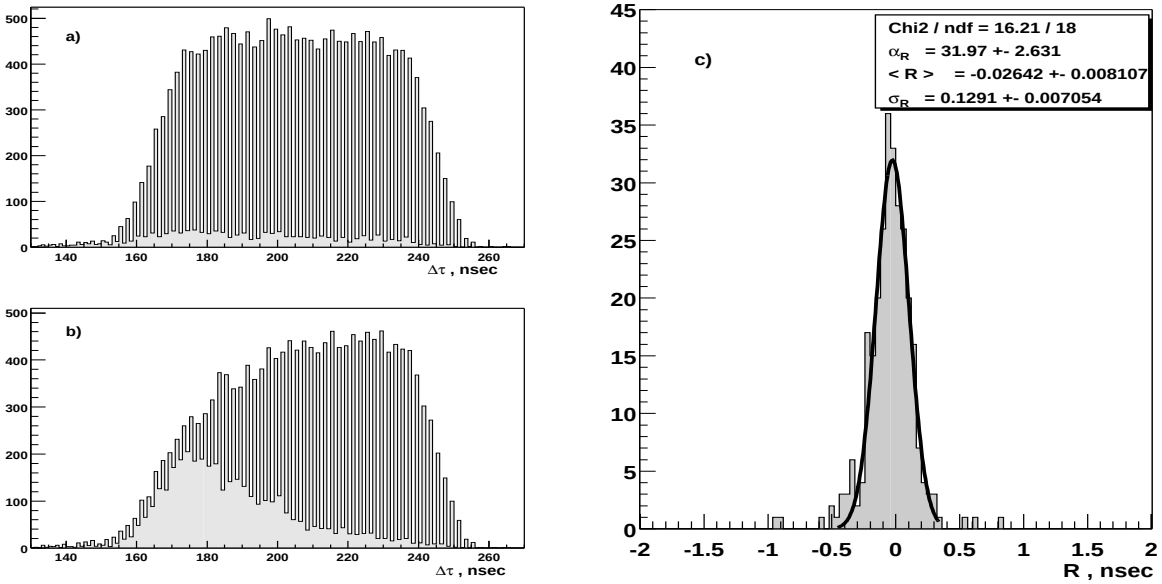


Figure 4-6: Illustration of the beam RF-structure: (a) $\Delta\tau$ distribution with properly calibrated TDC-s, (b) $\Delta\tau$ distribution when the $c_1$ parameter of the TDC of the RF-signal is miscalibrated by less than 1%, (c) R-distribution for a single scintillator channel, fitted with a Gaussian curve (figure courtesy of H. Egiyan [74]).

a sensitive test of the accuracy of the TDC calibrations (subsection 4.1.1), since in case of miscalibrated TDC-s one can see a pattern similar to one shown in Fig. 4-6-b . Extra corrections may be needed to the $c_1$ TDC calibration parameter, defined in eq. (4.1), if this type of pattern appears in the plot in Fig. 4-6.

The time offset for each scintillator counter is defined as [75]:

$$R = \mathrm{mod}_{\Delta T}\left(T_{SC} - T_{flight} - T_{RF} + 100 \cdot \Delta T\right) - \frac{\Delta T}{2}, \tag{4.8}$$

where $\Delta T$ was defined in eq. (4.5). R determines how much the time signal given by the scintillator counter $T_{SC}$ should be delayed in order to align it with the RF-signal.

The distribution of events versus the offset $R$ for a single Time-of-Flight channel is shown in Fig. 4-6-c. The position of the peak defines the time offset to be subtracted from

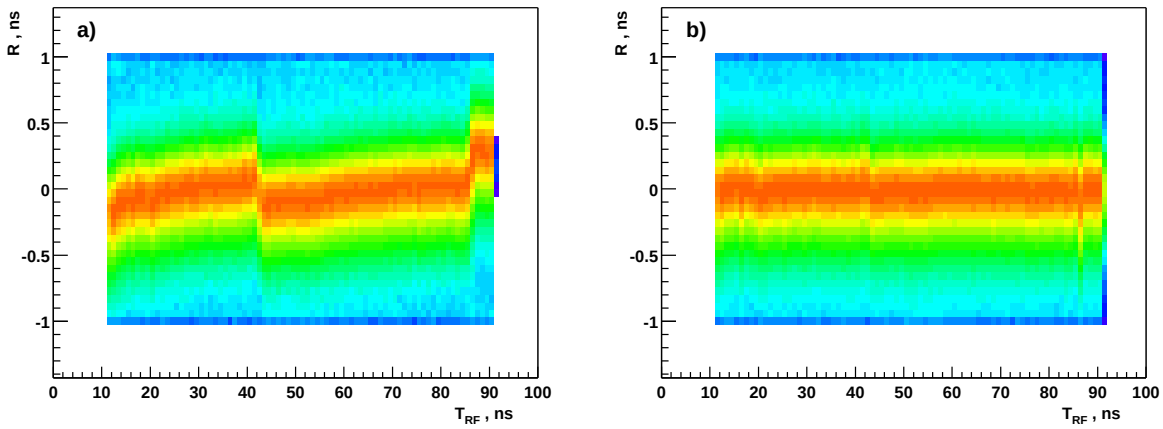


Figure 4-7: Two dimensional plot showing versus $T_{rf}$ for (a) uncalibrated RF-signal and (b) calibrated RF-signal (figure courtesy of H. Egiyan [74]).

the $T_{SC}$ when calculating the mass of the particle using TOF information. The width of the distribution depends on the timing characteristics of the scintillator, the quality of the calibration for that particular channel, and the TDC calibration of the RF signal (section 4.1.6). If the RF signal TDC is miscalibrated, then the plot of $R$ vs. $T_{RF}$ will exhibit a slight slope.

After a proper calibration the $R$ versus $T_{RF}$ distribution must look like a horizontal band, as illustrated in Fig. 4-7-b. Then one can vary the slope parameter of the scintillator TDC calibration to find the value which produces the narrowest width of the $R$-distribution shown in Fig. 4-6.

Once the RF and the Time-of-Flight TDC-s are calibrated to produce satisfactory results, the next step is to fit the $R$-distributions for each counter with a Gaussian curve to determine the peak positions. The obtained values are called "fine tuning constants". Since the electrons are predominantly produced in the forward direction, pions must be used to determine the fine tuning constants for the backward strips. The disadvantage of using pions is that, unlike electrons, they have a significantly smaller $\beta$, and therefore one has to

use the pion momentum from tracking to determine their velocity. Protons are even less useful, because they have significant energy losses on their way to the scintillators. For the reasons mentioned above, the fine tuning of the forward scintillators from (1-20) is done using electrons, while the remaining channels are calibrated with pions, identified by their $dE/dx$ signature (Fig. 4-5).

Most of the channels gave Gaussian $R$-distributions, whereas the channels from 40 and up were producing double peaks, caused by the fact that two actual scintillator strips are connected to a single electronic channel[1]. For the low energies, the timing resolution obtained, $\sigma_t \approx 2$ ns is sufficient to reliably separate pions and protons at such large angles, because these backward tracks typically have momentum less than 1 GeV/c.

After the fine tuning is done, all scintillator counters are aligned with the RF signals. But there still can be an offset between different paddles, because their timing might be aligned with RF-signals corresponding to different electron bunches. Therefore, any time offset between any two channels must be a multiple of 2.0039 ns. A procedure was developed [75] to solve this ambiguity in selection of the reference timing signal using the events containing an electron and at least one pion. This procedure, known as "crude tuning", consists of three steps. The first is to equalize the time delays for the first ten channels in each sector.

Once the timing for the first ten channels of all sectors are aligned, one has to find the relative delays between sectors, which again can only be multiple of 2.0039 ns. To find these timing offsets, we use events containing an electron in one of the ten forward scintillator counters of the sector being calibrated, and a pion in the first ten counters of sector 1, chosen as a reference.

The final step in the paddle-to-paddle calibration procedure is the alignment of the time

[1] At the present time, this is compensated using tracking information to identify the individual paddles in the pair.

delays for the channels from 11 to 48. For this purpose, events containing an electron and at least one pion are selected. The electron is required to be detected in any of the first ten paddles in any sector, while the pion signal must be in the scintillator being calibrated.

The paddle-to-paddle calibration makes use of the `p2p_delay_el` code and is described in detail in reference [74].

### 4.1.8 Alignment of the TOF System to the RF-signal

To determine hadronic masses using flight time information, one has to know the start time of the event. For the electron runs the natural choice would be using the electron timing to determine the start time of the event at the target vertex. Then the flight time of the hadron and the corresponding resolution are given by:

$$T^{\pi}_{flight} = T^{\pi}_{SC} - \left( T^{e}_{SC} - \frac{L^{e}_{track}}{c} \right) \tag{4.9}$$

$$\delta T^{\pi}_{flight} = \sqrt{{\delta T^{\pi}_{SC}}^2 + {\delta T^{e}_{SC}}^2 + \left( \frac{\delta L^{e}_{track}}{c} \right)^2} \tag{4.10}$$

where $L^{e}_{track}$ is the length of the electron track from the vertex to the scintillator and $c$ is the speed of the electron, taken equal to the speed of light. The electron timing resolution $\delta T^{e}_{SC}$ makes a significant contribution into the uncertainty of the determination of the flight time. One of the ways of eliminating the contribution from the electron timing errors and improving the resolution of the hadron flight time is to use the RF-signal to determine the event start time. In fact, after the paddle-to-paddle calibration procedure is complete, the timing of all scintillator counters are adjusted to the same RF bunch. Therefore, the

RF-corrected flight time, defined as:

$$T^{\pi}_{flight} = T^{\pi}_{SC} - \left( T^{e}_{SC} - \frac{L^{e}_{track}}{c} - R^{e} \right) \tag{4.11}$$

$$\delta T^{\pi}_{flight} = \sqrt{(\delta T^{\pi}_{SC})^2 + \left( \frac{\delta L^{e}_{track}}{c} \right)^2} \tag{4.12}$$

can be used to calculate the velocity of hadrons. Equation (4.11) is valid as long as all Time-of-Flight counters are adjusted with respect to the RF-signal. But because the tuning of the beam may change the path length of the electrons from the injector to the target, and because the signal propagation speed in the cables may vary with time, this alignment had to be done for each run.

### Calibration Results

The procedures described above were done to ensure that the offline CLAS analysis software reliably distinguish among different types of hadrons. The timing resolution determined by the Time-of-Flight calibrations directly affects the level of non-physical background.

Figures 4-8 (a) and (b) and 4-9 illustrate the quality of the PID (particle identification) calibration. In 4.8(b) the dependence of $\beta$ versus momentum for positively charged particles is shown (all scintillators combined). The mass of the hadron can be calculated knowing its velocity and momentum. The mass spectrum from an empty target run at 4.4 GeV electron beam energy is shown in Fig. 4.8(a). Clearly distinguishable are the peaks corresponding to the proton, pion and deuteron, and somewhat smaller kaon and triton peaks.

At very low momentum the resolution of the TOF system is adequate for separation of positrons, pions and muons from pion decays, as illustrated in Fig. 4-9. The feasibility for separation of these three types of particles is strongly momentum dependent, because

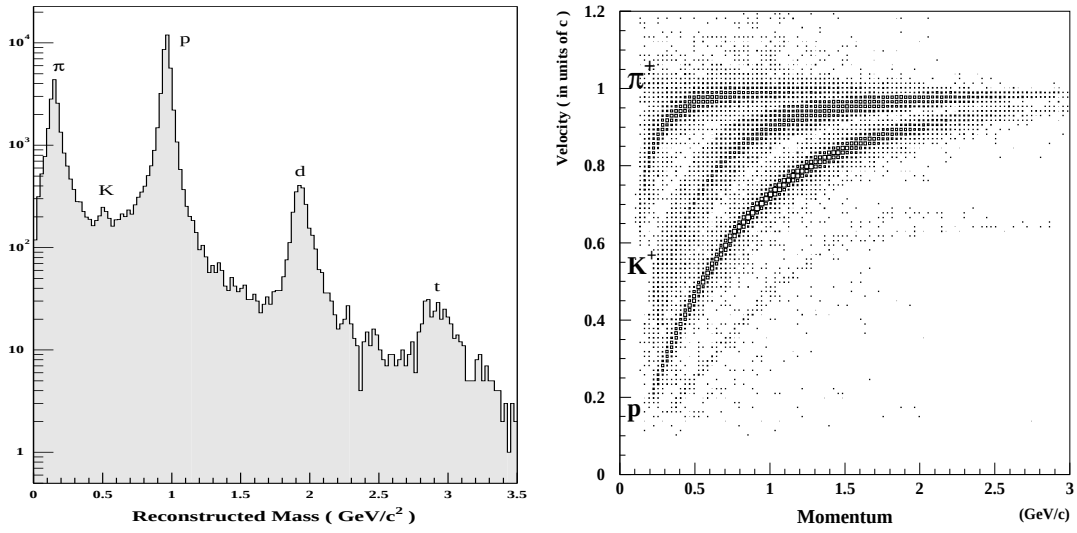


(a) (b)

Figure 4-8: (a) Mass spectrum of hadrons from an empty target run. (b) Plot of $\beta$ versus momentum. Here the kaon band was artificially enhanced. The pion and proton bands are reliably separated up to 2.5 GeV/c momenta (from [74]).

at higher momentum the mass resolution deteriorates and these peaks merge. For this reason the CLAS particle identification procedure presumes all these particle to be pions by default.

For further information as well as technical details regarding the Time-of-Flight calibration, the reader is referred to [76].

## 4.2 Electromagnetic Calorimeter Time Calibration

The electromagnetic calorimeters are an important component of the particle identification scheme since the EC time provides the start signal for the $SC^e$, $SC^\pi$ and RF TDCs.

Also, neutral particles in CLAS are detected in the electromagnetic calorimeters. The neutron's time of flight is the only measurement of its energy because the neutron does

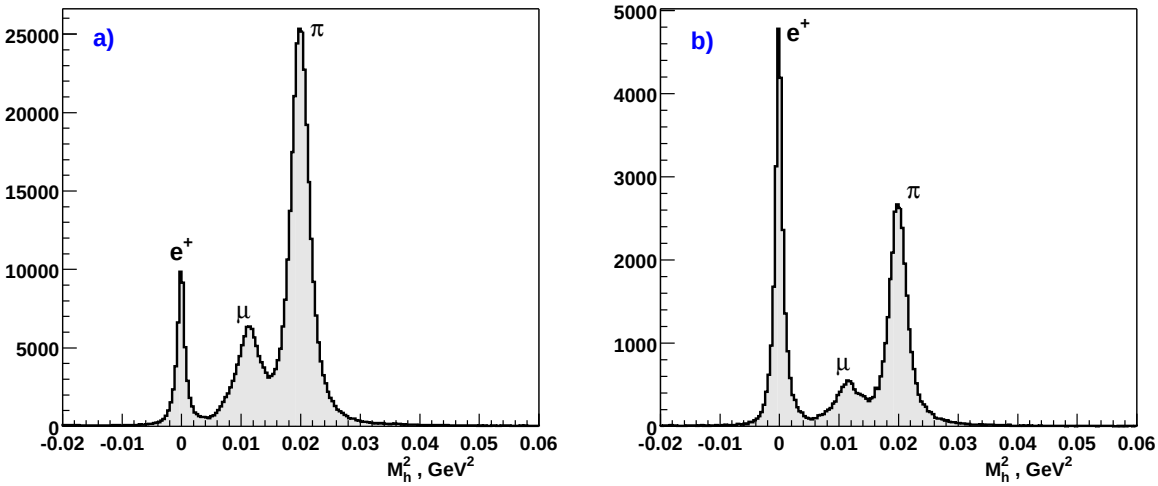


Figure 4-9: Mass squared for backward flying particles (paddles 20 and above) with momentum below 0.25 GeV/c (a) without any sector cut (b) the electron and the other particle are required to be in the same sector (from [74] ).

not deposit all its energy in the calorimeter. This makes EC time calibration essential for experiments that detect neutrons in the final state.

We use electron time measured by Time-of-Flight to calibrate EC time measurements. First we identify an electron. Because there is no magnetic field between the scintillator counters and the electromagnetic calorimeters, the track is straight. If we assume that $t_{sc}$ is correctly calibrated, we can predict the time measured by EC as:

$$t_{ec} = t_{sc} + \frac{d_{ecsc}\cos\alpha}{c}$$

where $d_{ecsc}$ is the distance between the EC and SC layers, $c$ is the electron velocity and $\alpha$ is the impact angle to the EC plane (see Fig. 4.10(a).

The value $t_{ec}$ is assigned to the EC scintillation bar with the largest ADC for each of the three views, exactly the same way as it is done in the reconstruction code [110]. The

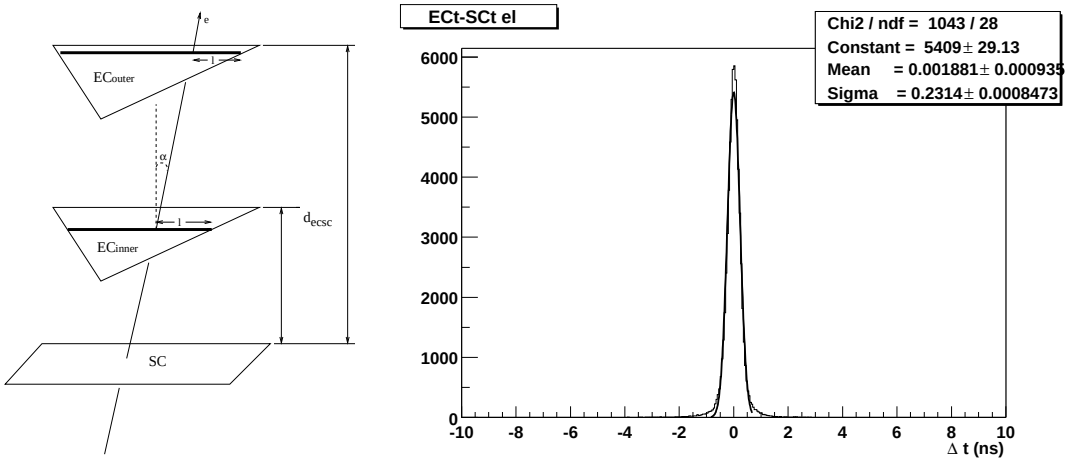


(a) (b)

Figure 4-10: (a) EC time extrapolation from SC time. Only the scintillation bar with the largest ADC value in one view for each EC layer is shown. (b) Obtained EC time resolution for electrons in sector 1 (from [71]).

time dependence is fitted with the function

$$t_{EC} = p_0 + p_1 \cdot tdc + \frac{p_2}{\sqrt{adc}} + p_3 \cdot l^2 + p_4 \cdot l^3 - \frac{l}{v_{eff}}$$

where $p_i$ are five fit parameters, $tdc$ and $adc$ are the TDC and ADC values, respectively, $l$ is the length from the hit point to the EC readout edge and $v_{eff}$ is the speed of light in the scintillator material. The first two terms are simple linear TDC response, the third term is the time-walk correction, the fourth and fifth terms are small corrections for the fact that signals arrive at the readout edge at slightly different times for scintillation bars connected to the same PMT and the last term is inserted to compensate the time for scintillation light to travel from hit point to readout edge.

The best fit constants are saved in the calibration database. The difference between the reconstructed EC time and the Time-of-Flight value defines the time resolution for electrons

(Fig. 4.10(b)). The overall $\sigma$ is $\sim$ 250 ps, which is partially due to the TOF resolution. If we take the TOF time resolution to be $\sim$ 150 ps (see previous section), then the electromagnetic calorimeter time resolution for electrons is approximately $\sqrt{250^2 - 150^2} = 200$ ps. For neutral particles, this figure is not as good. A neutron can interact anywhere within the thickness of the calorimeter which is as large as 40 cm. In a rough approximation, this results in an uncertainty in the flight path equal to half this thickness, which for a neutron with $\beta$=1 is equivalent to a time uncertainty of $\pm$700 ps. For lower $\beta$ it will be even larger. Therefore, for neutrons, the resolution obtained can not be below $\pm$700 ps.

For a detailed description of the EC calibration procedure as well as for technical details, the reader is referred to [71].

## 4.3 Calibration of the Drift Chambers

The primary purpose of the drift chambers calibration is to refine the position measurements from time based tracking (TBT). Specifically, the calibration constants for the time-to-distance function need to be calibrated and checked. This involves choosing calibration runs evenly spaced throughout the running period and the processing of at least 100K events from each of those runs. The exact frequency by which runs should be calibrated depends on the run period. Obviously, if the calibration constants change by a large amount from one calibration run to another the frequency of updating calibrations should be increased. In general, the tracking calibrations are checked for every day of the running period.

While the primary purpose of drift chamber calibration is to obtain a first set of time based tracking calibrations, it also provides a good opportunity to assess the overall quality of all calibrations. Problematic running periods can be identified, and runs can be selected for the next stage of analysis.

The drift chambers are calibrated by parametrizing the drift velocity function. 36 out of 365 runs collected during the E2A run time were chosen for calibration purposes, covering every day of the run period. The calibration program `dc_calib_check-2-0` presented in [77] was used to calibrate these runs.

### 4.3.1 Drift Chamber Nomenclature

The CLAS drift chambers can be separated in several ways. Figure 4-11 gives a basic idea of how the chambers are arranged.

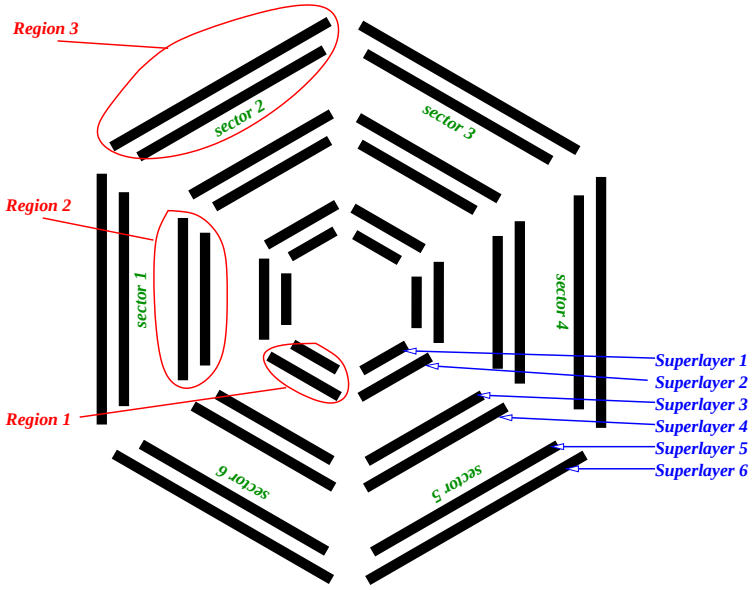


Figure 4-11: Schematic of CLAS drift chambers showing how regions and superlayers are named. The picture represents a slice through the CLAS perpendicular to the beam line at about the target position.

Each of the six sectors of CLAS has an identical set of drift chambers. Each set can be separated by region or by superlayer. Practically, each region is a separate physical volume containing two superlayers. Each superlayer contains six layers of sense wires,

except superlayer 1 which has only 4 layers. Each superlayer of each sector is calibrated separately, for a total of 36 sets of parameters [70].

When a charged particle goes through the drift chambers, each of the 34 layers is hit.[2] Each hit detected in the chamber is used to determine the particle's track via a least squares fit which is done within the CLAS reconstruction program. Two terms are used to describe the distance of the charged particle track from a sense wire:

*DOCA* (Distance Of Closest Approach) is the distance from the sense wire to the track as determined using information from all the hit wires.

*DIST* is the predicted distance from the sense wire to the track. This is calculated from the drift time and some other parameters.

Additionally, the *residual* is defined as:

$RESI = |DOCA| - |DIST|$

This is also known as the "time residual" because its sign is determined by the sign of any systematic time shift. The residuals are the primary means of measuring the resolution of the drift chambers. We estimate standard deviations (residual sigma) of the residual distributions by means of a Gaussian fit. Note also that $DIST$ is positive definite, while DOCA is assigned a sign determined by whether the track passed to the right or to the left of the wire.

### 4.3.2 Parameterization Method

The CLAS drift chambers are calibrated by parameterizing the drift velocity function for every superlayer in every sector. The drift velocity function is the relation between the calculated distance of closest approach (DIST) of a particle track to the drift time $t_d$. The

[2] In practice, we find an average of 30 hits per time-based track. This is mostly due to inefficiencies or holes in the chamber's fiducial volume

drift time $t_d$ is defined as the time necessary for the ions created by the particle to drift to the sense wire (see figure 4-12).

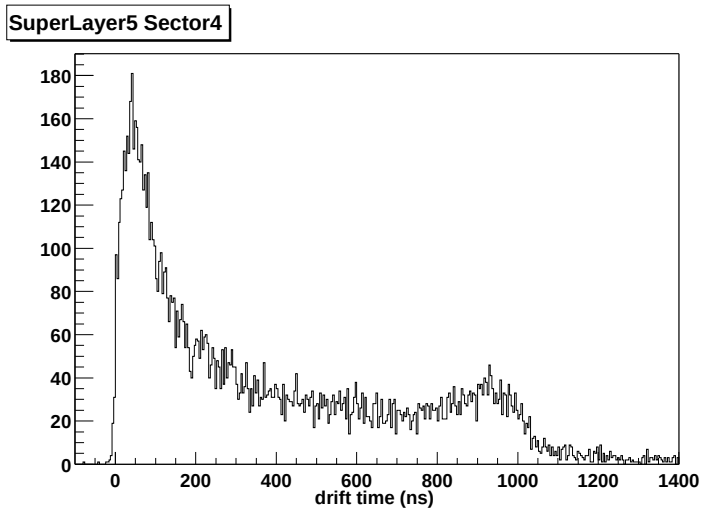


Figure 4-12: Drift time for superlayer 5 in sector 4.

The function's parameters are determined by fits to DOCA versus time plots produced from CLAS data. Figure 4-13 shows a typical DOCA versus time distribution.

The DOCA values are obtained from fits of global tracks (i.e. fits which include all layers) and the drift times are calculated from the wire's TDC values accounting for fixed cable delays and event-dependent delays such as flight time.

### 4.3.3 Calibration Quality

The quality of the calibration is double-checked by examining quantities like the time residual sigmas (resolution), TBT hits per track and $\chi^2$ values obtained for all 36 fits [3]. Figure 4.14(1) shows residual sigmas as function of calibration run number for two cases: superlayer 3, averaged for 6 sectors and sector 3 averaged for 6 superlayers. Different symbols

[3] 6 sectors $\times$ 6 superlayers

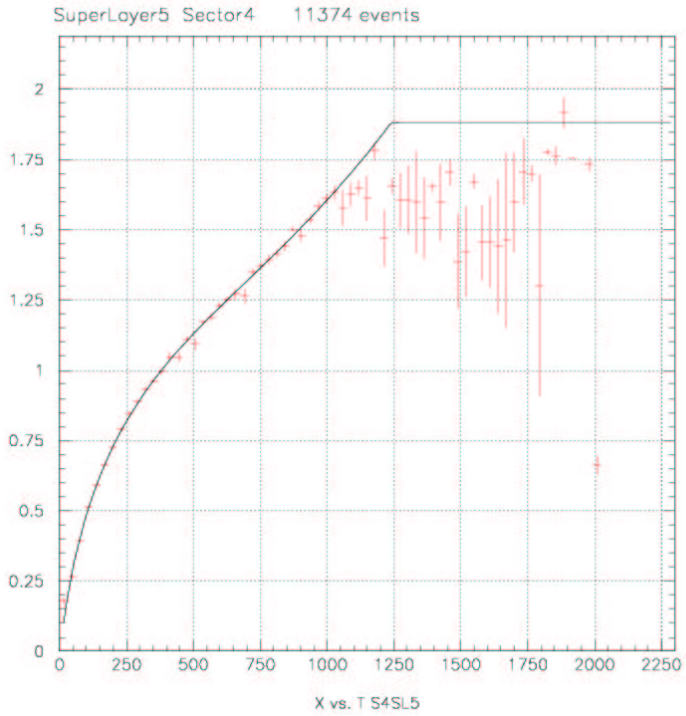


Figure 4-13: Drift velocity function for superlayer 5, sector 4. On the vertical axis is DOCA (cm) and on the horizontal axis is the drift time $t_d$ (ns).

on the plots correspond to different beam energy of the calibration runs. Slight changes of the resolution are due to beam energy changes.

Figure 4.14(2) shows the TBT hits per track as a function of superlayer number and sector number averaged over all calibration runs. The number of hits per track for superlayer 1 differs from the same quantity measured for the other superlayers due to the fact that superlayer 1 has only 4 layers. Figure 4-15 shows the residual sigma as a function of superlayer number and sector number averaged over all the calibration runs.

A more detailed description of drift chamber calibration procedure is given in [77, 70].

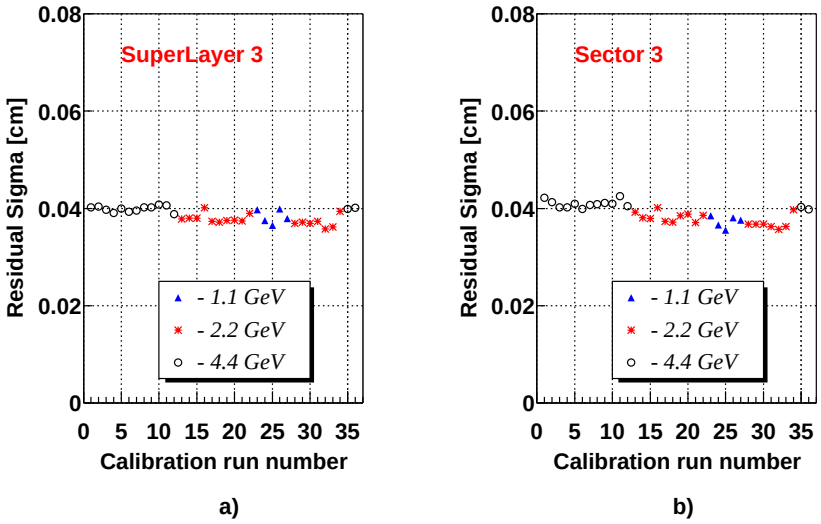


(1) Residual sigmas versus calibration run number: a) superlayer 3 averaged for 6 sectors and b) Sector 3 averaged for 6 superlayers. Different markers correspond to different beam energies of the runs. Calibration run number corresponds to the time of data taking (covers every day of the running period).

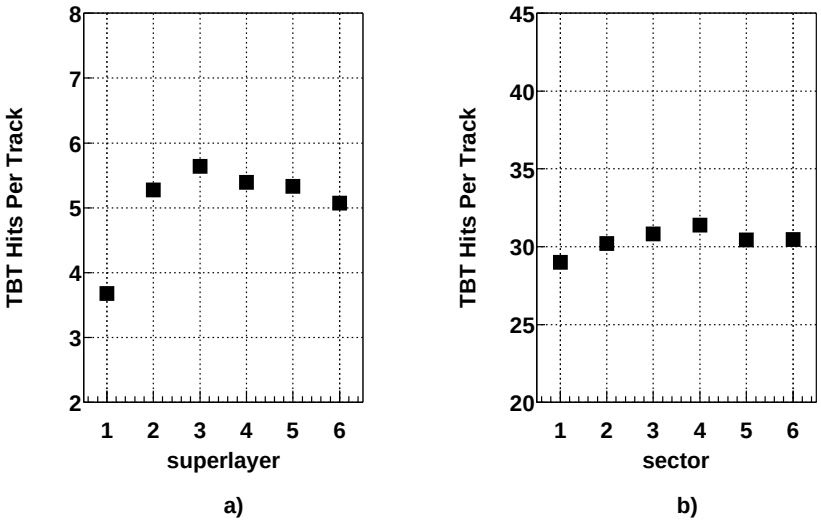


(2) Hits per track versus a) superlayer averaged over 6 sectors and b) sector averaged over 6 superlayers. Both a) and b) are average values over the 36 calibration runs.

Figure 4-14: Indicators of calibration quality (E2A data).

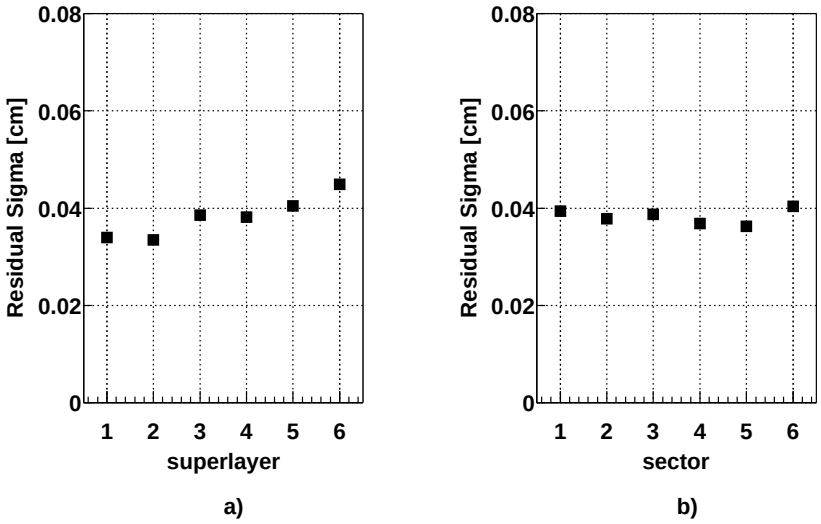


Figure 4-15: Resolution versus a) superlayer averaged over 6 sectors and b) sector averaged over 6 superlayers. Both a) and b) are averaged over the 36 calibration runs (E2A data).

# DATA SELECTION AND ANALYSIS

## 4.4 Electron Identification

Based on our "single electron trigger" configuration, an event was recorded if there was a signal in the electromagnetic calorimeters and Čerenkov counters (except 4.4 GeV runs where the CC was not in the trigger). At the analysis stage, our aim is to recognize as many scattered electrons as possible without significantly contaminating the data sample.

To double-check the particles that the SEB [110] labeled as electrons, we looked at the ratio of the particle's energy deposited in the EC to the momentum measured by the DC (sampling fraction) [78, 110]. The reconstruction code stores information about the deposited energy in the inner ($E_{in}^{EC}$), outer ($E_{out}^{EC}$) and the whole ($E_{tot}^{EC}$) electromagnetic

calorimeters (section 3.2.5). We use this as a supplementary check of the reconstruction accuracy. Because $E_{in}^{EC}$ or $E_{out}^{EC}$ were frequently absent, we took

$$E_{tot}^{EC} = \max(E_{in}^{EC} + E_{out}^{EC}, E_{tot}^{EC}) \tag{4.13}$$

A study of the relationship between the deposited energy in the electromagnetic calorimeters and the momentum of the electron has been done. Figure 4-16 shows this dependency for

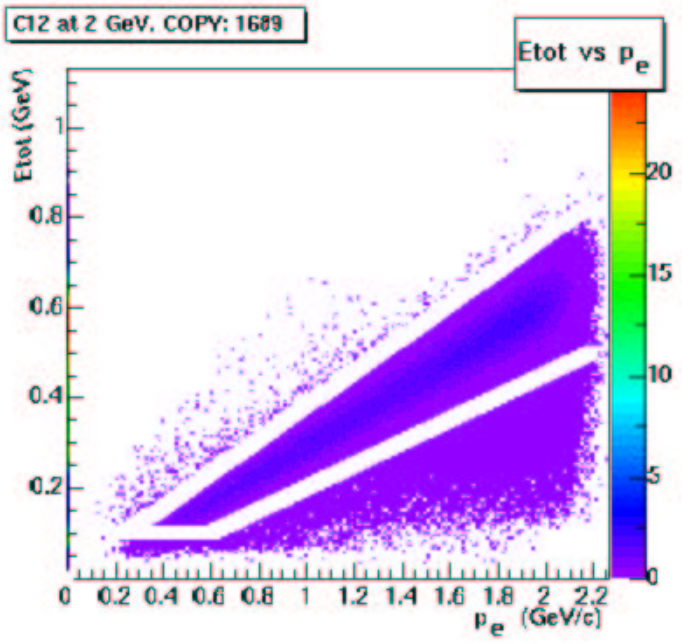


Figure 4-16: Dependence of the total deposited energy in the forward calorimeter ($E_{tot}^{EC}$) versus the electron momentum $p_e$. The data shown is for $^{12}$C (e,e') at 2.261 GeV and the cut is defined by the conditions (4.14) and (4.15).

$^4$He data at $E_{beam} = 2.261$ GeV. A threshold

$$E_{tot}^{EC} > E_{thresh} \tag{4.14}$$

| Target | $E_{beam}$(GeV) | $E_{tot}^{thres}$(GeV) | $a_{EC}$(GeV) | $b_{EC}$(c.u.) | $a'_{EC}$(GeV) | $b'_{EC}$(c.u.) |
|---|---|---|---|---|---|---|
| $^4$He | 2.261 | 0.10 | 0.251 | -0.049 | 0.390 | 0.003 |
| | 4.461 | 0.33 | 0.273 | -0.118 | 0.371 | 0.042 |
| $^{12}$C | 2.261 | 0.10 | 0.252 | -0.053 | 0.376 | 0.004 |
| | 4.461 | 0.33 | 0.277 | -0.140 | 0.366 | 0.041 |

Table 4.2: $E_{tot}$ threshold and constants for the $3\sigma$ cut from (4.15).

is set in order to eliminate the minimum ionizing particles. The $3\sigma$ cut is defined by

$$a_{EC} + b_{EC}p_e < E_{tot}^{EC} < a'_{EC} + b'_{EC}p_e \tag{4.15}$$

with $a_{EC}, a'_{EC}, b_{EC}$ and $b'_{EC}$ four fit constants ( table 4.4) and $p_e$ the electron momentum. The cut is determined by the fit of the $3\sigma$ ridge of the $E_{tot}^{EC}$ versus $p_e$ distribution. Similar conditions have been applied to all the data sets. Also a sector by sector comparison has been done and we concluded that an overall cut is sufficient.

To summarize, we require that electrons satisfy the following conditions:

1. Čerenkov counters status is OK (excepting the 4.461 GeV data)

2. $3\sigma$ cut on $E_{tot}$ versus momentum $p_e$

3. $E_{in} > 0.055$ GeV or $E_{in} = 0$ (from trigger; if $E_{in} = 0$ then the information is missing)

4. be above the $E_{tot}$ recommended threshold [79]

For our data, SEB sometimes mislabelled electrons as Id=0 (i.e. as an unidentified negative track). The procedure we described above will account such an SEB Id=0 particle as electron, if it fulfills the above conditions. The gain of our selection method with respect to the SEB labeled electrons is of 3-10%.

## 4.5 Electron Momentum Corrections

Geometrical uncertainties in the detector alignment and in the magnetic field mapping can influence the measurements of the momenta. What one can do, using as a reference some well known process, is to derive a correction procedure that would restore the true values. One such procedure is based upon elastic electron-proton scattering. Assuming that the beam energy is exact and that the polar scattering angle $\theta$ is accurately determined, the scattered electron momentum can be calculated and compared with the measured one. The ratio of these two values gives a correction factor which depends solely on the angles $\theta$ and $\phi$ in the lab frame and therefore can be applied to other target data as well. A detailed description of this procedure is given in [81] and included in appendix A.

The electron momentum corrections were less than 3 %, typically 1–2 %.

## 4.6 Electron Fiducial Cuts

For electron identification, in most cases, valid signals in all four detectors are required. Electron detection efficiency around the mid plane in each sector is reproducible in the GSIM simulations. Due to the complicated readout structures of electromagnetic calorimeters and Čerenkov counters, detection and reconstruction efficiencies are not well understood in the regions close to the torus coils, and close to the dead channels of detector elements. In order to minimize systematic uncertainties in the physics analysis it is important to accept events in the fiducial region of the detector, where efficiencies are flat and understood. Fiducial cuts define a region in ($\theta$, $\phi$) space for a given momentum, where detection efficiency is almost constant with $\phi$ and can be reproduced in simulations. These functions depend on the actual run conditions (bad channels, target position, trigger, etc.). The procedure of

deriving the fiducial cut functions for liquid target, at 4.4 GeV beam, with no Čerenkov counters in the trigger is presented in detail in [82] and appendix B.

## 4.7 Proton Identification

The CLAS allows separation of protons and kaons for momenta up to 1.6 GeV/c and of protons and pions up to 3 GeV/c. For the present analysis our main concern is contamination of protons with pions.

Protons are identified by the charge and momentum measured using the track length provided by the DC tracking and the time-of-flight measured at the SC. The final `rootDST` stores the $\beta$ and the momentum of the particle. A positively charged particle is identified as a proton if it has the smallest $|\beta_{measured} - p/\sqrt{p^2 + m^2}|$ compared to $\pi^+$, $K^+$ or deuteron, where $p$ is the momentum measured by the tracking.

In figure 4-17 one can see that the bands for protons and pions are clearly visible and well separated. This separation is done in the lower level software [69, 110] and we use the result. A more rigorous proton selection can be done using a $dE/dx$ cut but this would be beyond the precision requirements of the present analysis.

## 4.8 Vertex Cuts

The two targets discussed in section 3.4 are different from one another in many respects.

The carbon $^{12}$C target is a graphite square less than 1mm thick, shifted by approximately 5.5 cm downstream from the center of the detector, downstream of the liquid target cell. The beam that passes through this target scatters before on the empty cell and gives spurious background. To eliminate this background we used tracking information to reconstruct

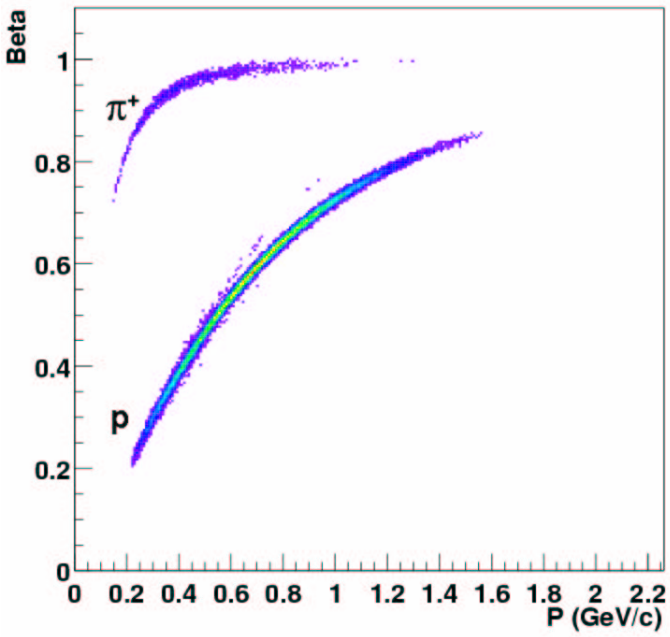


Figure 4-17: Plot of $\beta$ versus momentum for positive tracks in CLAS. Notice the clear separation between $\pi^+$ and protons. $K^+$ are too faint to be seen on this plot.

the reaction vertex and match this with the physical position of the target. Figure 4-18 illustrates the steps of this procedure. On the electron-proton $z$-vertex distribution in (a) we identify the most intense ridge as the $^{12}$C target and the faint bands as (from top to bottom) the heat insulation and the output and input windows of the empty liquid target cell. Then it is simple to fit the uppermost ridge (b) and cut around it. Sub-figure (d) shows the acceptable region, where VZ_e and VZ_p stand for the $z$-projection of the electron and proton reconstructed vertex, respectively.

The situation is slightly different in the case of the helium target. The $^{12}$C target flips out of the beamline but we have the cell windows and heat shield to worry about now, since the beam passes through them before and after scattering on the $^4$He nuclei. To ensure that the electron-proton pairs detected originate in the target, we used the empty target

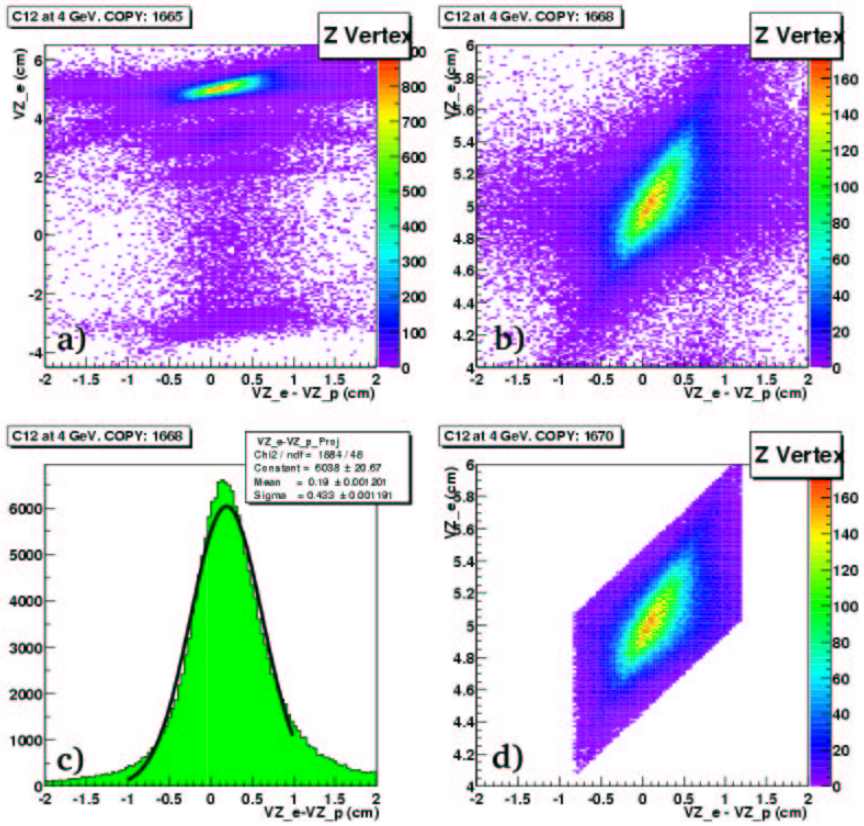


Figure 4-18: Solid Target: The intense band in (a) is the $^{12}$C target whilst the three faint bands are the walls of the liquid target cell and the insulation. We fit the ridge of the 2-d distribution (b) and cut 0.5 cm under and above it. The center is determined by the fit in (c) which gives a vertex resolution $\sigma_v = 4.3$ mm.

data taken with the same cell to identify the contribution from the cell material. Similar to the case of $^{12}$C target, one can recognize in figure 4-19(a) the insulation and the input and output windows (in this order, from top to bottom). Same fit-and-cut procedure produces the result in Fig. 4-19(d).

## 4.9 Beam Charge Asymmetry

The beam charge asymmetry (BCA) is defined as the ratio of the normalized beam intensities for the two helicities. To ensure that integrated currents for the two helicity signs are

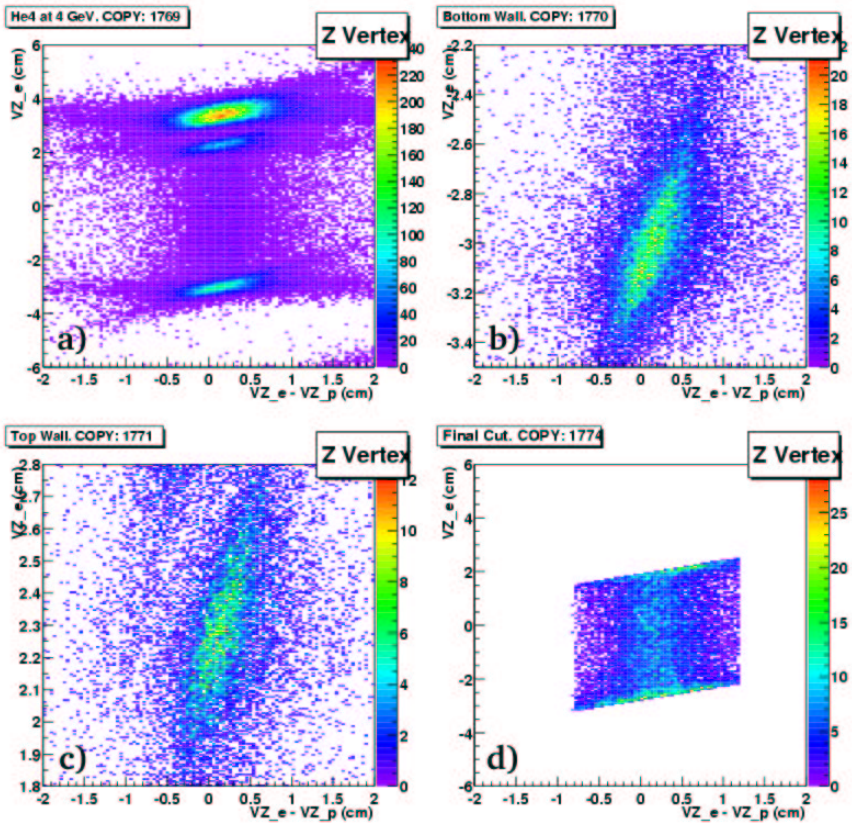


Figure 4-19: Liquid Target: the three visible bands in (a) are the thermal insulation and the target walls (in this order, from top to bottom). The position of the ridges in (b) and (c) is determined by a slice fit of the 2-d distributions. The cuts are positioned 3 mm inside the walls (d).

equal to each other and to correct any possible $y$-offset in our asymmetry measurement, we calculated the beam charge asymmetry on a run by run basis and corrected our data for it.

We calculate the BCA using the inclusive $(e, e')$ electron yields at positive $(N_o^+)$ and negative $(N_o^-)$ beam helicities for each run:

$$\mathcal{A}_Q = \frac{N_o^+}{N_o^-} \tag{4.16}$$

This method is based upon the fact that the inclusive $(e, e')$ cross-section has no helicity dependence. Another way to extract the BCA would be using the Faraday cup readings, but

this was found to depend on various beam parameters including the beam current and the resolution of the charge integrator used to digitize the Faraday cup signal [84]. Figure 4-20 shows the run by run values of the beam charge asymmetry measure using inclusive $(e, e')$ events.

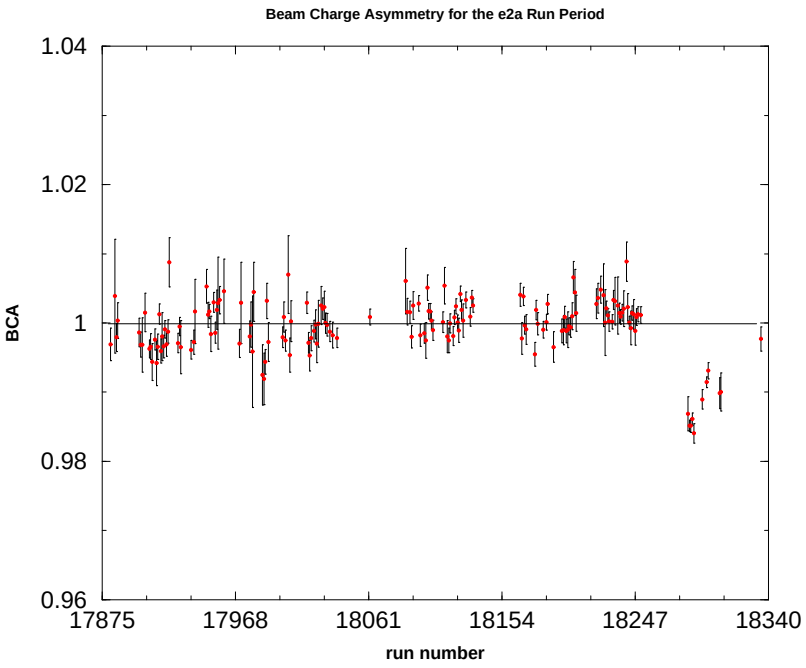


Figure 4-20: Beam Charge Asymmetry (BCA) for the whole E2A run period. The error bars are statistical.

In these conditions, eq.(2.15) is written as:

$$A'_{LT} = \frac{1}{P_B} \frac{d^5\sigma^+ - A_Q d^5\sigma^-}{d^5\sigma^+ + A_Q d^5\sigma^-} \tag{4.17}$$

| $^4$He Target | | | |
|---|---|---|---|
| Step | $E_{beam}$ (GeV) | 2.261 | 4.461 |
| | Total Triggers | 310 M | 442 M |
| 1 | Reconstructed Events | 113 M | 102 M |
| 2 | Events after electron selection | 83 M | 51 M |
| 3 | Number of $ep$ coincidences | 17 M | 6 M |
| 4 | Quasielastic $(e, e'p)$ | 3.8 M | 1/3 M |
| 5 | Calculated points (DWIA+RMSGA) | 486 | 324 |

| $^{12}$C Target | | | |
|---|---|---|---|
| Step | $E_{beam}$ (GeV) | 2.261 | 4.461 |
| | Total Triggers | 323 M | 346 M |
| 1 | Reconstructed Events | 98 M | 66 M |
| 2 | Events after electron selection | 71 M | 33 M |
| 3 | Number of $ep$ coincidences | 17 M | 6 M |
| 4 | Quasielastic $(e, e'p)$ | 2.7 M | 1/4 M |
| 5 | Calculated points (OMEA+RMSGA) | 666 | 441 |

Table 4.3: The $^4$He and $^{12}$C data samples (M stands for 'millions'). Theoretical calculations were added as number of kinematical points computed. Each theoretical point requires 10 to 20 minutes of CPU time.

## 4.10 Final Data Statistics

We presented the raw data sample at the beginning of this chapter and then we described the criteria used to select clean physics events. Table 4.3 summarizes the surviving statistics at various steps in this process and figures 4-21 to 4-28 show the $(e, e'p)$ accessible kinematics.

The quasielastic kinematics requirement implies that the energy and momentum of the virtual photon can be transferred to a single nucleon, the ejected proton. For selecting this

regime, we use the condition $\omega_1 < \omega < \omega_2$ where the limits are

$$\begin{aligned} \omega_1 &= (1/2 - a_1)Q^2/m_p + \Delta E \\ \omega_2 &= (1/2 + a_2)Q^2/m_p + \Delta E \end{aligned} \tag{4.18}$$

with $a_2 = 0.2$, $a_1 = a_2/[1 + 1/[2(1 + 1/2^2)]] \approx a_2$ taken simply for symmetry, and $\Delta E$ is a shift due to the momentum dependence of the nucleus-nucleon potential, taken equal to 0.03 GeV. In other words, we symmetrically cut on one side and the other of the quasielastic ridge $\omega = Q^2/2m_p + \Delta E$ (histograms (f) in figures 4-21 to 4-24). The cut in (4.18) is roughly equivalent to $0.7 < x_B < 1.6$, where $x_B$ is the Bjorken variable. Figures 4-25 to 4-28 show the quasielastic spectra defined with (4.18). At step 4 in table 4.3 a cut on the missing energy

$$E_m < 0.1 \text{ GeV} \tag{4.19}$$

is added to condition (4.18). This cut is not shown in figures 4-25 to 4-28.

The effect of fiducial cuts on our data sample was studied. The fiducial cuts reduce the statistics to almost half (see appendix B), while no visible improvement in the data selection is obtained. Therefore, fiducial cuts were not used in the present measurement of the beam helicity asymmetry.

We need to make a note that no radiative corrections were applied to our data since the statistics are low and we integrate over a large missing energy range (rather than separating the $s$ and $p$ shells in $^{12}$C ).

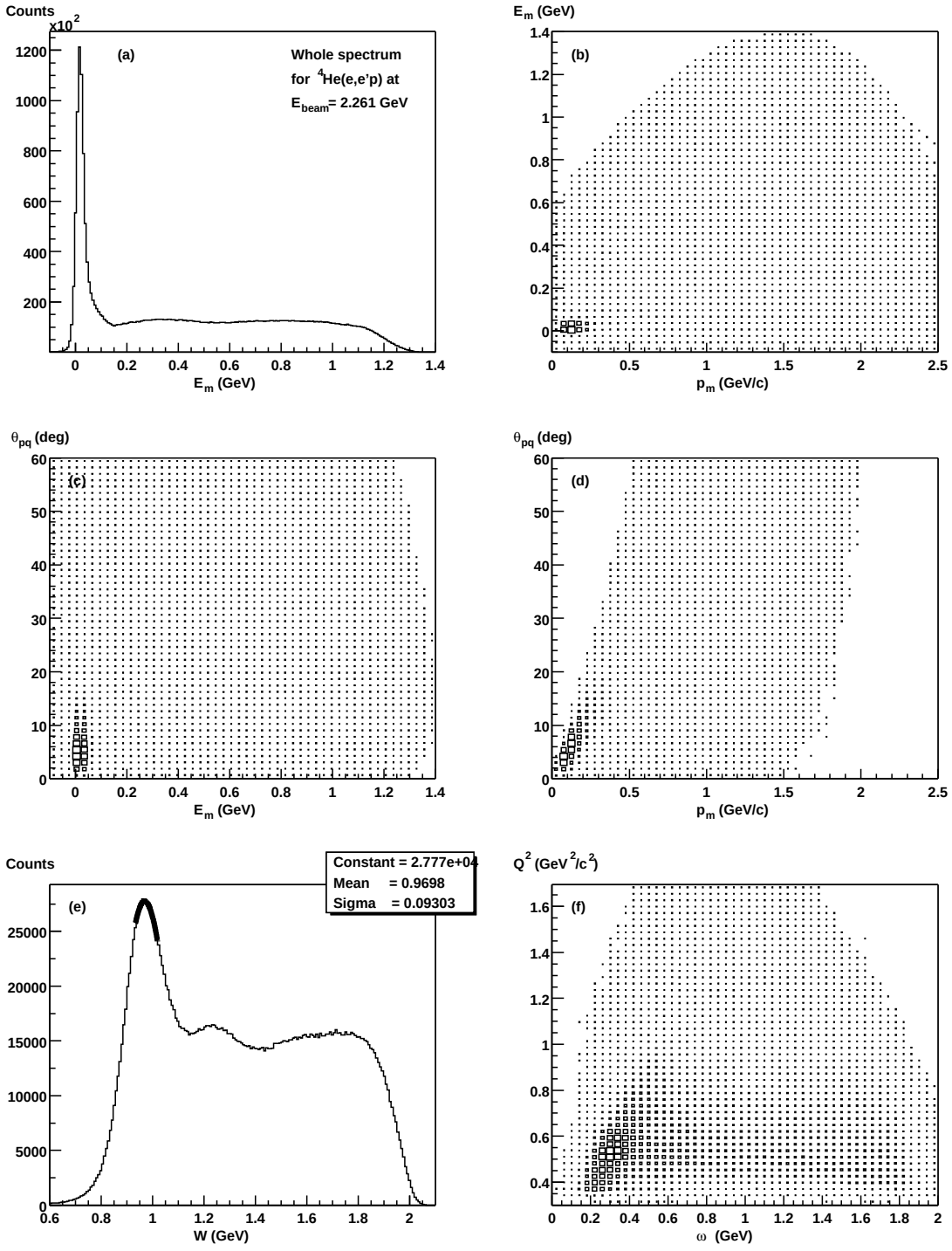


Figure 4-21: Accessible spectra for $^4$He$(e,e'p)$ at 2.261 GeV beam energy: (a) missing energy $E_m$, (b) missing energy vs. missing momentum $p_m$, (c) polar angle $\theta_{pq}$ versus missing energy $E_m$, (d) polar angle $\theta_{pq}$ versus missing momentum $p_m$, (e) invariant mass $W$ for the $(e,e'p)$ reaction and (f) $Q^2$ versus $\omega$ distribution.

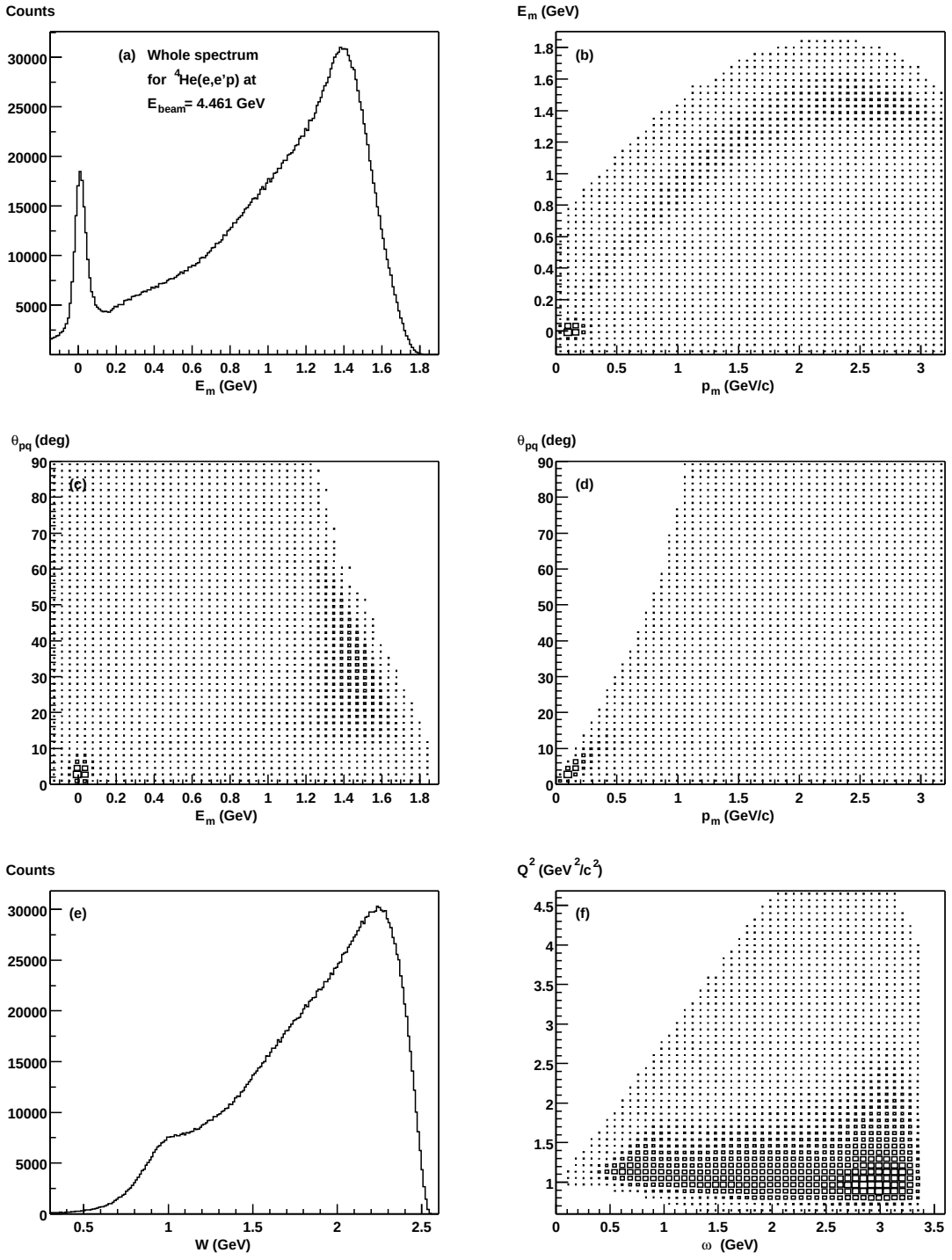


Figure 4-22: Accessible spectra for $^4$He$(e,e'p)$ at 4.461 GeV beam energy: (a) missing energy $E_m$, (b) missing energy vs. missing momentum $p_m$, (c) polar angle $\theta_{pq}$ versus missing energy $E_m$, (d) polar angle $\theta_{pq}$ versus missing momentum $p_m$, (e) invariant mass $W$ for the $(e,e'p)$ reaction and (f) $Q^2$ versus $\omega$ distribution.

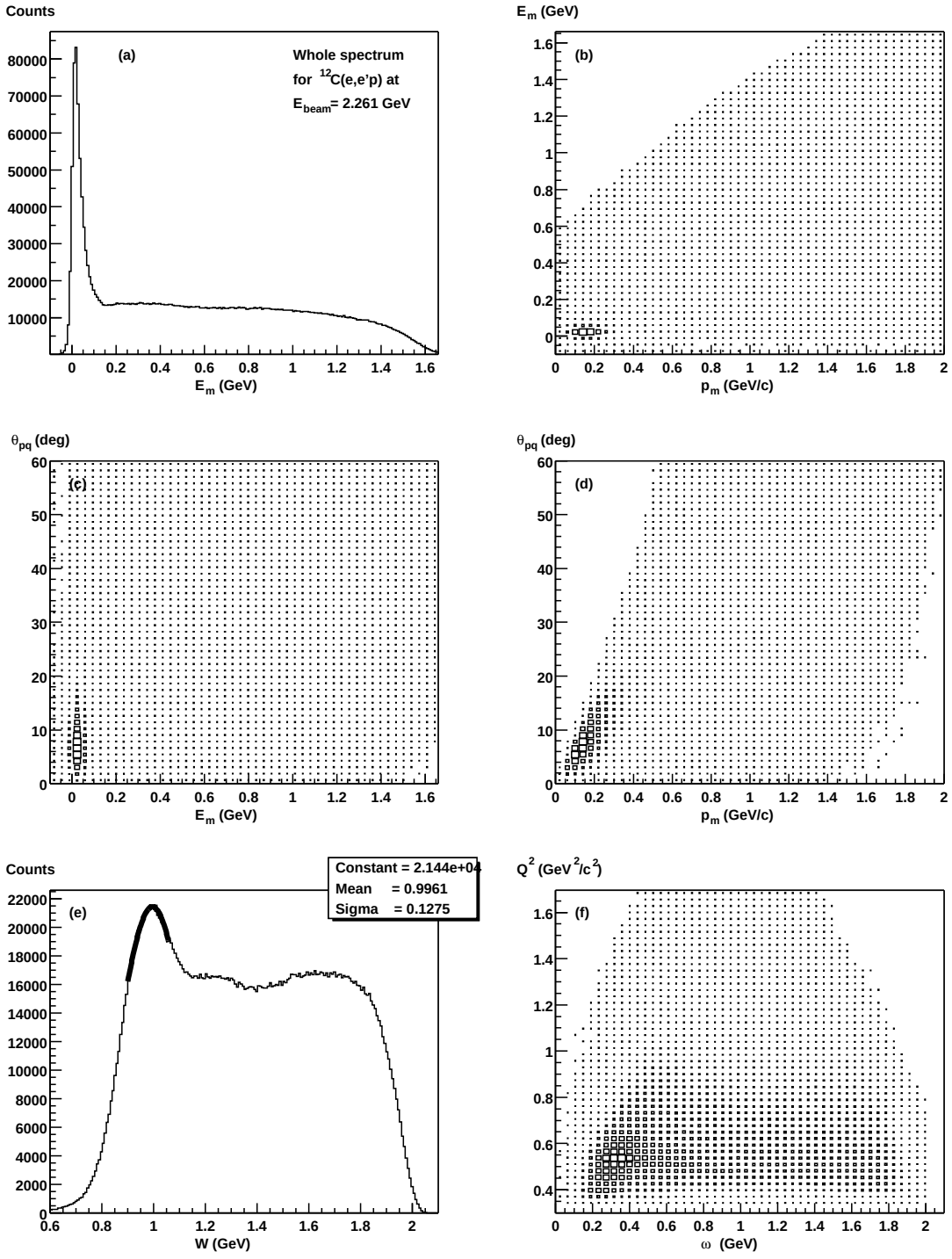


Figure 4-23: Accessible spectra for $^{12}C(e,e'p)$ at 2.261 GeV beam energy: (a) missing energy $E_m$, (b) missing energy vs. missing momentum $p_m$, (c) polar angle $\theta_{pq}$ versus missing energy $E_m$, (d) polar angle $\theta_{pq}$ versus missing momentum $p_m$, (e) invariant mass $W$ for the $(e,e'p)$ reaction and (f) $Q^2$ versus $\omega$ distribution.

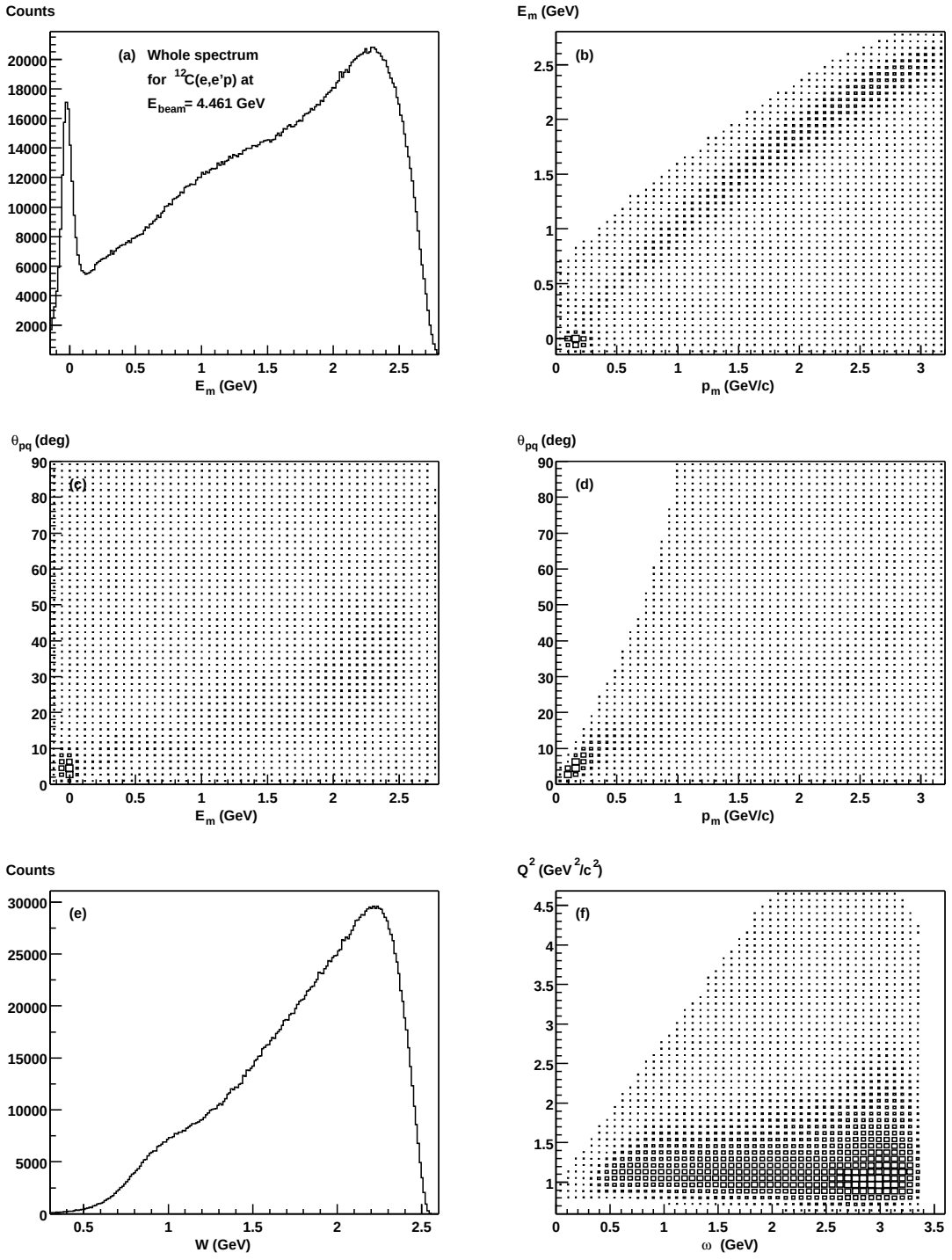


Figure 4-24: Accessible spectra for $^{12}C(e,e'p)$ at 4.461 GeV beam energy: (a) missing energy $E_m$, (b) missing energy vs. missing momentum $p_m$, (c) polar angle $\theta_{pq}$ versus missing energy $E_m$, (d) polar angle $\theta_{pq}$ versus missing momentum $p_m$, (e) invariant mass $W$ for the $(e,e'p)$ reaction and (f) $Q^2$ versus $\omega$ distribution.

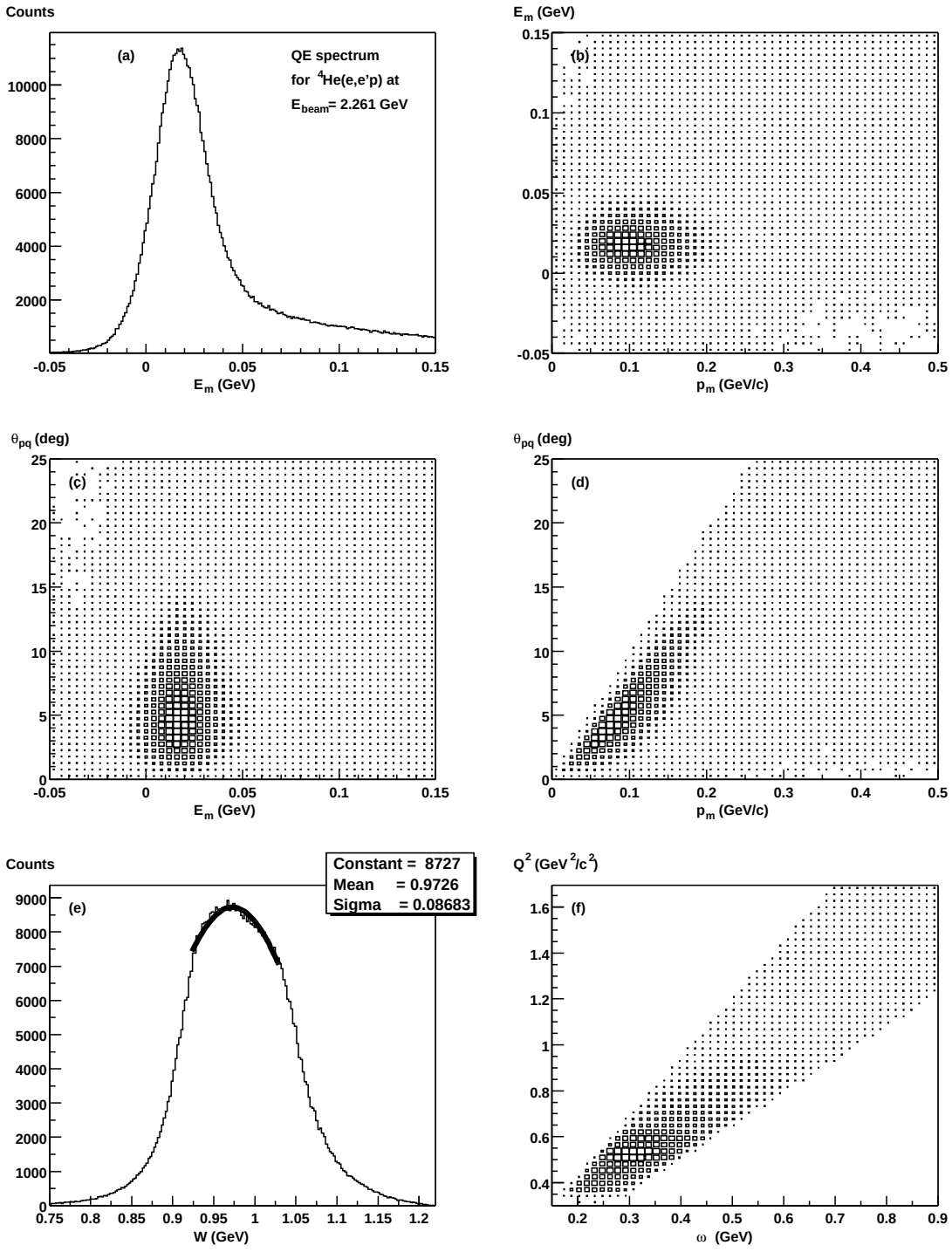


Figure 4-25: Quasielastic spectra for $^4$He$(e,e'p)$ at 2.261 GeV, obtained with eq.(4.18): (a) missing energy $E_m$, (b) missing energy vs. missing momentum $p_m$, (c) polar angle $\theta_{pq}$ versus missing energy $E_m$, (d) polar angle $\theta_{pq}$ versus missing momentum $p_m$, (e) invariant mass $W$ for the $(e,e'p)$ reaction and (f) $Q^2$ versus $\omega$ cut. The $E_m$ cut (4.19) in not shown. Compare to figure 4-21.

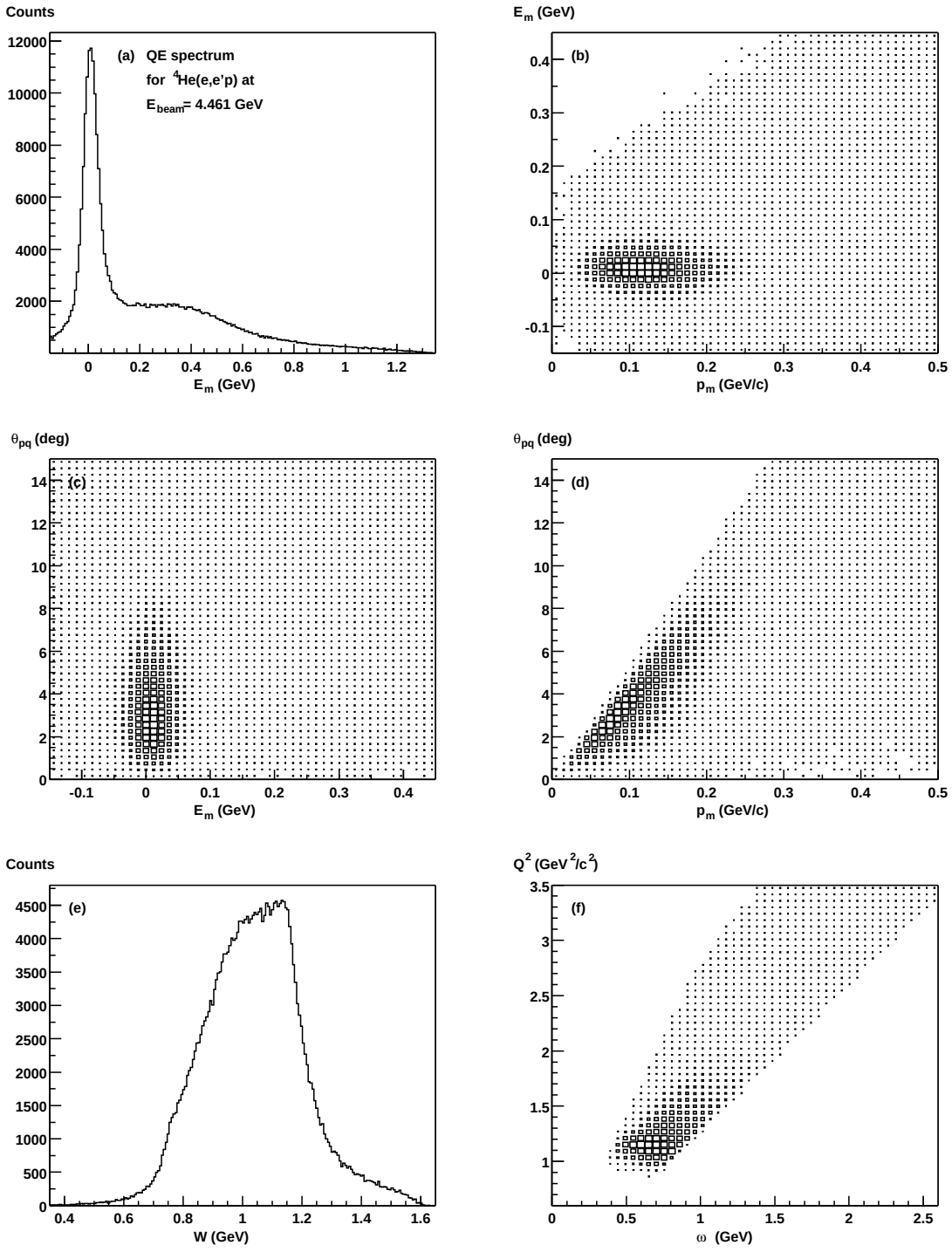


Figure 4-26: Quasielastic spectra for $^4$He$(e,e'p)$ at 4.461 GeV, obtained with eq.(4.18): (a) missing energy $E_m$, (b) missing energy vs. missing momentum $p_m$, (c) polar angle $\theta_{pq}$ versus missing energy $E_m$, (d) polar angle $\theta_{pq}$ versus missing momentum $p_m$, (e) invariant mass $W$ for the $(e,e'p)$ reaction and (f) $Q^2$ versus $\omega$ cut. The $E_m$ cut (4.19) in not shown. Compare to figure 4-22.

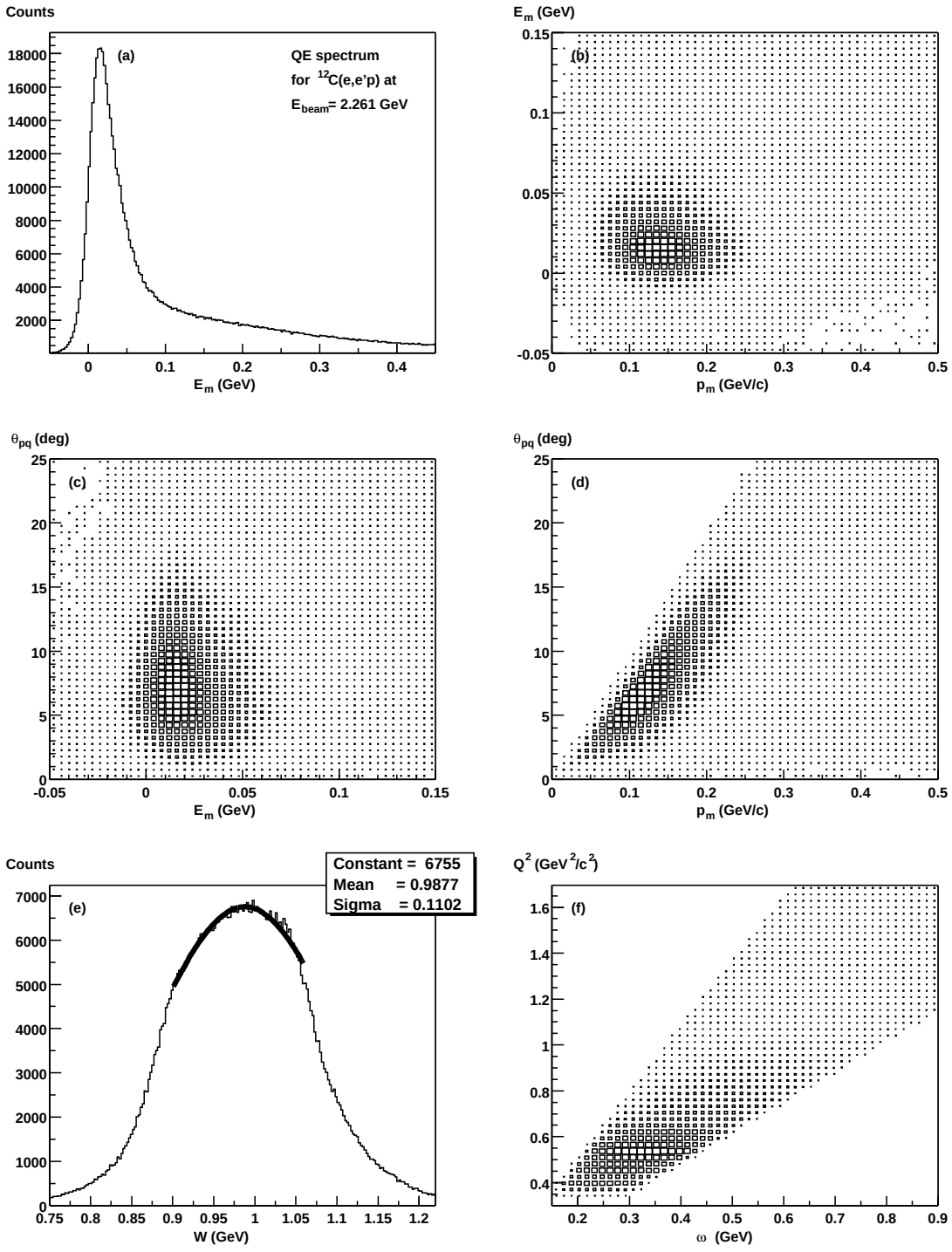


Figure 4-27: Quasielastic spectra for $^{12}C(e,e'p)$ at 2.261 GeV, obtained with eq.(4.18): (a) missing energy $E_m$, (b) missing energy vs. missing momentum $p_m$, (c) polar angle $\theta_{pq}$ versus missing energy $E_m$, (d) polar angle $\theta_{pq}$ versus missing momentum $p_m$, (e) invariant mass $W$ for the $(e,e'p)$ reaction and (f) $Q^2$ versus $\omega$ cut. The $E_m$ cut (4.19) in not shown. Compare to figure 4-23.

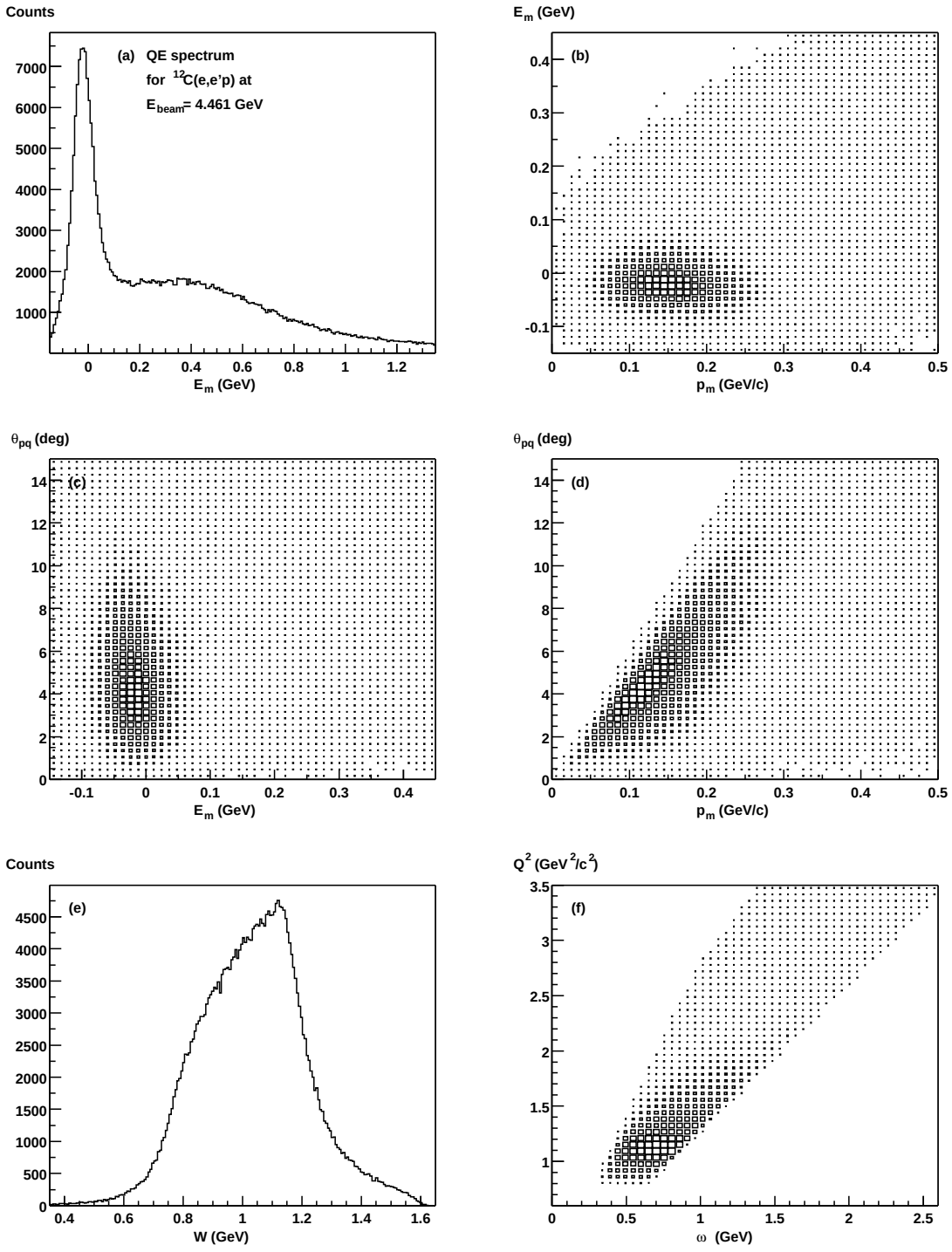


Figure 4-28: Quasielastic spectra for $^{12}C(e,e'p)$ at 4.461 GeV, obtained with eq.(4.18): (a) missing energy $E_m$, (b) missing energy vs. missing momentum $p_m$, (c) polar angle $\theta_{pq}$ versus missing energy $E_m$, (d) polar angle $\theta_{pq}$ versus missing momentum $p_m$, (e) invariant mass $W$ for the $(e,e'p)$ reaction and (f) $Q^2$ versus $\omega$ cut. The $E_m$ cut (4.19) in not shown. Compare to figure 4-24.

## 4.11 Statistical and Systematic Uncertainties

In the asymmetry measurement most of the systematic uncertainties related to the experimental setup are divided out. The only contributions are from the statistical errors on the number of counts and the uncertainty in the measurement of beam polarization.

To measure the helicity beam asymmetry defined in equation (4.17), we calculate for each $\Delta\omega\Delta Q^2\Delta\theta_{pq}\Delta\phi_{pq}$ bin the ratio

$$A_m = \frac{N^+ - A_Q N^-}{N^+ + A_Q N^-} \tag{4.20}$$

where $N^+$ and $N^-$ are, respectively, the number of $(e, e'p)$ events with positive and negative helicity within the chosen kinematic bin and $A_Q$ is the beam charge asymmetry (BCA) correction defined in section 4.9. Taking into account that our measured asymmetries are typically below 0.05, one can confidently approximate $N^+ \approx N^- \approx N/2$ and then the total statistical error can be expressed as:

$$(\delta A_m)^2 = \frac{(1 - A_m^2)}{N} \frac{A_Q}{(1 + A_Q)^2} \left[ 4 + N \left( \frac{\delta A_Q}{A_Q} \right)^2 \right] \tag{4.21}$$

As described in section 4.9, the beam charge asymmetry $A_Q$ is calculated using inclusive $(e, e')$ yields, typically with 3–4 orders of magnitude higher statistics than $N$. The error on $A_Q$ is in general much less than one percent while $A_Q$ is a number very close to 1. Then its contribution can be neglected and one remains with

$$\delta A_m = \sqrt{(1 - A_m^2)/N} \tag{4.22}$$

which is dominated by the $1/N$ dependence.

The formulas above were obtained assuming that the yields $N^+$ and $N^-$ obey a Poisson distribution. This is true in practice although it was argued that the two yields should be described by a binomial distribution [85]. We count the $h = +1$ and $h = -1$ events separately, with no constraints imposed on the sum $N = N^+ + N^-$. However, the two methods to calculate the statistical errors converge towards the same result when the asymmetry is very small:

$$\lim_{A_m \to 0} \frac{\delta A_m^{Binom}}{\delta A_m^{Poiss}} \sim \lim_{A_m \to 0} \sqrt{\frac{1 - A_m^2}{1 + A_m^2}} = 1 \tag{4.23}$$

Since the measured asymmetries are always below 0.05, the ratio in eq. (4.23) is somewhere between 0.9975 and 1.

To account for the partial polarization of the incident beam, the measured asymmetry $A_m$ is scaled by the beam polarization $P_B$ to obtain the true asymmetry $A'_{LT}$:

$$A'_{LT} = \frac{A_m}{P_B} \tag{4.24}$$

The total error in the measurement of $A'_{LT}$ is composed of the statistical error on $A_m$ and the uncertainty introduced by the polarization measurement:

$$\delta A'_{LT} = |A'_{LT}| \left[ \left( \frac{\delta A_m}{A_m} \right)^2 + \left( \frac{\delta P_B}{P_B} \right)^2 \right]^{1/2} \tag{4.25}$$

The beam polarization was measured to be 0.63 with a relative error of approximately 5% (appendix C). The statistical error on $A_m$ is never better than 20%.

Equation (4.25) refers to the error on $A'_{LT}$ for a chosen $\Delta\phi_{pq}$ bin. However, it is not these quantities that are reported, but the result obtained by fitting the $A'_{LT}$ versus $\phi_{pq}$ dependence.

Following equation (2.16), one would have to fit the $A_{LT'}$ versus $\phi_{pq}$ dependence with a three-parameter function:

$$A'_{LT}(\phi_{pq}) = a_{LT'} \sin\phi_{pq}/(1 + a_{LT}\cos\phi_{pq} + a_{TT}\cos 2\phi_{pq}) \quad (4.26)$$

$$a_\kappa = v_\kappa f_\kappa/(v_L f_L + v_T f_T) \qquad \kappa = TT, LT, LT' \quad (4.27)$$

where $a_{LT'}$,$a_{LT}$ and $a_{TT}$ are then relative strengths with respect to the direct part: $v_L f_L + v_T f_T$.

When the asymmetry signal is weak, the effect of the cosine terms in the denominator of (4.26) is unnoticeable. There are cases, though, where the deformation of the sinusoid is visible with the naked eye, as illustrated in Fig.4-29. This figure shows a comparison between fits made with the three parameter function from (4.26) and a one-parameter function

$$A'_{LT}(\phi_{pq}) = A\sin\phi_{pq} \quad (4.28)$$

The fitting algorithm used is MINUIT embedded in the `Root` package [102].

In graph (a) from figure 4-29, the fit result for $A_{LT'}$ is $-0.023 \pm 0.005$. For (b), the value of $A_{LT'}$ can be calculated from the fit parameters as $A_{LT'}(\phi_{pq} = 90^o) = a_{LT'}/(1 - a_{TT})$. The value obtained is $-0.023 \pm 0.025$, *i.e.* within 1–2 % difference but with a much larger error bar. Graphs (c) and (d) show another case. The (c) fit gives $A'_{LT} = -0.017 \pm 0.0035$ and from (d) one obtains $A'_{LT} = -0.015 \pm 0.0059$. The two values are within 12 % difference but with error bars of 20% and 40%, respectively. The parameters that are in the denominator of (4.26) prove rather difficult to fit: $a_{TT}$ was obtained with a 47% uncertainty while $\delta a_{LT} \approx 200\%$.

Based on these and other cases studied, we concluded that the contribution of the

$a_{LT}$ and $a_{TT}$ terms to the asymmetry amplitude fit can be neglected and the simpler parameterization from eq.(4.28) can be used. The statistical error is minimized while the systematic error introduced by this approximation is negligible.

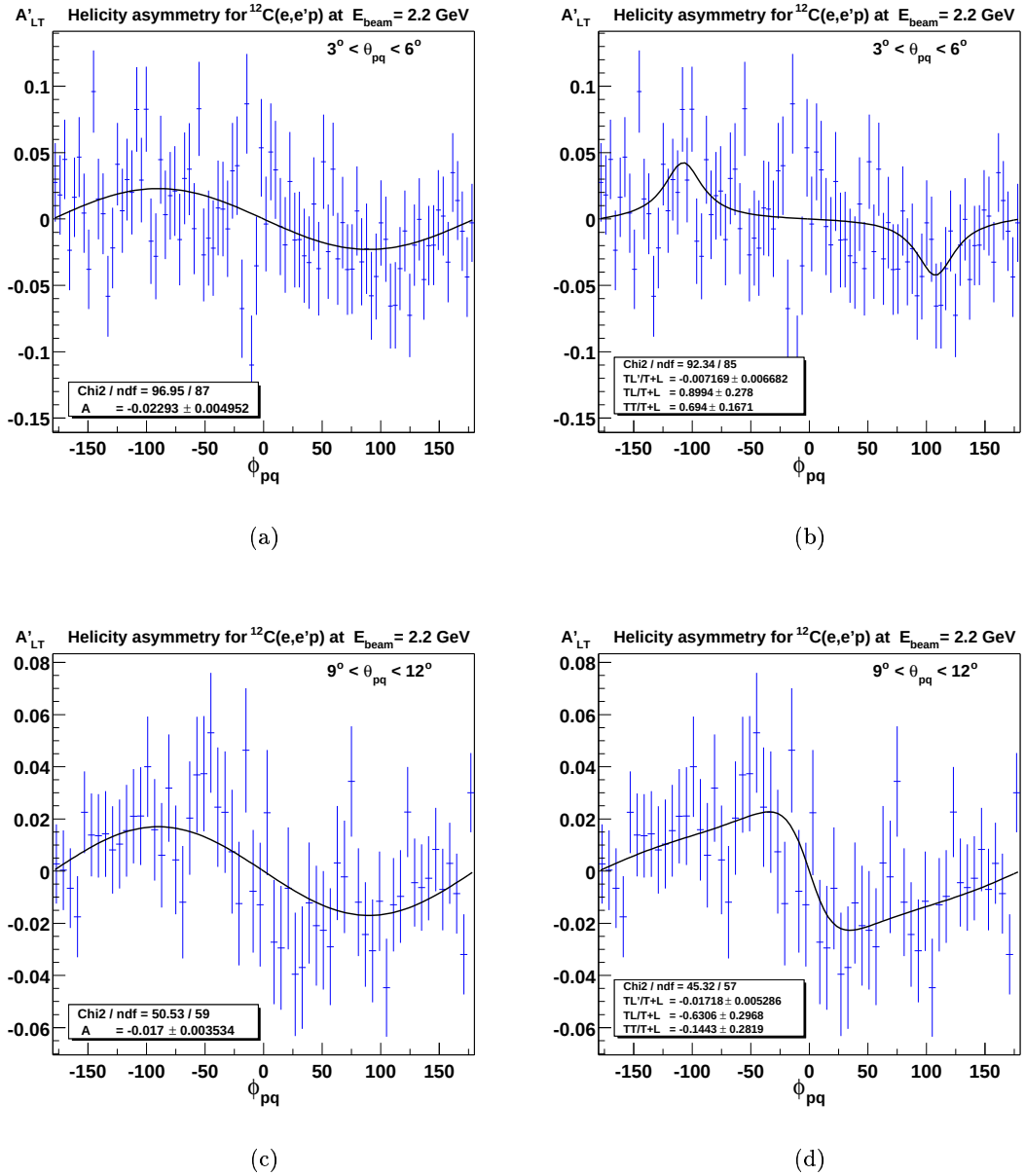


Figure 4-29: Polar angle dependence of the $A'_{LT}$: comparison between fits done with a sinusoid (a,c) and with the function from equation (4.26) (b,d).

# CHAPTER 5

# Results and Discussion

In this chapter we present the results of our measurements. We compare the quasielastic data with theoretical calculations based on the models introduced in chapter 2. We then dedicate a section to the study of $A'_{LT}$ variation across a wide missing energy range. The chapter closes with conclusions and an outlook.

The measured asymmetries are compared with three theoretical models. The traditional comparison with DWIA employs calculations provided by J. Kelly [88, 53]. The other two sets of calculations - OMEA and RMSGA - are based on codes provided by the Gent group [24, 44, 51]. All three models were reviewed in chapter 2. For the OMEA and RMSGA, bound-state wavefunctions (bswf) are calculated within the context of a mean-field approximation to the $\sigma - \omega$ model [90, 91]. With the DWIA, the NLSH bound-state wavefunction [92] was used. Both DWIA and OMEA carbon calculations are based on the EDAIC optical potential of Cooper *et al.* [48]. In all calculations, the $\Gamma_{cc2}$ hadronic current operator (2.21) and the Coulomb gauge (2.22) were used. Except in the DWIA, the electron distortion has been neglected, since its effect for nuclei as light as the $^4$He and $^{12}$C is very small.

## 5.1 Results

Measurements in the quasielastic region are summarized in tables 5.3 to 5.6 and the corresponding plots are presented in figures 5-4 to 5-12. At 2.2 GeV beam energy, the four-momentum range investigated spans from 0.35 to 1.80 GeV$^2$/c$^2$ and at 4.4 GeV from 0.80 to 2.40 GeV$^2$/c$^2$. Each of these intervals is divided in four $Q^2$ bins, according to table 5.1.

The $^{12}$C quasielastic data is accompanied by OMEA calculations at all kinematics and by RMSGA calculations at high $Q^2$, where the latter model is applicable. The $^4$He data is compared with RMSGA and DWIA. The theory curves are obtained by interpolating points calculated by formula (5.9). The interpolation function used is a cubic splines. The error bars shown on the data points are purely statistical, as they are on all the graphs presented henceforth. The systematic error to be added in quadrature is of a few percent (see section 4.11).

Tables 5.3 to 5.6 can be used to study the variation of $A'_{LT}$ with missing momentum. Figures 5-8 to 5-12 show these dependencies.

The missing energy dependence of $A'_{LT}$ is explored up to 1 GeV. The data are tabulated in tables 5.7 and 5.8 and presented in figures 5-13 and 5-14.

The measured asymmetries are of the order of a few percent but the experimental points fall close to the predictions of theory; higher statistics and a larger acceptance range would be required to really constrain the models.

### 5.1.1 Polar angle dependence

To make a connection with the previous experiments [25, 26], the first variation studied is that of $A'_{LT}$ with the polar angle. As a reminder, the polar angle $\theta_{pq}$ was defined as the angle between the direction of $\boldsymbol{q}$ and the momentum $\boldsymbol{p}$ of the ejected proton, measured in

the laboratory frame (see figure 2-2). Increasing polar angle is accompanied by increasing missing momentum.

Figure 5-4 presents the $^4$He data at 2.2 GeV beam energy. The $Q^2$ interval was split in four bins, each 0.360 GeV$^2$/c$^2$ wide. The figure contains four plots, according to this division. DWIA calculations[1] accompany the data for in all four $Q^2$ bins. The RMSGA curves are drawn only for the $q > 1$ GeV/c regions, since the RMSGA parameters (appendix D.1) can not be safely extrapolated at lower momentum transfers.

The data are characterized by small statistical errors at small angles, where the asymmetries should vanish with the phase-space anyway. The errors increase with the angle, since the statistics are poorer at higher $\theta_{pq}$.

The asymmetry is positive at lower angles, has a maximum and then decreases towards negative values at high $\theta_{pq}$. The maximum is located at $24^o$ on plot (a) and migrates towards lower angles with increasing $Q^2$.

Qualitatively, both models reproduce the features of the data. Quantitatively, the DWIA overestimates while RMSGA underestimates the features. We must mention that a comparison of the models with the data at high $\theta_{pq}$ must be viewed in the light of the discussion from subsection 2.7.1 where we have seen that at high $\theta_{pq}$, corresponding here to large missing momentum, multi-nucleon contributions become dominant.

The 4.4 GeV helium data are presented in figure 5-5 and listed in table 5.4. The statistics are lower for this data set, compared with the 2.2 GeV set. Though less visible, the same evolution of $A'_{LT}$ is present here: located at about $15^o$ in plot (a), the maximum travels to lower angles with increasing $Q^2$. The large statistical uncertainties do not allow for a good comparison between the two models in this case.

[1] the DWIA calculation is presented with a sign opposite to that of its author

The set presented in figure 5-6 is the $^{12}$C at 2.2 GeV, which can be said is our best data set. Higher statistics enable a more accurate comparison between measurement and theory. The data exhibits negative asymmetries at low $\theta_{pq}$ and then intersects zero several times. The main feature is the strong positive maximum, similar with what we have seen on the $^4$He data.

Since the CLAS missing energy resolution is around 100 MeV, we are unable to separate the $s$- and $p$-shells in the $^{12}$C data, as one could deduce from comparing spectra from sections 2.7.1 and 4.10. This separation would require a resolution of better than 10 MeV. In these conditions, the calculations correspond to a mixture of $s$ and $p$ contributions, in the assumption of fully occupied shells. The interplay between the two shells is important, since they contribute with opposite signs, as illustrated in figure 5-3. However, the data and theory both show that the $p$-shell contribution is larger.

The OMEA shows very good agreement with the data. With regard to the position of the maximum, the agreement improves with $Q^2$. With regard to its value, the match is even better. The RMSGA shows a maximum of about the same magnitude with the data and the OMEA but it overshoots its position on the lower $Q^2$ plots. On (d), it would be hard to give a verdict.

The asymmetries for the 4.4 GeV $^{12}$C data set are plotted in figure 5-7 and listed in table 5.6. A comparison between the two models is made difficult by the large statistical uncertainties.

### 5.1.2 Missing momentum dependence

Data from tables 5.3 to 5.6 can also be used to illustrate the missing momentum dependence of $A'_{LT}$. Figures 5-8 to 5-12 show the corresponding plots. The procedure employed to draw

the theoretical curves remains the one described in section 5.2.

The $p_m$ dependence of $A'_{LT}$ is easier to interpret. The interference maximum discussed in the previous section is stationary in $p_m$ coordinates, located at about 0.300 GeV/c.

Some comments about the range of validity of our models would be appropriate here. The DWIA and OMEA are based on optical potentials. These optical potentials are obtained from fits to data up to energies of 1.05 GeV. Above this energy range, we use a completely untested extrapolation of a phenomenological optical potential well beyond its region of applicability. Besides, at large missing momenta above 0.300 GeV/c it is very likely that more complicated reaction mechanisms (channel coupling, two-nucleon knockout, etc.) come into play. Therefore, a comparison of the theory with the data above 0.3 GeV/c missing momentum must be viewed in this context. This observation applies to the $\theta_{pq}$ dependencies shown in the previous section and it explains why conclusions for the region above $15^o$ were avoided.

The features discussed in section 5.1.1 are more visible in missing momentum. Although the maximum is at the limit of applicability of the model, it is interesting how the DWIA predicts the steep inversion on plot (b) from figure 5-8.

Regarding the $^{12}$C 2.2 GeV data, a trend that can be clearly seen on the plots in figure 5-11 is that the agreement between RMSGA and OMEA improves with $Q^2$. This is not unexpected, since the domain of validity for RMSGA is for four-momentum transfers of 1 GeV$^2$/c$^2$ and above. OMEA is designed to bridge the low and high $Q^2$ regimes.

Comparing the carbon and helium data sets, two important observations can be made. Both sets feature the strong interference maximum of approximately +5% at 0.3 GeV/c in missing momentum. The difference is that, while $^4$He steadily rises from zero values at $p_m = 0$ GeV/c, the $^{12}$C descends towards negative asymmetry values at low missing

momentum and crosses zero before reaching the maximum. The theory explains this effect as due to the $^{12}$C $p$-shell contribution. As it was illustrated in figure 5-3, the contributions of the $s$ and $p$ shells are of opposite sign.

The 4.4 GeV sets for both targets are compromised by large statistical errors.

### 5.1.3 Missing energy dependence

The missing energy dependence of $A'_{LT}$ was studied for an $E_m$ range spanning up to 1 GeV. The plots are shown in figures 5-13 and 5-14 and listed in tables 5.7 and 5.8. Theoretical calculations were not performed here, therefore the following plots contain experimental data only.

The missing momentum range was split in two bins: bin 1 is from 0.0 to 0.200 GeV/c and bin 2 from 0.200 to 0.450 GeV/c. The whole $E_m$ range was split in 10 equal bins 0.100 GeV wide, numbered from 0 to 9.

Figure 5-13 shows $A'_{LT}$ versus $E_m$ for $^4$He . The very first point on all the plots corresponds to the valence knockout kinematics, investigated in the previous two sections. In agreement with what we observed, this lowest $E_m$ data point shows positive asymmetries for $^4$He and a negative asymmetry in the case of $^{12}$C (figure 5-14).

One common feature of the two data sets, $^4$He and $^{12}$C, is the positive maximum situated around 0.250 GeV in $E_m$, probably corresponding to the $\Delta$ (1232) resonance (see spectra from figures 4-21 and 4-22).

The presence of the carbon $p$-shell can be again seen on figure 5-14.a. While the helium data (Fig. 5-13.a) shows a positive asymmetry for the first missing energy bin, the carbon exhibits a negative asymmetry at low missing energy. From the previous subsection, we know that the negative asymmetries in the first $E_m$ bin in the $^{12}$C are to be atributed to

| $Q^2$ bin | $E_B$ = 2.261 GeV | | $E_B$ = 4.461 GeV | |
|---|---|---|---|---|
| | $Q^2_{min}$ | $Q^2_{max}$ | $Q^2_{min}$ | $Q^2_{max}$ |
| 1 | 0.350 | 0.712 | 0.800 | 1.200 |
| 2 | 0.712 | 1.075 | 1.200 | 1.600 |
| 3 | 1.075 | 1.438 | 1.600 | 2.000 |
| 4 | 1.438 | 1.800 | 2.000 | 2.400 |

Table 5.1: Table explaining the $Q^2$ binning of the data used in tables 5.3 to 5.6 ($Q^2$ is in GeV$^2$/c$^2$). Please refer to figures 4-21 to 4-24.

the $p$-shell contribution.

## 5.2 Comparison with the Theory

Given the large acceptance of our spectrometer, the detector acceptances do not cancel out in the asymmetry ratio in a trivial manner. This section explains how the theoretical asymmetries are constructed in order to enable a realistic comparison between theory and measurement.

The overall data binning scheme chosen for this report is presented in table 5.1. The quasielastic event selection described by equation (4.18) selects a finite region around the $\omega = Q^2/2m_p$ ridge (see figures 4-25 to 4-28). Within this region, bin widths of $\Delta\theta_{pq} = 3^o$ and $\Delta Q^2 \simeq 0.362 - 0.400$ Gev$^2$/c$^2$ were used. These values were chosen as a compromise between being large enough for statistical precision and small enough to reveal changes in the physics.

For each of the four $\Delta\omega\Delta Q^2\Delta\theta_{pq}$ bins described in table 5.1, we can define the asymmetry (4.20), which can be expressed in terms of cross-section as:

$$A_m(\omega_0, Q_0, \theta_{pq,0}) = \frac{\int_{\Delta\omega\Delta Q^2\Delta\theta_{pq}} \mathcal{L}\,\sigma^h_m(\omega, Q, \theta_{pq})\epsilon(\omega, Q, \theta_{pq})d\omega dQ^2 d\theta_{pq}}{\int_{\Delta\omega\Delta Q^2\Delta\theta_{pq}} \mathcal{L}\,\sigma^0_m(\omega, Q, \theta_{pq})\epsilon(\omega, Q, \theta_{pq})d\omega dQ^2 d\theta_{pq}} \qquad (5.1)$$

where $\mathcal{L}$ is the luminosity, $\epsilon$ is the detector efficiency and the integral is carried over the chosen $\Delta\omega\Delta Q^2\Delta\theta_{pq}$ bin. By $\sigma^h$ and $\sigma^0$ we denoted the polarized and unpolarized parts of the total differential cross-section, respectively. The subscript "$m$" suggests that these are measured values. The measured cross-section is differential in $\omega, Q^2$ and $\theta_{pq}$. The $\phi_{pq}$ dependence was lost when the asymmetry at $\phi_{pq} = 90^o$ is extracted by means of the fit described in section 4.11.

The polarized and unpolarized parts of the total differential cross-section are given by:

$$\sigma^h = \sigma^+ - \sigma^- \qquad \sigma^0 = \sigma^+ + \sigma^- \tag{5.2}$$

according to equation (2.13). In chapter 2 we denoted these quantities by $\Delta$ and $\Sigma$ but we use this new notation here in order to avoid confusion with the summation sign.

The value $A_m$ is assigned to the kinematic coordinates $\omega_0, Q_0, \theta_{pq,0}$ defined as the averages:

$$x_0^\alpha = \frac{\int_{\Delta\omega\Delta Q^2\Delta\theta_{pq}} x^\alpha \sigma_m^0(\omega,Q,\theta_{pq})\epsilon(\omega,Q,\theta_{pq})d\omega dQ^2 d\theta_{pq}}{\int_{\Delta\omega\Delta Q^2\Delta\theta_{pq}} \sigma_m^0(\omega,Q,\theta_{pq})\epsilon(\omega,Q,\theta_{pq})d\omega dQ^2 d\theta_{pq}} = \langle x^\alpha\rangle_{\Delta\omega\Delta Q^2\Delta\theta_{pq}} \tag{5.3}$$

where $x^\alpha$ is each of the $\omega, Q, \theta_{pq}$ variables.

We must note that, based on definition (4.20), a different quantity could be constructed:

$$\bar{A}(\omega_0,Q_0,\theta_{pq,0}) = \frac{1}{K}\sum_{k=1}^{K}\frac{N_k^+ - A_Q N_k^-}{N_k^+ + A_Q N_k^-} \overset{K\to\infty}{\longrightarrow} \int A'_{LT}(\omega,Q,\theta_{pq})\frac{d\omega dQ^2 d\theta_{pq}}{\Delta\omega\Delta Q^2\Delta\theta_{pq}} \tag{5.4}$$

where $N_k$ is the number of counts in the sub-bin $k$ and $\sum_{k=1}^{K} N_k = N$. In this case the detector efficiencies cancel out completely but the statistical error increases with $K$. The integration methods (5.1) and (5.4) would be perfectly equivalent in the case when the sum

(5.4) has only one term ($K = 1$), i.e. the integration range is so small that:

$$\int_{x_0-\Delta x/2}^{x_0+\Delta x/2} A(x)\,\epsilon(x)\,dx \equiv A(x_o)\epsilon(x_0)\Delta x \tag{5.5}$$

where $x$ is the set of variables $\omega, Q, \theta_{pq}$ and $dx = d\omega dQ^2 d\theta_{pq}$ is an infinitesimal volume in the phase-space. This would be practically the case in a fixed-geometry experiment that would use a small acceptance detector, as in the previous OOPS experiments [25, 26].

However, formula (5.1) has several advantages in that it emerges naturally from the analysis method and it minimizes the statistical error. Therefore, in this thesis, the reported asymmetries are constructed according to equation (5.1).

An ideal comparison with the theory would require performing the integrals in (5.1) with the cross-sections $\sigma_m^h$ and $\sigma_m^0$ replaced by the theoretical ones: $\sigma_t^h$ and $\sigma_t^0$, respectively. For practical purposes, given that theoretical calculations are time consuming, it is convenient to reduce the calculations to the smallest set possible.

If the integrals in (5.1) could be split in $K$ pieces, each small enough to be approximated by its average value of asymmetry, this would be written as

$$A_m(\omega_0, Q_0, \theta_{pq,0}) = \frac{\sum_{k=1}^{K} \int_{[\Delta\omega\Delta Q^2\Delta\theta_{pq}]_k} \sigma_m^h(\omega, Q, \theta_{pq})\epsilon_k(\omega, Q, \theta_{pq})d\omega dQ^2 d\theta_{pq}}{\sum_{k=1}^{K} \int_{[\Delta\omega\Delta Q^2\Delta\theta_{pq}]_k} \sigma_m^0(\omega, Q, \theta_{pq})\epsilon_k(\omega, Q, \theta_{pq})d\omega dQ^2 d\theta_{pq}} \tag{5.6}$$

where $[\Delta\omega\Delta Q^2\Delta\theta_{pq}]_k$ denotes the $k$-th subinterval such that their sum gives the original integration range from (5.1)

$$\sum_{k=1}^{K} [\Delta\omega\Delta Q^2\Delta\theta_{pq}]_k = \Delta\omega\Delta Q^2\Delta\theta_{pq}$$

We approximate each integral in the sums with

$$\int_{(\Delta\omega\Delta Q^2\Delta\theta_{pq})k} \sigma_m^\alpha(\omega,Q,\theta_{pq})\epsilon_k(\omega,Q,\theta_{pq})d\omega dQ^2 d\theta_{pq} \simeq \tag{5.7}$$
$$\simeq \sigma_{mk}^\alpha(\omega_k,Q_k,\theta_{pq,k})\epsilon_k(\omega_k,Q_k,\theta_{pq,k})[\Delta\omega\Delta Q^2\Delta\theta_{pq}]_k$$

where $\alpha$ stands for 0 or $h$ and the $\omega_k, Q_k, \theta_{pq,k}$ are the average kinematic coordinates of the subinterval calculated as in (5.3). Combining (5.6) and (5.7) and factorizing each term of the sum into an asymmetry and a weighting factor:

$$\begin{aligned} A_m(\omega_0,Q_0,\theta_{pq,0}) &= \sum_{k=1}^{K}\left[\left(\frac{\sigma_{mk}^h}{\sigma_{mk}^0}\right)\left(\frac{\sigma_{mk}^0\epsilon_k\left[\Delta\omega\Delta Q^2\Delta\theta_{pq}\right]_k}{\sum\limits_{k=1}^{K}\sigma_{mk}^0\epsilon_k\left[\Delta\omega\Delta Q^2\Delta\theta_{pq}\right]_k}\right)\right] = \\ &= \sum_{k=1}^{K} A_{mk}w_k \end{aligned} \tag{5.8}$$

where the first term in the square bracket is equated to $A_{mk}$ and the second to the weighting factor $w_k$.

Previous comparisons of the models employed in our calculations show that they successfully reproduce unpolarized cross-sections for $^4$He , $^{12}$C and $^{16}$O data [45]. The measured asymmetry (5.1), corrected for beam polarization as in (4.24), can be compared with a quantity constructed by replacing the $A_{mk}$ with their calculated counterparts:

$$A_t(\omega_0,Q_0,\theta_{pq,0}) = \sum_{k=1}^{K} A_{tk}(\omega_k,Q_k,\theta_{pq,k})\, w_k \tag{5.9}$$

while keeping the experimental weighting factors $w_k$. This way, the detector acceptances are incorporated into the $w_k$. The weights are straightforward to calculate as ratios of experimental yields $w_k = N_k/N$ where $N = \sum_k N_k$.

| K | Grid Size | i | j | $Q^2_{min}$ (GeV$^2$/c$^2$) | $Q^2_{max}$ (GeV$^2$/c$^2$) | $a_1$ | $a_2$ | $w_k(0)$ |
|---|---|---|---|---|---|---|---|---|
| 1 | 1×1 | 0 | 0 | 0.712 | 1.075 | 0.172 | 0.200 | 1.000 |
| 4 | 2×2 | 0 | 0 | 0.712 | 0.894 | 0.172 | 0.000 | 0.238 |
| | | 0 | 1 | 0.894 | 1.075 | 0.172 | 0.000 | 0.183 |
| | | 1 | 0 | 0.712 | 0.894 | 0.000 | 0.200 | 0.354 |
| | | 1 | 1 | 0.894 | 1.075 | 0.000 | 0.200 | 0.225 |
| 9 | 3×3 | 0 | 0 | 0.712 | 0.833 | 0.172 | 0.060 | 0.099 |
| | | 0 | 1 | 0.833 | 0.954 | 0.172 | 0.060 | 0.081 |
| | | 0 | 2 | 0.954 | 1.075 | 0.172 | 0.060 | 0.066 |
| | | 1 | 0 | 0.712 | 0.833 | 0.060 | 0.063 | 0.144 |
| | | 1 | 1 | 0.833 | 0.954 | 0.060 | 0.063 | 0.129 |
| | | 1 | 2 | 0.954 | 1.075 | 0.060 | 0.063 | 0.100 |
| | | 2 | 0 | 0.712 | 0.833 | 0.063 | 0.200 | 0.167 |
| | | 2 | 1 | 0.833 | 0.954 | 0.063 | 0.200 | 0.132 |
| | | 2 | 2 | 0.954 | 1.075 | 0.063 | 0.200 | 0.085 |
| 16 | 4×4 | 0 | 0 | 0.712 | 0.803 | 0.172 | 0.089 | 0.053 |
| | | 0 | 1 | 0.803 | 0.894 | 0.172 | 0.089 | 0.046 |
| | | 0 | 2 | 0.894 | 0.984 | 0.172 | 0.089 | 0.037 |
| | | 0 | 3 | 0.984 | 1.075 | 0.172 | 0.089 | 0.031 |
| | | 1 | 0 | 0.712 | 0.803 | 0.089 | 0.000 | 0.072 |
| | | 1 | 1 | 0.803 | 0.894 | 0.089 | 0.000 | 0.067 |
| | | 1 | 2 | 0.894 | 0.984 | 0.089 | 0.000 | 0.063 |
| | | 1 | 3 | 0.984 | 1.075 | 0.089 | 0.000 | 0.053 |
| | | 2 | 0 | 0.712 | 0.803 | 0.000 | 0.096 | 0.093 |
| | | 2 | 1 | 0.803 | 0.894 | 0.000 | 0.096 | 0.086 |
| | | 2 | 2 | 0.894 | 0.984 | 0.000 | 0.096 | 0.069 |
| | | 2 | 3 | 0.984 | 1.075 | 0.000 | 0.096 | 0.054 |
| | | 3 | 0 | 0.712 | 0.803 | 0.096 | 0.200 | 0.094 |
| | | 3 | 1 | 0.803 | 0.894 | 0.096 | 0.200 | 0.081 |
| | | 3 | 2 | 0.894 | 0.984 | 0.096 | 0.200 | 0.058 |
| | | 3 | 3 | 0.984 | 1.075 | 0.096 | 0.200 | 0.044 |

Table 5.2: Division table for the convergence study. The $Q^2$ bin chosen is bin $\mathcal{N}^o 2$ from table 5.1. Coefficients $a_1$ and $a_2$ are the ones that enter in equation (4.18). The weighting factors $w_k$ listed on the last column are for bin $\mathcal{N}^o 0$ in $\theta_{pq}$ (corresponding to $0^o < \theta_{pq} < 3^o$). The convergence plots corresponding to this data sub-sample are shown in figure 5-1.

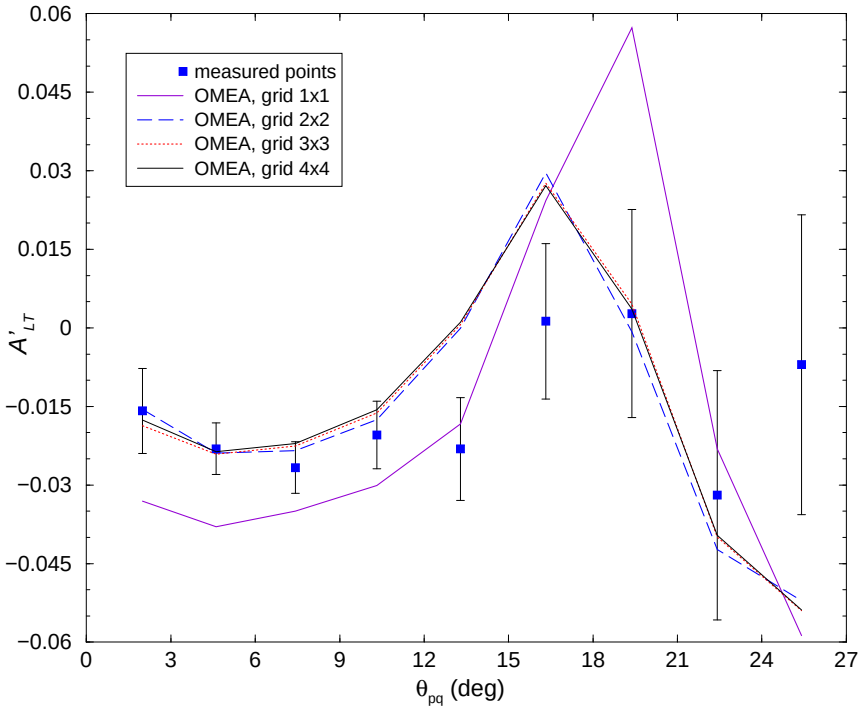


Figure 5-1: Convergence test on $^{12}$C at 2.261 GeV, $Q^2$ bin $\mathcal{N}^o2$. The theory calculation is done with OMEA, and the calculated points are linked by straight lines. Please refer to table 5.2.

To enable such a comparison, one had to find the smallest integer $K$ for which all the $k$ sub-bins in (5.6) are *sufficiently small* such that the approximation (5.7) holds. To do this, we carried out a convergence study based on the theory codes. Sample bins were chosen and the quantity (5.9) was calculated for several values of $K$. The dependency chosen for the study is that of $A'_{LT}$ versus polar angle. The convergence study was done on several data sub-samples. The procedure is illustrated in table 5.2 and figure 5-1 for the case of $^{12}$C at 2.261 GeV, kinematic bin $\mathcal{N}^o2$ (see table 5.1). The table shows the bin subdivision in $2\times2$, $3\times3$ and $4\times4$ grids. Figure 5-1 shows the corresponding calculations, accompanied by the data. There is a significant difference between the calculation at the weighted center of the bin and the first sampling sum ($K=4$, $2\times2$ grid). But the calculations corresponding to the sums with $K>1$ converge rapidly. Our conclusion was that a $2\times2$ grid is sufficient. Similar

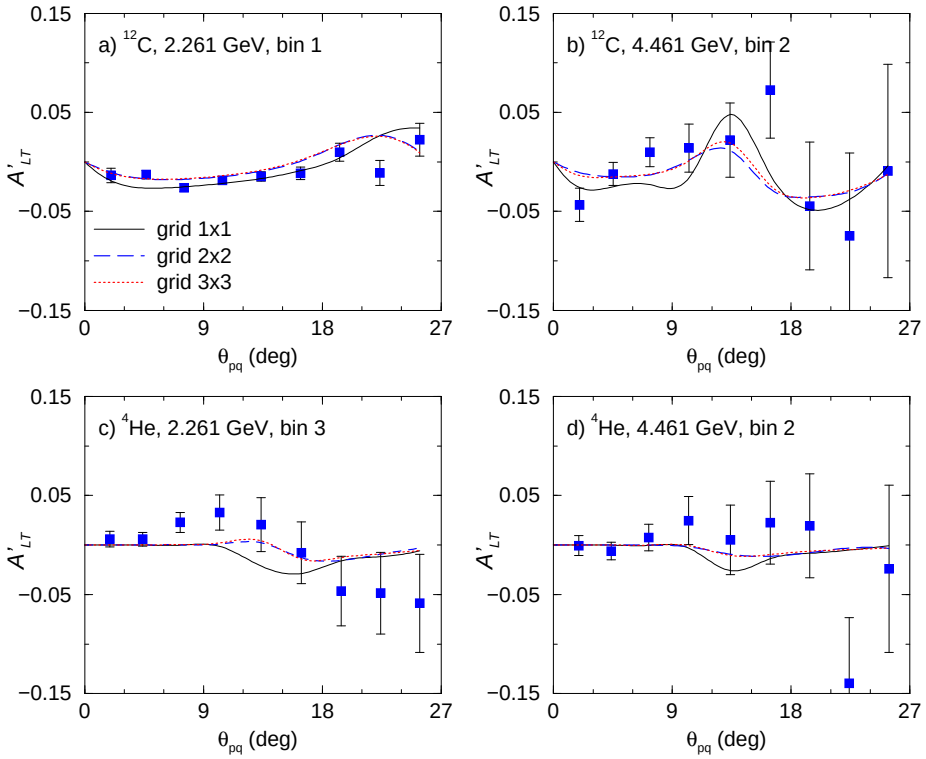


Figure 5-2: Convergence test: other cases. The theory calculation is done with OMEA (a,b) and with RMSGA (c,d)[3]. The calculated points are interpolated with Splines.

tests on other data sub-samples, shown in figure 5-2, are consistent with this conclusion.

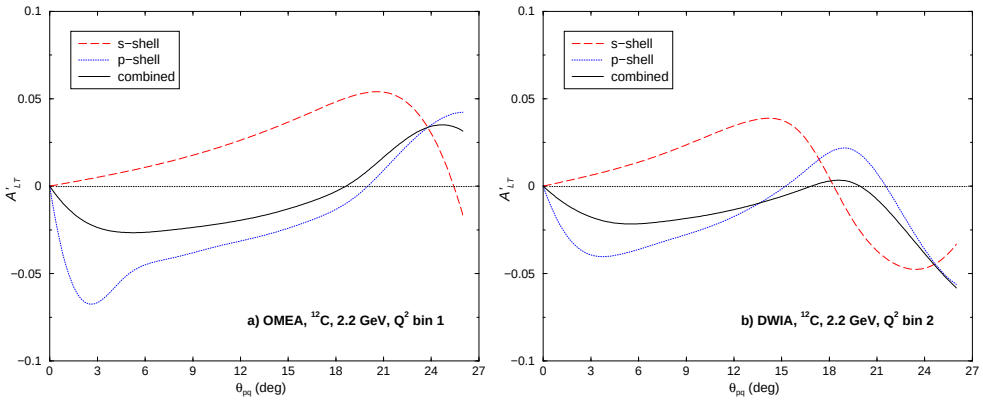


Figure 5-3: Illustration of the opposite sign contributions of the $s$- and $p$-shells in $^{12}$C . The calculations are done with (a) unweighted OMEA and (b) theory weighted DWIA. The calculated points are interpolated with cubic Splines.

| Bin ($n$) | $\theta_{pq}$ ($^o$) | q ($\frac{\text{GeV}}{\text{c}}$) | $\omega$ (GeV) | $Q^2$ $(\frac{\text{GeV}}{\text{c}})^2$ | $p_m$ ($\frac{\text{GeV}}{\text{c}}$) | $E_m$ (GeV) | $A'_{LT}$ DWIA | $A'_{LT}$ RMSGA | $A'_{LT}$ (meas) | $\delta A'_{LT}$ (stat) |
|---|---|---|---|---|---|---|---|---|---|---|
| 1 | 1.97 | 0.811 | 0.329 | 0.549 | 0.063 | 0.021 | 0.0014 | n/a | -0.0007 | 0.0043 |
| 2 | 4.55 | 0.807 | 0.326 | 0.545 | 0.088 | 0.022 | 0.0035 | n/a | 0.0052 | 0.0029 |
| 3 | 7.44 | 0.799 | 0.319 | 0.537 | 0.121 | 0.023 | 0.0069 | n/a | 0.0034 | 0.0030 |
| 4 | 10.38 | 0.789 | 0.311 | 0.526 | 0.157 | 0.025 | 0.0121 | n/a | 0.0091 | 0.0037 |
| 5 | 13.35 | 0.780 | 0.303 | 0.516 | 0.193 | 0.028 | 0.0204 | n/a | 0.0110 | 0.0049 |
| 6 | 16.34 | 0.773 | 0.297 | 0.509 | 0.230 | 0.032 | 0.0333 | n/a | 0.0109 | 0.0068 |
| 7 | 19.36 | 0.773 | 0.297 | 0.510 | 0.268 | 0.039 | 0.0533 | n/a | 0.0156 | 0.0093 |
| 8 | 22.40 | 0.781 | 0.303 | 0.518 | 0.309 | 0.045 | 0.0763 | n/a | 0.0085 | 0.0120 |
| 9 | 25.43 | 0.790 | 0.309 | 0.529 | 0.350 | 0.051 | 0.0746 | n/a | -0.0261 | 0.0143 |
| 1 | 1.94 | 1.062 | 0.507 | 0.870 | 0.072 | 0.020 | 0.0019 | n/a | 0.0052 | 0.0053 |
| 2 | 4.48 | 1.056 | 0.501 | 0.864 | 0.106 | 0.021 | 0.0052 | n/a | 0.0054 | 0.0040 |
| 3 | 7.34 | 1.045 | 0.488 | 0.853 | 0.152 | 0.023 | 0.0114 | n/a | 0.0034 | 0.0048 |
| 4 | 10.29 | 1.033 | 0.475 | 0.842 | 0.200 | 0.027 | 0.0232 | n/a | 0.0046 | 0.0072 |
| 5 | 13.29 | 1.030 | 0.471 | 0.839 | 0.252 | 0.033 | 0.0463 | n/a | 0.0213 | 0.0113 |
| 6 | 16.37 | 1.037 | 0.479 | 0.847 | 0.307 | 0.043 | 0.0855 | n/a | 0.0414 | 0.0157 |
| 7 | 19.44 | 1.044 | 0.484 | 0.855 | 0.361 | 0.049 | 0.0582 | n/a | -0.0298 | 0.0186 |
| 8 | 22.45 | 1.043 | 0.482 | 0.856 | 0.410 | 0.054 | -0.0895 | n/a | -0.0166 | 0.0203 |
| 9 | 25.44 | 1.037 | 0.472 | 0.853 | 0.456 | 0.056 | -0.1318 | n/a | -0.0116 | 0.0230 |
| 1 | 1.91 | 1.318 | 0.706 | 1.239 | 0.080 | 0.018 | 0.0022 | 0.0000 | 0.0060 | 0.0079 |
| 2 | 4.39 | 1.311 | 0.697 | 1.233 | 0.124 | 0.020 | 0.0063 | 0.0001 | 0.0058 | 0.0068 |
| 3 | 7.24 | 1.301 | 0.685 | 1.224 | 0.183 | 0.023 | 0.0157 | 0.0003 | 0.0229 | 0.0101 |
| 4 | 10.24 | 1.296 | 0.678 | 1.220 | 0.248 | 0.030 | 0.0383 | 0.0009 | 0.0329 | 0.0178 |
| 5 | 13.36 | 1.305 | 0.691 | 1.225 | 0.318 | 0.041 | 0.0686 | 0.0024 | 0.0205 | 0.0273 |
| 6 | 16.43 | 1.307 | 0.691 | 1.230 | 0.384 | 0.049 | -0.0961 | -0.0128 | -0.0079 | 0.0312 |
| 7 | 19.43 | 1.300 | 0.678 | 1.229 | 0.445 | 0.052 | -0.1467 | -0.0156 | -0.0465 | 0.0351 |
| 8 | 22.42 | 1.285 | 0.656 | 1.221 | 0.501 | 0.056 | -0.1324 | -0.0092 | -0.0486 | 0.0412 |
| 9 | 25.38 | 1.279 | 0.647 | 1.218 | 0.559 | 0.059 | -0.1049 | -0.0032 | -0.0588 | 0.0496 |
| 1 | 1.88 | 1.557 | 0.906 | 1.605 | 0.087 | 0.018 | 0.0023 | -0.0001 | 0.0003 | 0.0120 |
| 2 | 4.31 | 1.546 | 0.890 | 1.598 | 0.140 | 0.019 | 0.0072 | -0.0003 | 0.0236 | 0.0116 |
| 3 | 7.17 | 1.535 | 0.874 | 1.590 | 0.211 | 0.025 | 0.0214 | -0.0018 | -0.0058 | 0.0208 |
| 4 | 10.28 | 1.538 | 0.878 | 1.594 | 0.294 | 0.036 | 0.0541 | -0.0272 | -0.0031 | 0.0391 |
| 5 | 13.42 | 1.545 | 0.887 | 1.600 | 0.375 | 0.047 | -0.0949 | -0.0298 | -0.0361 | 0.0502 |
| 6 | 16.43 | 1.538 | 0.876 | 1.597 | 0.449 | 0.051 | -0.1064 | -0.0244 | -0.0690 | 0.0581 |
| 7 | 19.39 | 1.515 | 0.838 | 1.592 | 0.517 | 0.054 | -0.0832 | -0.0063 | -0.0115 | 0.0705 |
| 8 | 22.36 | 1.506 | 0.826 | 1.585 | 0.585 | 0.056 | -0.0549 | -0.0056 | -0.0667 | 0.0974 |
| 9 | 25.43 | 1.503 | 0.819 | 1.589 | 0.657 | 0.060 | -0.0054 | -0.0019 | 0.2554 | 0.1294 |

Table 5.3: Summary table for $^4$He at 2.262 GeV. The four sections correspond to the four $Q^2$ intervals (see table 5.1). Bins are determined by the conditions 4.18 and 4.19 on $\omega$, $Q^2$ and $E_m$ combined with the condition $3(n-1) < \theta_{pq} < 3n$ where $3^o$ is the $\theta_{pq}$ bin width and $n$ is an integer between 1 and 9. Values on columns 2-4 and 6-7 are weighted averages within the ($Q^2$, $\theta_{pq}$) bin. The calculations were done as described in section 5.2.

| Bin ($n$) | $\theta_{pq}$ ($^o$) | q ($\frac{\text{GeV}}{\text{c}}$) | $\omega$ (GeV) | $Q^2$ $\left(\frac{\text{GeV}}{\text{c}}\right)^2$ | $p_m$ ($\frac{\text{GeV}}{\text{c}}$) | $E_m$ (GeV) | $A'_{LT}$ DWIA | $A'_{LT}$ RMSGA | $A'_{LT}$ (meas) | $\delta A'_{LT}$ (stat) |
|---|---|---|---|---|---|---|---|---|---|---|
| 1 | 1.94 | 1.253 | 0.656 | 1.139 | 0.092 | -0.016 | 0.0010 | 0.0000 | 0.0141 | 0.0164 |
| 2 | 4.47 | 1.246 | 0.644 | 1.137 | 0.131 | -0.021 | 0.0029 | 0.0001 | 0.0088 | 0.0128 |
| 3 | 7.33 | 1.234 | 0.626 | 1.131 | 0.184 | -0.028 | 0.0072 | 0.0002 | 0.0176 | 0.0166 |
| 4 | 10.30 | 1.224 | 0.615 | 1.119 | 0.243 | -0.025 | 0.0171 | 0.0007 | -0.0203 | 0.0245 |
| 5 | 13.40 | 1.220 | 0.619 | 1.106 | 0.304 | -0.013 | 0.0387 | 0.0050 | 0.0423 | 0.0334 |
| 6 | 16.45 | 1.214 | 0.611 | 1.100 | 0.362 | -0.002 | 0.0315 | 0.0025 | 0.0433 | 0.0397 |
| 7 | 19.40 | 1.209 | 0.603 | 1.097 | 0.418 | 0.000 | -0.0595 | -0.0050 | -0.0093 | 0.0465 |
| 8 | 22.39 | 1.201 | 0.586 | 1.099 | 0.472 | 0.004 | -0.0726 | -0.0060 | 0.0601 | 0.0582 |
| 9 | 25.45 | 1.200 | 0.588 | 1.094 | 0.529 | 0.008 | -0.0631 | -0.0018 | 0.0449 | 0.0740 |
| 1 | 1.90 | 1.414 | 0.784 | 1.386 | 0.083 | 0.012 | 0.0011 | 0.0000 | -0.0006 | 0.0101 |
| 2 | 4.37 | 1.406 | 0.774 | 1.379 | 0.130 | 0.013 | 0.0037 | -0.0000 | -0.0061 | 0.0088 |
| 3 | 7.22 | 1.394 | 0.758 | 1.368 | 0.194 | 0.016 | 0.0094 | -0.0001 | 0.0076 | 0.0135 |
| 4 | 10.24 | 1.390 | 0.753 | 1.364 | 0.265 | 0.024 | 0.0225 | -0.0018 | 0.0246 | 0.0243 |
| 5 | 13.39 | 1.402 | 0.770 | 1.374 | 0.341 | 0.037 | 0.0240 | -0.0092 | 0.0052 | 0.0351 |
| 6 | 16.41 | 1.397 | 0.760 | 1.374 | 0.408 | 0.043 | -0.0702 | -0.0113 | 0.0224 | 0.0418 |
| 7 | 19.39 | 1.383 | 0.739 | 1.366 | 0.471 | 0.047 | -0.0704 | -0.0077 | 0.0194 | 0.0524 |
| 8 | 22.41 | 1.369 | 0.717 | 1.360 | 0.533 | 0.051 | -0.0599 | -0.0030 | -0.1397 | 0.0662 |
| 9 | 25.40 | 1.357 | 0.700 | 1.352 | 0.593 | 0.055 | -0.0447 | -0.0034 | -0.0241 | 0.0845 |
| 1 | 1.87 | 1.669 | 1.001 | 1.785 | 0.091 | 0.014 | 0.0014 | -0.0001 | 0.0146 | 0.0145 |
| 2 | 4.28 | 1.660 | 0.990 | 1.777 | 0.148 | 0.017 | 0.0045 | -0.0004 | -0.0113 | 0.0143 |
| 3 | 7.16 | 1.655 | 0.983 | 1.773 | 0.226 | 0.022 | 0.0145 | -0.0024 | 0.0028 | 0.0267 |
| 4 | 10.30 | 1.666 | 0.998 | 1.779 | 0.318 | 0.038 | 0.0326 | -0.0253 | -0.0342 | 0.0484 |
| 5 | 13.45 | 1.667 | 0.999 | 1.780 | 0.404 | 0.044 | -0.0482 | -0.0182 | 0.0073 | 0.0636 |
| 6 | 16.43 | 1.643 | 0.962 | 1.774 | 0.478 | 0.048 | -0.0398 | -0.0084 | -0.0121 | 0.0778 |
| 7 | 19.30 | 1.622 | 0.930 | 1.767 | 0.549 | 0.053 | -0.0283 | -0.0027 | 0.0250 | 0.1018 |
| 8 | 22.30 | 1.609 | 0.909 | 1.763 | 0.626 | 0.052 | -0.0082 | -0.0038 | -0.0372 | 0.1538 |
| 9 | 25.40 | 1.615 | 0.923 | 1.756 | 0.705 | 0.056 | 0.0330 | 0.0027 | -0.0044 | 0.2307 |
| 1 | 1.83 | 1.926 | 1.230 | 2.195 | 0.099 | 0.014 | 0.0018 | -0.0002 | -0.0182 | 0.0222 |
| 2 | 4.19 | 1.912 | 1.211 | 2.187 | 0.164 | 0.016 | 0.0062 | -0.0010 | -0.0157 | 0.0249 |
| 3 | 7.13 | 1.904 | 1.200 | 2.184 | 0.257 | 0.025 | 0.0245 | -0.0115 | 0.0389 | 0.0549 |
| 4 | 10.29 | 1.924 | 1.225 | 2.202 | 0.363 | 0.039 | -0.0409 | -0.0265 | 0.0452 | 0.0995 |
| 5 | 13.38 | 1.897 | 1.188 | 2.188 | 0.456 | 0.041 | -0.0458 | -0.0156 | -0.1490 | 0.1192 |
| 6 | 16.29 | 1.872 | 1.148 | 2.186 | 0.539 | 0.047 | -0.0315 | -0.0038 | -0.0724 | 0.1600 |
| 7 | 19.27 | 1.832 | 1.091 | 2.168 | 0.621 | 0.053 | -0.0073 | -0.0049 | 0.1206 | 0.2300 |
| 8 | 22.15 | 1.846 | 1.095 | 2.208 | 0.722 | 0.060 | 0.0451 | 0.0053 | 0.1337 | 0.3836 |
| 9 | 25.73 | 1.866 | 1.149 | 2.160 | 0.823 | 0.040 | -0.0510 | 0.0046 | -0.2014 | 0.5515 |

Table 5.4: Summary table for $^4$He at 4.462 GeV. The four sections correspond to the four $Q^2$ intervals (see table 5.1). Bins are determined by the conditions 4.18 and 4.19 on $\omega$, $Q^2$ and $E_m$ combined with the condition $3(n-1) < \theta_{pq} < 3n$ where $3^o$ is the $\theta_{pq}$ bin width and $n$ is an integer between 1 and 9. Values on columns 2-4 and 6-7 are weighted averages within the ($Q^2$, $\theta_{pq}$) bin. The calculations were done as described in section 5.2.

| Bin ($n$) | $\theta_{pq}$ ($^o$) | q ($\frac{\text{GeV}}{\text{c}}$) | $\omega$ (GeV) | $Q^2$ $(\frac{\text{GeV}}{\text{c}})^2$ | $p_m$ ($\frac{\text{GeV}}{\text{c}}$) | $E_m$ (GeV) | $A'_{LT}$ OMEA | $A'_{LT}$ RMSGA | $A'_{LT}$ (meas) | $\delta A'_{LT}$ (stat) |
|---|---|---|---|---|---|---|---|---|---|---|
| 1 | 1.99 | 0.822 | 0.342 | 0.559 | 0.072 | 0.030 | -0.0105 | n/a | -0.0136 | 0.0073 |
| 2 | 4.66 | 0.819 | 0.338 | 0.557 | 0.095 | 0.028 | -0.0172 | n/a | -0.0129 | 0.0042 |
| 3 | 7.52 | 0.812 | 0.330 | 0.550 | 0.126 | 0.026 | -0.0176 | n/a | -0.0260 | 0.0036 |
| 4 | 10.44 | 0.801 | 0.319 | 0.540 | 0.161 | 0.026 | -0.0149 | n/a | -0.0186 | 0.0038 |
| 5 | 13.38 | 0.790 | 0.309 | 0.528 | 0.196 | 0.028 | -0.0094 | n/a | -0.0148 | 0.0047 |
| 6 | 16.34 | 0.780 | 0.300 | 0.518 | 0.231 | 0.032 | 0.0005 | n/a | -0.0115 | 0.0063 |
| 7 | 19.33 | 0.775 | 0.296 | 0.513 | 0.267 | 0.039 | 0.0175 | n/a | 0.0098 | 0.0089 |
| 8 | 22.36 | 0.777 | 0.297 | 0.515 | 0.306 | 0.047 | 0.0268 | n/a | -0.0112 | 0.0126 |
| 9 | 25.40 | 0.786 | 0.305 | 0.525 | 0.347 | 0.054 | 0.0098 | n/a | 0.0224 | 0.0167 |
| 1 | 1.99 | 1.068 | 0.515 | 0.876 | 0.082 | 0.029 | -0.0155 | -0.0077 | -0.0159 | 0.0081 |
| 2 | 4.60 | 1.063 | 0.508 | 0.872 | 0.113 | 0.026 | -0.0239 | -0.0126 | -0.0231 | 0.0049 |
| 3 | 7.43 | 1.052 | 0.495 | 0.862 | 0.155 | 0.026 | -0.0235 | -0.0158 | -0.0267 | 0.0049 |
| 4 | 10.32 | 1.039 | 0.479 | 0.850 | 0.201 | 0.028 | -0.0175 | -0.0203 | -0.0204 | 0.0065 |
| 5 | 13.29 | 1.029 | 0.468 | 0.841 | 0.250 | 0.033 | -0.0001 | -0.0251 | -0.0231 | 0.0098 |
| 6 | 16.32 | 1.031 | 0.470 | 0.843 | 0.302 | 0.043 | 0.0296 | -0.0102 | 0.0013 | 0.0149 |
| 7 | 19.39 | 1.039 | 0.478 | 0.851 | 0.357 | 0.053 | -0.0007 | 0.0126 | 0.0027 | 0.0198 |
| 8 | 22.41 | 1.041 | 0.478 | 0.854 | 0.407 | 0.059 | -0.0423 | 0.0300 | -0.0320 | 0.0238 |
| 9 | 25.42 | 1.035 | 0.471 | 0.849 | 0.454 | 0.061 | -0.0521 | 0.0337 | -0.0070 | 0.0286 |
| 1 | 1.99 | 1.326 | 0.716 | 1.246 | 0.092 | 0.027 | -0.0195 | -0.0160 | -0.0309 | 0.0116 |
| 2 | 4.52 | 1.317 | 0.704 | 1.240 | 0.131 | 0.024 | -0.0286 | -0.0241 | -0.0264 | 0.0077 |
| 3 | 7.31 | 1.303 | 0.685 | 1.229 | 0.184 | 0.024 | -0.0266 | -0.0310 | -0.0227 | 0.0093 |
| 4 | 10.23 | 1.294 | 0.674 | 1.221 | 0.245 | 0.029 | -0.0060 | -0.0406 | 0.0060 | 0.0154 |
| 5 | 13.29 | 1.298 | 0.680 | 1.223 | 0.313 | 0.042 | 0.0432 | 0.0228 | 0.0464 | 0.0254 |
| 6 | 16.40 | 1.304 | 0.686 | 1.229 | 0.381 | 0.053 | -0.0267 | 0.0384 | -0.0042 | 0.0341 |
| 7 | 19.37 | 1.294 | 0.670 | 1.226 | 0.441 | 0.057 | -0.0591 | 0.0328 | 0.0117 | 0.0409 |
| 8 | 22.37 | 1.281 | 0.650 | 1.218 | 0.497 | 0.060 | -0.0633 | 0.0148 | -0.0857 | 0.0518 |
| 9 | 25.38 | 1.275 | 0.640 | 1.217 | 0.555 | 0.063 | -0.0469 | -0.0057 | 0.0245 | 0.0669 |
| 1 | 1.97 | 1.561 | 0.909 | 1.610 | 0.098 | 0.026 | -0.0224 | -0.0212 | -0.0310 | 0.0166 |
| 2 | 4.45 | 1.550 | 0.894 | 1.604 | 0.146 | 0.023 | -0.0304 | -0.0305 | -0.0198 | 0.0122 |
| 3 | 7.21 | 1.533 | 0.871 | 1.590 | 0.211 | 0.025 | -0.0228 | -0.0423 | -0.0144 | 0.0179 |
| 4 | 10.22 | 1.528 | 0.863 | 1.589 | 0.288 | 0.035 | 0.0302 | -0.0066 | 0.0101 | 0.0347 |
| 5 | 13.37 | 1.538 | 0.878 | 1.596 | 0.371 | 0.049 | -0.0071 | 0.0450 | 0.0306 | 0.0523 |
| 6 | 16.40 | 1.527 | 0.860 | 1.594 | 0.444 | 0.055 | -0.0608 | 0.0228 | -0.0165 | 0.0675 |
| 7 | 19.39 | 1.512 | 0.841 | 1.580 | 0.513 | 0.060 | -0.0675 | 0.0016 | -0.0350 | 0.0890 |
| 8 | 22.31 | 1.501 | 0.813 | 1.591 | 0.580 | 0.062 | -0.0234 | -0.0254 | 0.0163 | 0.1271 |
| 9 | 25.40 | 1.492 | 0.804 | 1.579 | 0.649 | 0.066 | 0.0089 | -0.0357 | 0.1536 | 0.1758 |

Table 5.5: Summary table for $^{12}$C at 2.262 GeV. The four sections correspond to the four $Q^2$ intervals (see table 5.1). Bins are determined by the conditions 4.18 and 4.19 on $\omega$, $Q^2$ and $E_m$ combined with the condition $3(n-1) < \theta_{pq} < 3n$ where $3^o$ is the $\theta_{pq}$ bin width and $n$ is an integer between 1 and 9. Values on columns 2-4 and 6-7 are weighted averages within the ($Q^2$, $\theta_{pq}$) bin. The calculations were done as described in section 5.2.

| Bin ($n$) | $\theta_{pq}$ ($^o$) | q $\left(\frac{\text{GeV}}{\text{c}}\right)$ | $\omega$ (GeV) | $Q^2$ $\left(\frac{\text{GeV}}{\text{c}}\right)^2$ | $p_m$ $\left(\frac{\text{GeV}}{\text{c}}\right)$ | $E_m$ (GeV) | $A'_{LT}$ OMEA | $A'_{LT}$ RMSGA | $A'_{LT}$ (meas) | $\delta A'_{LT}$ (stat) |
|---|---|---|---|---|---|---|---|---|---|---|
| 1 | 1.98 | 1.194 | 0.598 | 1.068 | 0.103 | -0.033 | -0.0091 | -0.0053 | -0.0460 | 0.0202 |
| 2 | 4.55 | 1.189 | 0.591 | 1.064 | 0.136 | -0.033 | -0.0130 | -0.0080 | -0.0444 | 0.0132 |
| 3 | 7.39 | 1.177 | 0.574 | 1.055 | 0.181 | -0.034 | -0.0123 | -0.0100 | 0.0169 | 0.0142 |
| 4 | 10.32 | 1.164 | 0.558 | 1.043 | 0.232 | -0.033 | -0.0077 | -0.0127 | -0.0189 | 0.0196 |
| 5 | 13.32 | 1.157 | 0.553 | 1.031 | 0.288 | -0.026 | 0.0081 | -0.0069 | -0.0060 | 0.0284 |
| 6 | 16.38 | 1.163 | 0.563 | 1.036 | 0.347 | -0.004 | 0.0012 | 0.0126 | -0.0197 | 0.0382 |
| 7 | 19.43 | 1.166 | 0.566 | 1.039 | 0.404 | 0.013 | -0.0235 | 0.0193 | 0.0145 | 0.0494 |
| 8 | 22.40 | 1.160 | 0.552 | 1.040 | 0.456 | 0.022 | -0.0301 | 0.0170 | -0.0424 | 0.0640 |
| 9 | 25.41 | 1.157 | 0.547 | 1.039 | 0.509 | 0.031 | -0.0306 | 0.0096 | 0.0789 | 0.0812 |
| 1 | 1.98 | 1.414 | 0.775 | 1.400 | 0.100 | -0.013 | -0.0109 | -0.0094 | -0.0433 | 0.0169 |
| 2 | 4.51 | 1.405 | 0.762 | 1.394 | 0.141 | -0.014 | -0.0150 | -0.0133 | -0.0123 | 0.0116 |
| 3 | 7.30 | 1.388 | 0.740 | 1.380 | 0.197 | -0.015 | -0.0131 | -0.0163 | 0.0099 | 0.0147 |
| 4 | 10.26 | 1.377 | 0.727 | 1.369 | 0.263 | -0.008 | 0.0019 | -0.0148 | 0.0140 | 0.0242 |
| 5 | 13.36 | 1.390 | 0.747 | 1.375 | 0.337 | 0.013 | 0.0115 | 0.0197 | 0.0221 | 0.0374 |
| 6 | 16.40 | 1.387 | 0.741 | 1.375 | 0.405 | 0.028 | -0.0272 | 0.0211 | 0.0725 | 0.0485 |
| 7 | 19.40 | 1.374 | 0.718 | 1.371 | 0.467 | 0.036 | -0.0353 | 0.0107 | -0.0446 | 0.0644 |
| 8 | 22.43 | 1.359 | 0.693 | 1.367 | 0.528 | 0.038 | -0.0307 | 0.0002 | -0.0746 | 0.0837 |
| 9 | 25.34 | 1.352 | 0.683 | 1.360 | 0.587 | 0.047 | -0.0115 | -0.0129 | -0.0092 | 0.1076 |
| 1 | 1.96 | 1.669 | 0.995 | 1.796 | 0.106 | -0.003 | -0.0122 | -0.0117 | -0.0125 | 0.0220 |
| 2 | 4.44 | 1.654 | 0.973 | 1.787 | 0.156 | -0.004 | -0.0158 | -0.0161 | 0.0217 | 0.0167 |
| 3 | 7.20 | 1.635 | 0.947 | 1.777 | 0.224 | -0.002 | -0.0093 | -0.0221 | -0.0178 | 0.0255 |
| 4 | 10.28 | 1.646 | 0.966 | 1.778 | 0.311 | 0.015 | 0.0268 | 0.0133 | 0.0371 | 0.0473 |
| 5 | 13.40 | 1.650 | 0.969 | 1.783 | 0.397 | 0.030 | -0.0153 | 0.0190 | 0.1114 | 0.0661 |
| 6 | 16.37 | 1.626 | 0.931 | 1.778 | 0.472 | 0.039 | -0.0371 | 0.0060 | -0.0266 | 0.0881 |
| 7 | 19.34 | 1.612 | 0.904 | 1.783 | 0.544 | 0.046 | -0.0283 | -0.0084 | 0.0486 | 0.1219 |
| 8 | 22.24 | 1.602 | 0.894 | 1.767 | 0.618 | 0.049 | -0.0002 | -0.0204 | 0.1582 | 0.2125 |
| 9 | 25.28 | 1.593 | 0.881 | 1.762 | 0.689 | 0.054 | 0.0122 | -0.0027 | -0.1582 | 0.2794 |
| 1 | 1.96 | 1.924 | 1.222 | 2.209 | 0.112 | -0.000 | -0.0142 | -0.0133 | -0.0007 | 0.0307 |
| 2 | 4.34 | 1.903 | 1.194 | 2.197 | 0.171 | -0.002 | -0.0148 | -0.0183 | 0.0004 | 0.0260 |
| 3 | 7.12 | 1.887 | 1.173 | 2.186 | 0.254 | 0.004 | 0.0065 | -0.0267 | -0.0705 | 0.0469 |
| 4 | 10.27 | 1.897 | 1.186 | 2.194 | 0.356 | 0.024 | 0.0203 | 0.0207 | 0.0265 | 0.0926 |
| 5 | 13.40 | 1.881 | 1.157 | 2.199 | 0.450 | 0.034 | -0.0266 | 0.0059 | -0.0918 | 0.1210 |
| 6 | 16.29 | 1.866 | 1.141 | 2.182 | 0.535 | 0.041 | -0.0384 | -0.0098 | 0.1531 | 0.1712 |
| 7 | 19.29 | 1.855 | 1.123 | 2.179 | 0.622 | 0.051 | 0.0023 | -0.0245 | -0.5146 | 0.3384 |
| 8 | 22.15 | 1.821 | 1.065 | 2.181 | 0.693 | 0.052 | 0.0148 | 0.0034 | -0.0936 | 0.4809 |
| 9 | 25.31 | 1.787 | 1.012 | 2.170 | 0.773 | 0.063 | 0.0269 | 0.0183 | -0.6516 | 0.8393 |

Table 5.6: Summary table for $^{12}$C at 4.462 GeV. The four sections correspond to the four $Q^2$ intervals (see table 5.1). Bins are determined by the conditions 4.18 and 4.19 on $\omega$, $Q^2$ and $E_m$ combined with the condition $3(n-1) < \theta_{pq} < 3n$ where $3^o$ is the $\theta_{pq}$ bin width and $n$ is an integer between 1 and 9. Values on columns 2-4 and 6-7 are weighted averages within the ($Q^2$, $\theta_{pq}$) bin. The calculations were done as described in section 5.2.

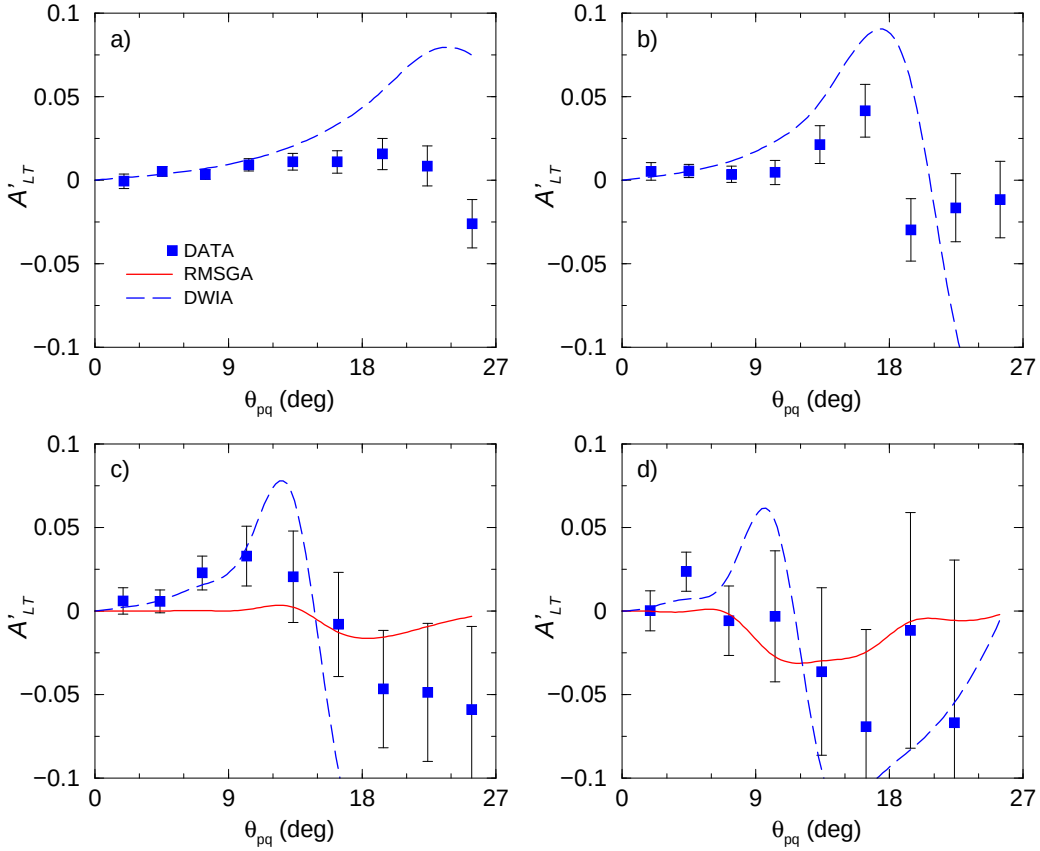


Figure 5-4: Dependence of $A'_{LT}$ versus $\theta_{pq}$ for $^4$He$(e,e'p)$ at 2.262 GeV. Measurements were done with an angle bin width of $\Delta\theta_{pq} = 3^o$, for four $Q^2$ bins along the quasielastic ridge. The $Q^2$ bins are set as follows: a) $0.350 < Q^2$ (GeV$^2$/c$^2$) $< 0.712$, b) $0.712 < Q^2$ (GeV$^2$/c$^2$) $< 1.075$, c) $1.075 < Q^2$ (GeV$^2$/c$^2$) $< 1.438$ and d) $1.438 < Q^2$ (GeV$^2$/c$^2$) $< 1.800$. There were no constrains on $p_m$ or $p'$. The solid (dashed) curves correspond to RMSGA (DWIA) calculations used as described in section 5.2. The data are listed in table 5.3. Errors shown are statistical.

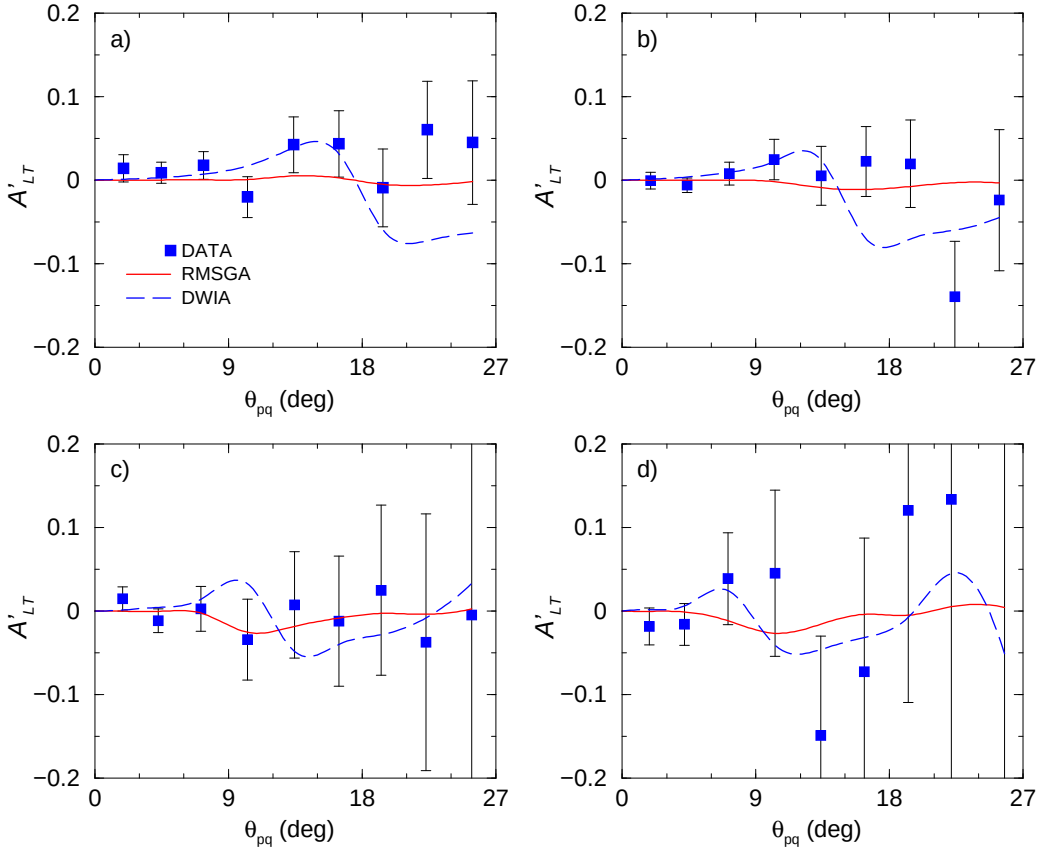


Figure 5-5: Dependence of $A'_{LT}$ versus $\theta_{pq}$ for $^4$He$(e,e'p)$ at 4.462 GeV. Measurements were done with an angle bin width of $\Delta\theta_{pq} = 3^o$, for four $Q^2$ bins along the quasielastic ridge. The $Q^2$ bins are set as follows: a) $0.800 < Q^2$ (GeV$^2$/c$^2$) $< 1.200$, b) $1.200 < Q^2$ (GeV$^2$/c$^2$) $< 1.600$, c) $1.600 < Q^2$ (GeV$^2$/c$^2$) $< 2.000$ and d) $2.000 < Q^2$ (GeV$^2$/c$^2$) $< 2.400$. There were no constrains on $p_m$ or $p'$. The solid (dashed) curves correspond to RMSGA (DWIA) calculations used as described in section 5.2. The data are listed in table 5.4. Errors shown are statistical.

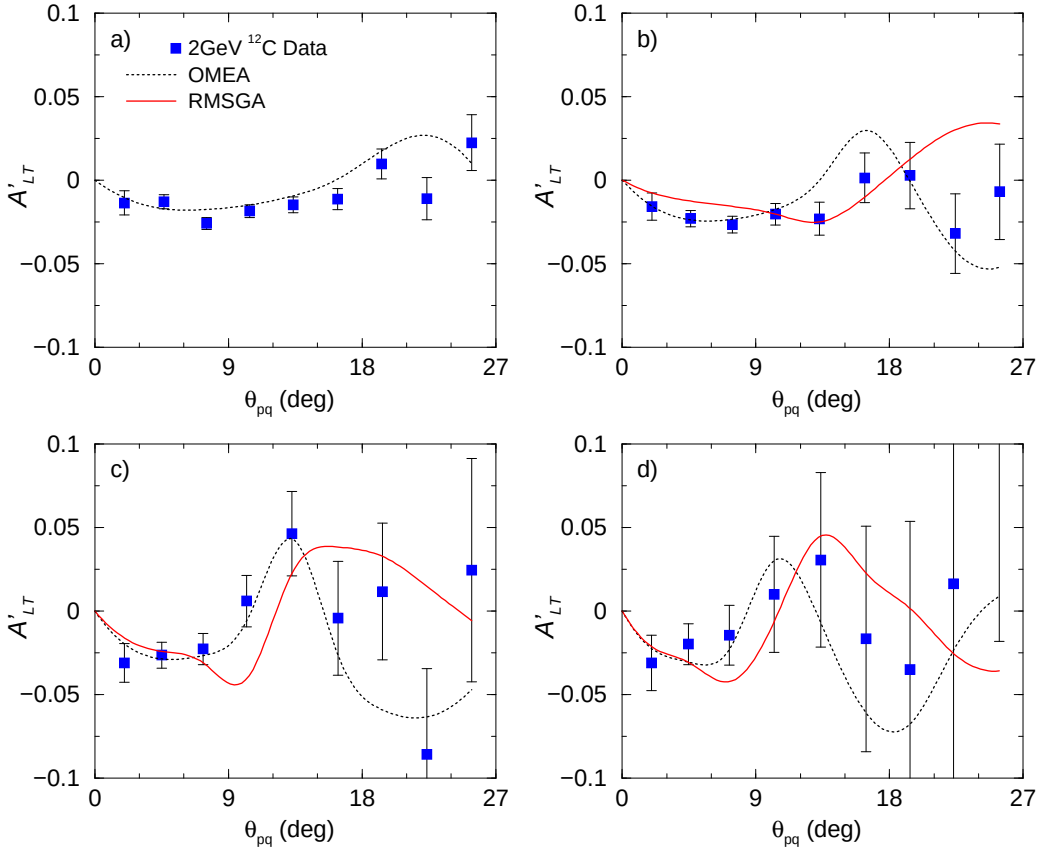


Figure 5-6: Dependence of $A'_{LT}$ versus $\theta_{pq}$ for $^{12}$C$(e,e'p)$ at 2.262 GeV. Measurements were done with an angle bin width of $\Delta\theta_{pq} = 3^o$, for four $Q^2$ bins along the quasielastic ridge. The $Q^2$ bins are set as follows: a) $0.350 < Q^2$ (GeV$^2$/c$^2$) $< 0.712$, b) $0.712 < Q^2$ (GeV$^2$/c$^2$) $< 1.075$, c) $1.075 < Q^2$ (GeV$^2$/c$^2$) $< 1.438$ and d) $1.438 < Q^2$ (GeV$^2$/c$^2$) $< 1.800$. There were no constrains on $p_m$ or $p'$. The solid (dotted) curves correspond to RMSGA (OMEA) calculations used as described in section 5.2. The data are listed in table 5.5. Errors shown are statistical.

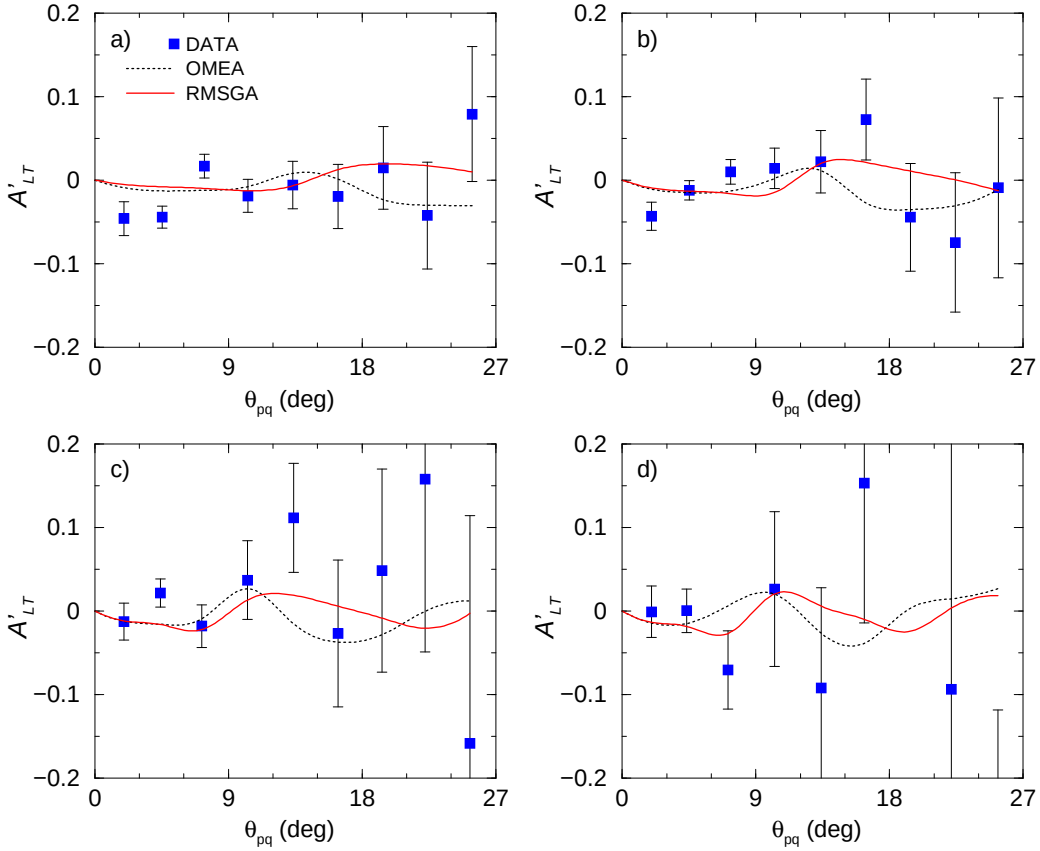


Figure 5-7: Dependence of $A'_{LT}$ versus $\theta_{pq}$ for $^{12}$C$(e,e'p)$ at 4.462 GeV. Measurements were done with an angle bin width of $\Delta\theta_{pq} = 3^o$, for four $Q^2$ bins along the quasielastic ridge. The $Q^2$ bins are set as follows: a) $0.800 < Q^2$ (GeV$^2$/c$^2$) $< 1.200$, b) $1.200 < Q^2$ (GeV$^2$/c$^2$) $< 1.600$, c) $1.600 < Q^2$ (GeV$^2$/c$^2$) $< 2.000$ and d) $2.000 < Q^2$ (GeV$^2$/c$^2$) $< 2.400$. There were no constrains on $p_m$ or $p'$. The solid (dotted) curves correspond to RMSGA (OMEA) calculations used as described in section 5.2. The data are listed in table 5.6. Errors shown are statistical.

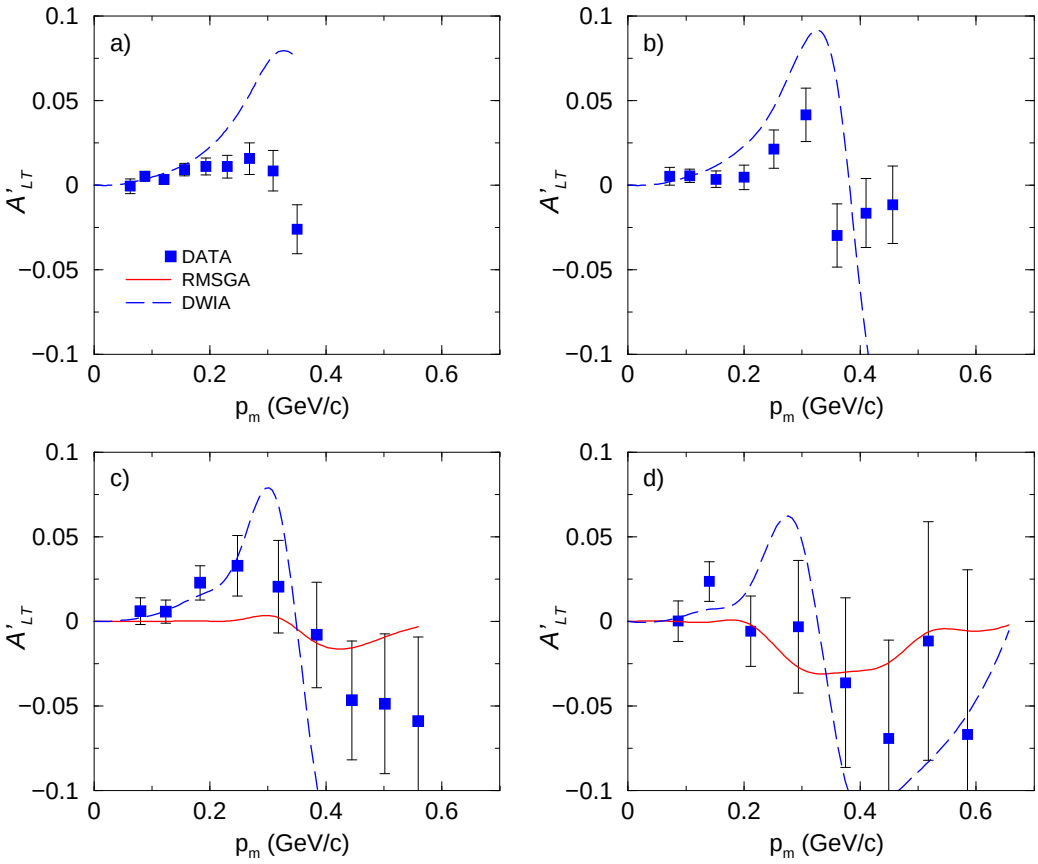


Figure 5-8: Dependence of $A'_{LT}$ versus missing momentum $p_m$ for $^4$He$(e,e'p)$ at 2.262 GeV, in four $Q^2$ bins along the quasielastic ridge. The $Q^2$ bins are set as follows: a) $0.350 < Q^2$ (GeV$^2$/c$^2$) $< 0.712$, b) $0.712 < Q^2$ (GeV$^2$/c$^2$) $< 1.075$, c) $1.075 < Q^2$ (GeV$^2$/c$^2$) $< 1.438$ and d) $1.438 < Q^2$ (GeV$^2$/c$^2$) $< 1.800$. The solid (dashed) curves correspond to RMSGA (DWIA) calculations used as described in section 5.2. The data used are listed in table 5.3. Errors shown are statistical.

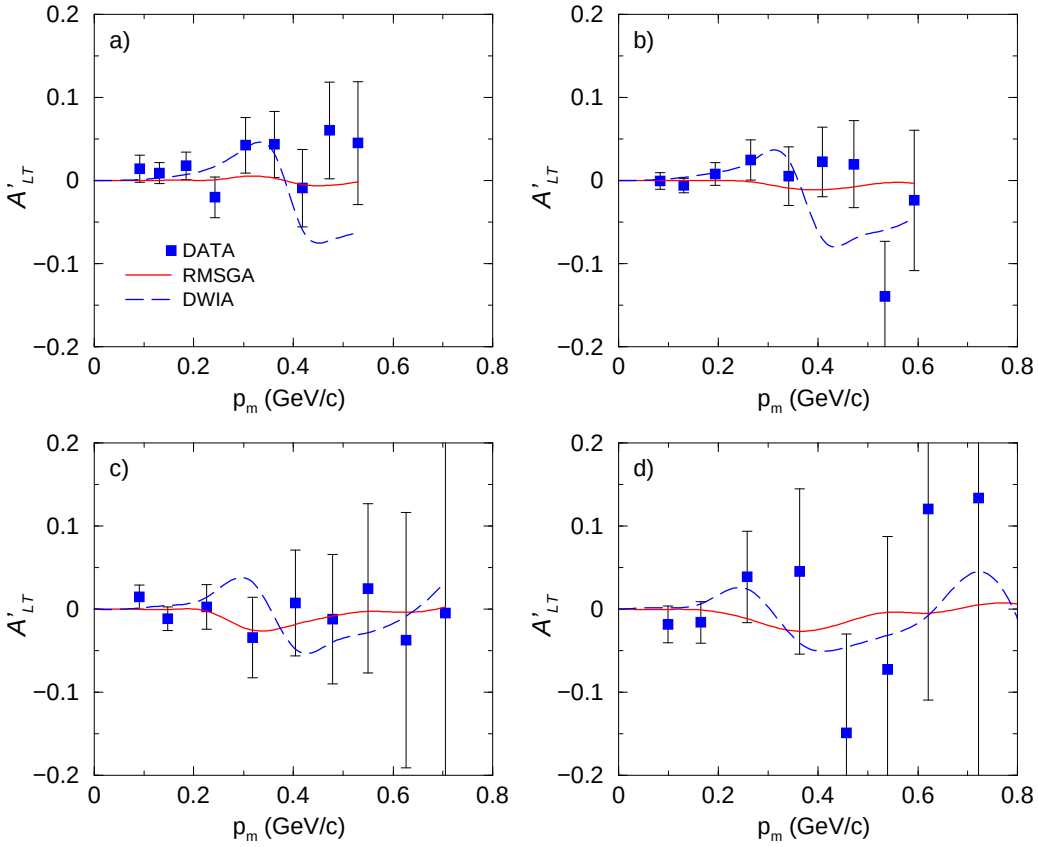


Figure 5-9: Dependence of $A'_{LT}$ versus missing momentum $p_m$ for $^4$He$(e,e'p)$ at 4.462 GeV, in four $Q^2$ bins along the quasielastic ridge. The $Q^2$ bins are set as follows: a) $0.800 < Q^2$ (GeV$^2$/c$^2$) $< 1.200$, b) $1.200 < Q^2$ (GeV$^2$/c$^2$) $< 1.600$, c) $1.600 < Q^2$ (GeV$^2$/c$^2$) $< 2.000$ and d) $2.000 < Q^2$ (GeV$^2$/c$^2$) $< 2.400$. The solid (dashed) curves correspond to RMSGA (DWIA) calculations used as described in section 5.2. The data used are listed in table 5.4. Errors shown are statistical.

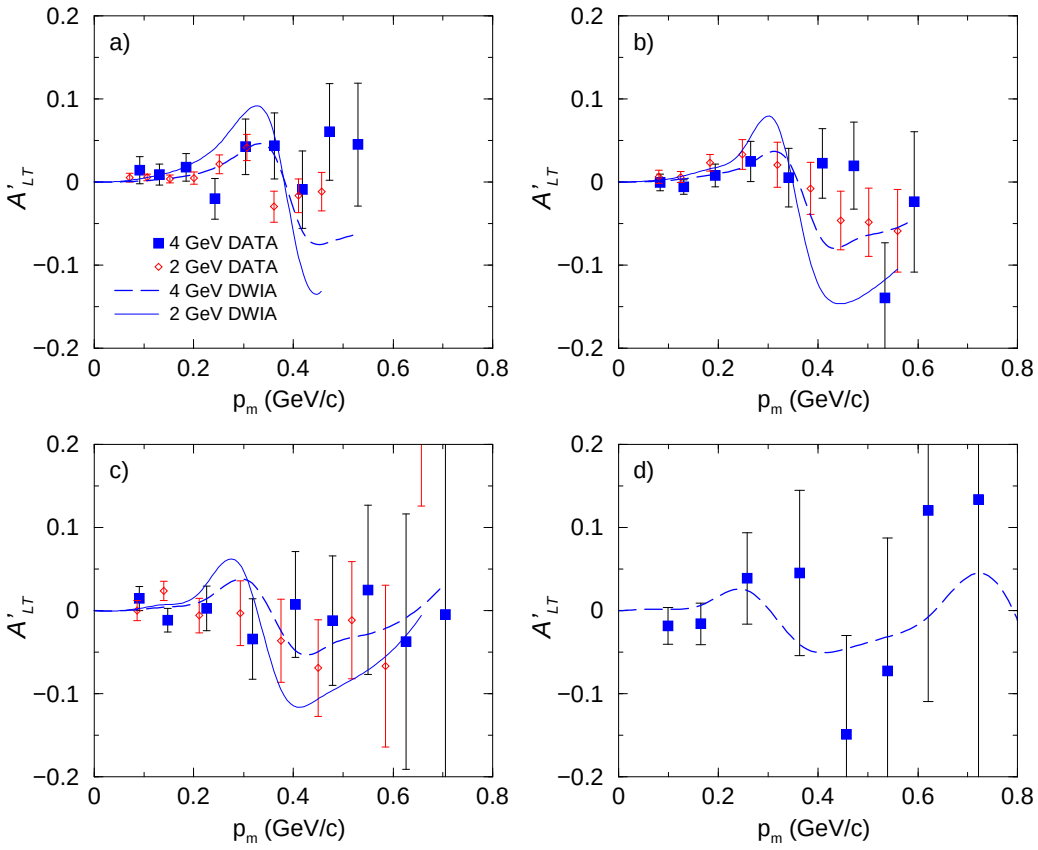


Figure 5-10: Consistency test between 2.262 and 4.462 GeV $^4$He data: $Q^2$ bin $n$ from 4.462 GeV (figure 5-9) is overlapped with bin $n-1$ from 2.262 GeV $^4$He (figure 5-8), where $n = 2, 3, 4$, corresponding (in this order) to graphs (a), (b) and (c).

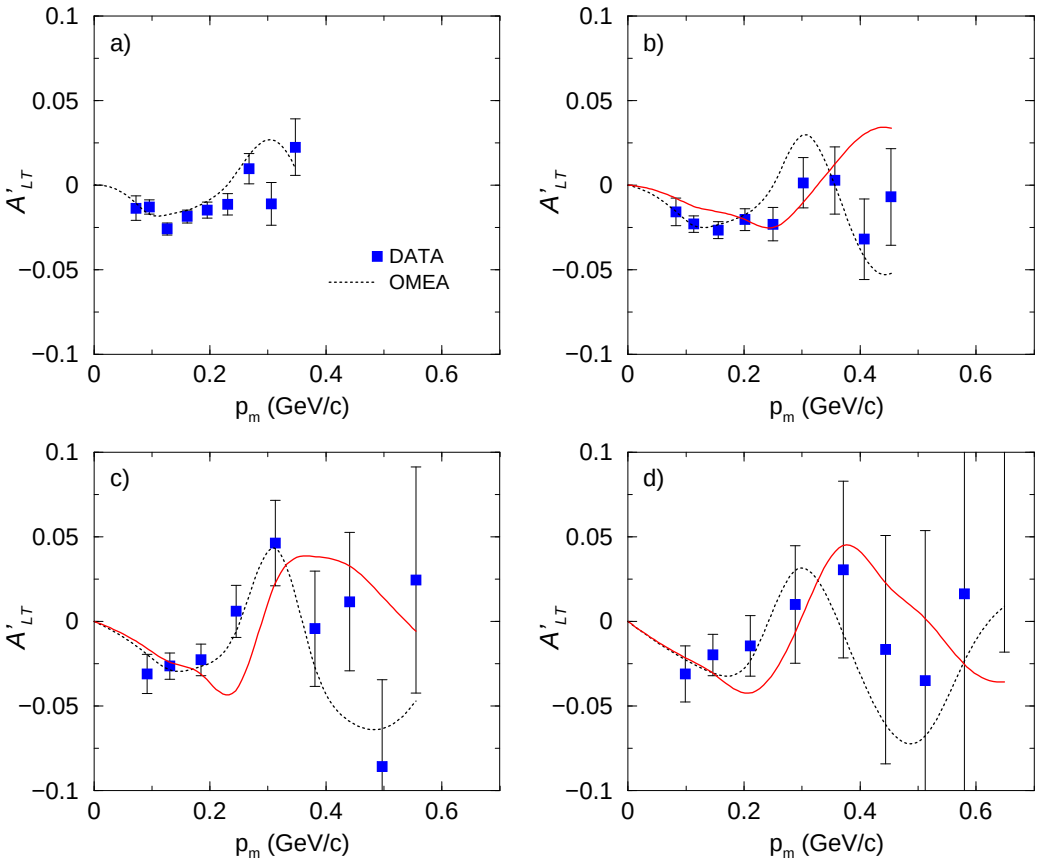


Figure 5-11: Dependence of $A'_{LT}$ versus missing momentum $p_m$ for $^{12}$C$(e,e'p)$ at 2.262 GeV, in four $Q^2$ bins along the quasielastic ridge. The $Q^2$ bins are set as follows: a) $0.350 < Q^2$ (GeV$^2$/c$^2$) $< 0.712$, b) $0.712 < Q^2$ (GeV$^2$/c$^2$) $< 1.075$, c) $1.075 < Q^2$ (GeV$^2$/c$^2$) $< 1.438$ and d) $1.438 < Q^2$ (GeV$^2$/c$^2$) $< 1.800$. The solid (dotted) curves correspond to RMSGA (OMEA) calculations used as described in section 5.2. The data used are listed in table 5.5. Errors shown are statistical.

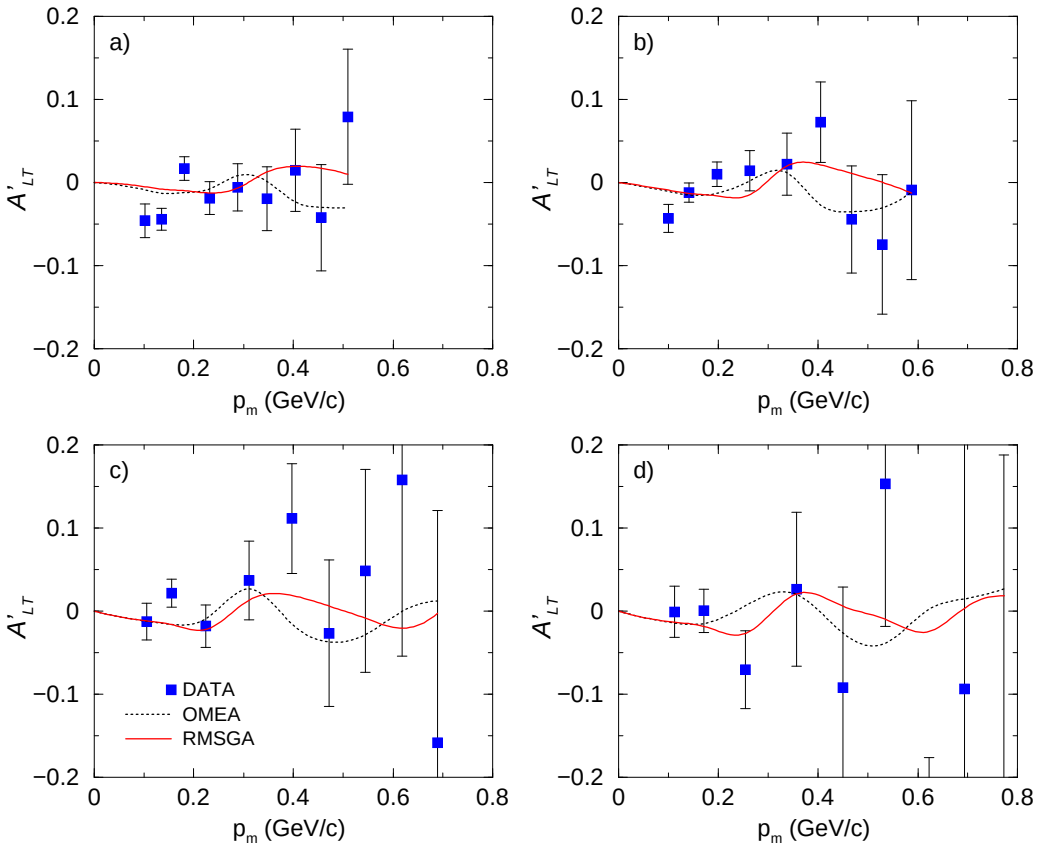


Figure 5-12: Dependence of $A'_{LT}$ versus missing momentum $p_m$ for $^{12}$C$(e, e'p)$ at 4.462 GeV, in four $Q^2$ bins along the quasielastic ridge. The $Q^2$ bins are set as follows: a) $0.800 < Q^2$ (GeV$^2$/c$^2$) $< 1.200$, b) $1.200 < Q^2$ (GeV$^2$/c$^2$) $< 1.600$, c) $1.600 < Q^2$ (GeV$^2$/c$^2$) $< 2.000$ and d) $2.000 < Q^2$ (GeV$^2$/c$^2$) $< 2.400$. The solid (dotted) curves correspond to RMSGA (OMEA) calculations used as described in section 5.2. The data used are listed in table 5.6. Errors shown are statistical.

| $E_{beam}$ (GeV) | $p_m$ bin | $E_m$ bin | q (GeV/c) | $\omega$ (GeV) | $\theta_{pq}$ (deg) | $p_m$ (GeV/c) | $E_m$ (GeV) | $A'_{LT}$ | $\delta A'_{LT}$ |
|---|---|---|---|---|---|---|---|---|---|
| 2.262 | 0 | 0 | 0.995 | 0.457 | 5.388 | 0.119 | -0.009 | 0.00221 | 0.00408 |
| 2.262 | 0 | 1 | 0.904 | 0.401 | 6.127 | 0.118 | 0.026 | 0.00549 | 0.00129 |
| 2.262 | 0 | 2 | 1.012 | 0.590 | 6.635 | 0.136 | 0.150 | 0.01690 | 0.00511 |
| 2.262 | 0 | 3 | 1.088 | 0.734 | 6.711 | 0.148 | 0.243 | 0.05843 | 0.00522 |
| 2.262 | 0 | 4 | 1.215 | 0.914 | 5.911 | 0.152 | 0.341 | 0.01410 | 0.00885 |
| 2.262 | 0 | 5 | 1.373 | 1.127 | 4.821 | 0.148 | 0.443 | -0.00103 | 0.01506 |
| 2.262 | 0 | 6 | 1.519 | 1.316 | 3.947 | 0.152 | 0.542 | -0.00211 | 0.02482 |
| 2.262 | 0 | 7 | 1.657 | 1.491 | 3.081 | 0.166 | 0.632 | 0.00930 | 0.05339 |
| 2.262 | 0 | 8 | 1.780 | 1.654 | 2.517 | 0.185 | 0.716 | 0.40018 | 0.32036 |
| 2.262 | 1 | 0 | 1.035 | 0.557 | 10.728 | 0.263 | -0.011 | -0.00871 | 0.00797 |
| 2.262 | 1 | 1 | 0.935 | 0.448 | 14.118 | 0.277 | 0.038 | 0.00405 | 0.00224 |
| 2.262 | 1 | 2 | 0.992 | 0.551 | 15.853 | 0.306 | 0.147 | 0.00543 | 0.00464 |
| 2.262 | 1 | 3 | 1.072 | 0.690 | 14.339 | 0.300 | 0.254 | 0.03714 | 0.00370 |
| 2.262 | 1 | 4 | 1.134 | 0.781 | 14.141 | 0.334 | 0.348 | 0.02829 | 0.00336 |
| 2.262 | 1 | 5 | 1.230 | 0.912 | 12.798 | 0.361 | 0.444 | 0.02584 | 0.00424 |
| 2.262 | 1 | 6 | 1.356 | 1.084 | 10.587 | 0.365 | 0.544 | 0.02755 | 0.00630 |
| 2.262 | 1 | 7 | 1.483 | 1.253 | 8.211 | 0.368 | 0.645 | 0.00891 | 0.00853 |
| 2.262 | 1 | 8 | 1.623 | 1.431 | 6.808 | 0.386 | 0.739 | 0.03252 | 0.01403 |
| 2.262 | 1 | 9 | 1.758 | 1.604 | 5.513 | 0.407 | 0.833 | 0.03077 | 0.03302 |
| 4.462 | 0 | 0 | 1.388 | 0.740 | 3.844 | 0.121 | -0.027 | -0.00511 | 0.00714 |
| 4.462 | 0 | 1 | 1.486 | 0.858 | 3.643 | 0.119 | 0.031 | 0.00297 | 0.00561 |
| 4.462 | 0 | 2 | 1.510 | 0.978 | 4.403 | 0.138 | 0.148 | 0.01746 | 0.01491 |
| 4.462 | 0 | 3 | 1.667 | 1.208 | 4.299 | 0.150 | 0.244 | 0.02766 | 0.01683 |
| 4.462 | 0 | 4 | 1.830 | 1.441 | 3.884 | 0.151 | 0.344 | 0.02356 | 0.02462 |
| 4.462 | 0 | 5 | 2.019 | 1.693 | 3.389 | 0.150 | 0.444 | -0.05970 | 0.03644 |
| 4.462 | 0 | 6 | 2.237 | 1.963 | 2.850 | 0.152 | 0.544 | 0.08877 | 0.05184 |
| 4.462 | 0 | 7 | 2.485 | 2.258 | 2.295 | 0.159 | 0.637 | -0.01154 | 0.09568 |
| 4.462 | 0 | 8 | 2.842 | 2.662 | 1.527 | 0.166 | 0.736 | 0.13265 | 0.23462 |
| 4.462 | 1 | 0 | 1.406 | 0.808 | 8.882 | 0.280 | -0.034 | 0.02113 | 0.01182 |
| 4.462 | 1 | 1 | 1.512 | 0.924 | 9.255 | 0.292 | 0.042 | 0.01202 | 0.00856 |
| 4.462 | 1 | 2 | 1.488 | 0.951 | 10.349 | 0.304 | 0.151 | 0.03348 | 0.01292 |
| 4.462 | 1 | 3 | 1.591 | 1.106 | 9.544 | 0.305 | 0.253 | 0.02014 | 0.01017 |
| 4.462 | 1 | 4 | 1.659 | 1.201 | 9.489 | 0.334 | 0.348 | 0.00768 | 0.00934 |
| 4.462 | 1 | 5 | 1.750 | 1.328 | 8.761 | 0.357 | 0.446 | 0.03448 | 0.01081 |
| 4.462 | 1 | 6 | 1.890 | 1.521 | 7.316 | 0.360 | 0.546 | 0.01538 | 0.01437 |
| 4.462 | 1 | 7 | 2.056 | 1.736 | 5.780 | 0.366 | 0.646 | -0.00693 | 0.01815 |
| 4.462 | 1 | 8 | 2.279 | 2.006 | 4.642 | 0.377 | 0.744 | 0.00047 | 0.02558 |
| 4.462 | 1 | 9 | 2.562 | 2.334 | 3.716 | 0.391 | 0.838 | -0.01120 | 0.04181 |

Table 5.7: Missing energy dependence of $A'_{LT}$ for $^4$He .

| $E_{beam}$ (GeV) | $p_m$ bin | $E_m$ bin | q (GeV/c) | $\omega$ (GeV) | $\theta_{pq}$ (deg) | $p_m$ (GeV/c) | $E_m$ (GeV) | $A'_{LT}$ | $\delta A'_{LT}$ |
|---|---|---|---|---|---|---|---|---|---|
| 2.262 | 0 | 0 | 0.968 | 0.428 | 6.751 | 0.138 | -0.009 | -0.03021 | 0.00468 |
| 2.262 | 0 | 1 | 0.920 | 0.416 | 6.916 | 0.134 | 0.031 | -0.01700 | 0.00156 |
| 2.262 | 0 | 2 | 1.014 | 0.588 | 6.704 | 0.140 | 0.146 | 0.00324 | 0.00517 |
| 2.262 | 0 | 3 | 1.097 | 0.740 | 6.393 | 0.144 | 0.244 | 0.03644 | 0.00578 |
| 2.262 | 0 | 4 | 1.216 | 0.910 | 5.806 | 0.151 | 0.342 | 0.03527 | 0.00900 |
| 2.262 | 0 | 5 | 1.362 | 1.108 | 4.858 | 0.150 | 0.441 | -0.00297 | 0.01552 |
| 2.262 | 0 | 6 | 1.507 | 1.298 | 3.983 | 0.156 | 0.541 | 0.08073 | 0.02747 |
| 2.262 | 0 | 7 | 1.652 | 1.481 | 3.194 | 0.169 | 0.632 | -0.01903 | 0.06585 |
| 2.262 | 0 | 8 | 1.806 | 1.672 | 2.482 | 0.182 | 0.715 | 0.17451 | 0.34245 |
| 2.262 | 1 | 0 | 0.999 | 0.502 | 11.241 | 0.255 | -0.010 | -0.01659 | 0.00703 |
| 2.262 | 1 | 1 | 0.937 | 0.438 | 13.732 | 0.271 | 0.040 | -0.00152 | 0.00217 |
| 2.262 | 1 | 2 | 0.985 | 0.531 | 16.093 | 0.312 | 0.145 | -0.00817 | 0.00380 |
| 2.262 | 1 | 3 | 1.063 | 0.668 | 14.856 | 0.312 | 0.251 | 0.02215 | 0.00395 |
| 2.262 | 1 | 4 | 1.128 | 0.767 | 14.152 | 0.333 | 0.348 | 0.02558 | 0.00385 |
| 2.262 | 1 | 5 | 1.218 | 0.892 | 12.764 | 0.355 | 0.445 | 0.02202 | 0.00462 |
| 2.262 | 1 | 6 | 1.334 | 1.050 | 10.851 | 0.366 | 0.544 | 0.02910 | 0.00645 |
| 2.262 | 1 | 7 | 1.460 | 1.218 | 8.663 | 0.372 | 0.644 | 0.02154 | 0.00916 |
| 2.262 | 1 | 8 | 1.589 | 1.385 | 7.104 | 0.389 | 0.740 | 0.02648 | 0.01471 |
| 2.262 | 1 | 9 | 1.728 | 1.561 | 5.890 | 0.408 | 0.833 | 0.00208 | 0.03384 |
| 4.462 | 0 | 0 | 1.336 | 0.677 | 4.611 | 0.135 | -0.039 | -0.02496 | 0.00676 |
| 4.462 | 0 | 1 | 1.483 | 0.860 | 4.172 | 0.133 | 0.034 | 0.00472 | 0.00933 |
| 4.462 | 0 | 2 | 1.509 | 0.982 | 4.441 | 0.141 | 0.147 | 0.00281 | 0.01689 |
| 4.462 | 0 | 3 | 1.652 | 1.191 | 4.296 | 0.149 | 0.245 | -0.01741 | 0.02088 |
| 4.462 | 0 | 4 | 1.828 | 1.434 | 3.873 | 0.150 | 0.344 | 0.04090 | 0.02946 |
| 4.462 | 0 | 5 | 2.024 | 1.691 | 3.337 | 0.150 | 0.443 | -0.03272 | 0.04223 |
| 4.462 | 0 | 6 | 2.244 | 1.963 | 2.819 | 0.153 | 0.543 | 0.06169 | 0.06575 |
| 4.462 | 0 | 7 | 2.496 | 2.261 | 2.336 | 0.161 | 0.634 | 0.13542 | 0.12191 |
| 4.462 | 0 | 8 | 2.751 | 2.564 | 1.705 | 0.172 | 0.730 | 0.43852 | 0.27658 |
| 4.462 | 1 | 0 | 1.368 | 0.750 | 8.802 | 0.270 | -0.041 | -0.00806 | 0.00903 |
| 4.462 | 1 | 1 | 1.477 | 0.878 | 9.928 | 0.298 | 0.043 | 0.00834 | 0.01019 |
| 4.462 | 1 | 2 | 1.493 | 0.948 | 10.422 | 0.306 | 0.151 | 0.02031 | 0.01290 |
| 4.462 | 1 | 3 | 1.568 | 1.069 | 9.966 | 0.313 | 0.251 | 0.01281 | 0.01162 |
| 4.462 | 1 | 4 | 1.638 | 1.170 | 9.658 | 0.335 | 0.348 | 0.00693 | 0.01150 |
| 4.462 | 1 | 5 | 1.735 | 1.306 | 8.840 | 0.353 | 0.447 | 0.02756 | 0.01339 |
| 4.462 | 1 | 6 | 1.879 | 1.499 | 7.472 | 0.360 | 0.546 | 0.01108 | 0.01701 |
| 4.462 | 1 | 7 | 2.045 | 1.711 | 6.019 | 0.368 | 0.645 | -0.01593 | 0.02168 |
| 4.462 | 1 | 8 | 2.252 | 1.965 | 4.874 | 0.379 | 0.744 | -0.00565 | 0.02987 |
| 4.462 | 1 | 9 | 2.517 | 2.275 | 3.854 | 0.392 | 0.839 | -0.02951 | 0.04993 |

Table 5.8: Missing energy dependence of $A'_{LT}$ for $^{12}$C .

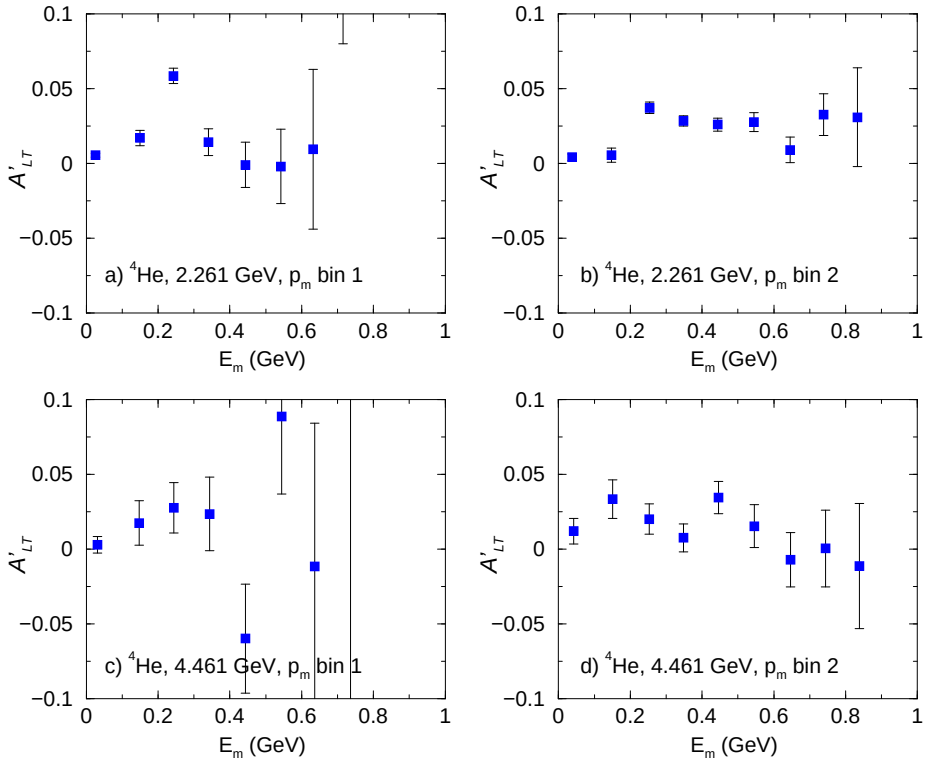


Figure 5-13: $A'_{LT}$ versus $E_m$ for helium. The two missing momentum bins are defined as follows: 1) $0.0 < p_m < 0.2$ and 2) $0.2 < p_m < 0.45$ with $p_m$ in GeV/c. No radiative corrections were applied. Errors shown are purely statistical.

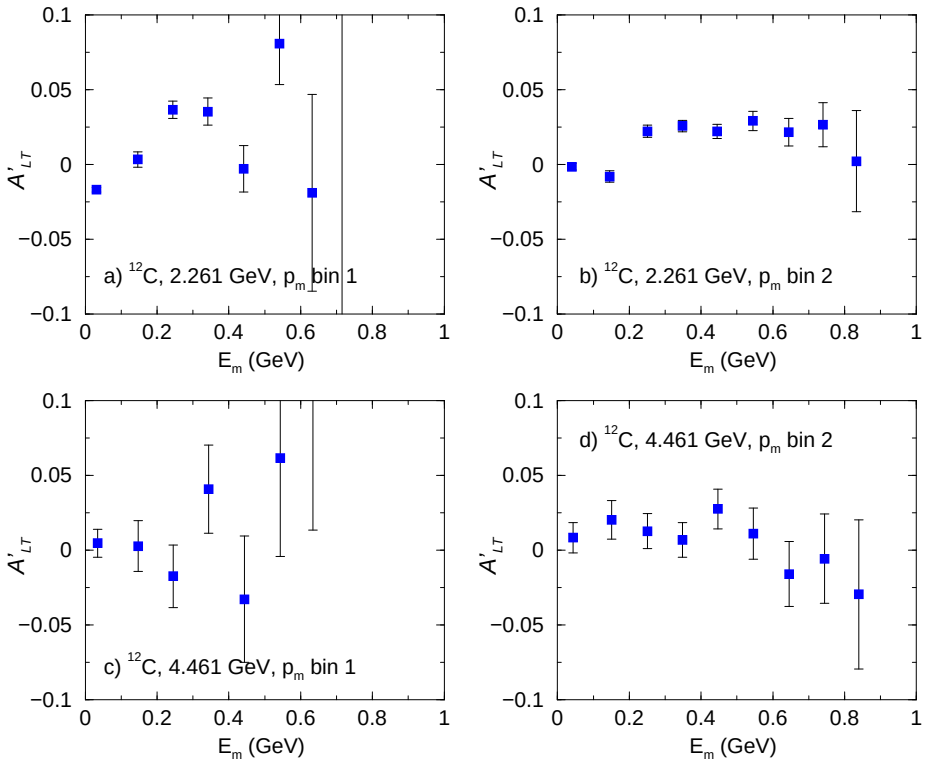


Figure 5-14: $A'_{LT}$ versus $E_m$ for carbon. The two missing momentum bins are defined as follows: 1) $0.0 < p_m < 0.2$ and 2) $0.2 < p_m < 0.45$ with $p_m$ in GeV/c. No radiative corrections were applied. Errors shown are purely statistical.

## 5.3 Summary

We have measured the $A'_{LT}$ asymmetry in quasielastic reactions on $^{12}$C and $^{4}$He in order to determine the contribution of final state interactions in the one-proton knockout reaction. The $A'_{LT}$ asymmetry arises as a result of the interference between the direct knock-out and the rescattering through FSI and therefore it is the most sensitive tool for their disentanglement.

Our measurements covered an unprecedented kinematic range, making use of the excellent capabilities of CLAS. The measurements covered a four-momentum range up to 2.4 GeV$^2$/c$^2$. The data acquired during the E2A were 310 million (M) triggers for $^{4}$He at 2.2 GeV beam energy and 442 M, 323 M, 346 M for $^{12}$C at 4.4 GeV, $^{4}$He at 2.2 GeV, $^{12}$C at 4.4 GeV, respectively. After event reconstruction, the statistics were 113 M events for $^{4}$He at 2.2 GeV beam energy and 102 M, 98 M and 66 M for $^{4}$He at 4.4 GeV, $^{12}$C at 2.2 GeV and 4.4 GeV, respectively. In the quasielastic regime the statistics used were 2.7 M for 2.2 GeV $^{4}$He and 0.3 M for 4.4 GeV helium, while for carbon they were 2.7 M and 0.25 M for 2.2 and 4.4 GeV beam energy, respectively.

To compare with theory, a total of 810 points were calculated for helium and 1100 for carbon. Our calculations were based on three models. The distorted wave impulse approximation (DWIA) [88, 53] and the optical potential in eikonal approximation (OMEA) model are based on optical potentials and their range of validity spans up to 0.300 GeV/c in missing momentum and up to 1 GeV$^2$/c$^2$ in $Q^2$. The relativistic multiple scattering Glauber approximation (RMSGA) is a high-$Q^2$ approximation valid for $Q^2 > 1$ GeV$^2$/c$^2$. The comparison of the theory with the data must be viewed in this context.

Let us summarize our findings:

1. Overall, the measured asymmetries in the quasielastic region were below 5%, typically in the range of 0-3% for data with good statistical uncertainties.

2. Large acceptance spectrometers like CLAS can extract good asymmetries as long as sufficient statistics are available

3. While areas of disagreement were observed, all models showed qualitative agreement with experiment. However, a detailed comparison with theory for $^{12}C$ would require separation of major shells, since they contribute with opposite sign to the asymmetry

4. Within the range of validity of the models and summing over the final states, we see no compelling evidence for exotic processes that would significantly modify the LT' interference.

Depending on the data set and the kinematics investigated, the measurements we made were characterized by statistical errors in the range of acceptable to large but with corresponding small systematic errors. This observation is an important point in assessing the potential of the technique for future measurements.

## 5.4 Outlook

In general, the inherent accuracy of the helicity asymmetry measurements and their insensitivity to mechanisms other than FSI make them a promising tool for evaluating rescattering effects consistently beyond the mean-field approach.

This survey demonstrates the feasibility of CLAS for these type of studies. Improvements in the event acquisition rate make it possible now to run at 4.4 kHz, compared with 2.2 kHz at the time of our experiment.

# List of References


[1] U. Amaldi *et al.* , Phys. Rev. Lett. **13**, 341 (1964)

[2] G. Campos Venuti *et al.* , Nucl. Phys., **A 205**, 628 (1973)

[3] K. Nakamura *et al.* , Nucl. Phys., **A 268**, 381 (1976)

[4] J. Mougey, *et al.* , Nucl. Phys., **A 262**, 461 (1976)

[5] S. Frullani and J. Mougey, Adv. Nucl. Phys. **14**, 1 (1984).

[6] P. K. A. de Witt Huberts, J. Phys., **G16**, 507 (1990)

[7] M. Leuschner *et al.* , Phys. Rev. **C49** 955 (1994)

[8] J. M. Finn, R. W. Lourie and B. H. Cottman, Phys. Rev. C **29**, 2230 (1984)

[9] R. W. Lourie *et al.* , Phys. Rev. Lett. **56**, 2364 (1986)

[10] P. Ulmer *et al.* , Phys. Rev. Lett. **59**, 2259 (1987)

[11] L. B. Weinstein *et al.* , Phys. Rev. Lett. **64**, 1646 (1990)

[12] M. Holtrop *et al.* , Phys. Rev. C **58**, 3205-3211 (1998)

[13] S. M. Dolfini, *et al.*, Phys. Rev. C, **60**(6), 064622, 1999; see also S. Dolfini, *et al.* , Phys. Rev. C, **51**, 3479 (1995)

[14] K. I. Blomqvist *et al.* , Phys. Lett., **B344**, 85 (1995)

[15] J. Gao, Phys. Rev. Lett. **84**, 3265 (2000)

[16] P. E. Ulmer *et al.* , nucl-ex/0111015, (2001)

[17] L. Lakehal-Ayat *et al.* , Nucl. Phys. A, **553**, 693 (1993)

[18] J. E. Ducret *et al.* , Nucl. Phys. A, **553**, 697 (1993)

[19] this is similar with what has been seen in inclusive scattering e.g. [8] or A.Zghiche *et al.* , Nucl. Phys. **A 572**, 513 (1994); *ibid.* **A 584**, 757 (1995)

[20] W. Bertozzi, Nucl. Phys. **A527** (1991) 347c-356c

[21] G. Co, A. M. Lallena and T. W. Donnelly, Nucl. Phys. **A469**, 684 (1987)

[22] Boffi, S., Giusti, C., Pacati, F. D., Nucl. Phys. **A435**, 697 (1985)

[23] Boffi, S., Giusti, C., Pacati, F. D., Radici, M., *Electromagnetic Response of Atomic Nuclei*, Oxford University Press, 1996

[24] D. Debruyne, Ph.D. thesis

[25] J. Mandeville, *et al.* , Phys. Rev. Lett., **72** 3325 (1994); see also [13]

[26] X. Jiang, Ph.D. Thesis, unpublished

[27] A. Dellafiore, F. Matera and M. Traini, Phys. Rev. C **43**, 2453

[28] J.-M. Laget, Phys. Rev. **C35** N2, 832 (1987)

[29] J.-M. Laget, Nucl. Phys. **A579**, 333 (1994)

[30] R. R. Whitney *et al.* , Phys. Rev. C **9**, 2230 (1974)

[31] H. Arenhövel, W. Leidman, L. Tomusiak, Phys. Rev. C **46**, 455 (1992)

[32] W. Fabian and H. Arenhövel, Nucl. Phys. **A314**, 253 (1979)

[33] J. M. Laget, Can. J. Phys., **62**, 1046 (1984)

[34] R. E. J. Florizone, Ph.D. Thesis, Feb 1999

[35] Acronym for Hartree-Fock random phase approximation, see [36] and references therein

[36] J. Ryckebusch *et al.* , Phys. Rev. C, **49**, 2704 (1994)

[37] A. Bianconi, S. Jeschonnek, N. N. Nikolaev, B. G. Zakharov Nucl. Phys. **A608** (1996) 437-468; Erratum-ibid. **A616** (1997) 680-686

[38] M. Kaku, *Quantum Field Theory*, Oxford University Press, 1993

[39] T. W. Donnelly and A. S. Raskin, Ann. Phys. 169 (**2**), 1986

[40] A. S. Raskin and T. W. Donnelly, Ann. Phys. (N.Y.) 191 (**1**), 1989

[41] R. Glauber and G. Matthiae, Nucl. Phys. B **21**, 135 (1970)

[42] G. Alkhazov, S. Belostotsky and A. Voroboyov, Phys. Rep. **42**, 135, (1978)

[43] S. Jeschonnek and T. Donnelly, Phys. Rev. C **59**, 2676, (1999)

[44] D. Debruyne, J. Ryckebusch, S. Janssen and T. Van Cauteren, Phys. Lett. **B527** (2002), 62-68.

[45] S. Dietrich *et al.* PLB **500** (2001) 47; MIT-Bates data: Phys. Rev. Lett. **80** (1998) 456; TJNAF, Hall A data: Phys. Rev. Lett. **84** (2000) 3265 and Phys. Rev. C **62** (2000) 057302

[46] R. Glauber, In *Lectures in Theoretical Physics* , vol. 1,
(ed. W. Brittain and L. G. Dunham), 315, Interscience, NY

[47] Y. Yin, D. Onley and L. Wright, Phys. Rev. C **45**, 1311 (1992); J. Udias, P. Sarriguren, E. Moya de Guerra, E. Garrido and J. Caballero, Phys. Rev. C **48**, 2731 (1993)

[48] E. Cooper, S. Hama, B. Clarck and R. Mercer, Phys. Rev. C **47**, 297 (1993)

[49] T. de Forest, Jr., Nucl. Phys. A, **392**, 232 (1983)

[50] J. Walecka, Ann. Phys. **83**, 471 (1974)

[51] D. Debruyne and J. Ryckebusch, Nuclear Physics A **699** (2002), 65-72

[52] N. Liyanage *et al.* , Phys. Rev. Lett. **86**, 5670 (2001)

[53] J. J. Kelly, Phys. Rev. C **60**, 044609 (1999)

[54] J. Ryckebusch *et al.* , Nucl. Phys. **A476**, 237 (1988) and **A503**, 694 (1989)

[55] J. M. Udias *et al.* , Phys. Rev. Lett. **83**, 5451 (1999)

[56] J. Kelly, UMd, MIT-Bates communication

[57] P. Schwandt *et al.* , Phys. Rev. C **26**, 55 (1982)

[58] J. R. Comfort and B. C. Karp, Phys. Rev. C **21**, 2162 (1980)

[59] D. F. Jackson and I. Abdul-Jalil, J. Phys. G **6**, 481 (1980)

[60] M. M. Giannini and G. Ricco, Ann. Phys. (N.Y.) **102**, 458 (1976)

[61] W. Brooks, Nucl. Phys. A, **663-664**, 1077, 2000

[62] CLAS conceptual design specifications, 1990

[63] M. D. Mestayer, *et al.*, Nucl. Instr. Meth., **A449**, 81, 2000

[64] E. S. Smith *et al.*, Nucl. Instr. Meth., **A432**, 265, 1999

[65] G. Adams *et al.*, Nucl. Instr. Meth., **A465**, 414, 2001

[66] M. Amarian *et al.*, Nucl. Instr. Meth., **A460**, 460, 2001

[67] N. Dashyan, private communication

[68] V. Blobel and the CLAS Software Group, "The BOS System for CLAS Software", Nov 25, 1995

[69] J. J. Manak, E.S.Smits, S.McAleer, S.Barrow, Jlab CLAS-NOTE 1999-016

[70] DC Calibration, R. Niyazov, Ph.D. Thesis, ODU, 2002

[71] EC Calibration, B. Zhang, Ph.D. thesis, MIT, 2002

[72] A. V. Vlassov, V. A. Serov, A. V. Stavinsky, Jlab CLAS-NOTE 1999-005, 1999

[73] E.S. Smith *et al.* , Jlab CLAS-NOTE 1999-011

[74] H. Egiyan, Ph.D. thesis, W&M, 2001

[75] L. Elouadrhiri, V.Burkhert, S.Stepanyan, K.Egiyan, Jlab CLAS-NOTE 1998-004

[76] S. Taylor, Ph.D. thesis

[77] D. Lawrence, M. Mestayer, JLab CLAS-NOTE 1999-018

[78] K. Egiyan *et al.* , CLAS-NOTE 2001-011

[79] K. Egiyan, CLAS-NOTE 1999-007

[80] V. Burkhert, private communication

[81] D. Protopopescu *et al.* , Jlab CLAS-NOTE 2001-008, 2001

[82] D. Protopopescu *et al.* , Jlab CLAS-NOTE 2000-007, 2000

[83] B. Zhang, private communication

[84] M. Anghinolfi *et al.* , JLab CLAS-NOTE 2001-020

[85] R. A. Schumacher, CMU, private communication

[86] L. Kramer *et al.* , Jlab CLAS-NOTE 2001-012

[87] S. Stepanyan *et al.* , JLab CLAS-NOTE 2001-006

[88] J. J. Kelly, Adv. Nucl. Phys. **23**, 75 (1996)

[89] J. Kelly, UMd, Private communication

[90] C. Horowitz and B. Serot, Nucl. Phys. **A368**, 503 (1981)

[91] B. Serot and J. Walecka, Adv. Nucl. Phys. 191, 1 (1986)

[92] M. M. Sharma, M. A. Nagarajan and P. Ring, Phys. Rev. Lett. **B312**, 377 (1993)

[93] S.Stepanyan, private communication

[94] K. Joo, private communication

[95] V. Chudakov, private communication

[96] A.P. Freyberger, private communication

[97] C.K.Sinclair, TJNAF-TN-97-021, see also [111]

## WWW-Based References

[98] DC construction, http://www.physics.odu.edu/htmlstuf/docs/dccon.htm

[99] E2AnaTool Package, Jlab software repository

[100] The ROOT System Homepage, http://root.cern.ch/

[101] A. Vlassov, CC calibration, http://www.jlab.org/~vlassov/cc/index.html

[102] The MINUIT Reference Manual,
http://wwwinfo.cern.ch/asdoc/minuit/minmain.html

[103] D.Protopopescu, Fiducial Cuts for CLAS at 4.4 GeV
http://einstein.unh.edu/protopop/FiducialCuts/fc4E2.html

[104] D.Protopopescu, C++ code bank, available on web at
http://einstein.unh.edu/protopop/cpp_codes.dir/cpp4E2.html

[105] D.Protopopescu, Electron Momentum Corrections for CLAS at 4.4 GeV,
http://einstein.unh.edu/protopop/MomentumCorrections/emc4E2.html

[106] E. Burtin, HAPPEX experiment description,
http://spin.ihep.su/spin98/papers/burtin.ps.gz

[107] Hall B electronic logbook, online at:
http://clasweb.jlab.org/clasonline/logbooksearch.html

[108] List of e2a Møller Runs,
http://einstein.unh.edu/protopop/Asymm/moller.html

[109] Experiment Schedule 1999,
http://www.jlab.org/exp_prog/experiment_schedule/

[110] S. Stepanyan, Simple Event Builder in RECSIS, JLab software repository

[111] The Spin Rotation Calculator, on the web at:
http://claspc10.jlab.org/spin_rotation/spin_rotation.pl
This page lists $\theta_W$ in degrees but the total precession angles in units of $\pi$.

[112] M. Holtrop, E2AnaTool software package, JLab software repository

# Appendix A

## ELECTRON MOMENTUM CORRECTIONS FOR 4.4 GeV DATA

Our lack of knowledge regarding the details of magnetic field mapping in the CLAS detector will influence the exactness of our measurements of the momentum vector. What one can do, using as a reference some well known process, is to introduce a function that will correct the momentum as a function of its orientation (one choice).

For this, it is handy to use a simple and well known interaction: elastic scattering of $e^-$ on H. This analysis presented in this material is done on E1 $H_2$ data at 4.4 GeV, at a torus current of 2250 A. From the whole invariant mass spectrum, we select the W range from 0.80 to 1.05 GeV, which corresponds to the elastic peak (see Fig.A-2). We discard data with $\theta < 16^o$. This selection leaves us with approximately 5% of the total number of events in the rootDST file. We make the assumption that the corrections derived in the elastic region will hold for the whole spectrum.

### A.1 METHOD

In general there is no consensus on the expression that the correction function should have. It clearly will depend on the absolute value $p$ of the momentum of the electron as well as on its angles $\theta$ and $\phi$, and we expect variations from sector to sector. The generic expression is then:

$$\mathbf{p}_{corr} = f(p, \theta, \phi, s) \tag{A.1}$$

where $p_{corr}$ will be the 'real' value, and $s$ indicates the sector.

Since the main uncertainties are due to the distribution of the torus field and angles mainly defined by DC geometry, we assume that the angles are measured correctly and the value of the momentum needs to be corrected. This is to say that eq.(A.1) may be written as:

$$p_{corr} = p \cdot \chi(\theta, \phi, s) \tag{A.2}$$

The geometry of the detector implies a certain correlation between the range of $\phi$ angle and the $\theta$ of a detected particle. At large $\theta$ values, the $\phi$ range is large and most of the particles are far from the edges of the fiducial region, while at small $\theta$, where the $\phi$ range is quite small, the influence of the vicinity of the coils is more significant (see figures A-3 and A-4). But the amount of this effect will be almost completely eliminated by the fiducial cuts.

In a good approximation, then, we can assume that the correction function $\chi$ from eq.(A.2) can be factorized as:

$$\chi(\theta, \phi, s) = f_2(\theta, s) \cdot f_1(\phi, s) \tag{A.3}$$

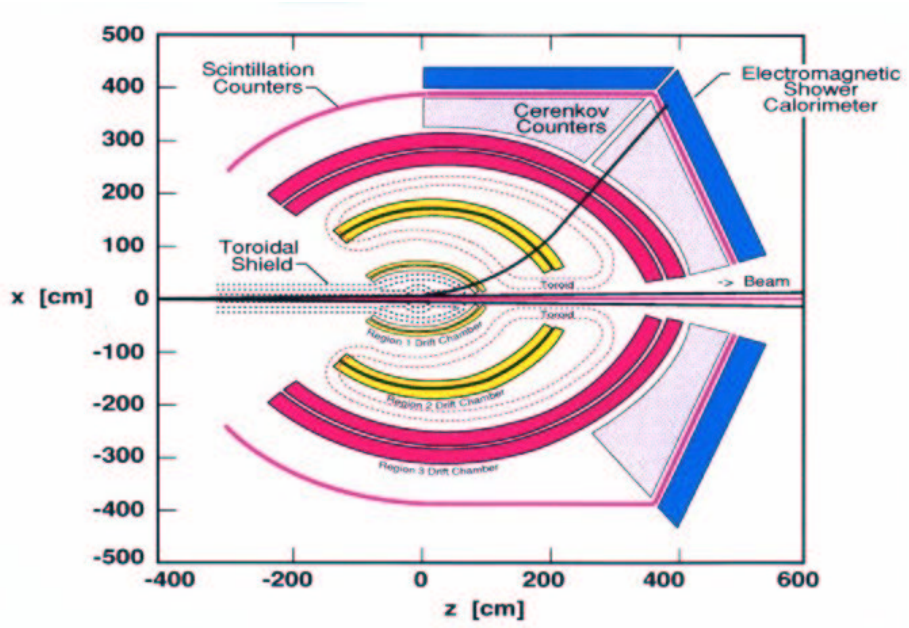


Figure A-1: Trajectory of an electron in CLAS.

where $f_1$ and $f_2$ are different functions for each sector $s$.

In this case, the procedure is simple: we correct the $\phi$ dependence, insert it into the code, and with it derive the $\theta$ correction functions. The overall correction function $\chi$ will be the product of the two.

## A.2 Correction Function

The correction functions are simply the ratio between the calculated modulus of the electron momentum $p_{calc}$ and the measured one $p_{exp}$, for each sector.

$$f_i(\alpha_i, s) = \frac{p_{calc}(\alpha_i, s)}{p_{exp}} \qquad \alpha_1 = \phi, \quad \alpha_2 = \theta \tag{A.4}$$

For the elastic scattering of electron we can approximate successfully:

$$p_{calc} = \frac{E_{beam}}{1 + E_{beam}(1 - \cos\theta)/m_p} \tag{A.5}$$

where $E_{beam} = 4.4$ GeV is the beam energy (we assume that this is accurately measured), and $m_p$ is the mass of the proton. The formula (A.5) contains no $\phi$ terms, and therefore we calculate $f_1$ based on the assumption of isotropy in $\phi$.

We plot then the ratio $f_1$ from (A.4) versus $\phi$ for each sector (please see the example in Fig.A-5). Obtained two-dimensional histograms, like the one in Fig.A-5.a, are sliced along $\phi$, each slice fitted with a Gaussian and the mean values plotted again versus $\phi$. The graph

in Fig.A-5.b shows the fit to the centroids of the Gaussians with a polynomial function. Then polynomial function is used as a correction function $f_1(\phi, s)$. In figure A.7(a) one can see how the position and width of the elastic peak in W is changed (compare with Fig.A-2).

After the $\phi$ correction is done, the same procedure is repeated for parameterizing $f_2(\theta)$. The algebraic functions that we found the most suitable (see figures A-5 and A-6) are:

$$f_1(\phi, s) = P_2(\phi, s) \quad (A.6)$$

$$f_2(\theta, s) = a_s + P_2(\theta, s) \cdot e^{-\theta} \quad (A.7)$$

where $P_2$ is a second degree polynomial and $a_s$ is a fit parameter. One notices that we tried to limit ourselves to the simplest functions. The correction in $\phi$ is a parabola, and we found that it fits very well the points in Fig.A-5.b within the region of interest. If at the extremities it goes wrong, it does not affect the final result because these regions will be cut out anyway when the fiducial cuts are applied.

The correction in $\theta$ is a little more complicated (eq.A.7). At larger $\theta$ angles $f_2(\theta)$ reaches a plateau. Therefore, we insert the offset $a_s$ and the inverse exponential function $e^{-\theta}$, with which we force the polynomial into a flat horizontal curve in this region (that will be approximately above $25^o$, as seen in figure A-6.b). Since we are not interested in what happens below $\theta = 16^o$, the continuation of the functions in this region is not guaranteed to hold.

As one may have noticed, not all the details of these plots have been fitted. What we intended to correct is the general trend and this is successfully accomplished with both $\theta$ and $\phi$.

The number of the resulting parameters is $6 \times (4+3) = 42$. The parameters of correction functions go into the file `EMCP_4GeV.par` that is read by **SetMomCorrParameters()** included in the **TE2AnaTool** package.

In Fig.A.7(b) you can see the final aspect of the elastic peak in W (the peak, ideally, should be centered at 0.9382 GeV/c$^2$, corresponding to the mass of proton $m_p$). Assuming that the resolution scales with the magnetic field, one expects from other such calibrations (e.g. E1 experiment) that a resolution between 19.6 and 24.0 MeV/c$^2$ is feasible. We get here an overall $\sigma = 20.3$ MeV/c$^2$.

A look at the energy spectra of the electrons in Fig.A-8 shows good agreement with the conclusions drawn in [103]. As we see in this figure, the shape of the distribution is not changed much by the momentum corrections, except the high energy/small $\theta$ region. This is due to the extremities of the fit curves as discussed above. Once we discard data below $\theta = 16^o$, the unphysical points vanish and the curve agrees with the one dictated by the fiducial cuts (see [ref.2]).

## A.3 Summary

We made the important assumption that the correction function can be factorized in a $\phi$- and a $\theta$-dependent part. We chose to correct the modulus rather than the orientation of the electron momentum vector. First the $\phi$ dependence is corrected, then included into the code, then used to derive the $\theta$-dependent correction. The corrected momentum vector preserves the angles from the EVNT bank but has the modulus modified by formula (A.2).

More detailed information about the procedure as well as for the codes used to derive these results, the reader is advised to consult the extensive documentation available on web in [105].

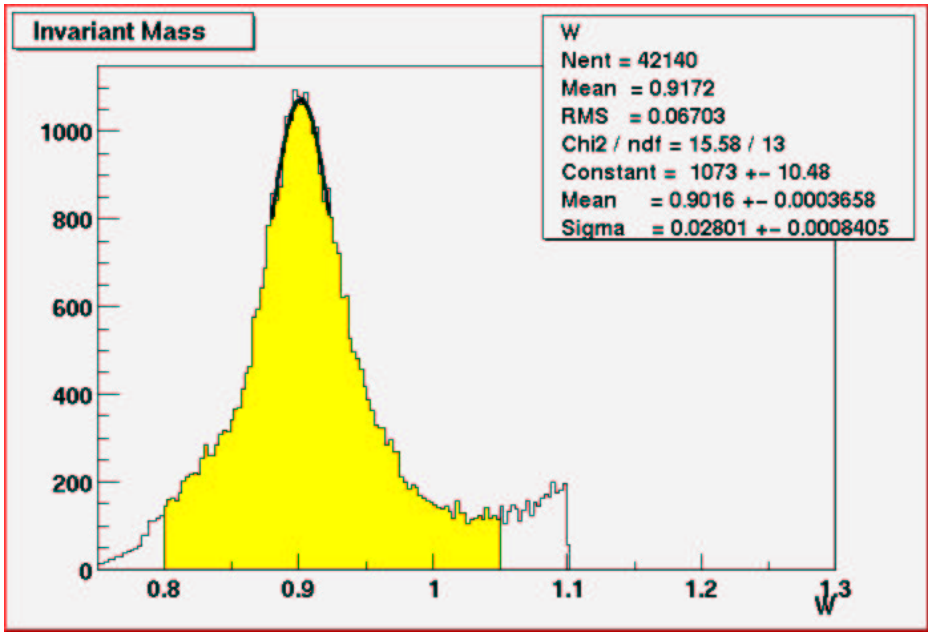


Figure A-2: The elastic peak in W before applying any corrections. All sectors together.

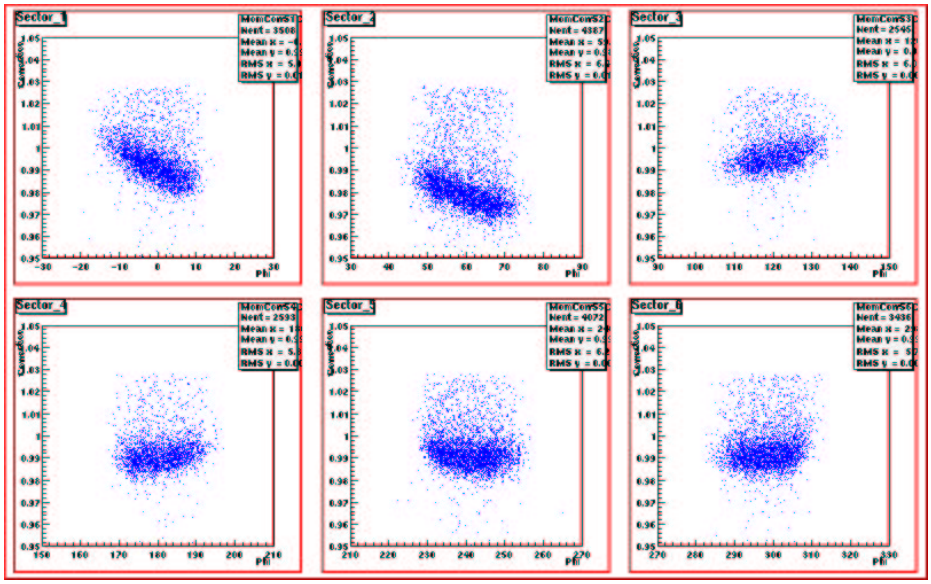


(a)

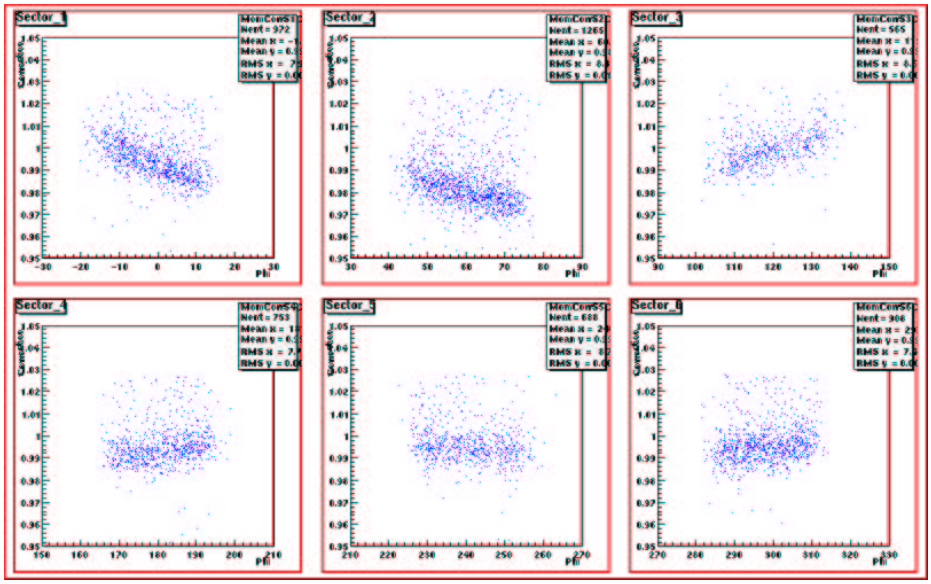


(b)

Figure A-3: Plots of the correction $f_1$ versus the angle $\phi$ for different $\theta$ intervals: $16^o < \theta < 20^o$ (a), $20^o < \theta \leq 25^o$ (b).

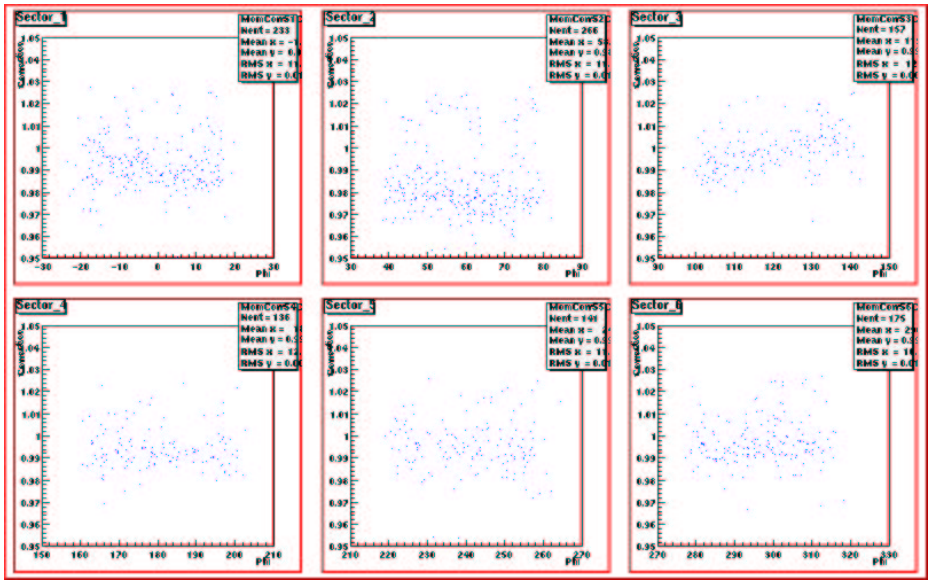


(a)

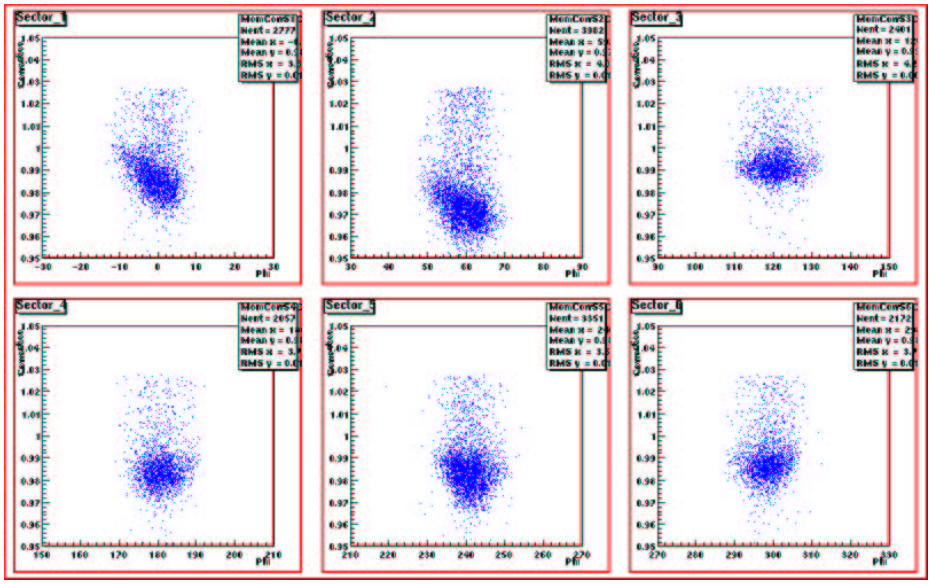


(b)

Figure A-4: Plots of the correction $f_1$ versus the angle $\phi$ for two other $\theta$ intervals: $theta > 25^o$ (a) and $\theta \leq 16^o$ (b).

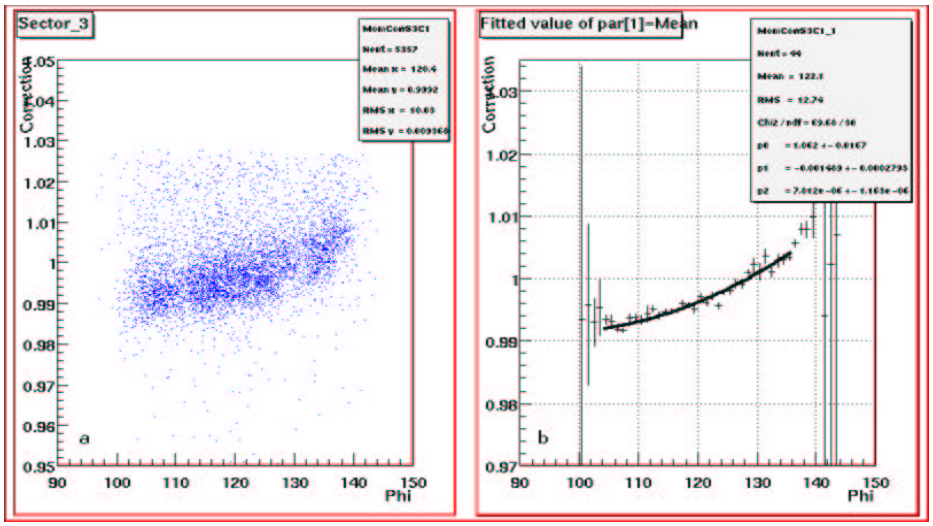


Figure A-5: Plots of the correction $f_1$ versus the angle $\phi$ for $\theta > 16^o$: a 2D Histogram (left) is sliced and fitted (right). Only sector 3 is shown. For the other five plots, please see [105]

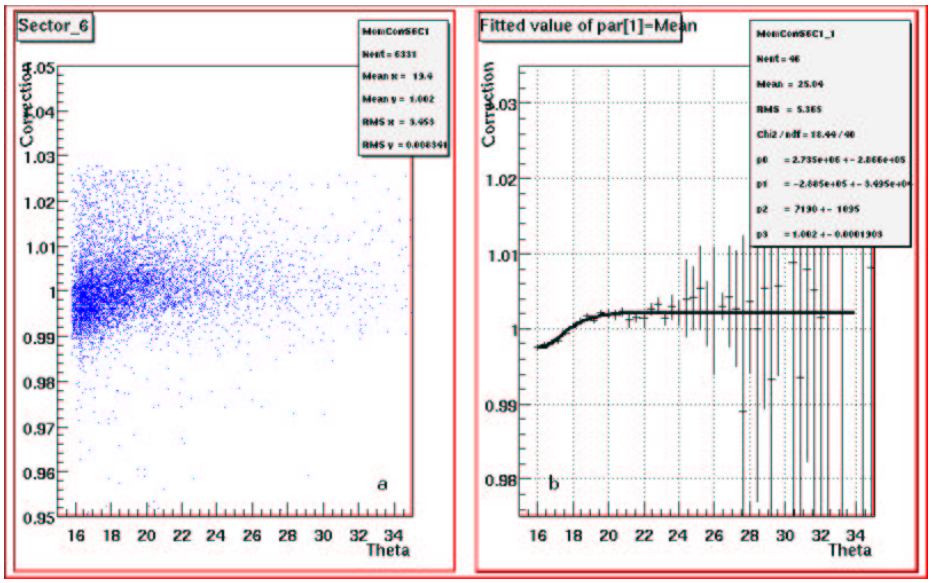


Figure A-6: Plot of the correction $f_2$ versus the angle $\theta$ (left) and the fit with the function from eq.(A.7) (right). Only sector 6 is shown. For the others, please consult [105].

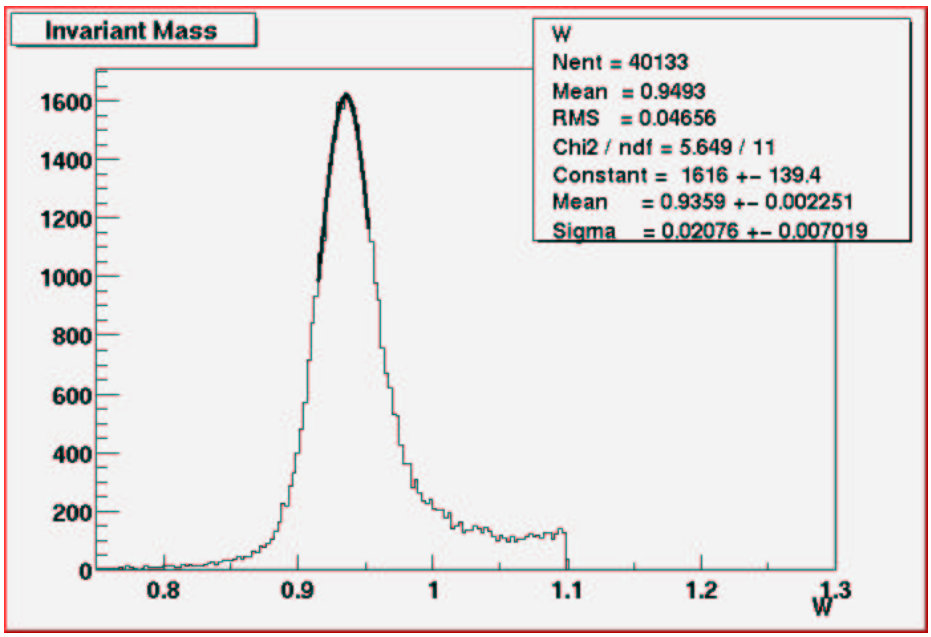


(a)

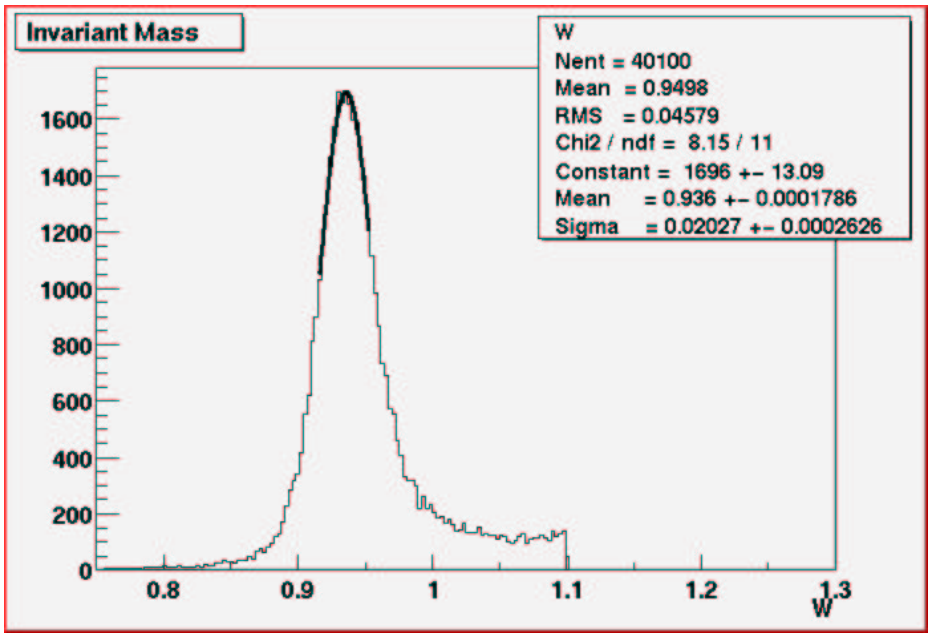


(b)

Figure A-7: The elastic peak in W (a) after $\phi$-corrections were applied. All sectors. The width decreases to 21 MeV and the mean value shifts to 0.936 MeV/$c^2$.(b) when all corrections are done: the peak is now even sharper.

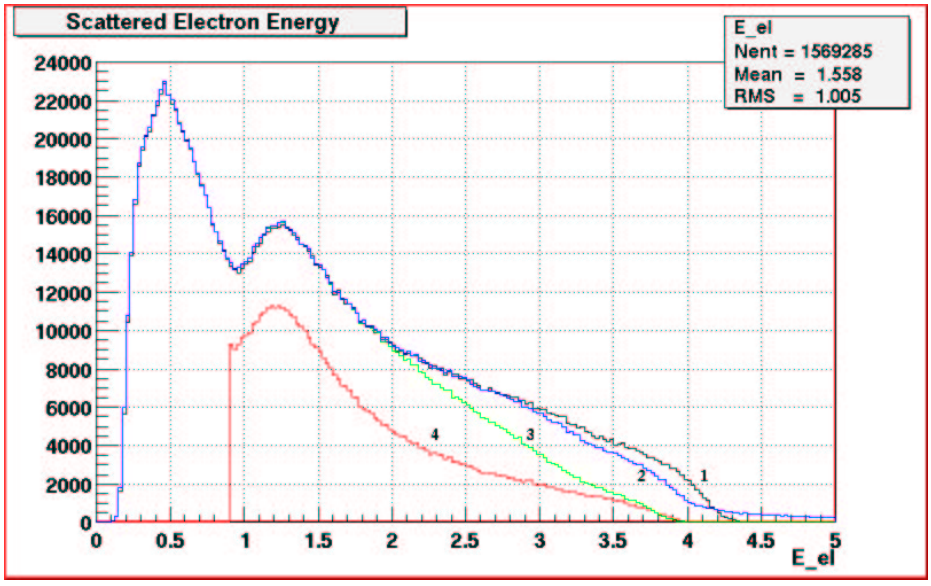


Figure A-8: The aspect of the energy spectrum before (1) after the corrections (2), with the events below $\theta = 16^o$ discarded (3) and with the fiducial cuts applied (4). The unphysical tail in (2) vanishes when the erroneous events are discarded. Notice the agreement with the fiducial cuts.

# Appendix B

## ELECTRON FIDUCIAL CUTS FOR 4.4 GeV DATA

### B.1 Introduction

In electron scattering experiments with CLAS, the recorded event is accepted for physics analysis if the scattered electron is identified. For electron identification, in most cases, valid signals in all four detectors are required. Electron detection efficiency around the mid plane in each sector is reproducible in the GEANT (GSIM) simulations. Due to the complicated readout structures of EC and CC, detection and reconstruction efficiencies are not well understood in the regions close to the torus coils, and close to the dead channels of detector elements. In order to minimize systematic uncertainties in the physics analysis it is important to accept events in the fiducial region of the detector, where efficiencies are understood.

Fiducial cuts for electrons in *ep* scattering experiments were derived earlier by V.Burkert *et. al.* [80] for the CLAS/E1 runs. These cuts define a region in the production ($\theta$, $\phi$) space for a given momentum, where detection efficiency is almost constant on $\phi$ and can be reproduced in simulations. Although these functions should, in principle, scale with momentum and the magnetic field, it is not always possible to use the same function due to different run conditions (bad channels, target position, trigger, etc.).

Data taken at beam energy $E_o$ = 4.4 GeV during the CLAS/E2 run do not have Čerenkov counters in the Level 1 trigger of the CLAS DAQ. The main motivation for excluding CC from the trigger is that a lot of E2-related physics proposals are focused around the kinematics of quasi-elastic, dip and $\Delta$ production regions, starting from momentum transfer $Q^2$ as low as possible. Scattered electron momentum in these conditions is generally above the pion threshold in CC, and $e/\pi$ rejection relies on forward electromagnetic calorimeters only. Excluding CC cut from electron identification makes the fiducial region very different from the previously defined region for E1. In this report we describe the procedure for electron selection and determination of the fiducial volume of the detector without Čerenkov counters.

To derive the fiducial cuts shown here, $^4$He data has been used. Due to different position along the beamline, when applied to solid target data, these cuts will be a bit too tight.

### B.2 Our Method

We define a "cut" as a two-dimensional doubly-curved surface passing through the three-dimensional $(p, \theta, \phi)$ space, enveloping the region that satisfies certain selection criteria. In our case, as we stated above, the criterion would be "uniform acceptance". We define apriori our "uniform acceptance" plateau as the region contained between the steep rise and the sudden drop on a counts vs. $\phi$ histogram drawn at given p and $\theta$".

To determine the equation of the cut surface, we do the following:

**1.** select "good" electrons with cuts on the forward electromagnetic calorimeter (EC)

**2.** select the flat acceptance regions for small bins of momenta in the $\theta$ and $\phi$ space.

**3.** fit the final coefficients with smooth functions of ($p$, $\theta$ and $\phi$).

As a note to the reader: frequent references in this text point towards the web-based documentation ([103] and [104]). The website contains complete documentation, programs and *all* the graphics to illustrate the procedure. Some file names are given in the text in the event that the reader would like to customize our codes and procedure for his(hers) fiducial cuts.

## B.3 Step One: Forward Calorimeter Cut

As was mentioned above only forward EC information will be used for electron identification. Since the ratio of the deposited energy in EC to the momentum of the particle measured in DC ($E_{EC}/p$) is the main tool for $\pi/e$ rejection, we will define the fiducial region as *a region where the electron distribution is constant on $\phi$ after the cut on deposited energy.* Consequently, regions where due to shower leakage measured energy is less than it should be are eliminated. (There are other cuts that will be used for final electron selection, like energy depositions in the inner and outer parts of EC, or the width of a shower. These quantities remain stable in the fiducial region defined above.)

The scintillators in the forward electromagnetic calorimeter are grouped in three planes, denoted as U, V and W. The scintillator bars in the U plane have an orientation perpendicular to the beam axis, while the scintillators in the V and W planes are rotated by $120^o$. In Fig.B.1(a) the distribution of electrons on the calorimeter sides is shown. This defines a natural system of coordinates that is the most convenient to use for defining geometrical cuts.

It is useful to study the variation of the ratio $E_{EC}/p$ versus calorimeter coordinates. Such a plot is shown in Fig.B.1(b), with $p > 0.9$ GeV. Plots for certain energy subranges are available for reference in [103].

As a first step electrons with $E_{EC}/p \geq 0.2$ will be selected (see Fig.B.1(b)). In Fig.B-3 a magnified plot of the above mentioned distribution is shown. For clarity, only electrons with momentum $p > 3.0$ GeV are kept here, given that electrons with momentum in this range are detected mainly at forward angles, and are more sensitive to our $uvw$ cut.

It is seen that in the regions $v \geq 371$ and $w \geq 407$, the ratio $E_{EC}/p$ drops dramatically. This is due to the electron shower leakage out of the sides of the calorimeter. Similar plots had been made for individual sectors and they are available in [103]. Cuts on the edges $u > 20$ cm, $v < 371$ cm and $w < 407$ cm were applied to select events with $E_{EC}/p > 0.2$ GeV. (It was concluded that using different cuts for each sector was not necessary.) Figure B-4 shows such a cut ($u > 20, v < 371, w < 407$ and $E_{EC}/p > 0.2$).

We have studied the behavior of the $E_{in}/E_{out}$ ratio versus the EC coordinates (with $E_{in}$, $E_{out}$ being the energy loss in the inner and the outer parts of the EC, respectively). But, as it can be found in [103], these quantities do not depend on the position on EC, after the above cuts.

Our final criteria for the preparatory cuts would then be:

$$u > 20, v < 371, w < 407, E_{EC}/p > 0.2 \tag{B.1}$$

Figure B-5 illustrates how this $uvw$ cut reflects onto the energy spectrum of the electrons that we detect.

The conditions in equation (B.1) are imposed on the data used to derive the fiducial cut, to select a set of well identified electrons. They will not explicitly show in the final cut, which is purely geometrical. Also, in the physics analysis, data below 0.9 GeV and $16^o$ in $\theta$ will be discarded, since this is below the trigger threshold and is clearly outside of the acceptance region of CLAS.

## B.4 Step Two: Finding the Uniform Acceptance Region

After we have selected "good" electrons, as described in the previous section, we proceed to study the dependence of the detector acceptance on angles and energy.

Figure B-6 shows some typical $(\phi, \theta)$ plots after the forward calorimeter cut has been applied.

The energy range was divided in small bins and then for each energy bin and for each sector two-dimensional distribution of events in $\theta$ and $\phi$ plane is studied. In figure B-7 a number of such distributions are presented. Regions with black points were cut out with cuts described above. The energy bin width is set to 100MeV. The energy bin $n$ is defined as the range between $0.1 \times n$ and $0.1 \times (n+1)$ GeV.

The histograms in Fig.B-6 exhibit a well contoured semicircular region, surrounded by a fuzzy region. We want to select this solid area of the histogram, which is the flat acceptance region, and discard the blurred area surrounding it. For this, we will fit its contour with a function $\phi(\theta, E_n, s)$, where $E_n$ is the energy bin, $s$ the sector and $\theta$ the angle.

Of course, before this, one needs to accurately define what means "flat". For this purpose, what we do is slice these two-dimensional plots in theta bins[1] of $1^o$, and fit these histograms with a trapezoidal function.

The function used is:

$$y = \begin{cases} p_4(x - p_2)/(p_0 - p_2) & \text{if} \quad p_2 \le x < p_0 \\ p_4 & \text{if} \quad p_0 \le x \le p_1 \\ p_4(x - p_3)/(p_1 - p_3) & \text{if} \quad p_1 < x \le p_3 \\ 0 & \text{if} \quad x < p_2 \quad \text{or} \quad x > p_3 \end{cases} \tag{B.2}$$

Some typical trapezoids (fitted $\theta$-slices) are shown in Fig.B-8. More can be found in [103]. Now, on these plots, the top horizontal side of the trapezoid is our "flat" acceptance region.

We found the procedure to give us reliable results in over 90% of the fits. The procedure is automatic and the code used (`concat.cc`) can be found in [104]. The few bad fits that occurred were not corrected manually, because the results (parameters) of these first

[1] bin $n$ is from $n$ degrees ($^o$) to $(n+1)$ degrees

generation fits are fitted as a function of $\theta$ afterwards. This way, both statistical and procedural errors are automatically minimized.

The coordinates of the edges of the top of the trapezoid, for each energy bin and sector are written to a file named `fiducial_00.dat`. This is a text file organized on six columns, each row containing the following: a version stamp, the energy bin number, $\theta$ bin, sector number, $p_0$ and $p_1$, where parameters $p_0$ and $p_1$ are the coordinates of the edges of the top of the trapezoid (see Fig.B-8).

We use another code (`fcfit.cc`[104]) to fit these points with a function $\phi = \phi(\theta, E_n, s)$, for every energy bin and sector. The procedure is completely automatic.

The function $\phi = \phi(\theta, E_n, s)$ that most accurately describes the contours in Fig.B-6 is [83]:

$$\phi(\theta) = \begin{cases} b(1 - ((\theta - t_0)a/b + 1)^{-1}) & \text{if} t_0 < \theta < t_1 \\ 0 & \text{otherwise} \end{cases} \tag{B.3}$$

where the coefficients $a, b, t_i$ contain the dependency on $E_n$ and $s$. The actual angle $\phi$ is obtained by scaling this formula for each sector:

$$f_{0,1}(\theta, E_n, s) = 60(s - 1) \mp \phi(\theta) \tag{B.4}$$

where the sign $+$ stays for the upper branch (with coefficients $a_1, b_1, t_0, t_1$) and the '$-$' sign is for the lower (described by $a_0, b_0, t_0, t_1$).

A plot illustrating this step is in Fig.B-9. These second generation set of parameters are saved into the file `fiducial_01.dat`, which is organized as follows: each row contains a version stamp, energy bin number, the limits $t_0$ and $t_1$ and the $a_0, b_0$, $a_1, b_1$ curvature and width parameters for the lower and upper halves, respectively (please see equations (B.3) and (B.4) and Fig.B-9).

## B.5 Step Three: Smooth It

What is new in the present procedure of deriving the fiducial cuts is that we did not limit ourselves to obtaining a set of empirical values but we tried to find a systematics that would give us a consistent set of parameters.

We have obtained 62 different 4-parameter functions $\phi = \phi(\theta, s)$, one for each sector and energy bin considered. Next, we want to fit the coefficients of these functions in order to obtain a smooth function $\phi = f_{0,1}(\theta, E, s)$ that is to be included in our TE2AnaTool package for current use in analysis. For this, we have another code, `fc2fit.cc [104]`, that reads the output tables of the previous step to produce the final parameter file.

We remind the reader that the function in equation (B.3) is used to define the acceptable angular range $(\phi, \theta)$ for the detected electron. In the present approach, we did not require that the accepted region is symmetric with respect to the mid-plane of the sector, so we have two sets of parameters $a, b$ for each energy bin and sector (upper and lower halves in Fig.B-9).

One believes that the first two parameters, $t_0$ and $t_1$, should reflect the geometry of the detection system. The parameters $a$ and $b$ are related to the range in $\phi$ that is acceptable for defined values of $\theta$, i.e. to the geometry of our detector. Thus, we expect that the

variation of these coefficients with the energy $E$ must be smooth. In figure B-10, one finds evidence that these dependencies can be described by smooth functions.

The fitting procedure that gives us the final set of parameters $t_0, t_1, a_0, b_0, a_1$ and $b_1$ is completely automatic. To describe the energy dependence of $t_0$ and $t_1$ we use a power function:

$$t_i = c_{1i} E^{c_{2i}} \qquad i = 0, 1 \tag{B.5}$$

and for the other four parameters a polynomial function of degree five:

$$P_5(E) = \sum_{n=0}^{5} c_n E^n \tag{B.6}$$

However, in the final version of the code, there is a switch that one can use to set always the lower limit for $t_1$ at $45^o$, which is actually the hardware limit on $\theta$ in the EC for straight tracks.

The third generation parameters all go into a file named: `fiducial_02.par`, that is read at initialization by the routine **SetFiducialCutParameters()**, included in the **TE2AnaTool** package. This file is organized on eight columns: first is a tag, second is the sector number, and the next six are the coefficients of the functions in equations (B.5)[2] and (B.6).

Figure B-11 shows the overall result of the fiducial cut as made by using the final version of the routine. Please notice the narrowing in the forward region.

In some sectors (see Fig.B-11), we notice some small gaps. These are better corrected for in a separate procedure that eliminates faulty scintillators and bad DC regions, therefore, the present version of fiducial cuts procedure does not contain this feature. Figure B-12 shows some energy bins after the fiducial cut.

It is interesting to see the energy distribution of the scattered electron after these cuts. Figure B-13 compares the shape of the distributions at various stages of our procedure. Let us take a look at it: we lose quite a lot of data with the *uvw* cut, but, again, this is "bad" data. The $E_{EC}/p$ condition cuts out even more, but we see that it doesn't bias the final distribution.

We notice a disproportionate loss of high energy electrons that is explained by the forward peaking of the high energy electrons, at angles where the CLAS acceptance is small, not flat and hence cut out by the fiducial cuts. Therefore, we would need more detailed methods for obtaining our acceptance function at energies above 3.5 GeV.

## B.6 Summary

We prepared the terrain with the forward calorimeter cut, eliminating by this the electrons that were not properly detected. We split the angle-energy range in small bins and find the contour of the region of interest, that is *the constant acceptance* plateau. We get from this a set of curves. What is inside the contour passes as OK, what is out is discarded.

[2] obviously, only two of the rows corresponding to the power functions contain nonzero values

Further, we wanted to eliminate the constraint of a fixed bin width, which is not very convenient if we want to ensure flexibility of the analysis software. Hence, we fitted each of the *coefficients* of these functions with a function depending only on energy and sector number. The parameters of the latter functions were saved in a file destined to the CLAS_PARMS directory or the database.

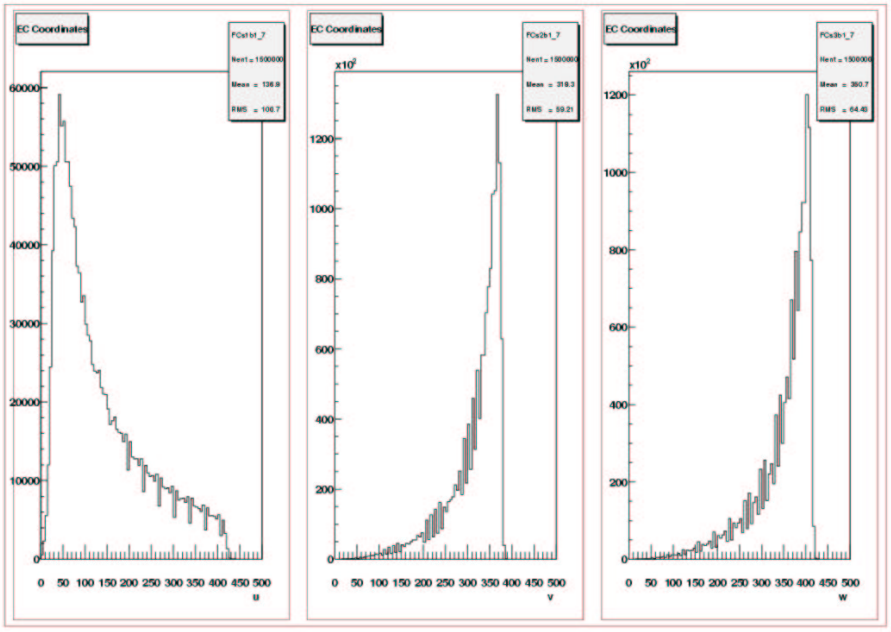


(a) Range of the calorimeter coordinates $u, v, w$. Dimensions on abscissa are in centimeters.

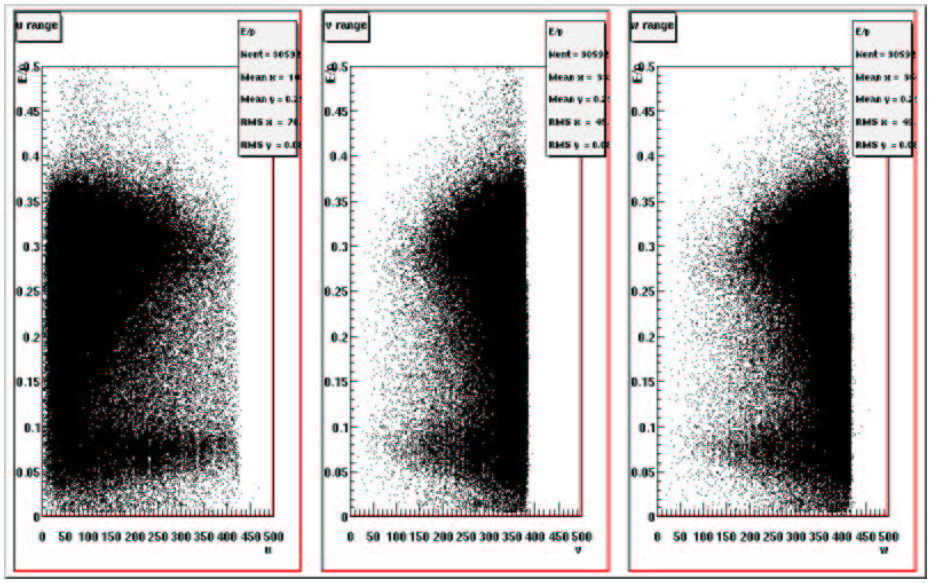


(b) Ratio $E_{EC}/p$ plotted versus each of the three calorimeter coordinates. All $p > 0.9$ GeV are considered here. For specific subranges please see [103]. Dimensions on abscissa are in centimeters.

Figure B-1: Forward calorimeter cut

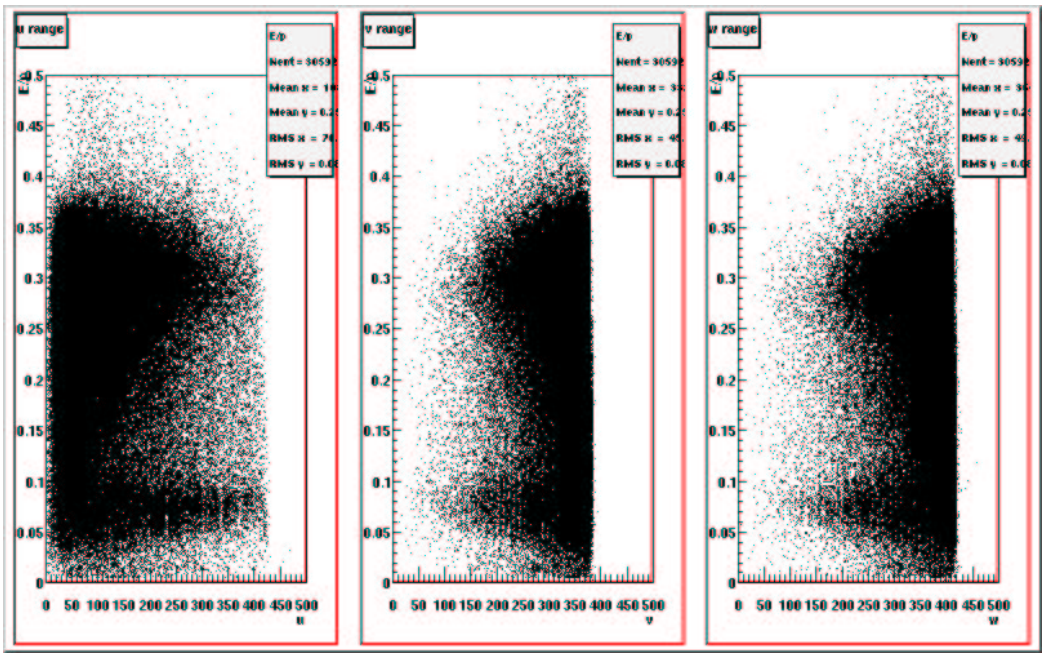


Figure B-2: Ratio $E_{EC}/p$ plotted versus each of the three calorimeter coordinates. All $p > 0.9$ GeV are considered here. For specific subranges please see [103]. Dimensions on abscissa are in centimeters.

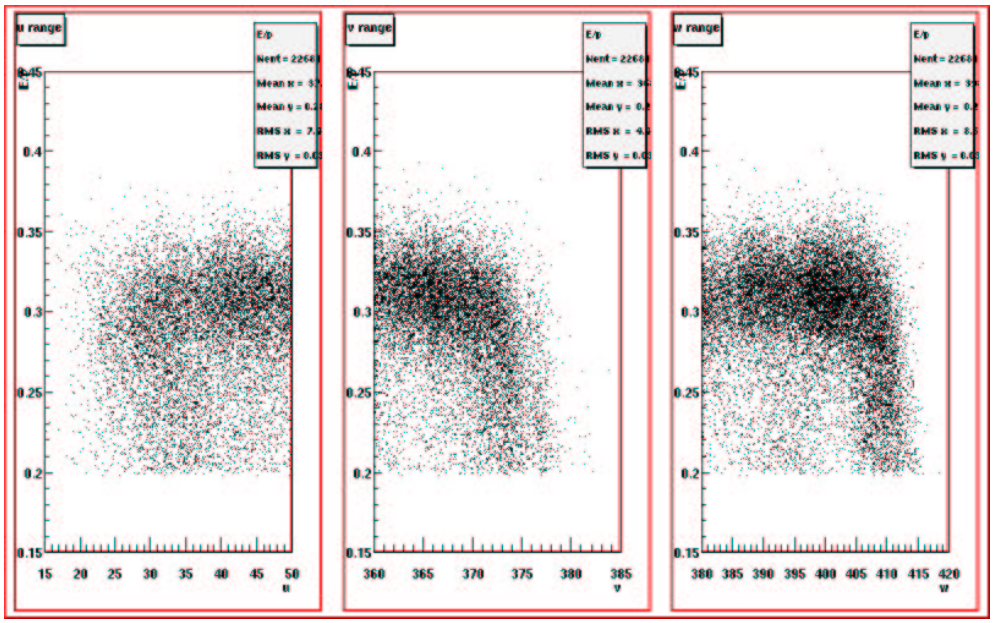


Figure B-3: Magnified view of the edges of the histogram in Fig.B.1(b) with a $p > 3.0$ GeV cut applied. One can easily notice the dramatic drop of the ratio $E_{EC}/p$ near the edges. Plots for each sector can be found in [103]. Dimensions on abscissa are in centimeters.

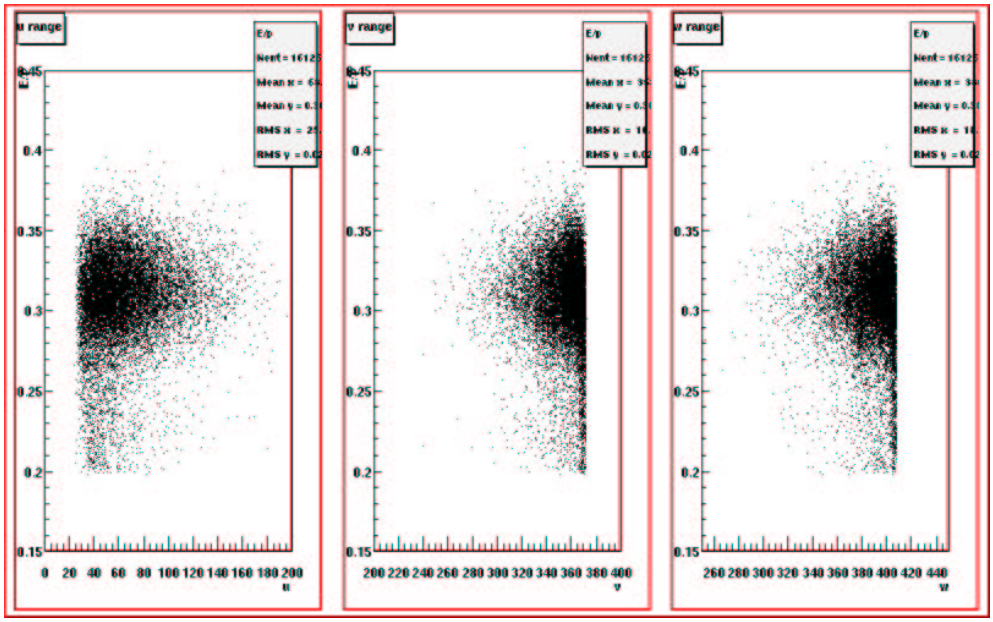


Figure B-4: Result of the cut on $u, v$ and $w$. Dimensions on abscissa are in centimeters.

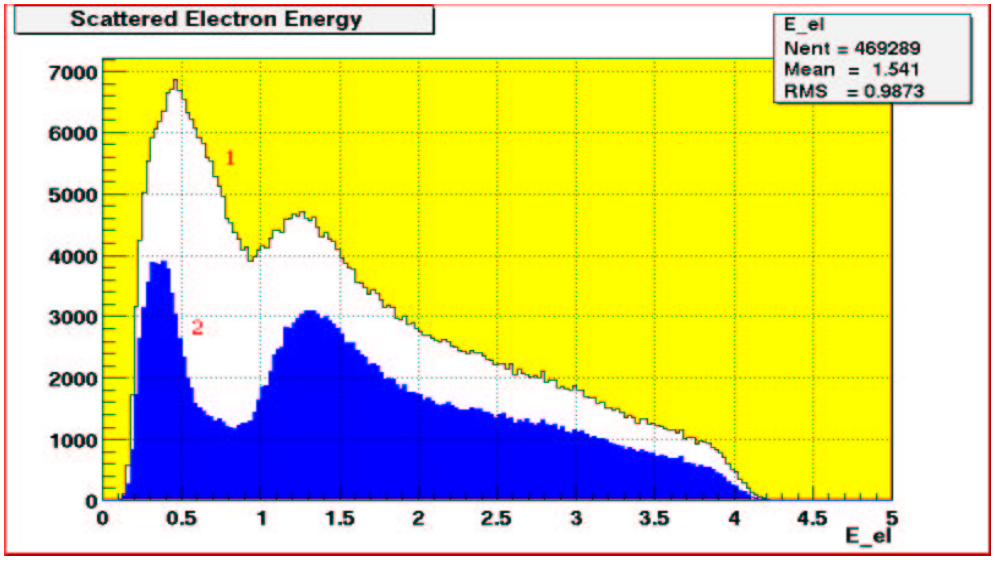


Figure B-5: Energy spectra of the electron before (1) and after (2) the forward calorimeter cut as given by equation (B.1). $E_{el}$ is in GeV.

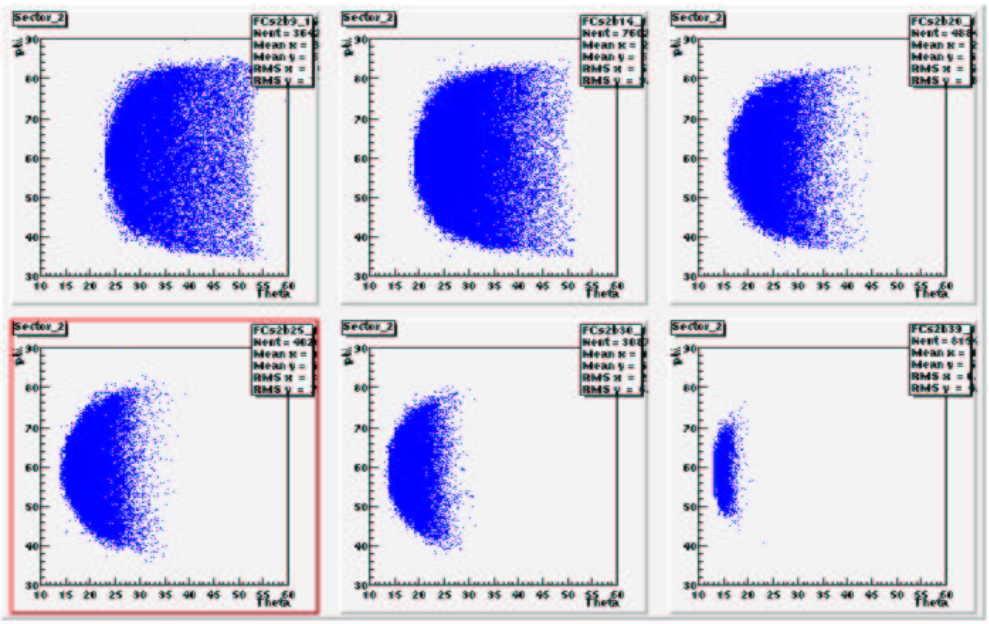

Figure B-6: Some typical plots of $\phi(\theta)$ dependency. For the rest, please consult reference [103]

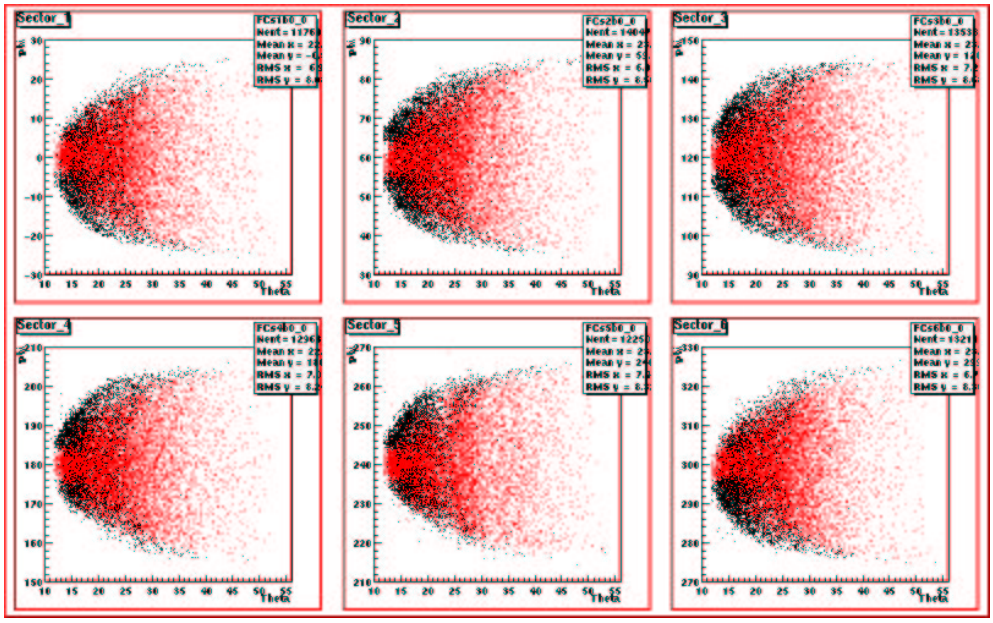

Figure B-7: Two dimensional histograms (counts vs $\theta$-$\phi$) showing the overall effect of the forward calorimeter cut. Black points show what is discarded by the cut. For more details, please consult [103].

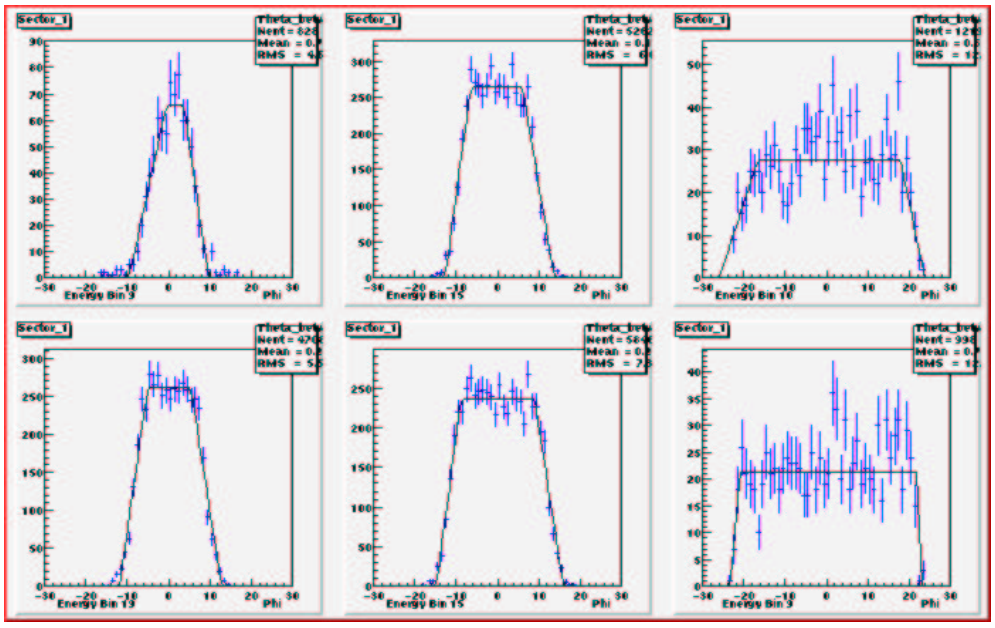


Figure B-8: Trapezoids fitted on histograms counts vs $\phi$ angle. We call the top "flat". Some typical examples. All the others can be found in [103].

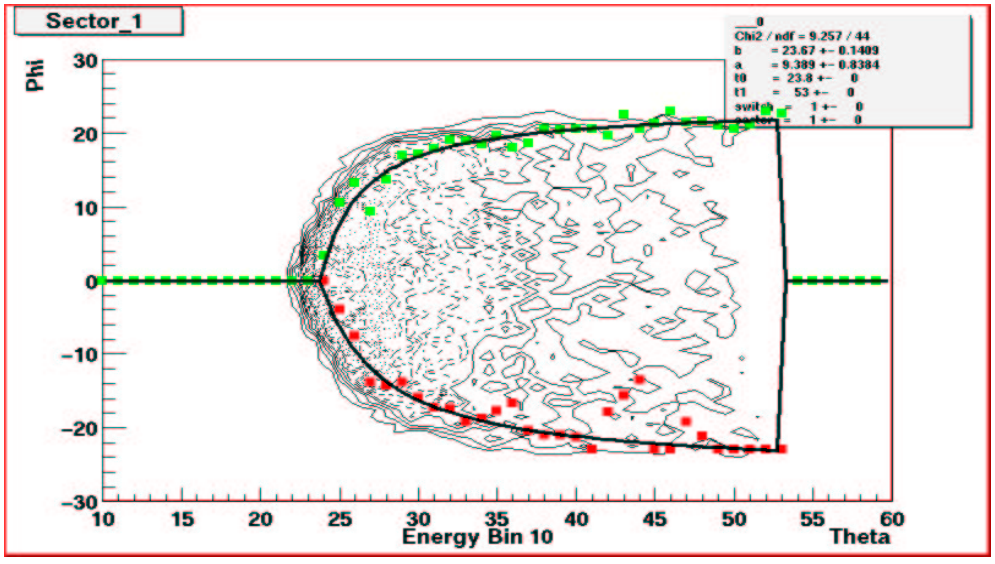


Figure B-9: Second generation fit. Energy bin 10 means 1.0 GeV $< p_{el} <$ 1.1 GeV. All other plots can be found in [103].

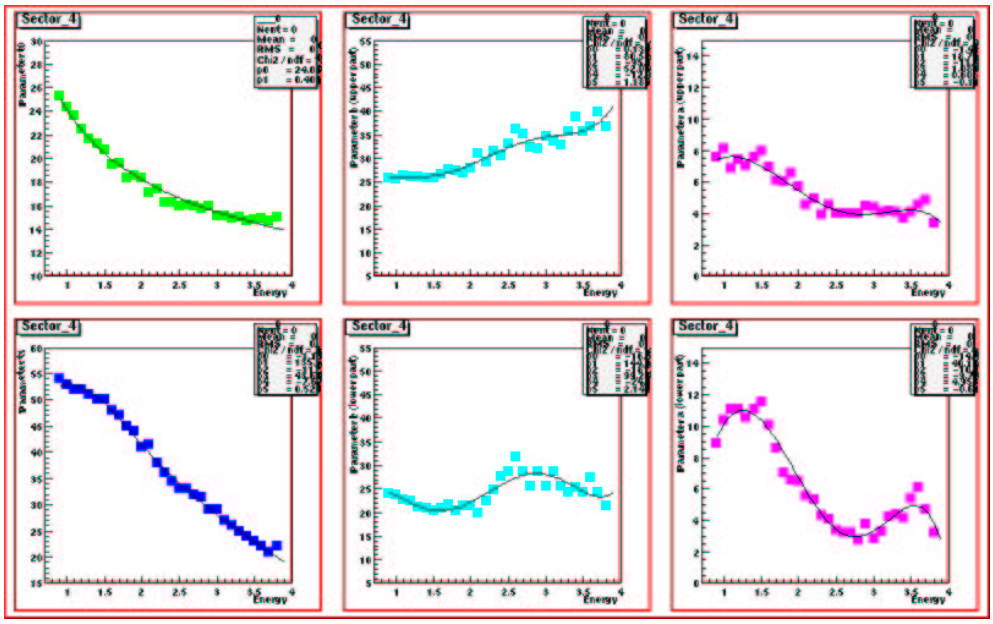


Figure B-10: Third generation fits. Each fit corresponds to one of the parameters in eq.(B.3). Only data for sector 4 is shown. For the others sectors, please consult [103]

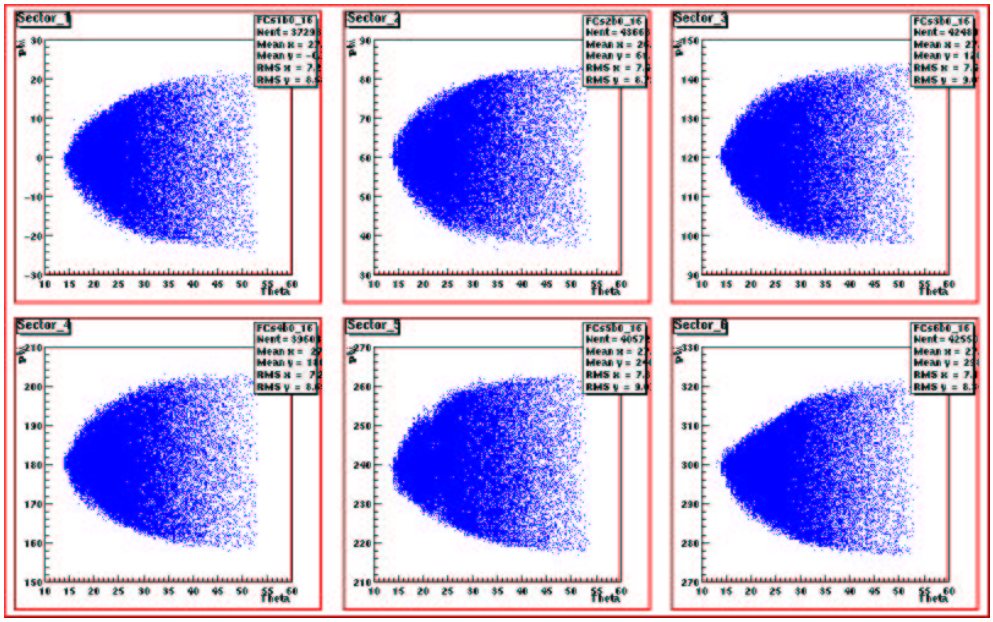


Figure B-11: Overall result of the cut. One can see that an asymmetrical shape resulted in some sectors. The fuzzy edges are due to bin overlap.

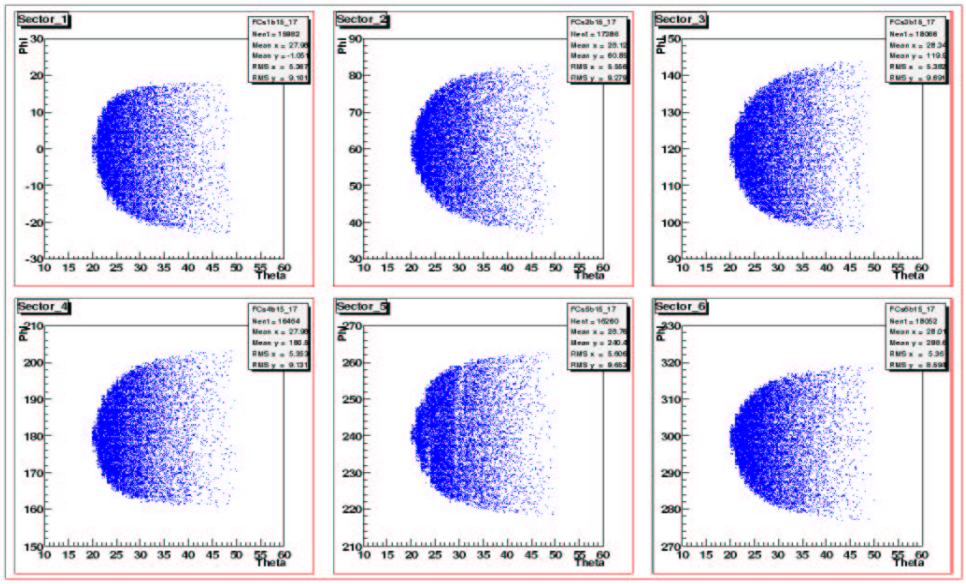


Figure B-12: Typical plots illustrating the result of the cut. Plase notice that some are asymmetrical. For more, please consult [103]

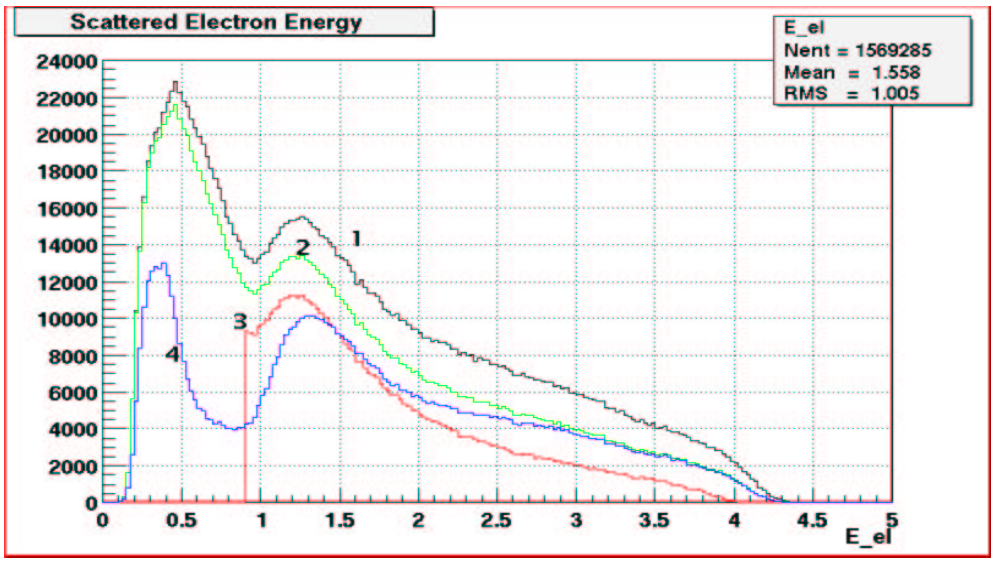


Figure B-13: Electron energy spectra at various stages of the procedure: before applying any cut (1), after the uvw cut (2), after the EC cut on $uvw$ and $E/p$ (4), final (3). On the last one, the region $p$ <0.9 GeV is ignored. $E_{el}$ is in GeV.

# Appendix C

## BEAM POLARIZATION AND HELICITY FOR E2A

To determine the beam polarization and the sign of the beam helicity one has to take into consideration a chain of factors: the polarity determined by the Møller runs, the half-wave plate position, the helicity bit encoding and, in our case, the delayed reporting scheme. If Møller runs are not available for a certain data set, then the polarization can be inferred by taking into account the beam polarization measured at the gun and the spin precession through the accelerator.

Beam polarization in Hall B is measured with a Møller polarimeter. In this device, the polarization is determined from the asymmetry of the counting rates when the helicity of the beam is reversed. About 20 minutes of measurement time or 3 M events are needed to take data with a statistical error below 1%.

The Møller data was analyzed online and the polarization data were saved in the runtime logbook [107, 108] and are presented in figure 3-8 and section C.2.

For the analysis of the 2.261 and 4.461 GeV data sets we use the average value of 63±2%. We estimate that the polarization measured by the Møller polarimeter is affected by a systematic error of approximately 3% coming primarily from uncertainties in the polarization of the Møller target.

The four days of 1.162 GeV $^{12}$C data (runs 18284 to 18335) were not in the original running plan for E2A [109] and no polarization measurement was conducted. To evaluate the average beam polarization for this period, we took the average value of the polarization for the rest of the run period, 63.0%, corrected it for precession (see subsection C.3) using the data from table C.7, and obtained a polarization in Hall B equal to $|(-0.28.) \times 63.0| = 17.6$ (%). We consider that such a value does not qualify for polarized beam measurements.

To summarize, we use $P_{beam} = (63 \pm 2 \pm 3)\%$ for the 2.261 and 4.461 GeV $^{12}$C and $^{4}$He data sets and we used the 1.161 GeV carbon data only for consistency checks.

We established with acceptable precision the absolute value of the beam polarization in the hall. Before we proceed to determine the absolute spin orientation, let us briefly review the beam characteristics.

The polarized electron source at CEBAF is an optically pumped strained GaAs crystal. A 780nm laser is used to project circularly polarized light onto the crystal. The laser is pulsed to the accelerator frequency of 0.5 GHz and the bunch-length is 50 ps. Left and right circular polarization of the laser beam are obtained with a Pockels cell by applying the voltage corresponding to the quarter wave retardation.

To eliminate possible bias, the helicity is flipped at a 30 Hz frequency and is phase locked to the 60 Hz AC cycle. Helicity pulses are associated in pairs of opposite helicity. The leading pulse helicity is chosen by a 24-bit pseudo-random number generator which also sends a signal to the DAQ to be recorded in the raw data file, to be stored in bits 15 and 16 of the word latch1 of TGBI bank [110].

The helicity signal is encoded in the cooked data files in various ways. In ntuple10, used by the E1C group, it is encoded into the EVNTCLAS variable (see description in subsection C.4) and in the analysis of the E2 RootDST-s, it is obtained with the use of THelicity class functions. Due to special demands imposed by the HAPPEX [106] parity violation experiment that was running in parallel in Hall A, the MCC[1] helicity signal was delayed by 8 pairs and therefore the true helicity had to be determined at the level of data analysis, as described in subsection C.5.

Another precaution that was taken was to insert periodically in the laser beam a $\lambda/2$ plate, which reverses helicities and thus provides a useful systematic check. The half wave plate position was saved in the EPICS database and is listed in subsection C.6.

The GetHelicity function returns $h$=+1 for bit16=1 and $h$=–1 for bit16=0 when the half wave plate position is OUT [112] and vice versa when the plate is IN, according to table C.3. What we have to establish is if indeed the reported $h$=+1 corresponds to positive beam helicity and $h$=–1 to negative beam helicity in the hall.

Our difficulty comes from the fact that we did not have a hydrogen target for an unequivocal determination of the sign of the helicity. Therefore, the correspondence between the helicity signal sent by the accelerator and the real helicity of the electron beam in the hall has to be deduced using CLAS E1C and Hall A data.

The E1C run period was right before the E2A data taking and the E1 group performed an absolute measurement of the sign of helicity.

**For the benchmark run 16833, taken at 4.247 GeV on 02/19/1999, between 19:23 and 21:46 when the the half wave plate was OUT, the values of EVNTCLAS=1,11 or 21 in ntuple10 corresponded to the negative beam helicity [94].**

Now, following subsection C.4, EVNTCLAS=1,11 or 21 in ntuple10 corresponds to helicity bit16=0 or $h$=–1 and then negative beam helicity would indeed correspond to $h$=–1 since the state was not altered by the $\lambda/2$ plate.

This conclusion is valid for the E2A data if the delayed reporting electronics introduced for HAPPEX did not alter the sign. To check this, Hall A data was used. Table C.1 shows that the Hall A helicity sign remains unchanged from February through May 1999 and that the absolute sign determined in Hall A is consistent with the Hall B benchmark (second row in table C.1), given the spin precession.

Considering the Wien angles listed in table C.7 and the spin precession as described in subsection C.3, the above correspondence applies to 2.261 GeV data as well, but must be reversed for the 1.161 $^{12}$C data set. These facts are all summarized in table C.1.

To summarize, we used online Møller data from the electronic logbook to figure out the beam polarization along the 2.261 and 4.461 GeV running. For the overall helicity sign, several paths of investigation were used, all leading to the same result:

(1) If the *spin precession* from the polarized gun to the hall is calculated, the Hall A helicity sign coincides with the Hall B sign

(2) A *Møller measurement* with positive Helmholtz yielded negative polarization in the hall when the $\lambda/2$ plate was OUT and the sign calculated with (1) was negative

(3) *Absolute measurement* conducted by the E1C group gives a negative sign of helicity where (1) and (2) gave negative polarization taking into account that the sign of helicity

[1] Machine Control Center, i.e. accelerator

| | Date | Wien | Linac | Hall A | | | | | Hall B | | | | | Comment |
|---|---|---|---|---|---|---|---|---|---|---|---|---|---|---|
| $\mathcal{N}^o$ | | $\theta_W(^o)$ | (MeV) | Time | WP | passes | hel | $\cos\theta_A$ | Time | WP | passes | hel | $\cos\theta_B$ | |
| 1 | 02/12 | 20.3 | 420 | 11:00 | IN | 2 | – | –1.00 | | | | | | E1C |
| 2 | 02/19 | 28.3 | 420 | 19:00 | OUT | 2 | + | –1.00 | 19:23 | OUT | 5 | – | +1.00 | K.J. [94] |
| 3 | 04/16 | 8.1 | 550 | 21:00 | OUT | 3 | + | –0.98 | 20:35 | OUT | 4 | – | +1.00 | E2A |
| 4 | 05/03 | 7.8 | 550 | 21:00 | OUT | 3 | + | –0.98 | 16:07 | OUT | 2 | – | +0.99 | |
| 5 | 05/16 | 3.8 | 550 | 14:00 | IN | 3 | – | –0.99 | | | | | | |
| 6 | 05/18 | 3.8 | 550 | 21:00 | OUT | 3 | + | –0.99 | 09:19 | OUT | 1 | + | –0.28 | |

Table C.1: Overall helicity sign comparison table. Absolute sign is defined as the beam helicity sign in the hall when bit16=0. Hall A values were provided by V. Chudakov [95]. Case $\mathcal{N}^o$6 had the Wien angle optimized for maximum polarization in Halls A and C.

measured in Hall A is consistent along the period considered (E1C to E2A)

## C.1 Møller Polarimetry

Møller polarimeters are widely used for electron beam polarization measurements in the GeV energy range. The Hall B beamline is equipped with one such device.

The Møller polarimeter consists of polarized electron target, (a magnetized foil that is moved onto the beam axis via a stepper) a set of Helmholtz coils to polarize the target, two quadrupole magnets and a pair of two lead scintillating fiber detectors. The polarimeter is remote controlled from the counting house.

The beam polarization is determined by measuring the asymmetry in the number of counts in a given detector as the beam helicity is flipped:

$$A_P = \frac{N^+ - N^-}{N^+ + N^-} \tag{C.1}$$

If the helicity correlated counts $N_\pm$ are normalized to the integrated beam current, then the beam polarization in the absence of background can be calculated with

$$P_B = \frac{A_P}{P_T A_{zz} F(\theta_s)} \tag{C.2}$$

where

$$F(\theta_s) = \cos\theta_s \cos\theta_T \left(1 + \frac{A_{xx}}{A_{zz}} \tan\theta_s \tan\theta_T \cos\phi_s \cos\phi_T\right)$$

and $\theta_T$, $\phi_T$ and $\theta_s$, $\phi_s$ are spherical angles of the target spin, respectively electron spin about the beam axis, $P_T$ is the target foil polarization and the asymmetries $A_{ii}$ are defined

as functions of the center-of-mass scattering angle $\theta$

$$\begin{aligned} A_{zz} &= -\frac{(7+\cos^2\theta)\sin^2\theta}{(3+\cos^2\theta)^2} \\ A_{xx} &= -A_{yy} = -\frac{\sin^4\theta}{(3+\cos^2\theta)^2} \end{aligned} \tag{C.3}$$

At the angle $\theta = 90^o$ the asymmetries $A_{xx}, A_{yy}$ and $A_{zz}$ are maximized. One can set the polarimeter so that this situation occurs.

## C.2 Møller Runs For E2A

The online Møller polarization data is listed in table C.2. For the first five entries, two values ($P$ and $P'$) were listed and the average was taken.

Where measurements with two target polarizations were done, they were combined before being plotted in figure 3-8. The $\pm$ polarization runs are taken so that one can correct for any beam charge asymmetry:

$$P_B = \frac{|P_-| + |P_+|}{2}$$

where $P_-$ is the measured beam polarization with negative target polarization and $P_+$ corresponds to a positive target run. This works because $A_{measured} \simeq A_{moller} + A_{beam}$, where $A$ stands for asymmetry [96].

When the $\lambda/2$ plate is OUT and the Møller target polarization is positive, the beam polarization in the hall was measured to be negative. This correspondence is consistent along the 2.261 and 4.461 GeV runs, except for the cases marked with asterisk where most probably the minus sign was mistakenly omitted by the person who logged the entry.

## C.3 Spin Precession

Following reference [97], the spin precession from the injector to Hall B gives the total angle:

$$\theta_B = P\left[2n_B^2 - n_B(1-2\alpha) - \alpha\right]\pi + \theta_W$$

where $n_B$ is the number of recirculation passes, $\theta_W$ is the Wien launching angle, $P = (E_l/m_e)[(g-2)/2]$, $E_l$ is the energy of a single linac (in MeV), $\alpha = 0.1125$ is the ratio of the injector energy to the linac energy, $m_e = 0.51099906$ MeV/c$^2$ and $[(g-2)/2] = 0.001159652$. The spin precession for Hall A is calculated similarly with the formula:

$$\theta_A = P\left[2n_A^2 - n_A\left(1-2\alpha-\frac{1}{2.4}\right) - \alpha\left(1-\frac{1}{4.8}\right)\right]\pi + \theta_W$$

Both linacs are assumed to operate at the same energy and therefore the number of passes and the beam energy in any particular hall are related by

$$n_{A,B,C} = (E_{A,B,C}/E_l - \alpha)/2$$

| Date | Run $\mathcal{N}^o$ | Foil | Helmholtz | P (%) | P'(%) | $\delta P$(%) | $\theta_W(^o)$ |
|---|---|---|---|---|---|---|---|
| | $E_{beam}$ = 4.461 GeV ($^4$He and $^{12}$C ) | | | | | | 7.9 |
| | $\lambda/2$ plate is OUT | | | | | | |
| 04/16 | 17892 | l | + | -59.5 | 60.9 | 1.7 | |
| | 17893 | r | + | -60.8 | 63.4 | 1.7 | |
| | 17894 | r | - | 62.0 | 65.7 | 1.7 | |
| | 17895 | l | - | 60.2 | 62.3 | 1.7 | |
| | 17898* | l | + | 62.1 | 64.1 | 1.6 | |
| | | Apf offline: (63.40 +/- 0.81)% | | | | | |
| | $\lambda/2$ plate is OUT | | | | | | |
| 04/19 | 17943* | | + | 64.13 | | | |
| | 17944 | | - | 60.60 | | | |
| | 17945 | Apf offline: (64.1 +/- 1.2)% | | | | | |
| | $E_{beam}$ = 2.261 GeV ($^4$He and $^{12}$C ) | | | | | | 8.0 |
| | $\lambda/2$ plate is IN | | | | | | |
| 05/02 | 18110* | l | + | 60.0 | | 3.0 | |
| | $\lambda/2$ plate is OUT | | | | | | |
| 05/08 | 18212* | l | + | 66.5 | | 3.0 | |
| | 18217 | l | + | -64.8 | | 0.6 | |
| | 18218 | l | - | 64.2 | | 0.8 | |
| 05/10 | 18253 | l | + | -67.0 | | 1.0 | |
| | 18254 | l | - | 67.7 | | 1.0 | |
| | $E_{beam}$ = 1.161 GeV ($^3$He and $^{12}$C ) | | | | | | 3.8 |
| | $\lambda/2$ plate is OUT | | | | | | |
| | No Møller Done | | | | | | |
| | $E_{beam}$ = 2.261 GeV ($^3$He and $^{12}$C ) | | | | | | 6.0 |
| | $\lambda/2$ plate is OUT | | | | | | |
| 05/19 | 18357 | l | + | -64.40 | | | |
| | 18358 | r | - | 66.84 | | | |
| | 18359 | r | - | 66.99 | | | |
| | 18360 | r | - | 65.83 | | | |
| | $\lambda/2$ plate is IN | | | | | | |
| 05/22 | 18396 | r | - | 64.08 | | 1.06 | |
| | 18397 | r | + | -64.20 | | 0.69 | |
| | $\lambda/2$ plate is OUT | | | | | | |
| 05/23 | 18423 | l | + | -66 | | | |
| | 18424 | l | - | 62 | | | |
| | $E_{beam}$ = 4.461 GeV ($^3$He and $^{12}$C ) | | | | | | 4.0 |
| 05/27 | 18478* | l | + | 61.7 | | | |
| | 18479 | l | - | 61.6 | | | |

Table C.2: Møller runs for the E2A run period from [107]. The target polarization is given by the Helmholtz coil polarity. The Wien angle data from the accelerator logbook (table C.5) were added here on the last column.

## C.4 Ntuple 10 Helicity Encoding

Helicity information comes in TGBI bank in the first word "latch1". Bit 15 of the word is a helicity clock and bit 16 is the helicity state. First bits contain information on L1 trigger bits. Here it is what it was in the N-tuple during E2A and E1C:

$$\text{EVNTCLAS} = (HelicityInformation + 1) + \ 10 \times (TriggerBit - 1)$$

Note that E2A ran with 3 trigger bits, but really only 2 where useful and that this encoding scheme has been changed lately [93].

HelicityInformation = TGBIFirstWord/10000. This will be $\geq 3$ if bit16 is set to 1 and will be $\leq 1$ if bit16=0, since $2^{14}$=16384, $2^{15}$=32768 and $2^{14}+2^{15}$=49152. So HelicityInformation can be = 0,1 if bit16=0, and 3,4 if bit16=1. To summarize, what we have for EVNTCLAS is the following:

- (1,2),(11,12),(21,22) correspond to b16=0
- (4,5),(14,15),(24,25) correspond to b16=1

## C.5 Decoding of the Delayed Helicity Signal

As mentioned earlier, the reported helicity information during our running period was delayed by 8 cycles due to the stringent requirements of the HAPPEX parity violation experiment. To retrieve the helicity state of a particular event, one would thus need to look at an event that is $8 * 1/30 = 0.26$ seconds later, or approximately 800 events. However, this becomes more complicated when there are gaps in the data (due to beam trips etc.) that may mean that there is no information available for those events.

An alternative method that was used in this data analysis is to predict the state of the pseudo-random generator, and then use this predicted value. Since we know the exact construction of the pseudo-random generator, we can simulate its behavior in software, and thus predict its state perfectly accurately at any time, given the state it is in at some other time.

The pseudo-random generator is built from a shift register and a NOT-XOR module. The bits of the shift register at numbers 23, 22, 21 and 16 are fed into the NOT-XOR, and the result of the NOT-XOR is the new bit that is shifted into the shift register at the

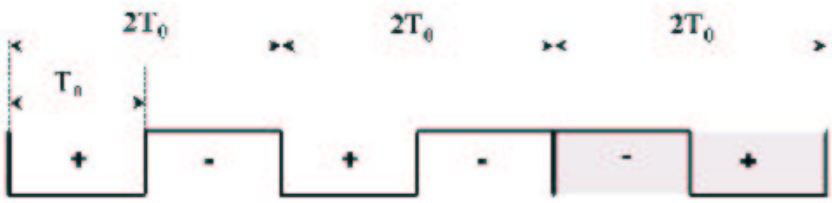


Figure C-1: Time structure of the polarized beam delivered by the accelerator. For E2A, $2T_0$ = 1/30 s. The shaded region shows a sign reversal produced by the random assignment function. (from Anghinolfi *et al.* [84]).

next clock cycle. This new bit is then either used directly of used inverted, depending on the "LATCH1" signal, to set the voltage on the Pockels cell and flip the helicity of the beam. The resulting train of bits is thus composed of helicity pairs: $(0,1)$ or $(1,0)$ in a pseudo-random sequence.

To predict this sequence we need to find the state of the shift register at the start of each run. This is done by looking at 24 consecutive clock cycles of the shift-register, and recording the input, i.e. the helicity bit. This set then forms the input to the calculation that can predict the state of the shift-register - and thus the helicity bit - at any time in the past or future, by knowing how many clock cycles have passed.

The code that does this simulation was written in such a way that it is self-checking. It starts with the status of the shift register at the beginning of the run. It then winds forward to the state that the shift register should be in, if there was no delay in the reporting. Then compares the predicted bit with the bit reported in the data, verifying that the prediction is correct. For delayed reporting, this then verified that the result obtained 8 clock cycles ago (approximately 800 events) was indeed correct. To calculate then what the bit actually is for this event we just wind the register forward 8 more clock cycles.

## C.6 Half-wave Plate Position

The $\lambda/2$ plate positions for the E2A run period as reported in the electronic logbooks of accelerator and Hall B is listed in table C.3. The E2A data acquisition started on April $16^{th}$, at 17:09 and the last E2A run ended on May $27^{th}$ at 21:54. Table table C.4 shows the $\lambda/2$ plate position in the period previous to E2A.

## C.7 Wien Angle Table

Wien angle values extracted from the MCC electronic logbook are listed in table C.5. The spin precession is described in subsection C.3.

| Date and Time | | State |
|---|---|---|
| 11 Apr 1999 | Sun 16:30:15 | 0 |
| 16 Apr 1999 | Fri 22:30:14 | 1 |
| 16 Apr 1999 | Fri 22:50:19 | 0 |
| 17 Apr 1999 | Sat 09:50:14 | 1 |
| 19 Apr 1999 | Mon 20:30:17 | 0 |
| 21 Apr 1999 | Wed 22:30:33 | 1 |
| 23 Apr 1999 | Fri 13:20:20 | 0 |
| 29 Apr 1999 | Thu 16:09:57 | 1 |
| 29 Apr 1999 | Thu 16:19:57 | 0 |
| 29 Apr 1999 | Thu 18:59:56 | 1 |
| 3 May 1999 | Mon 06:59:55 | 0 |
| 5 May 1999 | Wed 07:20:19 | 1 |
| 7 May 1999 | Fri 07:30:24 | 0 |
| 14 May 1999 | Fri 02:20:22 | 1 |
| 17 May 1999 | Mon 20:20:25 | 0 |
| 18 May 1999 | Tue 14:30:20 | 1 |
| 18 May 1999 | Tue 18:00:23 | 0 |
| 20 May 1999 | Thu 00:10:25 | 1 |
| 22 May 1999 | Sat 23:00:21 | 0 |
| 25 May 1999 | Tue 14:20:20 | 1 |
| 10 Jun 1999 | Thu 08:40:25 | 0 |

Table C.3: Half-wave plate position during the E2A run period: 1 means IN, 0 is OUT. From [93, 94].

| Date and Time | | State |
|---|---|---|
| 5 Jan 1999 | Tue 16:44:57 | 0 |
| 6 Jan 1999 | Wed 15:14:42 | 1 |
| 11 Jan 1999 | Mon 10:30:50 | 0 |
| 14 Jan 1999 | Thu 11:45:28 | 1 |
| 14 Jan 1999 | Thu 13:30:21 | 0 |
| 23 Jan 1999 | Sat 11:00:13 | 1 |
| 25 Jan 1999 | Mon 11:00:20 | 0 |
| 28 Jan 1999 | Thu 13:45:11 | 1 |
| 30 Jan 1999 | Sat 10:00:10 | 0 |
| 6 Feb 1999 | Sat 12:00:11 | 1 |
| 7 Feb 1999 | Sun 12:45:10 | 0 |
| 10 Feb 1999 | Wed 10:30:13 | 1 |
| 12 Feb 1999 | Fri 18:00:10 | 0 |
| 15 Feb 1999 | Mon 17:14:40 | 1 |
| 16 Feb 1999 | Tue 09:30:15 | 0 |
| 16 Feb 1999 | Tue 11:30:21 | 1 |
| 16 Feb 1999 | Tue 18:30:10 | 0 |
| 19 Feb 1999 | Fri 23:15:10 | 1 |
| 21 Feb 1999 | Sun 16:45:12 | 0 |
| 24 Feb 1999 | Wed 13:30:12 | 1 |
| 27 Feb 1999 | Sat 00:30:12 | 0 |
| 23 Mar 1999 | Tue 16:00:27 | 1 |
| 23 Mar 1999 | Tue 17:00:24 | 0 |
| 24 Mar 1999 | Wed 13:00:23 | 1 |
| 24 Mar 1999 | Wed 13:10:30 | 0 |
| 28 Mar 1999 | Sun 17:40:18 | 1 |
| 28 Mar 1999 | Sun 23:00:11 | 0 |
| 29 Mar 1999 | Mon 03:50:11 | 1 |
| 29 Mar 1999 | Mon 13:20:19 | 0 |
| 29 Mar 1999 | Mon 15:50:11 | 1 |
| 30 Mar 1999 | Tue 09:40:12 | 0 |
| 10 Apr 1999 | Sat 19:20:17 | 1 |

Table C.4: Half-wave plate position for February-April 1999: 1 means IN, 0 is OUT. From [93, 94].

| Date | Wien angle $\theta_W$ ($^o$) | Comments |
|---|---|---|
| 02/17 | 28.1 | E1C |
| 02/18 | 30.0 | |
| 03/25 | 37.1 | |
| 03/29 | -2.5 | |
| 04/01 | 8.0 | |
| 04/14 | 7.9 | E2A |
| 04/26 | 8.0 | |
| 04/28 | 7.6 | |
| 05/13 | 6.0 | |
| 05/18 | 3.8 | $^{12}$C , 1.161 GeV |
| 05/27 | 4.0 | |

Table C.5: Wien angles from MCC electronic logbook.

# Appendix D

## MISCELLANEOUS

### D.1 Nucleon-nucleon scattering parameters

Nucleon-nucleon scattering parameters $\sigma_{pN}^{tot}, \beta_{pN}$ and $\epsilon_{pN}$ (eq. 2.40) are shown in figures D-1 and D-2.

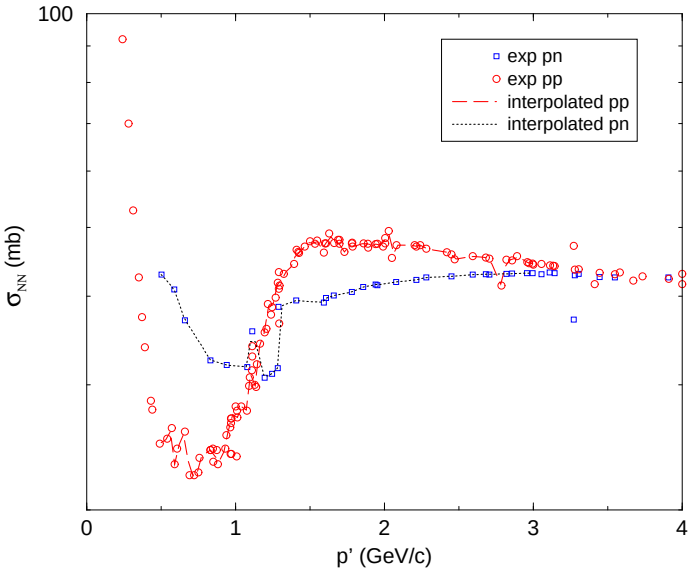


Figure D-1: Nucleon-nucleon scattering data: $\sigma_{pN}^{tot}$ cross sections. Abscissa $p'$ is the proton momentum. From [24].

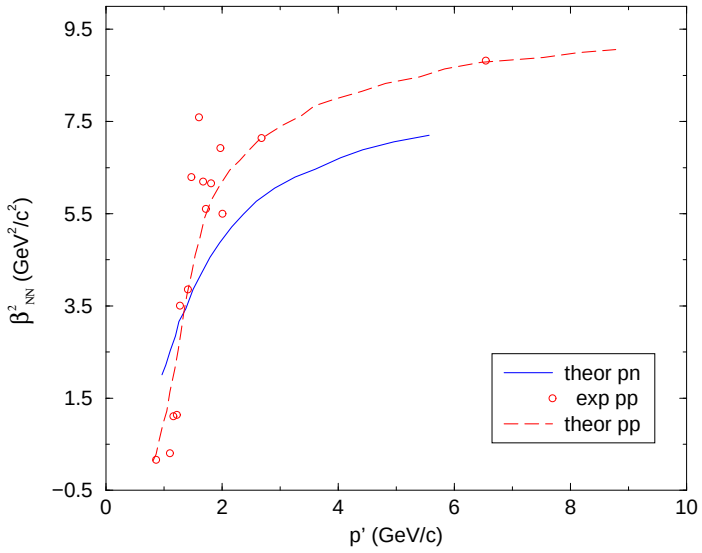


(a)

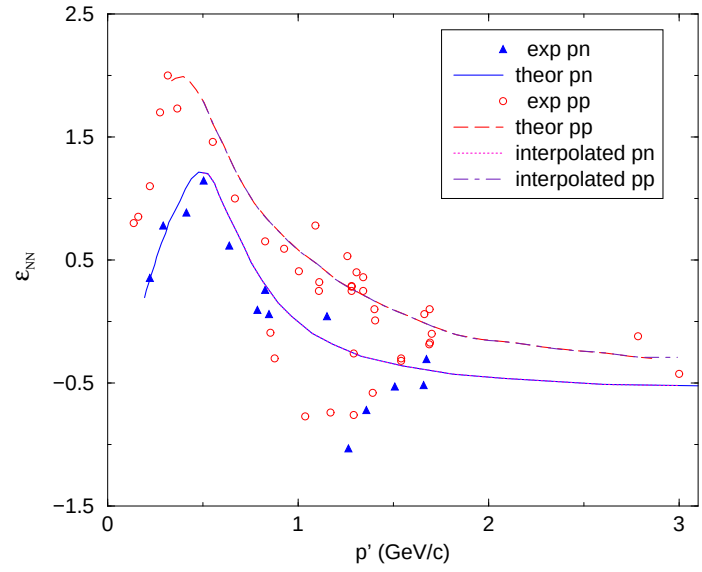


(b)

Figure D-2: Nucleon-nucleon scattering data: (a) the slope parameters $\beta_{pN}$ and (b) the ratio of the real to imaginary scattering amplitude $\epsilon_{pN}$. Abscissa $p'$ is the proton momentum. From [24].

## D.2 Blueprint of the CLAS Target System

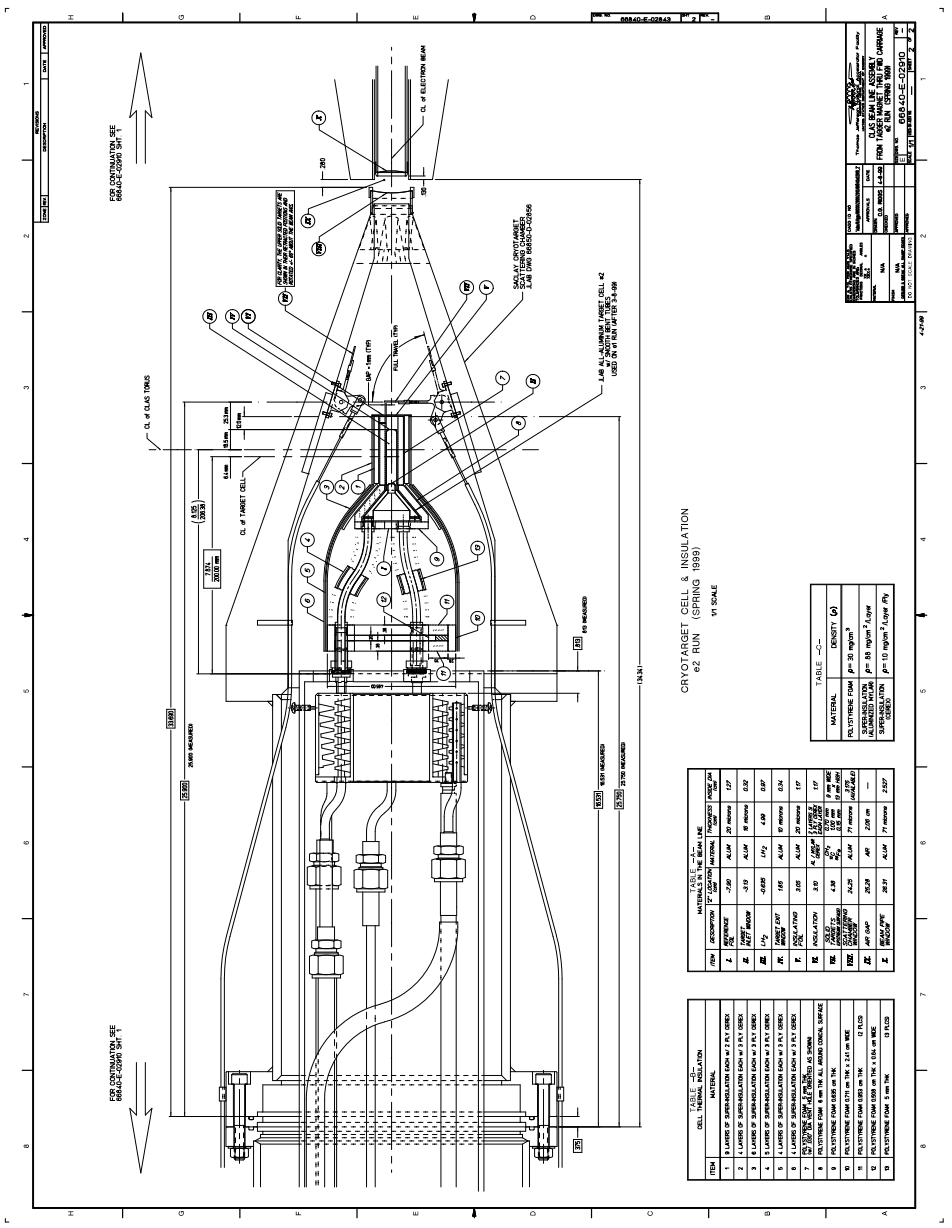

## D.3 Shell Script for TOF Calibration

```
#!/usr/bin/tcsh -f
#
# runs executables for gmean and attenuation length calibration
# @ protopop 08/04/1999
#
# This script follows exactly the procedure for the calibration of
# geometrical mean and attenuation length, but it spares you the effort of
# writing the configuration files, reformatting the outputs for the next
# step, creating links etc., where errors are very likely to occur. tofs
# uses the executables gmean_cooked, hscan_means, min_means_main,
# tof_calib, hscan_atten, min_atten, adc_const. The script checks the
# intermediate files and, if needed, prompts the user to make the
# appropriate corrections. At the end, tofs puts the constants in a
# standard file format and e-mails a report to the user. The execution
# takes 1 to 2 hours

if ($#argv == 0) then
 echo "Usage: tofs run_number"
 echo "e.g. tofs 12345 "
 exit
endif

# INPUT FILES:
# needed: clas_0xxxxx.A00     for     tof_calib
#         dst0xxxxx.Axx.B0x   for    gmean_cooked
#
# you can change this to full path of input files:
# e.g. set destination = `echo $2` and delete the following if-s

echo " "
set destination = "/work/clas/disk1/protopop/work/"
echo Will read from $destination.
ls  $destination/cooked | grep $1.A00
ls  $destination/data | grep $1.A00

# DEFINITIONS:
set cooked_file = `ls $destination/cooked | grep dst | grep $1.A00`
set raw_file = `ls $destination/data | grep clas_0 | grep $1.A00`
set arch = ~/calibration/p2p_delay_el/archive

# all EXECUTABLES should be in the current directory.
# needed:  gmean_cooked
```

```
#          hscan_means
#          min_means_main
#          tof_calib
#          hscan_atten
#          min_atten
#          adc_const
#
echo ------------------------------------------------------------------

# GMEAN_COOKED:
echo Doing calibration on geometric mean of MIP peak position:
 echo Reading $cooked_file ...
 gmean_cooked -n500000 -ogmean$1.hbook  $destination/cooked/$cooked_file

rm hscan_input hscan_data min_input min_parm min_kumac min_output

# HSCAN_MEANS:
 rm hscan_input
 rm hscan_data
 ln -s gmean$1.hbook hscan_input
 ln -s gmean$1.dat hscan_data
 ls -lgF hscan_input
 ls -lgF hscan_data
hscan_means <<+
y
g
+

# MIN_MEANS_MAIN:
rm min_input
rm min_parm
rm min_kumac
ln -s gmean$1.dat  min_input
ln -s gmean$1.parm min_parm
ln -s min_means$1.kumac min_kumac
ln -s gmean$1.out min_output
# show
ls -lgF min_input
ls -lgF min_kumac
ls -lgF min_parm
ls -lgF min_output
min_means_main

# CLEANING:
rm hscan_input
```

```
rm hscan_data
rm min_input
rm min_parm
rm min_kumac
rm min_output

echo "GMEAN -> DONE"

echo ------------------------------------------------------------
echo Starting attenuation length calibration:
echo Reading $raw_file ...
set n = 0
# LOOP OVER SECTORS
while ($n < 6)
 @ n++
 echo ------------------------------------------------------------
 banner $n
 tof_calib -n500000 -s$n -o$1s$n.hbook -A $destination/data/$raw_file
# tof_calib -n500000 -s$n -o$1s$n\_gmean.hbook -c -R $destination/$raw_file
#
# HSCAN:
#
# Files used:
#
# Histogram input file:         hscan_input
# ASCII output file:            hscan_data
# ASCII data file               min_input       output of hscan
# Fitted parameters             min_parm        used to update map file
# Minuit List Output            min_output
# Kumac File to view results    min_kumac       PAW with file = hscan_input
#
# deletes, then defines new input and output links
#
 rm hscan_input hscan_data min_input min_parm min_kumac
 ln -s $1s$n.hbook hscan_input
 ln -s $1s$n\_atten.dat hscan_data
 ln -s $1s$n\_atten.dat min_input
 ln -s $1s$n\_atten.parm min_parm
 ln -s $1s$n\_atten.kumac min_kumac
# show
 ls -lgF hscan_input
 ls -lgF hscan_data
 ls -lgF min_input
 ls -lgF min_kumac
 ls -lgF min_parm
```

```
 echo Now scanning ...
 hscan_atten
#
# MINIMIZATION:
 min_atten
 cp min_kumac min$1s$n.kumac
 end
# END LOOP

# CLEANING:
rm hscan_input
rm hscan_data
rm min_input
rm min_parm
rm min_kumac

echo ----------------------------------------------------
echo Checking gmean$1.parm ...
set egm = `cat gmean$1.parm | grep \* | cut -d"*" -f1 | cut -d. -f2`
if ($egm > 0) then
 echo Please correct error in gmean$1.parm:
 cat gmean$1.parm | grep \*
 xterm -e pico gmean$1.parm
else
 echo File gmean$1.parm is OK.
endif

set m = 0
echo Doing a check on the atten.parm files ..
#ls -al | grep _atten.parm
while ($m < 6)
  @ m++
  set lines = `wc -l $1s$m\_atten.parm | cut -d"1" -f1`
  if ($lines < 48) then
     echo "Error in" $1s$m\_atten.parm. Please correct it:
     xterm -e pico $1s$m\_atten.parm
  else
     echo $1s$m\_atten.parm is OK
  endif
end

echo ----------------------------------------------------
echo Concatenating the parm files into atten$1.parm ...
cat $1s1_atten.parm >! atten$1.parm
set m = 1
```

```
while ($m < 6)
 @ m++
 cat $1s$m\_atten.parm >> atten$1.parm
end
# show
ls -al | grep atten$1.parm

echo "ATTEN -> DONE"

echo ------------------------------------------------------
echo Now producing the file for map ...
# ADC_CONST:
cp gmean$1.parm gmean.parm
cp atten$1.parm atten.parm
sleep 3
adc_const
cp adc.4map adc$1.4map
ls -al | grep adc$1.4map
# this file has seven columns; use awk to put constants in the map
# CLEANING:
rm gmean.parm atten.parm adc.4map

echo Saving to archive ...
cp adc$1.4map $arch/
cp atten$1.parm $arch/temp/
cp gmean$1.parm $arch/temp/
cd $arch
chmod a-w *.4map
ls -al | grep adc$1.4map
cd temp/
ls -al | grep $1.parm
echo "ADC_CONST -> DONE"

echo ---------------------------------------------------
echo "Now sending mail to user ..."
echo " " >! letter
echo "New sets of constants for the map are in:" >> letter
echo " " >> letter
echo $arch/adc$1.4map >> letter
echo " " >> letter
mail $user@jlab.org < letter
rm letter

echo "DONE"
```